Environment-sensitive targeted fluorescent probes for live-cell imaging

Dmytro Danylchuk

UNIVERSITÉ DE STRASBOURG

ÉCOLE DOCTORALE DE SCIENCES CHIMIQUES

Laboratoire de bioimagerie et pathologies – UMR 7021

CNRS

THÈSE présentée par :

Dmytro DANYLCHUK

soutenue le : **9 février 2021**

pour obtenir le grade de : **Docteur de l'université de Strasbourg**

Discipline/ Spécialité : chimie/chimie organique

Environment-sensitive targeted fluorescent probes for live-cell imaging

THÈSE dirigée par :

[Dr. KLYMCHENKO Andrey]	Directeur de recherche CNRS, Université de Strasbourg
[Dr. CHABERT Philippe]	Ingénieur de Recherche CNRS, Université de Strasbourg

RAPPORTEURS :

[Prof. MATILE Stefan]	Professeur, Université de Genève
[Prof BURGER Alain]	Professeur, Université Côte d'Azur

AUTRES MEMBRES DU JURY :

[Dr. HE Hai-Tao]	Directeur de recherche CNRS, Centre d'Immunologie de Marseille-Luminy

Direction de la **recherche**
et de la **valorisation**
Collège **doctoral**
Université de Strasbourg

Déclaration sur l'honneur
Declaration of Honour

J'affirme être informé que le plagiat est une faute grave susceptible de mener à des sanctions administratives et disciplinaires pouvant aller jusqu'au renvoi de l'Université de Strasbourg et passible de poursuites devant les tribunaux de la République Française.

Je suis conscient(e) que l'absence de citation claire et transparente d'une source empruntée à un tiers (texte, idée, raisonnement ou autre création) est constitutive de plagiat.

Au vu de ce qui précède, **j'atteste sur l'honneur que le travail décrit dans mon manuscrit de thèse est un travail original et que je n'ai pas eu recours au plagiat ou à toute autre forme de fraude.**

I affirm that I am aware that plagiarism is a serious misconduct that may lead to administrative and disciplinary sanctions up to dismissal from the University of Strasbourg and liable to prosecution in the courts of the French Republic.

I am aware that the absence of a clear and transparent citation of a source borrowed from a third party (text, idea, reasoning or other creation) is constitutive of plagiarism.

In view of the foregoing, ***I hereby certify that the work described in my thesis manuscript is original work and that I have not resorted to plagiarism or any other form of fraud.***

Nom : Prénom : DANYLCHUK Dmytro

Ecole doctorale : ED222

Laboratoire : UMR 7021 CNRS

Date : 15/03/21

Signature :

Acknowledgements

I would like to express my gratitude to my supervisor Dr. Andrey Klymchenko for the valuable advice, supervision, patience and support, as well as for the experience I acquired during my work here. Without your efforts this project could never be finished.

I would also like to thank Dr. Philippe Chabert for the valuable help and advice in both laboratory work and administrative routine. Additional thanks for cultural insights you have kindly provided and your cakes.

I would like to express my gratitude to Dr. Delphine Garnier, Dr. Estefania Oliva of PACSI team for the help with analysis, which was often tricky. I also thank Romain Vauchelles of PIQ team for the valuable advice and help with microscopy experiments and data analysis.

I would like to thank Dr. Sasha Koniev, Dr. Sergii Kolodych and the members of the team of Alain Wagner for the help with synthesis, especially for providing the facilities and reagents when they were urgently needed.

I thank my labmates and colleagues for the help with experiments, as well as for all the fun we had together.

I express my gratitude to Dr. Prof. Vasyl Pivovarenko for the tutorship, advice and help, which eventually led me to Strasbourg.

I thank Hanna for supporting, helping and motivating me.

I thank my family for their constant support and belief in me.

Contents

List of used abbreviations

3HF	3-hydroxyflavone
4DMP	4-(N,N-dimethylamino)phthalimide
6DMN	6-(N,N-dimethylamino)-2,3-naphthalimide
ACQ	Aggregation-induced quenching
AIE	Aggregation-induced emission
ATP	Adenosine triphosphate
BME	β-mercaptoethanol
BODIPY	Boron-dipyrromethene
BSA	Bovine serum albumine
CHO	Chinese hamster ovary
DCDHF	Dicyanodihydrofuran
DCM	Dichloromethane
DCVJ	9-(dicyanovinyl)julolidine
DIPEA	Diisopropylethyl amine
DMABN	4-dimethylaminobenzonitrile
DMEM	Dulbecco`s modified eagle medium
DMF	N,N-dimethylformamide
DMNB	4,5-dimethoxy-2-nitrobenzyl
DOPC	Dioleoyl-*sn*-glycero-3-phosphocholine
DPBS	Dulbecco's Phosphate Buffered Saline
DPPC	Dipalmitoyl-*sn*-glycero-3-phosphocholine
DNA	Deoxyribonucleic acid
ER	Endoplasmic reticulum
ESI	Electrospray ionization
ESIPT	Excited state intramolecular proton transfer
FBS	Fetal bovine serum
FLIM	Fluorescence lifetime imaging
FRET	Förster resonance energy transfer
GP	Generalized polarization
GPI	Glycophosphatidylinositol
GPMV	Giant plasma membrane vesicle
GUV	Giant unilamellar vesicle
HATU	1-[Bis(dimethylamino)methylene]-1H-1,2,3-triazolo[4,5-b]pyridinium 3-oxide hexafluorophosphate
HBON	2-(2-hydroxy-4-dimethylaminophenyl)benzo-[d]oxazole
HBSS	Hank`s balanced salt solution
HEPES	4-(2-hydroxyethyl)-1-piperazineethanesulfonic acid
HOBt	3-hydroxybenzotriazole
HPS	Hexaphenylsilole
HRMS	High resolution mass spectrometry

HSA	Human serum albumin
ICT	Intramolecular charge transfer
LD	Lipid droplet
LUV	Large unilamellar vesicle
MEA	β-mercaptoethylamine
MES	2-(N-morpholino)ethanesulfonic acid
NIR	Near infrared
NMR	Nuclear magnetic resonance
PAINT	Point accumulation imaging in nanoscale topography
PALM	Photoactivated localization microscopy
PEG	Poly(ethylene glycol)
PET	Photoinduced electron transfer
PM	Plasma membrane
POPC	1-palmitoyl-2-oleoyl-*sn*-glycero-3-phosphocholine
QY	Quantum yield
RESOLFT	Reversible saturable optical linear fluorescence transitions
RNA	Ribonucleic acid
SIM	Structured illumination microscopy
SLB	Supported lipid bilayer
SM	Sphingomyelin
SMLM	Single molecule localization microscopy
SPAAC	Strain-promoted azide-alkyne cycloaddition
SRM	Super-resolution microscopy
SR-PAINT	Spectrally resolved point accumulation imaging in nanoscale topography
SSIM	Saturated structured illumination microscopy
STED	Stimulated emission depletion
STORM	Stochastic optical reconstruction microscopy
TCEP	Tris(2-carboxyethyl)phosphine
THF	Tetrahydrofuran
TFA	Trifluoroacetic acid
TLC	Thin layer chromatography
TMR	Tetramethyl-rhodamine
TPE	Tetraphenylethylene
TPE	Two-photon excitation
WGA	Wheat germ agglutinin

1. Bibliographic overview

1.1. Fluorescence

Fluorescence is a phenomenon of light emission by molecule in singlet excited state which occurs after absorption of light.[1] A molecule in a singlet ground state (S_0) can switch to excited state by absorbing an incident photon ($h\nu_A$) with the energy corresponding to the gap between the states (Fig. 1.1.1). This transition is followed by rapid internal conversion, resulting in a non-radiative relaxation to the lowest excited state (S_1). Further decay from the S_1 state can be either radiative (accompanied by an emission of photon – fluorescence) or non-radiative (also called quenching) (Fig. 1.1.1). Fluorescence lifetime can be described as an average time a fluorophore molecule spends in excited state. The ratio between the photons emitted and the photons absorbed by the molecule, termed quantum yield, depends on the comparative rates of the decay processes. At high concentrations the quantum yield values tend to fall drastically, as the fluorescent species can form non-emissive aggregates, which leads to fluorescence quenching.[1]

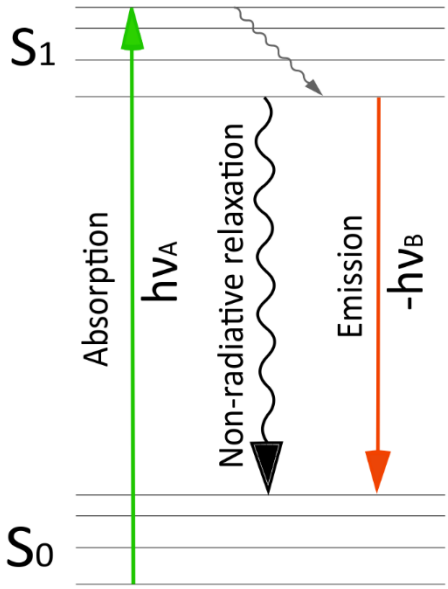

Fig. 1.1.1. Simplified Jablonski diagram

Fluorescence imaging is a highly attractive technique for studying live cells due to its several distinctive features[2]: it is non-invasive, fast and versatile; it has high spatial resolution and molecular specificity and does not require sophisticated equipment or sample preparation (compared to other imaging techniques, such as electron microscopy).[3, 4] However, fluorescence imaging requires contrast agents – fluorescent probes.

1.2. Fluorescent probes

Fluorescent probes are the molecules, which can be used as markers in fluorescence microscopy. The design of a fluorescent probe includes three main parts (Fig. 1.2.1):

1) A fluorophore, usually an organic dye. The choice of fluorophore allows to finely tune the properties of probe absorption and emission;

2) A targeting group. Introduction of targeting moieties ensures selective accumulation of the probe only in certain parts of a live cell, which is necessary to diminish as much as possible the background fluorescence and the undesired fluorescence signal from outside the region of interest;

3) A linker group. Linkers serve as spacers between a fluorophore and a targeting group, allowing the dye to position itself more freely after binding with the target, thus preventing perturbation of fluorophore emission. Additionally, linker groups can increase probe solubility in water and improve binding kinetics.

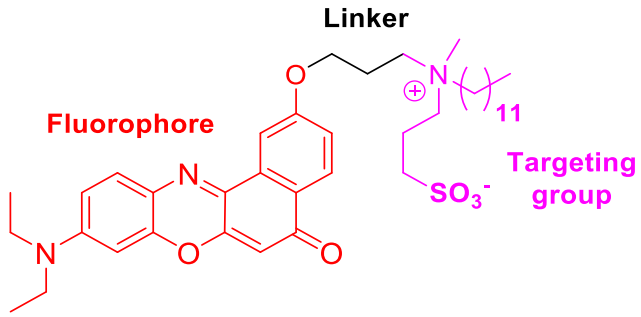

Fig. 1.2.1. Molecular design of a fluorescent probe.

The main photophysical characteristics of a fluorescent probe include excitation and emission wavelength, brightness and photostability.[5]

Probe excitation wavelength defines the possible cell phototoxicity and autofluorescence related to imaging (which both increase in case of dyes with absorption at shorter wavelengths). Probe emission wavelength defines whether the two different probes can be imaged separately in the same sample. These two characteristics also define the compatibility of the probe used with the light sources and emission bandpass filters of the fluorescent microscope used.

Additionally, biological samples transmit light better at longer wavelengths with maximum in the near infrared region, allowing for more efficient probe excitation and higher overall image quality, especially for tissue or *in vivo* imaging.[6]

Brightness, which is the product of extinction coefficient of probe absorption and quantum yield of probe emission, is important to obtain a quality image with high signal to noise ratio. This parameter is highly important, as, typically, the concentrations of dyes used in fluorescence imaging should be as low as possible.[7]

Photostability of a fluorescence probe reflects its stability upon excitation. The probes with higher photostability degrade much slower during imaging, which is important for longer imaging times, notably tracking. Additionally, probe photodegradation can lead to the formation of reactive radical species and singlet oxygen with high cell toxicity.

The probes that change one or several characteristics of their emission upon binding to the target allow improving signal-to-noise ratio and decreasing the fluorescence background, which result in a higher image quality. Changes in the probe fluorescence emission intensity (intensiometric response) or spectral changes (ratiomeric response) are also of key importance for fluorescence sensing and imaging of a biomolecular target or a given biophysical property. The probes with intensiometric response are termed fluorogenic probes, while the ones with ratiometric response are called chromogenic probes. The probes used for live cell imaging are often designed to be poorly emissive in water due to different fluorescence quenching mechanisms.

1.3. Environment-sensitive fluorescent probes

Environment-sensitive probes are able to alter their fluorescence emission in response to the changes in their environment, allowing to monitor non-invasively the parameters of interest in live cells, such as microviscosity, polarity, lipid order, membrane tension, temperature, etc.

In case of fluorogenic environment-sensitive probes the fluorescence emission intensity changes as a function of the parameter of interest. However, as the emission intensity also depends on the probe concentration, a second reference environment-insensitive fluorophore can be added into the probe design. In this case, it is possible to calculate the ratio between the two emission intensities coming from the two fluorophores, which is concentration-independent. Alternatively, one can rely on fluorescence lifetime imaging, which also does not depend on concentration.

In case of chromogenic probes with environment sensitivity, it is possible sense the changes in the parameter of interest by measuring the fluorescence intensities at two different wavelengths and calculating the ratio, which is independent of the probe concentration and some instrumental parameters.

The dyes, possessing environment sensitivity, can be divided into several broad categories, depending on the photophysical processes involved in sensing:

1) Dyes, exhibiting charge or proton transfer in the excited state;
2) Dyes, capable of ground state isomerization;
3) Dyes, capable of excited state conformational change;
4) Dyes with environment-sensitive aggregation or disaggregation

1.3.1 Probes based on intramolecular charge transfer

The classical environment-sensitive probes are based on solvatochromic dyes comprising of conjugated aromatic system with donor and acceptor groups at two sides, so-called push-pull fluorophores. This type of structure allows the electron density to shift from the donor to acceptor part after an absorption of light, forming a highly dipolar excited state in a process, termed intramolecular charge transfer (ICT).[8] The excited state dipole is stabilized by varied degrees through the interactions with the dipoles of solvent molecules (Fig 1.3.1, A). Thus, in more polar solvents the energy gap between the two states decreases and, consequently, the emission maximum is shifted towards longer wavelengths (Fig. 1.3.1, B, C). There are many examples of ICT fluorescent probes operating in different regions of visible spectra and NIR, described in the literature, notably those based on Prodan, pyrene, dapoxyl, nitrobenzooxadiazole (NBD), 4-(N,N-dimethylamino)phthalimide (4DMP), dicyanodihydrofuran (DCDHF), and Nile Red fluorophores (Fig 1.3.1, B).[8]

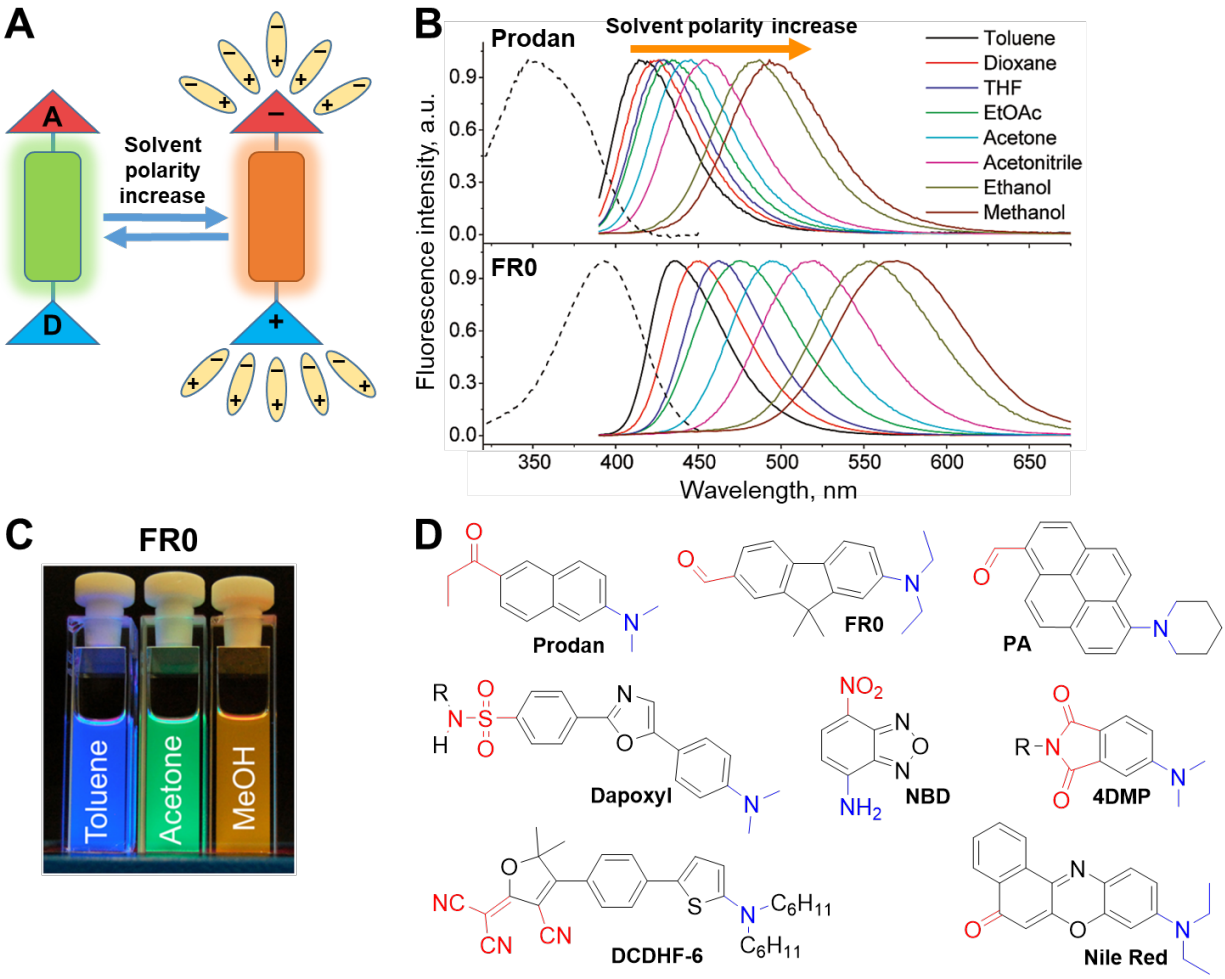

Fig 1.3.1. Fluorescent ICT probes. Mechanism of sensing of push-pull fluorophores (A). Absorption (dash) and fluorescence (solid) spectra of Prodan and FR0 probes in solvents of different polarity (B) Adapted from [9]. Photograph of cuvettes with FR0 probe in different solvents

(C) Adapted from [9]. Examples of ICT fluorophores (D). Donor groups are marked in blue, acceptor groups are marked in red.

Due to their sensitivity to the polarity of environment, the probes with intramolecular charge transfer are capable of sensing changes in the intrinsic biophysical properties of membranes, such as polarity, hydration, lipid order, electrostatics, microviscosity, etc.[8, 10] The variations of these parameters are accompanied by changes in the effectivity of dipolar relaxation processes, thus affecting the emission wavelength of push-pull fluorophores. In addition, the ICT probes, which are vertically oriented in biomembranes, are also capable of sensing electric fields, notably transmembrane potential, as it was shown for styrylpyridinium dyes.[11]

Push-pull dyes are particularly useful for imaging of liquid ordered (Lo) and liquid disordered (Ld) phase domains.[12] According to the hypothesis of lipid rafts[13], these phospholipid domains are crucial for organization and normal functioning of plasma membrane, however, they are hard to detect due to the small size and highly dynamic nature. The Lo phase domains consist of tightly packed saturated lipids and cholesterol and are characterized by less polar environment compared to loosely packed Ld phase, comprising unsaturated lipids. The two phases can be distinguished by solvatochromic ICT probes, which exhibit a blue shift in fluorescence emission from the probe molecules in Lo phase compared to ones in the Ld.[14] This difference is attributed to the less hydrated lipid interphase in case of Lo phase and slower water dipolar relaxation process.[14] Thus, an environment-sensitive probe NR12S, based on Nile Red fluorophore, was used to distinguish between the lipid domains in giant unilamellar vesicles (GUVs) (Fig. 1.3.2).[15] By measuring the fluorescence intensity of the probe in two spectral regions (Fig. 1.3.2, B) it is possible to distinguish clearly the domains with different lipid order through changes in the ratio between the two emission channels (Fig. 1.3.2, C).

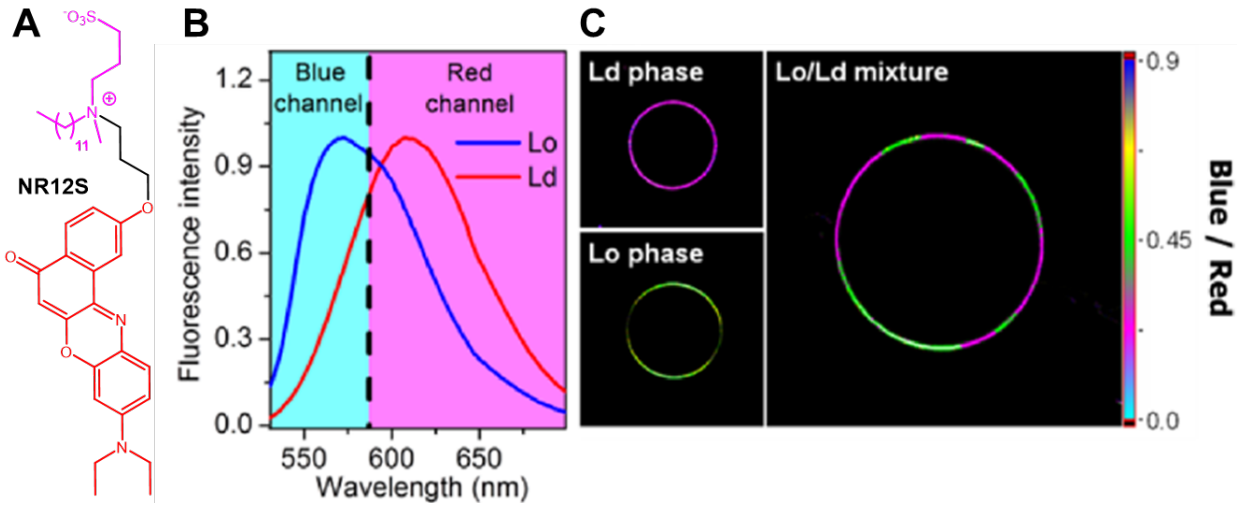

Fig. 1.3.2. Fluorescence microscopy imaging of Lo and Ld phases in GUVs using NR12S. Structure of NR12S ICT probe (A). Normalized fluorescence spectra of NR12S in Ld (DOPC) and Lo (SM/Chol) phases of LUVs (B). The cyan and magenta regions separated at 585 nm represent the detection range for the blue and red channels of the microscope. Ratiometric

microscopy images with GUVs, composed of DOPC (Ld phase), SM/Chol (Lo phase), and DOPC/SM/Chol (mixed Lo/Ld phases) (C). The color of each pixel represents the value of the intensity ratio I_{blue}/I_{red}, while the pixel intensity corresponds to the total intensity at both channels. Adapted from [15].

The intrinsic sensitivity of ICT fluorophores to polarity makes them excellent candidates for the polarity probing in live cells. Thus, a solvatochromic pyrene-based dye PA (Fig. 1.3.3, A) was utilized to image the varying polarity in different cellular compartments in live HeLa cells. The probe easily internalizes into live cells, indiscriminately staining all the lipid compartments (Fig. 1.3.3, B). By plotting the ratio between the fluorescence emission intensities measured at ranges between 550-700 and 470-550 nm (Fig.1.3.3, C),[16] it is possible to compare the polarity of different cell regions. As an example, this experiment shows lipid droplets to be the most apolar parts in the cell, and that the plasma membrane exhibits generally less polar environment when compared to intracellular membranes.[16]

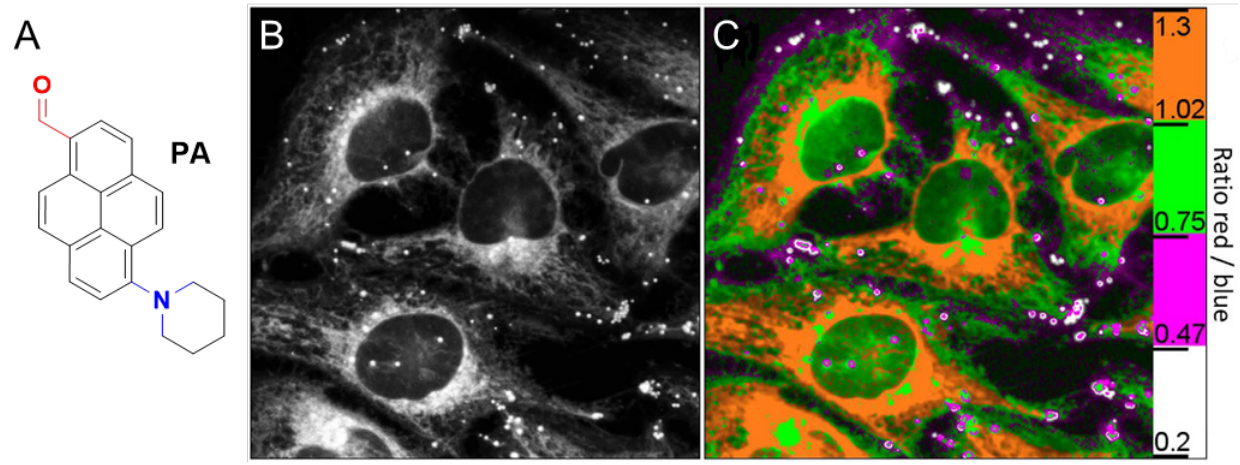

Fig. 1.3.3. Structure of push-pull PA probe (A). Integral fluorescence intensity microscopy image (B) and ratiometric microscopy image (C) of HeLa cells stained with 100 nM of PA. Modified from [16].

Another important application of solvatochromic probes is their ability to detect biomolecular interactions, which is an alternative to traditional detection based on fluorescence anisotropy and Förster resonance energy transfer (FRET).[17] When the two biomolecules interact, it leads to exclusion of the local water molecules, which can be sensed by an ICT probe as a decrease in environment polarity. The examples of solvatochromic probes include amino acid analogues of Prodan[18] and 6-(N,N-dimethylamino)-2,3-naphthalimide (6DMN),[19] used to probe protein electrostatics and protein-protein interactions, correspondingly, and a Nile Red-based probe,[20] used for wash-free detection of G protein-coupled oxytocin receptor. In the latter case, an introduction of targeting group through a PEG8 linker helped to diminish nonspecific interaction with serum and lipid membranes in cells.

Recent works with fluorophores, based on intramolecular charge transfer (ICT), revealed two features of these systems. First, push-pull dyes have relatively low photostability, especially

in non-polar medium, as it favours the formation of a triplet excited state through intersystem crossing, followed by photooxidation.[9, 16] Second, most of solvatochromic fluorophores are quenched in polar protic media, mostly due to twisted intramolecular charge transfer (TICT) or electron transfer phenomena.[21] This results in low quantum yield of these dyes in protic solvents, such as water, which, together with red-shifted emission from the dyes in aqueous medium, allows to reduce the undesired background fluorescence signal during fluorescence microscopy.

1.3.2 Probes based on intramolecular proton transfer

Excited-state intramolecular proton transfer (ESIPT) process occurs when after excitation a push-pull dye is able to switch between two emissive tautomeric forms (Fig. 1.3.4, A). As a result, ESIPT dyes typically exhibit two distinct fluorescence emission bands corresponding to normal (N^*) and tautomeric (T^*) excited states. For instance, in some 3-hydroxychromones (Fig. 1.3.4) the equilibrium between these forms is dependent on solvent polarity and H-bond donor ability.[22] The ratio between the fluorescence intensities of the two bands (N*/T*) increases with an increase in the solvent polarity and H-bond donor ability (Fig. 1.3.4, B), as polar and especially protic solvents inhibit ESIPT reaction.[22]

Solvent-dependent dual emission can be observed for most dyes only in media with a certain polarity range, however it can be finely tuned by changing the molecular design of the probe.[23] Thus, introduction of strong electron-donor groups shifts the region of probe dual emission into media of medium polarity due to an enhancement of the dipole in the N* state, as it was reported to 3-hydroxychromones [24] (Fig. 1.3.4, B).

The structure of this class of environment-sensitive probes includes a heteroatom with a free electron pair in close proximity to a phenolic hydroxyl, with an ability to form 5- or 6-membered H-bonding ring, with the typical examples including 3-hydroxyflavone (3HF), p-N,N-ditolylaminosalicylaldehyde (SAN), (2-(2-hydroxy-4-dimethylaminophenyl)benzo-[d]oxazole (HBON) and 2-((2-(2-hydroxyphenyl)benzo-[d]oxazol-6-yl)methylene)-malononitrile (diCN-HBO) fluorophores (Fig 1.3.4, C).[25]

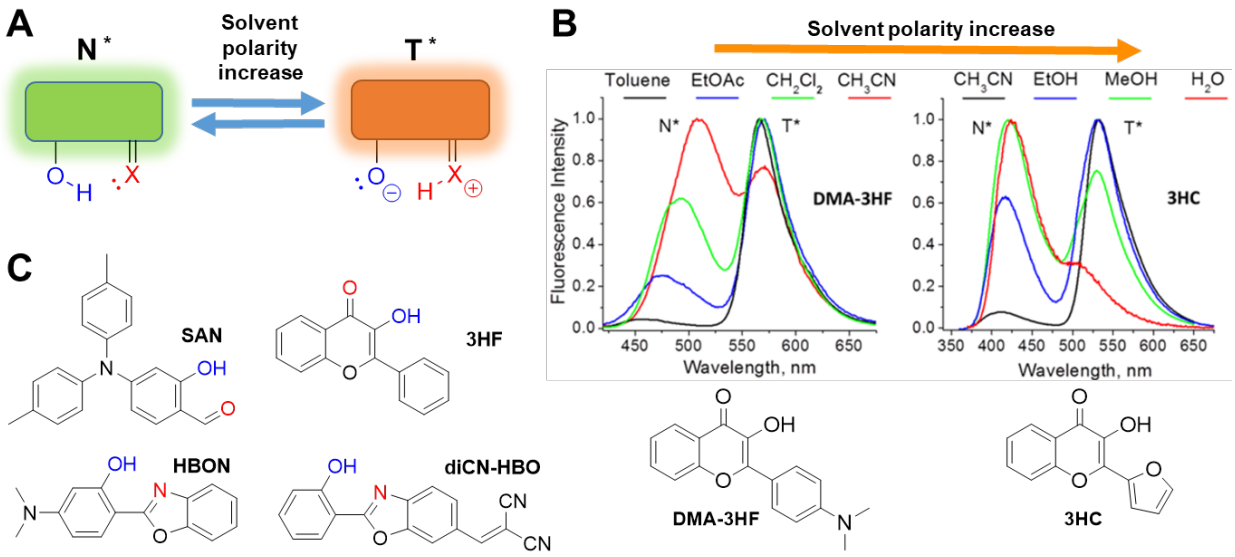

Fig 1.3.4. Fluorescent ESIPT probes. Mechanism of sensing (A). Fluorescence emission spectra of ESIPT probes DMA-3HF and 3HC in solvents of different polarity (B) Adapted from [8]. Examples of ESIPT fluorophore structures (C). Proton donor hydroxyl groups are marked in blue, proton acceptor heteroatoms are marked in red.

ESIPT probes can be used to sense several parameters in lipid bilayer, with the relative sensitivity being dependent on the fluorophore orientation. The dyes, which are vertically oriented in the bilayer, are more suitable for sensing of dipole (F8N1S and PPZ8, Fig. 1.3.5, A)[26] and transmembrane potentials (di-SFA, Fig 1.3.5, A)[27], while those with tilted orientation are sensitive towards surface potential and lipid order.[28, 29] As an example, the probe F2N12S (Fig. 1.3.5, A) is capable of detecting the changes in lipid composition during apoptosis (programmed cell death).[30] The fluorophore, which resides exclusively at the outer plasma membrane leaflet, responds to the apoptosis-associated changes in lipid composition of the outer membrane leaflet due to the accompanying changes in the surface charge (Fig. 1.3.5, B).[30] In apoptotic cells, F2N12S exhibits an increased intensity of N^* emission band (Fig. 1.3.5, C), which makes it possible to distinguish the normal and apoptotic cells using ratiometric microscopy imaging (Fig. 1.3.5, D).

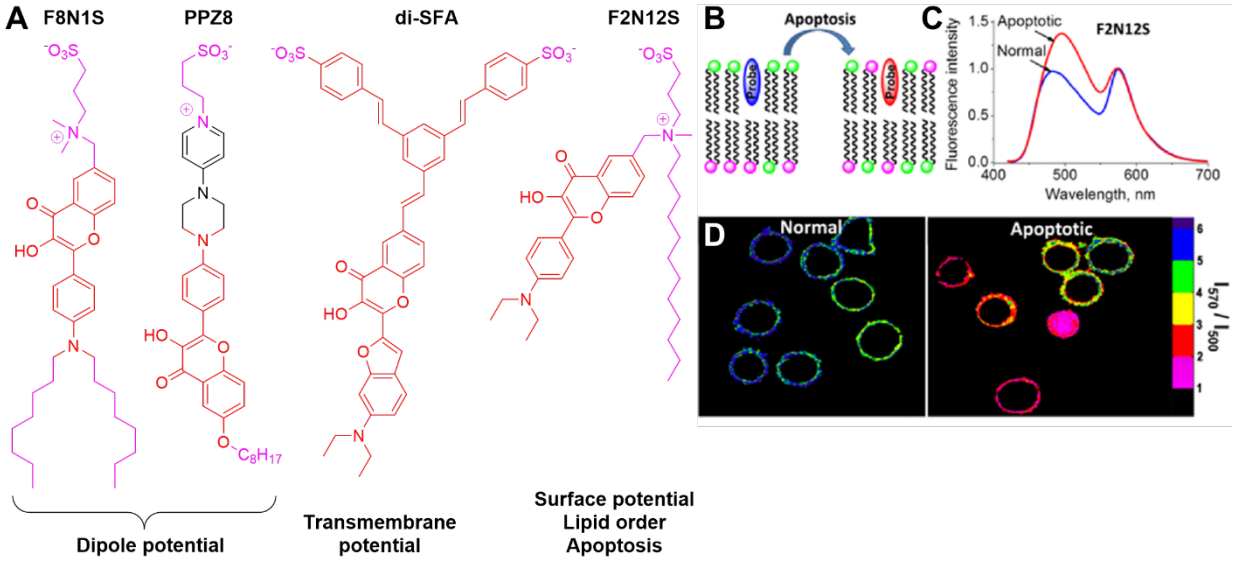

Fig 1.3.5. Application of ESIPT 3-hydroxychromone dyes for studying lipid membranes. Structures of membrane probes based on 3-hydroxychromone (A). Schematic presentation of the colour response of the probe F2N12S in plasma membranes during apoptosis (B) and detection of apoptosis by F2N12S using fluorescence spectroscopy (C) and microscopy (D). Adapted from [8].

Solvatochromic ESIPT probes also were used to create sensors with fluorogenic or ratiometric response to detect various ions and small biologically active molecules in live cells.[31]

1.3.3 Probes based on ground state isomerization

Xanthene dyes

One of the important mechanisms used to obtain an environment-sensitive fluorogenic response is a ground-state isomerization (Fig. 1.3.6, A). This mechanism is particularly important for fluorescein[32] and rhodamine[8, 33] dyes. For these fluorophores, a nucleophilic carboxylate group in the o-position of side phenyl is able to attack the electrophilic center of the heterocycle, forming a non-emissive spirolactone (Fig. 1.3.6, B). The equilibrium between the two forms can be shifted by changes in pH, solvent polarity or presence of specific molecules.[8] Importantly, the formation of spirolactone in rhodamines is a reversible process, which takes place only in apolar media, however, an introduction of Si-rhodamines (Fig. 1.3.6, C) allowed to obtain the probes undergoing cyclization at much higher polarity (Fig. 1.3.6, D).[34-36] The conjugates of this dye with targeting moieties underwent transition to the open form only upon binding to target proteins, such as tubulin, actin, SNAP tag, etc. Such fluorogenic response allowed to use the probes in wash-free conditions for multicolor background-free imaging using conventional and super-resolution microscopy (Fig. 1.3.6, E-F).[35]

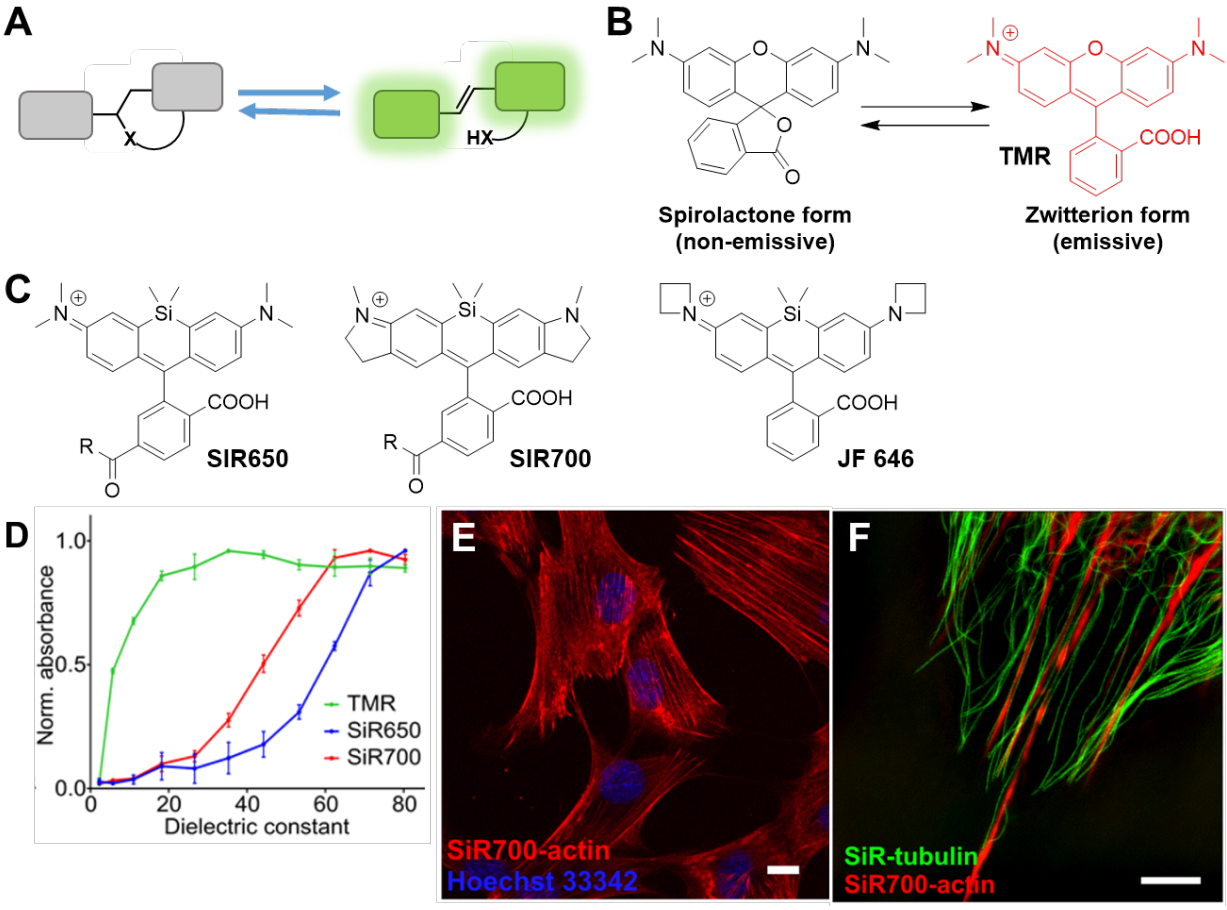

Fig 1.3.6. Probes based on ground state isomerization. Concept (A) and mechanism of ground state isomerization in rhodamine fluorophores (B). Structure of Si-rhodamine-based probes (C). Sensitivity of zwitterion-spirolactone equilibrium of TMR (green), carboxy-SIR650 (blue) and carboxy-SiR700 (red) to the dielectric constant of solvent (D). An increase in absorbance corresponds to the appearance of emissive zwitterionic form. Confocal images of human primary fibroblasts stained with the SiR700-probe (red) and Hoechst 33342 nuclear stain (blue) (E). Scale bars = 10 μm. Two-color super-resolved SIM image of human primary fibroblasts stained with SiR-tubulin (green) and SiR700-actin (red) (F). Scale bars = 10 μm (E) and 5 μm (F). Adapted from [35].

Oligothiophene dyes

In case of oligothiophene dyes the sensitivity towards the environment is achieved through a ground state planarization (Fig. 1.3.7).[37] This class of fluorophores comprises of four thiophene moieties (Fig. 1.3.7, A), which are twisted in ground state due to steric hindrance, however can become flat in response to changes in membrane fluidity (Fig. 1.3.7, B).[37] In case of moderate deplanarization the highly solvatochromic push–pull quaterthiophene scaffolds are able to

respond to changes in membrane fluidity in lipid bilayer or to an increase in membrane potentials with a bathochromic shift of probe absorption.

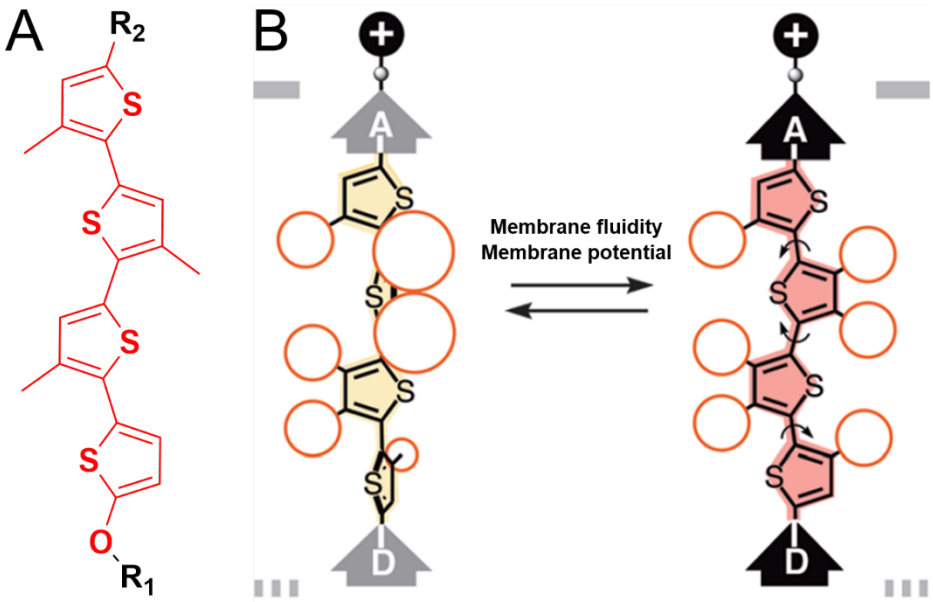

Fig. 1.3.7. Planarizable oligothiophene dyes. Tetrathiophene fluorophore structure (A) and sensing mechanism (B). The probe planarization is affected by lateral crowding along the scaffold (marked by red circles) and fluorophore polarization by terminal donors (marked as D), acceptors (marked as A), and charges (marked as +). Adapted from [37].

Further modification of oligothiophene fluorophore moiety led to a discovery of a class of environment-sensitive dyes, also termed "flippers", which are able to sense changes in the membrane tension and lipid order.[38] Membrane tension by itself is in an important cell parameter, which is tightly regulated during cell migration[39-42] and spreading,[43] membrane trafficking[44] and phagocytosis.[44] Additionally, through the membrane tension it is possible to detect the changes in lipid order.[38] The flipper probes comprise of two flat heterocyclic moieties connected through a single bond (Fig. 1.3.8, A). Due to a steric hindrance in a twisted ground state, the conjugation between the two aromatic fragments is distorted. However, the dye can become more planar in rigid environments, such as liquid ordered (Lo) phase in lipid membranes (Fig. 1.3.8, B), which is accompanied by a bathochromic shift in absorption. The two lipid phases, Lo and liquid disordered (Ld), can be distinguished though the changes in the probe excitation spectrum, while the emission spectrum remains unchanged. These probes were utilized to perform two-color imaging of phase domains in giant vesicles using excitation at two wavelengths.[45] Alternatively, the flipper probes also decrease their fluorescence lifetime in response to a decrease in membrane tension, which allowed to use FLIM for imaging of membrane tension in giant unilamellar vesicles (Fig. 1.3.8, C-D)[38] and organelles in live cells.[46]

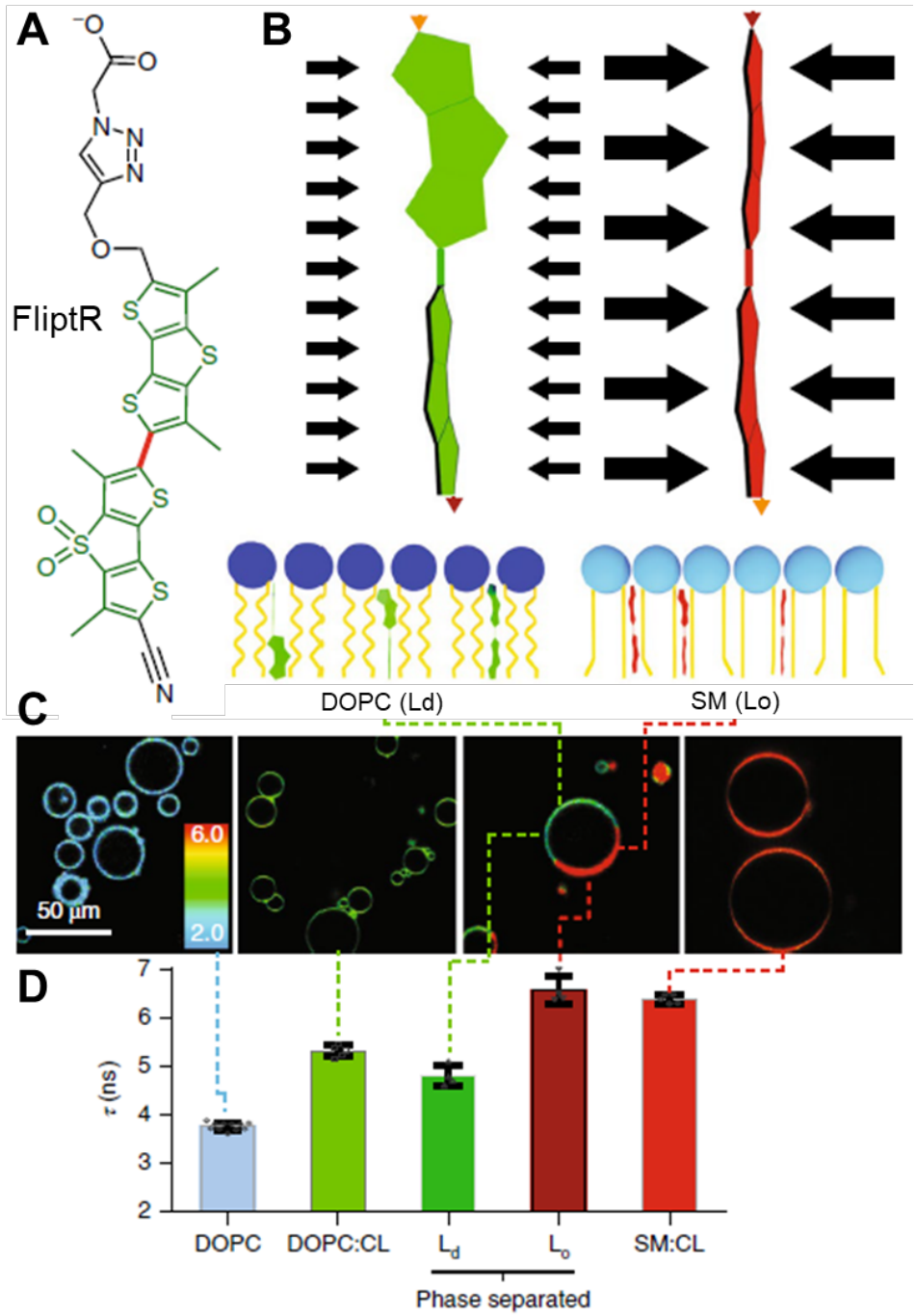

Fig. 1.3.8. Fluorescent flipper probes. Structure (A) and mechanism of lipid order sensing (B) of a fluorescent flipper probe FliptR. Fluorescence lifetime τ1 images of FliptR as a function of lipid composition in giant unilamellar vesicles, from liquid-disordered membrane (Ld) to increasingly liquid-ordered membrane (Lo) (C). The corresponding lifetime mean values are shown in the histogram (D). The colour bar in (C) corresponds to lifetime in nanoseconds (ns). Adapted from [38]

1.3.4 Probes based on excited state conformational change

Molecular rotors

The environment-sensitive fluorophores, which are able to undergo an intramolecular twisting motion in their excited state, are termed molecular rotors.[21] The structure of a molecular rotor typically comprises an electron donor group conjugated to an electron acceptor group via alternating single and double bonds. At the ground state the p-orbitals are aligned due to conjugation, which results in a molecule adopting planar conformation. Upon excitation, the molecule exhibits intramolecular charge transfer, leading to a planar excited state, which can dissipate part of its energy through a rotation around σ-bonds (Fig. 1.3.9, A) in a process, termed twisted intramolecular charge transfer (TICT).[47] As a consequence, molecular rotors either present two emission bands with the twisted conformation emitting at longer wavelength due to the lower energy gap between the excited and the ground state when compared to planar conformation or emit only from the planar state, if the energy gap for twisted conformation is too low, leading to non-radiative energy dissipation. A well-studied example of dual emissive molecular rotor is 4-dimethylaminobenzonitrile (DMABN)[47] (Fig. 1.3.9, B), while such fluorophores as 9-(dicyanovinyl)julolidine (DCVJ) and 5-arylboron-dipyrromethene (Fig. 1.3.9, B) emit only from the planar conformation of excited state[47-49]. The effect of environment on the emission in molecular rotors consists of several contributions[47]:

1) an influence of environment polarity on the stability of polar excited state;

2) an influence of environment microviscosity on the rate of intramolecular twisting in the excited state.

Polar solvents stabilize twisted conformation over the planar one, due to the twisted state having a larger dipole moment. Moreover, for the same reason a stronger bathochromic shift of TICT state is observed in polar media when compared to that of a planar excited state. On the other hand, more viscous media leads to an increase in the energy barrier between the planar and the twisted states, which reduces the rate of intramolecular rotation, thus increasing the fluorescence lifetime and quantum yield of fluorescence from planar excited state. Due to a higher local viscosity in Lo compared to Ld in lipid membranes, molecular rotors can distinguish between the two phases, as it was shown for C-Laurdan-2 probe.[50] Molecular rotors were also used to sense viscosity in model membranes and live cells (Fig. 1.3.9, C-E)[48, 51-53] to monitor polymerization processes[54, 55] and to study conformation and assembly of proteins.[56, 57] In live cells, the microviscosity is of a particular interest, as it determines the lateral diffusion in biomembranes, while also affecting the enzymology, metabolism, and protein folding.[51]

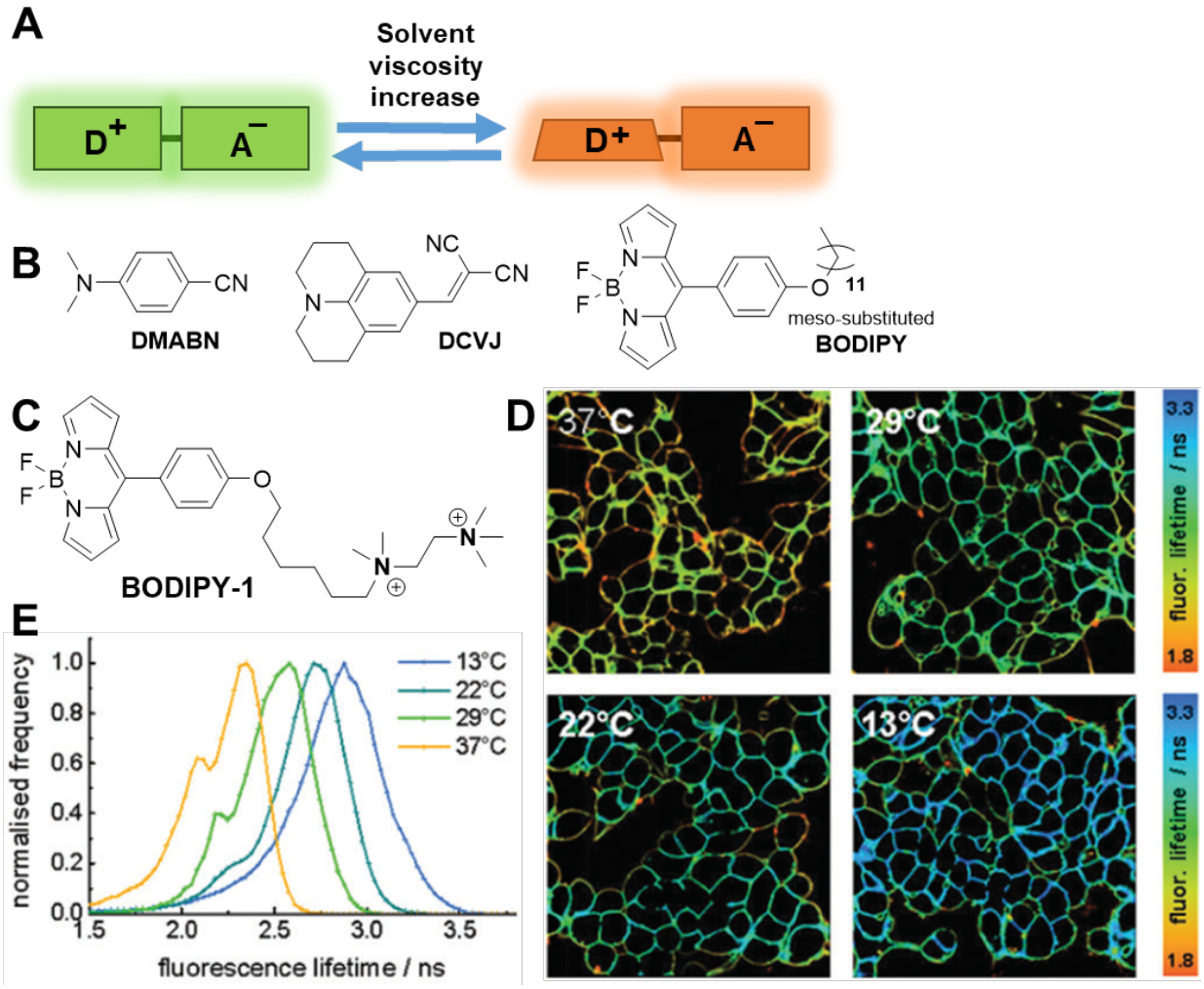

Fig. 1.3.9. Fluorescent molecular rotor probes. Mechanism of sensing (A) and structures of molecular rotors (B). Structure of BODIPY 1 microviscosity probe (C) and its fluorescence lifetime maps in the plasma membranes of SH-SY5Y cells at four different temperatures (D). Adapted from [58]. Averages histograms corresponding to FLIM images of the SH-SY5Y plasma membranes at four different temperatures (E). Adapted from [58].

In case of dual-emission of a probe it is possible to sense local microviscosity directly by analyzing the ratio between fluorescence intensities of the two emission bands, however, the emission intensity of molecular rotors with a single band also depends on other parameters, such as dye concentration, fluid optical properties in heterogeneous systems, and fluctuations in laser excitation power.[59] The possible ways to circumvent this hindrance include:

1) utilization of FLIM, as the fluorescence lifetime of the planar excited state is concentration-independent[48];

For a family of meso-substituted BODIPY molecular rotors it was proved, that both the quantum yield and the fluorescence intensity of planar excited state depend on viscosity (Fig. 1.3.9, C-E). Utilization of FLIM does not require to change significantly the molecular design.

2) creation of a FRET system by including a second viscosity-insensitive dye in probe design[60, 61] (Fig. 1.3.10, A);

This strategy adds a second reference fluorophore, which acts both as a reference viscosity-insensitive emitter and as a FRET donor. The emission of a reference dye is not affected by viscosity (peak **1** in Fig. 1.3.10, B), however the fluorescence intensity of a molecular rotor increases with an increase in viscosity (peak **2** in Fig. 1.3.10, B). Thus, the ratio between fluorescence intensities for a molecular rotor and a reference dye becomes dependent only on the environment microviscosity, which allows to obtain accurate viscosity values when performing the ratiometric imaging.

Notably, molecular rotors, in addition to their sensitivity towards viscosity, can be also affected in varied degrees by temperature changes.[62] Such molecular rotors as DCVJ and meso-substituted BODIPY with a substituent in p-position of meso-phenyl ring are little or completely not sensitive towards temperature changes.[63, 64] However, introduction of a single methyl group and extended conjugation chain allows to increase greatly the temperature sensitivity while also decreasing the probe sensitivity to microviscosity,[65] with an alternative approach based on utilization of modified rhodamine or rosamine dyes (Fig. 1.3.10, C).[66]

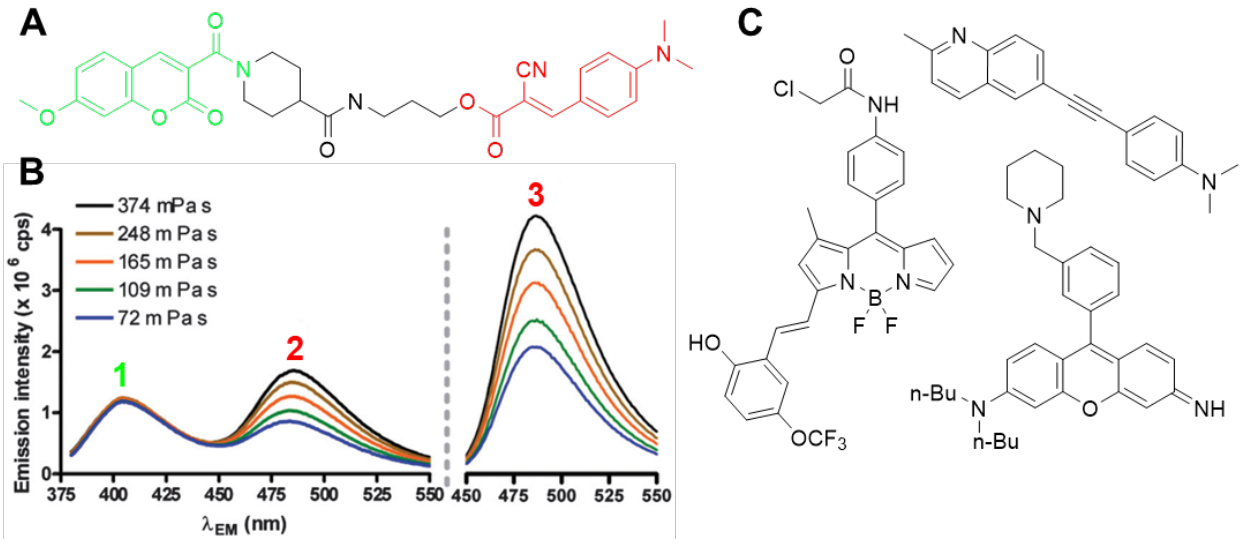

Fig. 1.3.10. Structure of a ratiometric viscosity probe (A). Viscosity sensitive TICT fluorophore and viscosity-insensitive coumarin are highlighted in red and green, respectively. Emission spectra of the probe in (A) in the mixtures of ethylene glycol and glycerol with different viscosity (B). Peak **1** represents coumarin emission and peak **2** – the molecular rotor emission through FRET from coumarin. Peaks **1** and **2** were acquired at the same excitation wavelength (λ_{ex} = 360 nm). Peak **3** is the emission from direct excitation of the TICT fluorophore at λ_{ex} = 444 nm. Only peaks **2** and **3** are viscosity dependent. Adapted from [47]. Structures of molecular rotors with sensitivity towards temperature (C).

Papillon probes

Another class of fluorescent probes, termed papillons, is capable of bending and unbending the fluorophore in excited state[67] (Fig. 1.3.11, A). As a result, the dyes are dual-emissive with the bands corresponding to a "closed" bent excited state with a blue-shifted

emission and an “open” planar one, which emits light with longer wavelength. These molecules, based on N,N’-diphenyl-dihydrodibenzo[a,c]phenazine fluorescent backbone (Fig. 1.3.11, B), are able to distinguish between the lipid phases in model membranes, changing the ratio between fluorescence intensities at the two emission wavelengths. The more rigid environment in Lo phase causes a shift of an equilibrium towards excited planar state when compared to Ld phase.[67] Notably, the papillon probes are insensitive towards the polarity of environment, with the excited state being sensitive to viscosity.[67, 68] According to the partitioning coefficients data, the dyes preferentially go to liquid disordered phase, however, this effect is compensated as the emission brightness is much higher for probes inside liquid ordered phase (Fig. 1.3.11, C).[67] Due to their intrinsic dual emission, papillon probes can be directly used for ratiometric imaging (Fig. 1.3.11, D-E), as the ratio between the two emission bands is concentration-independent. Spectroscopic probes and environment sensitivity of these dyes can be finely tuned by changing the probe molecular design, *e.g.* by introducing electron donating groups (Fig. 1.3.11, B).[67]

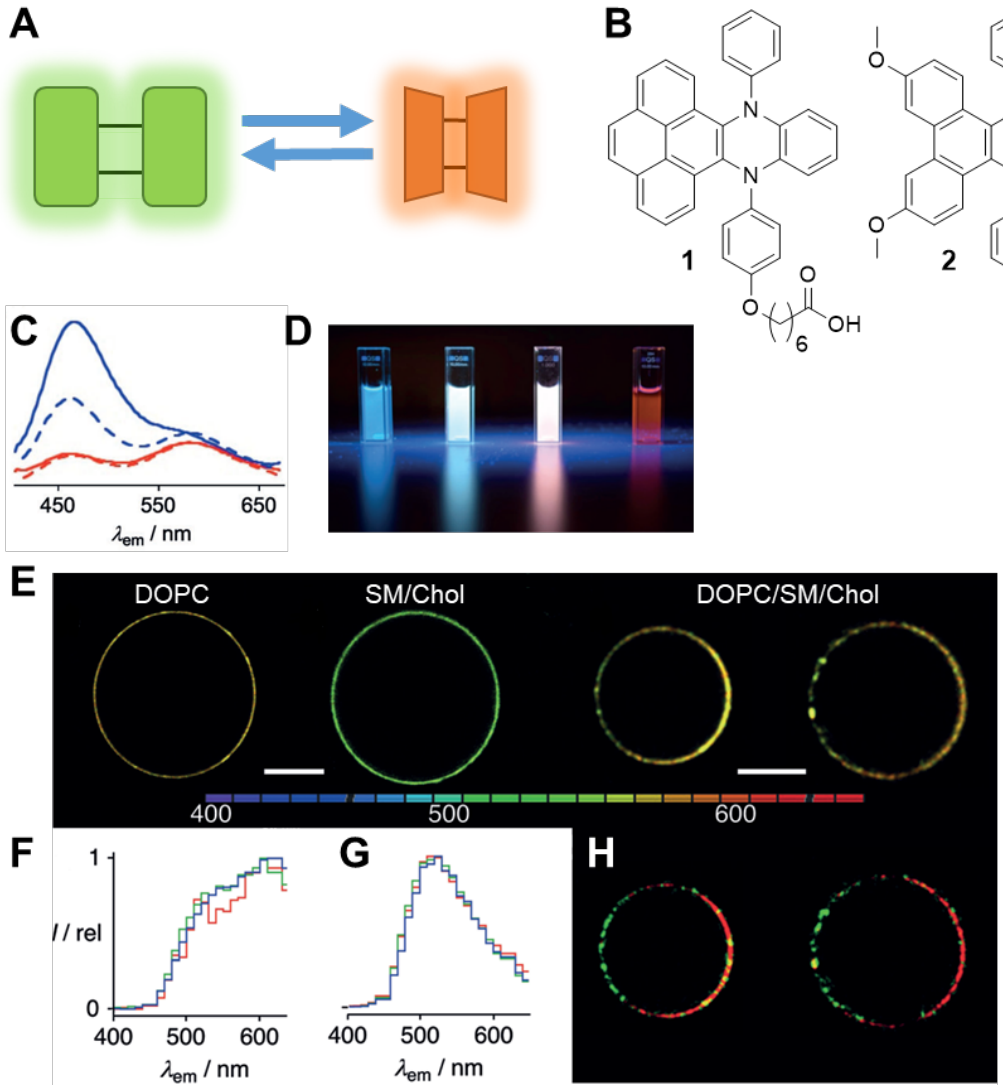

Fig. 1.3.11. Mechanism of sensing (A) and structures (B) of papillon probes. Non-normalized fluorescence emission of papillon **1** in DPPC LUVs (Lo, solid) and DOPC LUVs (Ld, dashed), at 55°C (red) and 25°C (blue) (C). Photographs of probe **1** in water, Lo DPPC LUVs, Ld

DOPC LUVs, and EtOAc (left to right) excited at 366 nm (D). TPE microscopy images (λ_{ex}=720 nm) of GUVs composed of DOPC (Ld), SM/Chol (Lo), and two different SM/DOPC/Chol GUVs in the presence of papillon **2** (E) (color bar: emission wavelengths in the 400–650 nm range, scale bar: 20 μM). Normalized emission spectra of entire GUVs composed of DOPC (F) and SM/Chol (G), with 0.5 μM (red), 1.0 μM (green), and μM mm (blue) of probe **2**. Spectrally unmixed images (H) of DOPC/SM/Chol GUVs in (E) using reference spectra in (F) and (G) showing Ld (red) and Lo domains (green). Adapted from [67].

1.3.5 Probes based on aggregation-caused quenching

Fluorescent dyes, being flat aromatic structures, exhibit a strong tendency to undergo π-stacking, forming non-fluorescent H-aggregates.[69] Strong hydrophobic interaction between the probe molecules favours aggregation-caused quenching (ACQ), whereas in the environment of low polarity the fluorophore molecules can disaggregate back into fluorescent monomers, thus creating a fluorogenic response. The probes, based on aggregation, can exhibit formation of either intramolecular or intermolecular aggregates.[8]

The advantage of probes based upon intramolecular aggregation is that this process does not depend on probe concentration. The simplest design for this probe type implies linking two fluorescent dyes using a flexible linker (Fig. 1.3.12, A), with the commercial probe YOYO-1 (Fig. 1.3.12, B) being a typical example. This dimeric probe does not fluoresce in water due to the formation of non-emissive H-aggregates, however it opens up upon binding to DNA, becoming highly emissive. A probe dimer in a completely open state is equal to the two separate fluorophore molecules in terms of fluorescence, allowing to create probes with high brightness. Intramolecular aggregation has been exploited to create a series of dimeric probes which can sense interactions with nucleic acids or DNA hybridization.[70]

Further development of this approach lead to creation of dye dimers, which are self-quenched in aqueous media inside the cell, unless they interact with specific short nucleic acid sequences (aptamers).[71] This methodology allows specific imaging of target RNA in live cells by genetically encoding the aptamer sequence in the region of interest. Thus, a probe Gemini-561, based on a sulforhodamine B dimer (Fig. 1.3.12, C), formed a bright complex with the corresponding aptamer o-Coral, expressed in the nucleus in mammalian cells (Fig. 1.3.12, D) through the means of genetic engineering.[71] The advantages of this dimeric probe include high brightness and photostability, which drastically enhance the quality of RNA imaging.

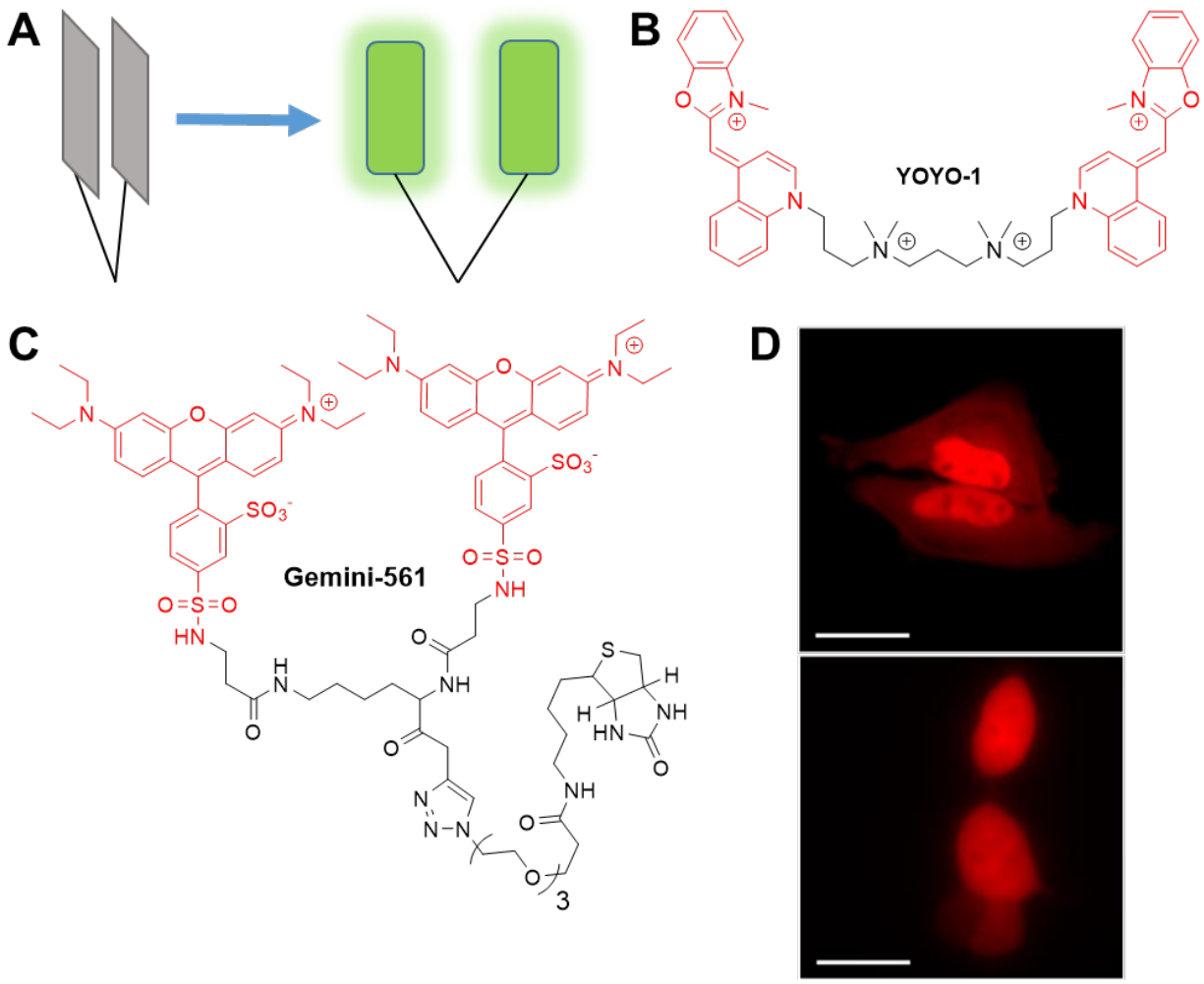

Fig. 1.3.12. Dimeric probes based on intramolecular aggregation-induced quenching. Mechanism of fluorogenic response of a dimeric probe (A) and the structure of YOYO-1 probe for nucleic acids (B). Structure of a dimeric sulforhodamine probe Gemini-561 (C). Live cell imaging of HeLa (top image) and HEK293T (bottom image) cells expressing U6-o-Coral in the nucleus (D). The cells were incubated with Gemini-561 (200 nM) for 5 min before imaging. Scale bars, 30 μm. Adapted from [71].

A dimeric probe for polarity sensing was created basing on a squaraine fluorophore system.[72] In this case, a decrease in polarity induces an unfolding of the dimer, followed by a fluorogenic response. Due to a dimerization-based molecular design it became possible to create a fluorescence probe with unprecedented brightness owing to exceptionally high molar extinction coefficient together with high quantum yield (*e.g.* ε ~ 700 000 M^{-1} cm^{-1} and QY~0.5 for the squaraine dimer).[72]

An alternative strategy used for creating ACQ probes is to exploit the formation of intermolecular aggregates. A number of organic dyes can form non-emissive aggregates in water. One of the ways to tune this behavior for a variety of commonly used fluorophores lies in utilization of a specially designed hydrophobic linker together with a targeting group.[73] The aggregates formed in aqueous medium are expected to disassemble upon binding with a receptor and produce a fluorogenic response. A similar approach lies in an addition of amphiphilic

fragments in probe molecular design.[8] The squaraine-based probe dSQ12S with two zwitterionic fragments and two alkyl chains (Fig. 1.3.13, right panel) exhibited >100-fold increase in fluorescence intensity in lipid membranes compared to the aggregated probe in aqueous medium.[74] After an introduction of a zwitterionic targeting group in the molecule a Nile Red-based probe NR12S exhibited a 25-fold drop in the quantum yield values in water compared to unsubstituted parent Nile Red dye[15] together with characteristic blue-shifted absorption, supposedly due to the formation of non-emissive H-aggregates of micellar structure.[15] In both cases the aggregates disassembled into discrete molecules upon binding to lipid membranes, which was accompanied by an increase in QY values (*e.g.* QY~0.45 in case of NR12S).

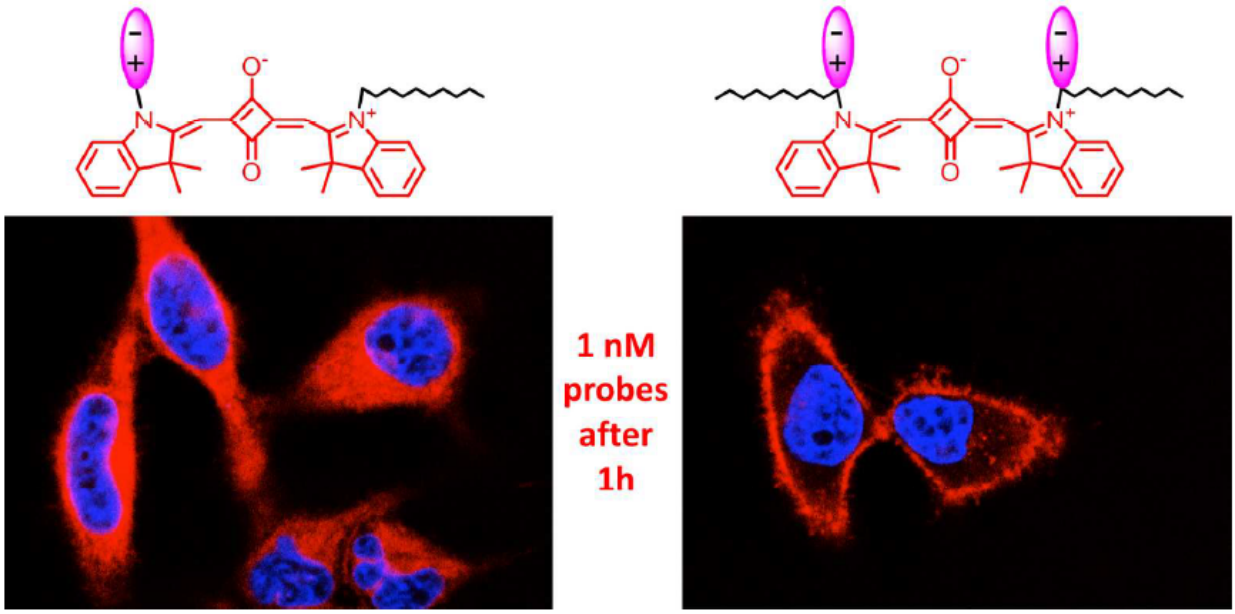

Fig. 1.3.13. Microscopy images of live HeLa cells stained with zwitterionic squaraine probes (in red). Both squaraines show virtually no fluorescence signal from the extracellular medium due to aggregation. Nuclei were stained with Hoechst 333258 dye (in blue). Adapted from[74]

1.3.6 Probes based on aggregation-induced emission

Fluorophore aggregation generally leads to the formation on non-emissive species, however, for organic dyes of special structure the aggregation can be accompanied by fluorescence enhancement of the initially non-fluorescent molecules (Fig 1.3.14, A).[75] This phenomenon, called aggregation-induced emission (AIE), is observed in aromatic molecules with propeller-like topology, such as tetraphenylethylene (TPE) and hexaphenylsilole (HPS) (Fig. 1.3.14, B).[76] In these dyes, the fluorescence in quenched in solution due to a rapid rotational or

vibrational energy dissipation, however, these processes are inhibited in aggregates due to physical stacking of the dye molecules, which consequently increases the fluorescence intensity by blocking the non-radiative pathways (Fig. 1.3.14, C).[75, 77] The AIE fluorophores possess remarkably high photostability and, for a large number of probes, high quantum yields.[76, 78, 79]

Usage of biocompatible AIEgens (Fig. 1.3.14, D) allowed to perform cell cytosol staining at high concentrations (Fig. 1.3.14, E), while also retaining low cytotoxicity.[80]

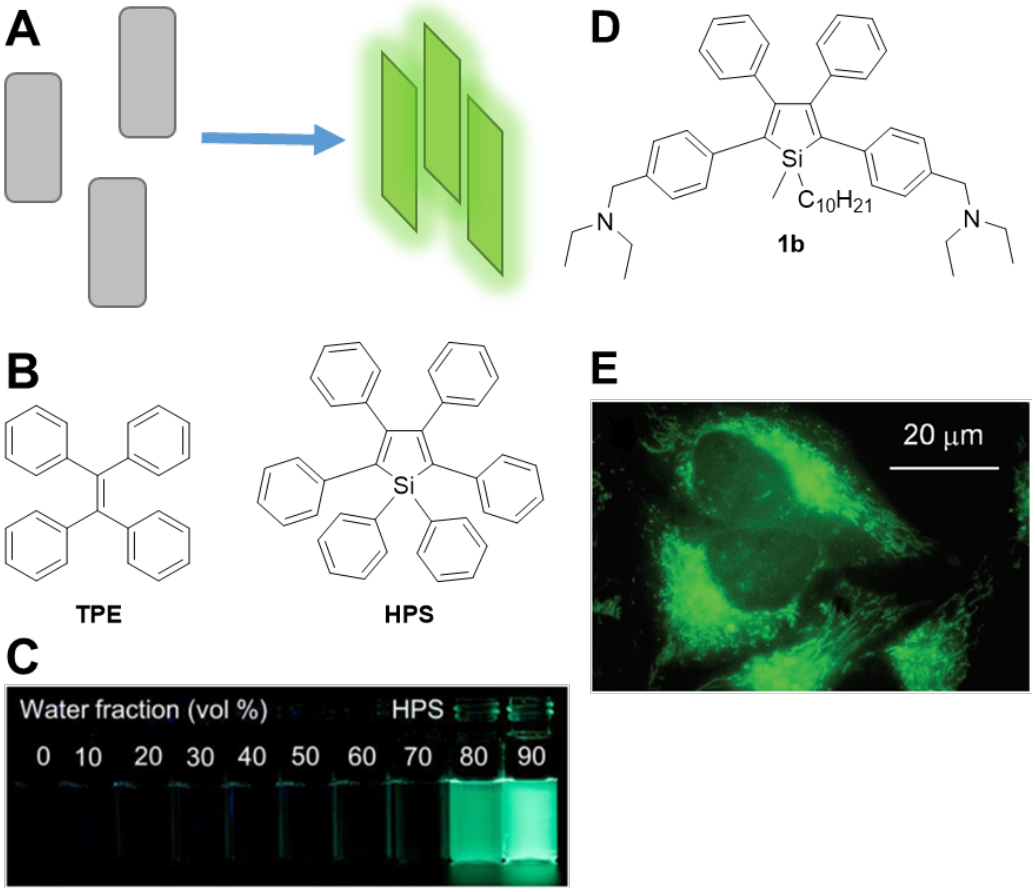

Fig. 1.3.14. AIE fluorophores. Mechanism of fluorogenic AIE response (A) and the structures of AIE dyes (B). Photograph of vials with a THF/water mixture and HPS (20 μM) under UV irradiation (C). Adapted from [76]. Structure of an AIE cytosol probe 1b (D) and a microscopy image of live HeLa cells stained by nanoaggregates of 1b (5 μM) (E). Adapted from [80].

In case of AIE fluorophores, there are several ways to achieve fluorogenic response, all eventually leading to restriction of intramolecular motion. It can be created using electrostatic attraction between the fluorophore and the target molecule, as shown for heparin detection.[81] A fluorescence turn-on can be also triggered by a multivalent complexation of a fluorophore with a biopolymer, which was used for melamine detection.[82] Fluorogenic AIE probes with hydrophobic molecular design can also become strongly emissive upon docking and aggregation in hydrophobic pockets of biomolecules, with an example of probes exploited for quantification of human serum albumin (HSA) and monitoring its conformational transitions.[83, 84] An addition of maleimide fragment to a TPE allowed to couple AIE with photoinduced electron transfer (PET) process,[85] resulting in fluorescence quenching both in solution and in aggregates. The probe

produces a fluorogenic response to the presence of cysteine due to a reaction of maleimide with thiol group of cysteine, blocking the PET process between maleimide and the TPE fragment. Due to an AIE effect, the sensing can be performed with high sensitivity in solid plates.[85]

AIE probes have been used to detect proteins, nucleic acid and polysaccharides[76, 86] as well as reactive small molecules and ions.[76] The AIE fluorophores with special design are also capable of sensing changes in environment parameters, such as mechanical forces, viscosity, pH and temperature.[76] Coupling of AIE mechanisms with either ICT or ESIPT mechanisms allows to create probes, which are sensitive towards the polarity of environment.[87, 88]

Overall, the environment-sensitive probes allow to monitor non-invasively the parameters of interest in live cells, such as microviscosity, polarity, lipid order, membrane tension, temperature, etc., by altering their fluorescence emission in response to the changes in the probe environment. There are several classes of environment-sensitive dyes, with varied relative sensitivity towards different parameters.

1.4 Organelle targeting of fluorescent probes

The majority of fluorophores, being aromatic organic molecules of relatively low polarity, tend to accumulate indiscriminately in all lipid compartments of live cells. On the one hand, such behavior allows to perform the so called cell mapping, when a single dye is used to sense fluctuations of a certain parameter within the different parts of a live cell or an organism, as it was done for polarity[16, 89-91] and viscosity.[92]

However, non-specific binding makes it rather challenging to distinguish and analyze quantitatively the fluorescence signal from only certain organelles in the cell. In order to circumvent this limitation, the probes can be modified with special groups, allowing for selective accumulation of the dyes in the organelles of interest, greatly reducing undesired staining and background fluorescence in cells.[46, 51, 52, 93-97]

There are several criteria, which can be used to evaluate the selectivity of fluorescent probe accumulation in the organelles of interest. The most straightforward approach is based on morphological criteria, when the image pattern is compared to the shape, size and localization of the target organelles in the cell. Though this method requires no additional fluorescent agents, it obviously cannot be used for quantitative measurements.

In case of addition of a second probe with known organelle specificity (*e.g.* probes, which are activated metabolically by enzymes, present exclusively in the target organelles, or genetically incorporated fluorescent proteins), it is possible to perform colocalization imaging. In this case, in addition to direct comparison of images obtained from the two emission channels corresponding to the two probes used in the same cell, it is also possible to quantify the colocalization using statistical approaches, such as Pearson`s correlation coefficient (PCC) and Mander`s correlation coefficient.[98] For instance, PCC values range from 1 for two images whose fluorescence intensities are perfectly, linearly related, to −1 for two images whose fluorescence intensities are perfectly, but inversely, related to one another, while the values near 0 indicate an absence of correlation. The choice of treatment method depends on the image properties, such as background and signal intensities for both channels, as well as on the purpose of analysis.[98]

1.4.1 Plasma membrane-targeted probes

Plasma membrane (PM), besides its primary function of delimiting and separating cell interior, is crucial for essential biological processes including neural communication, cellular uptake, muscle contraction, cell trafficking, migration and signaling.[13, 44, 99, 100] In addition, the morphology of cell plasma membrane can provide the information regarding the cell status such as cell division or cell death processes,[101] while also indicating cell damage.[102] Thus, imaging of plasma membrane is important for both biological research and early medical diagnosis.[103-105]

Utilization of fluorescent probes with environment sensitivity allows, in addition to visualization of PM, to study the different fundamental properties of the biomembranes, such as lipid order, polarity, microviscosity and membrane tension.[8]

The lipids in plasma membrane are believed to distribute inhomogeneously, forming transient relatively ordered membrane microdomains, termed lipid rafts.[13, 106] Lipid rafts are considered to be highly dynamic, both in terms of lateral mobility and association-dissociation and enriched in cholesterol and sphingolipids.[106, 107] These nanodomains (10–200 nm) can undergo the clustering induced by protein–protein and protein–lipid interactions, forming microscopic domains (>300 nm) (Fig. 1.4.1),[106] which act as functional platforms for the regulation of various cellular processes.[13]

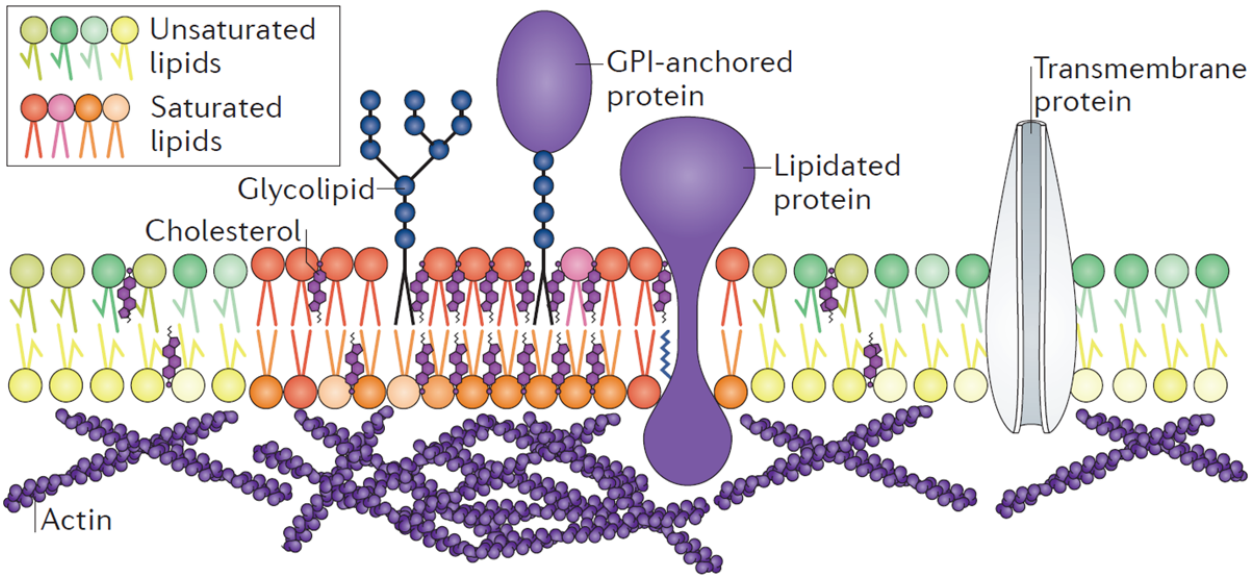

Fig. 1.4.1. Lateral inhomogeneity of cell plasma membrane. Lipid rafts are enriched in sphingolipids, cholesterol, saturated phospholipids, glycolipids, lipidated proteins and glycosylphosphatidylinositol (GPI)-anchored proteins. In addition to membrane components, cortical actin plays an active part in domain maintenance and remodelling. Adapted from [106].

In model membranes, these domains are identified in terms of lipid order,[108, 109] with the liquid-ordered phases (Lo) rich in sphingomyelin and cholesterol "swim" in a pool of liquid disordered phase (Ld), formed by unsaturated lipids. Enrichment of hydrophobic components endows Lo phase domains with distinct physical properties, such as increased lipid packing and decreased fluidity.[106] Lipid order can be sensed either through monitoring the local viscosity by molecular rotors[49] or lipid packing by mechanosensitive dyes[45, 67] as well as through local polarity using ICT or ESIPT dyes.[8, 110, 111] Solvatochromic dyes in Lo phases generally report less polar environment when compared to Ld, as the tight backing of lipid ordered phase excludes polar water molecules and freezes dipolar relaxation processes.[12, 14, 15, 109]

In addition to lateral inhomogeneity, plasma membrane also reveals a difference in membrane composition between the outer and the inner leaflets. In live cells the outer leaflet is mainly represented by sphingomyelin and phosphatidyl choline, while the inner one contains mostly phosphatidyl ethanolamine and phosphatidyl serine.[112, 113] This heterogeneity results in higher lipid order at the outer leaflet.[114] In order to increase the probe sensitivity to the changes in the lipid order, it is important to ensure that the probe is localized specifically in the outer membrane leaflet. However, this approach requires introduction of a special molecular design for the probes, which would inhibit or slow down the dye flip-flop process.[15]

Microscopic viscosity is essential for determination of lateral diffusion in biomembranes, while also affecting metabolism, enzymology and protein folding.[51] This parameter can be measured using either molecular rotors[51, 115, 116] or flipper probes,[67] as well as by ICT solvatochromic probes.[10]

Imaging of the membrane tension, an important parameter during membrane trafficking[44], phagocytosis, [44] cell migration [39-42] and spreading,[43] can be performed utilizing the flipper probes.[38, 46]

Local membrane polarity is a complex parameter combining presence of dipoles, hydration, solvent relaxation and lipid order,[12, 25] which can be studied using ICT solvatochromic fluorescent dyes.[117] The changes in the membrane polarity of live cells reflect various processes, such as oxidative stress,[118-120] starvation[118] and apoptosis,[30, 121, 122] and allow to distinguish between normal and cancer cells.[123]

Fluorescently labeled lectins, notably wheat germ agglutinin (WGA) and concanavalin A, are popular fluorescent membrane probes. Despite their ease of use and efficiency, the drawbacks of these probes include high price significantly larger probe size compared to molecular probes. Additionally, WGA binds N-acetyl-D-glucosamine and sialic acid,[124] and the direct positioning of fluorophore inside membrane is not assured, which hinders the imaging of plasma membrane lipids.

The small size of fluorescent probes with chemical targeting groups, also having high lipid bilayer affinity, allows their precise localization in the lipid bilayer, which is indispensable for studies of lateral distribution of lipids in biomembranes.[12, 125] The moieties, used to create plasma membrane-targeted probes, are usually amphiphilic molecules which include a hydrophobic long alkyl chain (typically C12) and a cationic or zwitterionic charged fragment (Fig. 1.4.2),[15, 74, 126, 127]. Long alkyl chains serve to increase probe affinity towards the lipid bilayer, and in some probes the aromatic fluorophore moiety itself can serve as a hydrophobic part. The main function of the charged fragment is to decrease the probe internalization and consequent non-discriminate staining of intracellular lipid components. Due to the structure of plasma membrane lipid bilayer, which possesses a negative surface charge, the charged molecules (especially zwitterions and anions) cannot easily pass through the membrane.

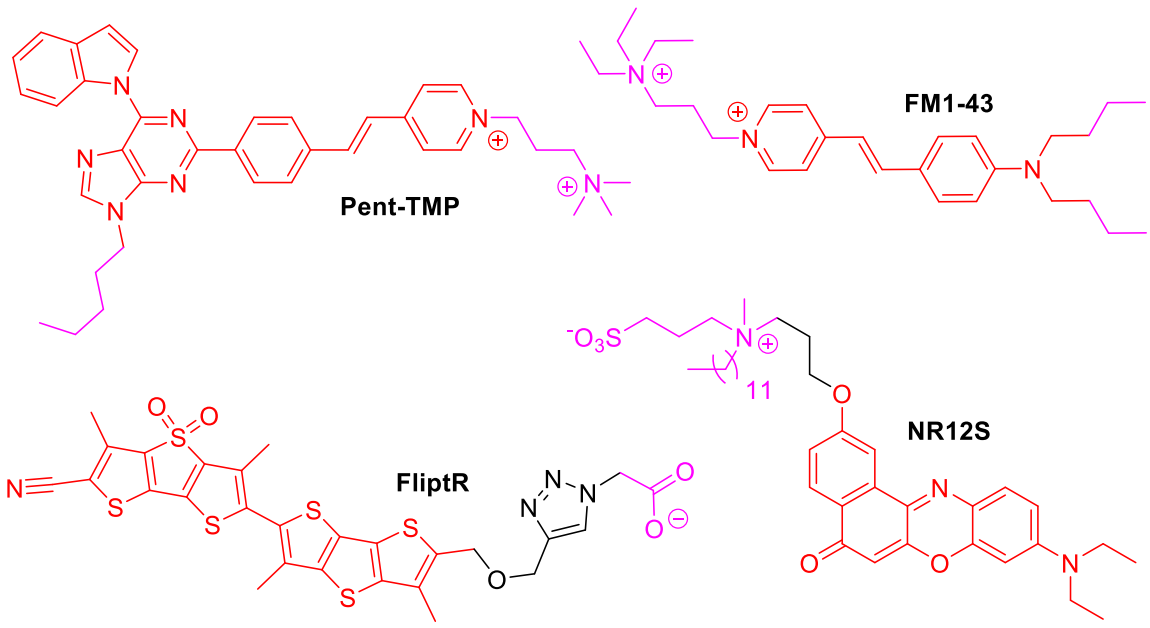

Fig. 1.4.2. Examples of different plasma membrane-targeted probes. Molecules bearing (poly)cationic charge (Pent-TMP and FM1-43), zwitterionic molecules (NR12S) and negatively charged molecules (FliptR).

Introduction of zwitterionic fragments allows to increase plasma membrane affinity while also reducing probe internalization (Fig. 1.4.3).[126, 128] Thus, in combination with bright squaraine fluorophore, it allowed imaging of plasma membranes at low concentrations up to 1 nM.[74] In addition, the presence of amphiphilic targeting motifs leads to aggregation in aqueous medium, eliminating the undesired background fluorescence for both probes (Fig. 1.4.3, B and C). Additionally, cyanine MemBright dyes stained neurons in a brighter manner compared to surrounding tissue, being promising candidates for applications in neuroscience.[126]

Nevertheless, zwitterionic targeting fragments do not change the overall probe charge, which can in principle affect the staining of the surface of microscopy support, as the glass of the surface is negatively charged and therefore attracts the positively charged probes, based on cationic fluorophores, such as cyanines and styryl dyes.

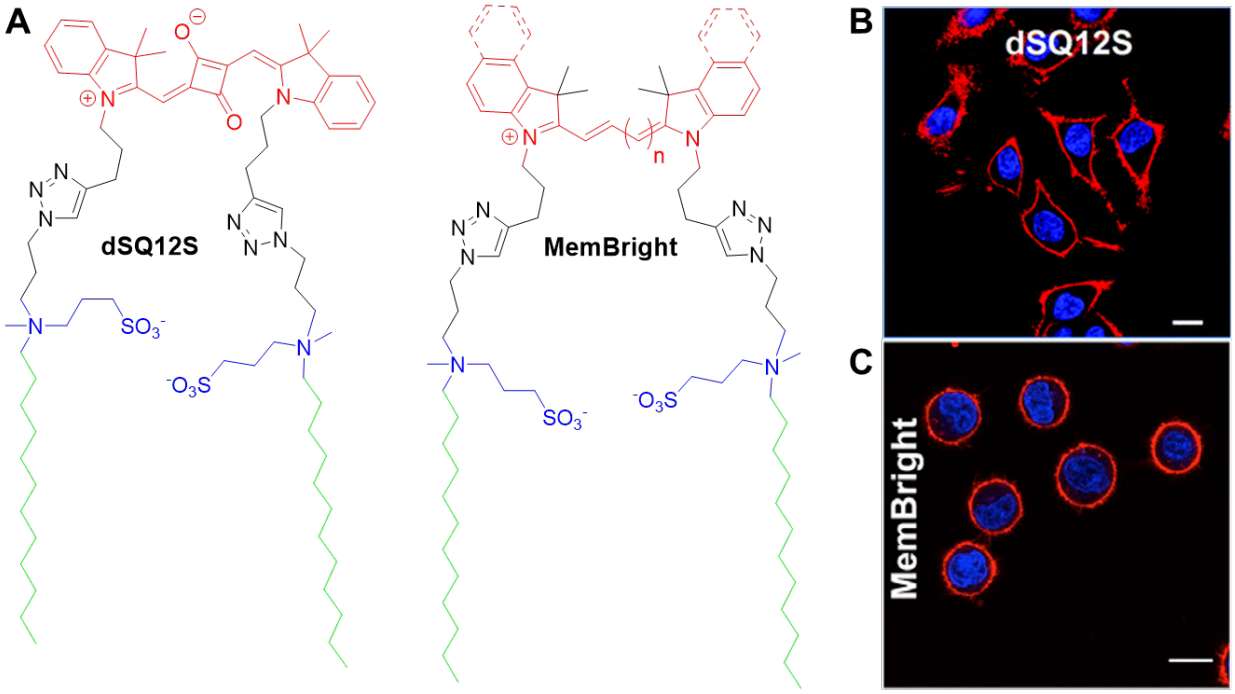

Fig. 1.4.3. Live cell microscopy with zwitterionic PM probes. Structures of plasma membrane probes with two zwitterionic targeting moieties (A). Microscopy image of live HeLa cell stained with dSQ12S probe (B). Microscopy image of live KB cell stained with MemBright (Cy3MB) probe (C). Cell nuclei in (B) and (C) were stained with Hoechst dye.

Rational design of environment-sensitive plasma membrane probes allows to monitor a variety of biological process in live cells, including cholesterol depletion in membranes,[15] apoptosis,[129] conformational changes of membrane proteins,[130] maturation of endosomes[131][and internalization of nanostructures.[132]

The probes for PM were created using various fluorophores, including BODIPY[128, 133, 134] and BF_2-azadipyrromethene,[135] styrylpyridinium,[136-139] fluorescein,[140, 141] Nile Red,[15] chromone,[30, 142] perylene,[143] oligothiophene,[38, 45] isoindoledione,[144] purine,[145] conjugated polymers,[146] squaraine[74] and cyanines.[102, 126, 139]

1.4.2 Mitochondria-targeted probes

Mitochondria are the major energy sources for predominant majority of the living organisms.[147] Through a chain of chemical and biological processes known as oxidative phosphorylation, mitochondria are able to produce molecules of adenosine triphosphate (ATP), which act as a coenzyme and fuel in various cellular activities, including biomolecular synthesis, cell division, and metabolism.[148]

The membranes of mitochondria are known to have high concentration of negative charges.[149] This peculiarity results in selective accumulation in mitochondria for those lipophilic molecules, which simultaneously possess positive charge (Fig. 1.4.4, A). Hence, most of the chemical mitochondria-targeting groups contain positively charged aromatic or heteroaromatic fragments, including triphenylalkylphosphonium, N-alkylpyridinium, N-alkylindolinium and N-alkylbenzimidazolium (Fig 1.4.4, B).[150-152]

Alternative strategy includes utilization of the mitochondrial import machinery, namely, signal peptides with a positively charged amphipathic a-helix formed at the N-terminus. These peptides can be recognized by the mitochondrial inner membrane translocase, thus allowing the delivery of cargo molecules, such as fluorescent dyes, inside mitochondria. Inspired by the natural system, researchers have refined the long-chain polypeptides to obtain the functioning moieties, most of which are either cationic (e.g. arginine, lysine) or hydrophobic (e.g. phenylalanine, cyclohexylalanine) peptides containing arginine-based functional groups (Fig. 1.4.4, C).[153]

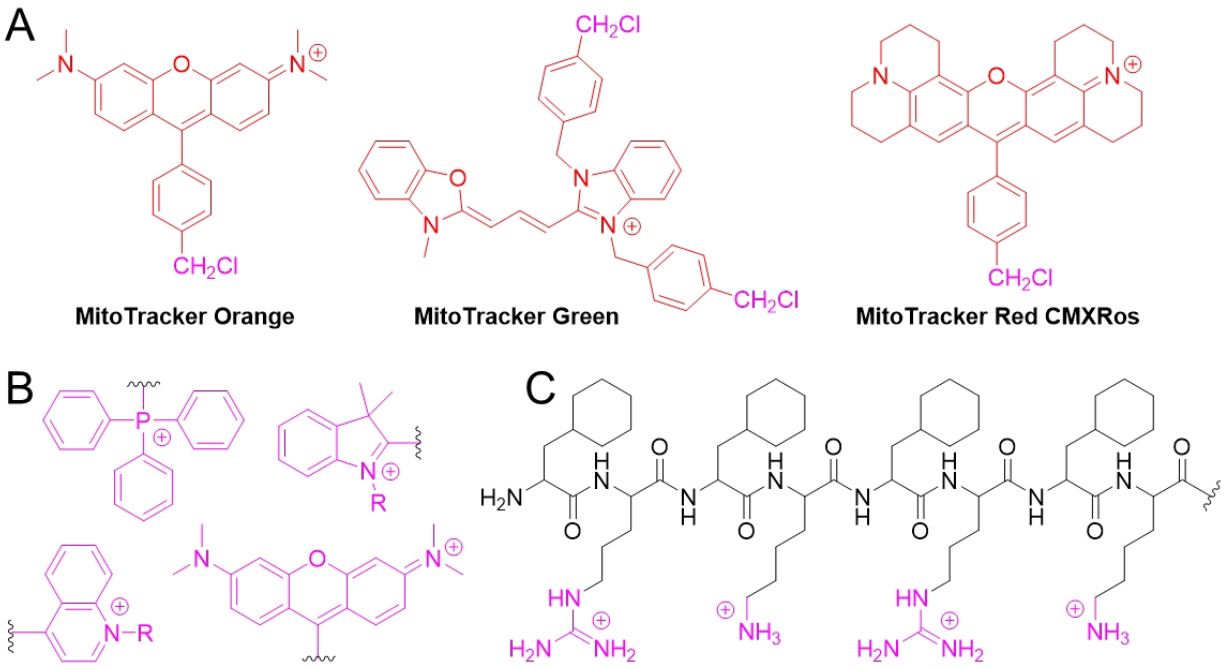

Fig. 1.4.4. Structures of mitochondria-targeted commercial probes (A). Structures of mitochondria-targeting chemical groups and motifs (B) and mitochondria-targeting peptides (C).

Mitochondria targeting groups were used to achieve selective accumulation for a number of fluorophores, including environment-sensitive ones, such as solvatochromic ICT fluorophores,[93] molecular rotors[51, 61, 97] and mechanosensitive flipper dyes.[46]

1.4.3 Lysosome-targeted probes

Lysosomes are spherical-shaped, catabolic organelles that ubiquitously exist in almost all eukaryotic cells and are mainly responsible for the degradation of biological macromolecules, forming the main part of cell digestive system.[154-156] The structure of the phospholipid bilayer of a lysosome wall is similar to one of plasma membrane. Lysosomes maintain a lower pH value (*ca.* 4.5) compared to that of the cytoplasm because of the proton-importing machinery of V-type ATPases.[155-157]

Most targeting approaches for lysosomes rely on the difference of pH between the interior of these organelles and the cytosol inside the cell. The probe design typically includes an addition of a tertiary amine fragment (Fig. 1.4.5).[150, 158, 159] Upon its internalization, an initially uncharged probe molecule can diffuse freely within the lipid compartments of the cell. However, when the probe enters lysosome with low pH interior, the amine becomes protonated, efficiently entrapping the fluorescent probe inside lysosomes, which results in selective probe accumulation.

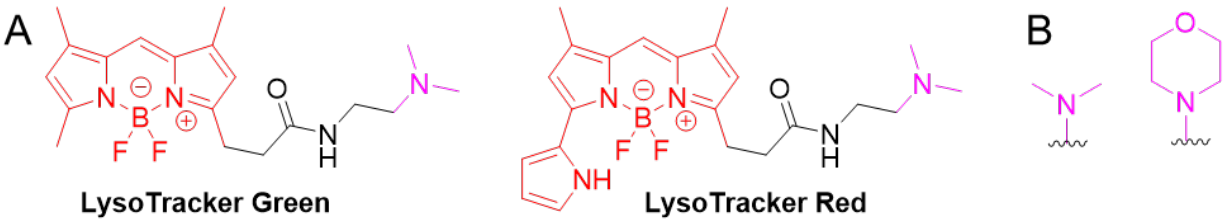

Fig. 1.4.5. Structures of lysosome-targeted commercial probes (A) and lysosome-targeting groups (B).

Lysosome targeting groups were used to achieve selective accumulation for a number of fluorophores, including environment-sensitive ones, such as molecular rotors[51, 62] and mechanosensitive flipper dyes.[46]

1.4.4 ER-targeted probes

The endoplasmic reticulum (ER) is the main place for protein biosynthesis, modification, folding and transportation. This organelle also plays an important role in biosynthesis of other molecules, like lipids and carbohydrates, and acts as well as a Ca^{2+} storage.[150] Endoplasmic reticulum can be divided into a rough ER and a smooth ER, with the former comprising ribosomes on its outer surface. Although originating from the nuclear DNA, the proteins are actually produced within the rough endoplasmic reticulum before being further distributed to their respective locations via the Golgi apparatus.[160] Endoplasmic reticulum comprises of open structures with a network of curved membranes known as cisterna.

The intrinsic molecular mechanism of ER-targeting of the fluorescent probes remains unclear, but the common features of these probes may be concluded as small amphiphilic or moderately lipophilic cationic molecules (Fig 1.4.6, A). The chemical moieties, used to achieve ER-targeting, can include p-toluene sulfonamide or PEG,[150] while the third approach towards ER localization exploits an incorporation of reactive groups, such as propylchloride or pentafluorophenyl moieties, (Fig. 1.4.6 B).[46, 94, 158, 161, 162] These groups are able to bind thiols in the endoplasmic reticulum, thus ensuring selective probe accumulation.

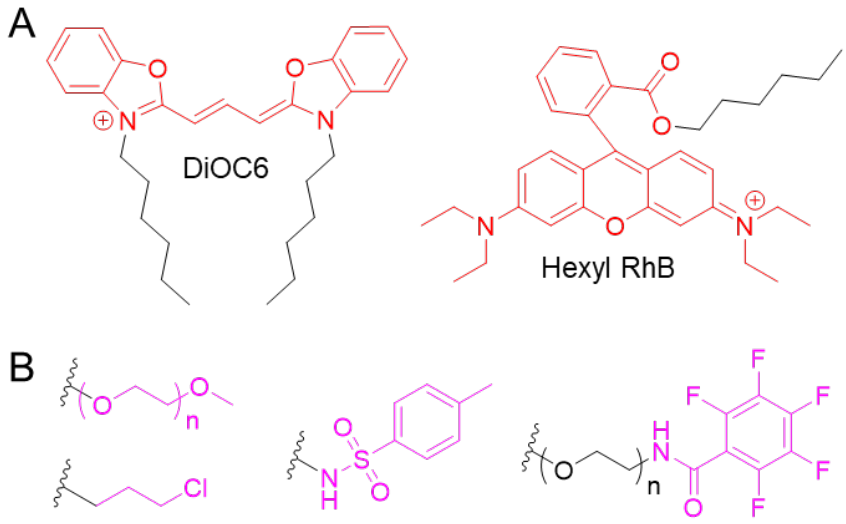

Fig. 1.4.6 Structures of dyes with selective ER accumulation (A) and ER-targeting moieties (B).

ER-targeting groups were used to achieve selective accumulation for a number of fluorophores, including environment-sensitive ones, such as solvatochromic ICT fluorophores,[94] molecular rotors[51] and mechanosensitive flipper dyes.[46]

1.4.5 Golgi-targeted probes

The Golgi apparatus is an important intracellular compartment for the modification, storage and transportation of lipids, carbohydrates and proteins.[150] The structure of this organelle highly resembles the one of ER, also comprising cisterna and some open structures. Notably, the structure of Golgi cisterna is asymmetric with cis face directed towards ER and trans face directed away from ER. Once the proteins reach the Golgi apparatus, they undergo various labeling procedures, including glycosylation, sulfation, and phosphorylation,[163] traversing within the cisterna from the cis face to the trans face.

The intrinsic rules for designing the Golgi apparatus-targeted probes are still vague, which hampers the development of related fluorescent probes.[150, 151] The existing residues, used to achieve selective Golgi accumulation rely mostly upon either substrates of enzymes, abundant in Golgi, or on specific biomolecules, which are transported and later processed in this organelle by cellular machinery (Fig 1.4.7). The biomolecules, used for selective probe accumulation in Golgi, include myristic acid,[164, 165] ceramide[166-168] and L-Cysteine (Fig.1.4.7). L-Cysteine was introduced recently as an efficient Golgi apparatus targeting ligand, inspired by cysteine-rich galactosyltransferase and protein kinase D, which are localized in Golgi.[169-171]

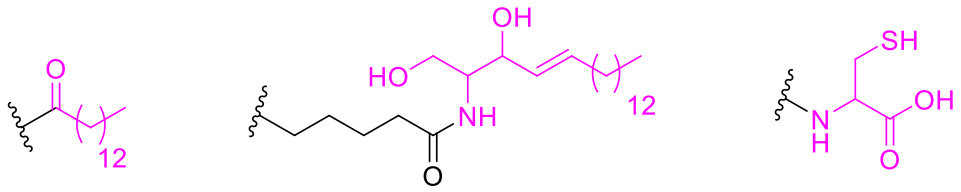

Fig 1.4.7. Structure of Golgi-targeting moieties.

1.4.6 Lipid droplets-targeted probes

Lipid droplets (LDs) are the cellular organelles with primary function of a lipid storage. LDs consist of a neutral lipid core, mainly containing triglycerides and sterol esters, which is covered by a phospholipid monolayer shell.[172, 173] The surface of these organelles is decorated by numerous proteins, many of which play functional roles in LD biology.[172, 173]

Recently, LDs have drawn considerable attention as they were shown to be involved in different cellular processes such as membrane formation, trafficking, and protein–protein interaction.[172, 174]

Most lipid droplet-targeted probes are small uncharged molecules of low polarity, in some cases bearing several short alkyl chains to increase probe hydrophobicity (Fig 1.4.8).[175] Another option includes probe design with increased bulkiness and hydrophobicity, as in case of the incorporation of cyclohexyl moieties, leading to partial probe exclusion from the biomembranes and, consequently, better selectivity towards lipid droplets.[176]

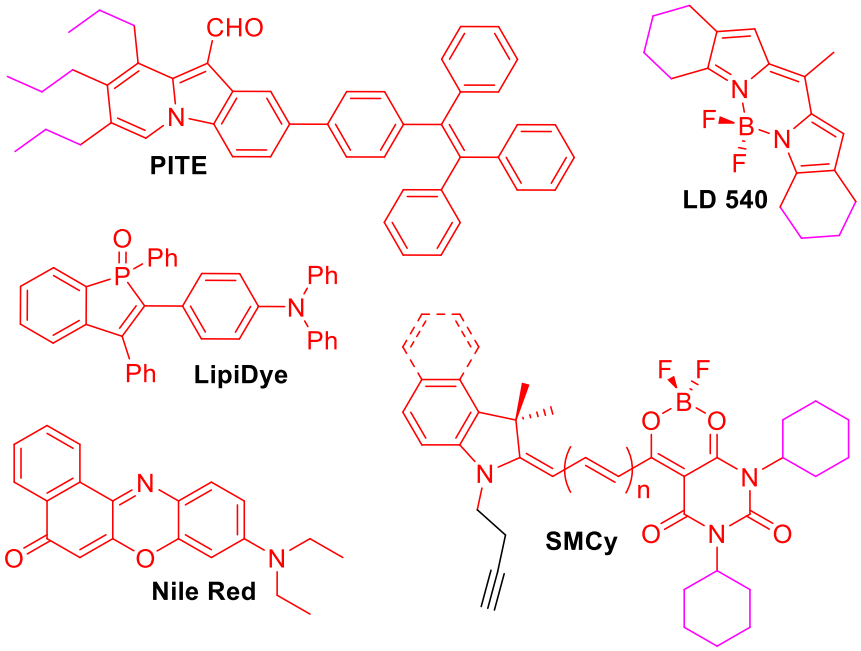

Fig 1.4.8. Structure of lipid droplet-selective fluorescent dyes and probes

Lipid droplets are a promising target for environment-sensitive probes, as it was recently discovered, that these organelles exhibit strong response in polarity when the cell is put into stress conditions, such as starvation or oxidative stress.[89]

An alternative developing approach towards lipid droplet targeting includes utilization of AIE dyes due to their intrinsic high hydrophobicity and capacity to light up in viscous apolar environemnts.[78, 177]

1.4.7 Nucleus-targeted probes

Nucleus plays an essential role in the storage of genetic information, protein expression, cell growth and reproduction.[178] The key feature used for designing nucleus-targeted probes is that nuclei comprise of negatively charged DNA molecules.[179] Most of the nucleus-targeted probes are cationic or polycationic molecules with planar aromatic motifs (Fig. 1.4.9).[151] Such design allows to create the probes which will strongly interact with nucleic acids by either binding the minor groove region of DNA double helix or by intercalating between the base pairs, while also having lower affinity towards lipids and proteins,[179, 180] which results in selective nuclei staining. Additionally, dimeric probes like YOYO-1 (Fig. 1.4.9) become highly emissive upon binding to negatively charged DNA and do not fluoresce in water due to the formation of non-emissive to H-aggregates.[70]

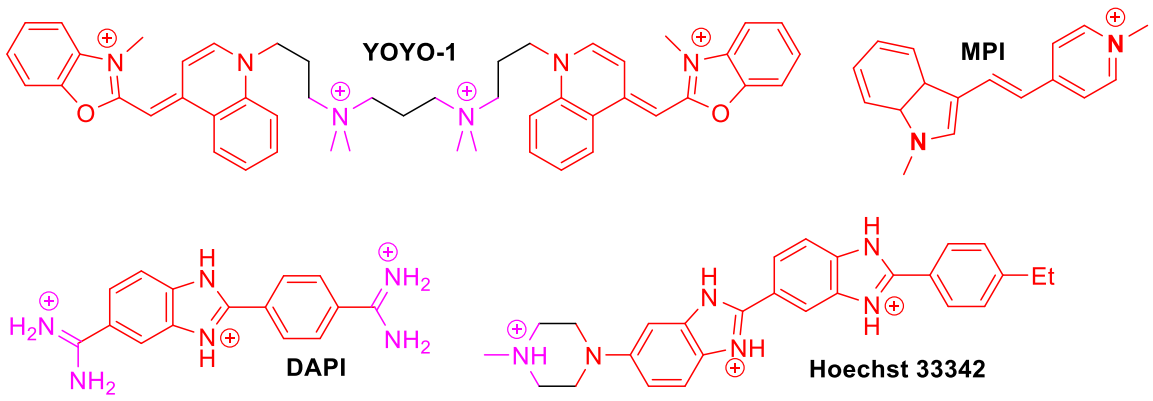

Fig 1.4.9. Structure of nucleus-selective fluorescent probes

Overall, an introduction of organelle-targeted groups into the probe molecular design allows to ensure its selective accumulation in the organelle of interest. Generally, the organelle targeting is ensured either by the distinct biophysical properties of the organelle or by the cellular machinery.

1.5. Fluorescent probes for super-resolution microscopy imaging

1.5.1 Basics of super-resolution microscopy

Spatial resolution is an important characteristic of microscopy imaging, determining the minimal distance between the two objects which can be detected separately. For conventional microscopy methods, spatial resolution is limited due to the diffraction of light into the far field (i.e., at a distance of many wavelengths from the emitter). This is referred to as the diffraction limit of light microscopy or Abbe's diffraction limit, in honor of Ernst Abbe. In Abbe`s works he articulated the inverse relationship between spatial resolution and numerical aperture,[181] which can be expressed by the following expression: $d \approx \lambda/2NA$, where d is spatial resolution of a microscope, λ corresponds to the wavelength of light used and NA is the numerical aperture of

the microscope objective lens. Practically, the modern microscopes, working in the visible range, allow to resolve objects being at least 200-250 nm apart. Electron microscopy and atomic force microscopy methods can provide much higher spatial resolution, however, these methods have certain limitations, concerning poor ability to monitor the distribution of specific molecules, lack of compatibility with live cells or organisms and an ability to obtain the signal exclusively from the sample surface.

Though it is impossible to directly cancel out the light diffraction, several approaches to bypass it have been developed, eventually leading to an attribution of a Nobel prize in 2014. These approaches, used in creation of super-resolution microscopy techniques, can be divided into two main categories.

The first category relies on patterned illumination or differential modulation of fluorescence emission of molecules within the diffraction-limited volume, thus achieving their separate detection. Stimulated emission depletion (STED) microscopy[182, 183] is one of the pioneering methods of this type, which was later generalized to reversible saturable optical linear fluorescence transitions (RESOLFT).[184] These methods overcome the diffraction limit by utilizing a focused excitation beam together with a donut-shaped "depletion" beam (Fig. 1.5.1), which effectively renders the fluorophores non-emissive either through stimulated emission (in STED)[182, 183] or through other mechanisms, such as photoswitching (in RESOLFT).[184] This combination results in the fluorophores being emissive only within the central region of the donut-shaped beam, where the depletion laser intensity is negligible, which creates a region of excited fluorophores, smaller than a typical focal spot of a light microscope.

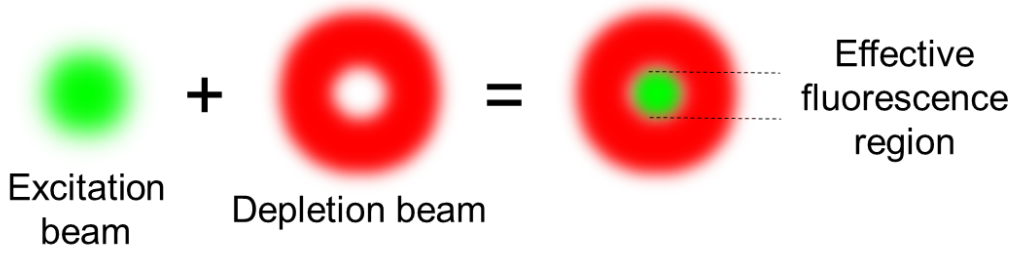

Fig 1.5.1. Principle of patterned fluorophore illumination in STED super-resolution microscopy

Alternatively, the donut beam can be used to achieve patterned activation, thus limiting the non-emissive region to the center of the beam.[185] The next step requires scanning the beams across the sample to create a super-resolved microscopy image. Various illumination patterns can be used to increase image resolution,[185] for instance, structured illumination microscopy (SIM) requires the sample to be excited with a number of standing waves with different phases or orientations.[186] The nonlinear form SIM (structured SIM, or SSIM) is able to bypass the diffraction limit using saturated response of fluorophores, similar to STED and RESOLFT, however, additional treatment of raw data is required to reconstruct the final image in case of SIM or SSIM approach.[185, 186]

One of the key requirements for the fluorophores used in STED, alongside with brightness, is photostability. The achievable image resolution for these techniques depends on the size of emission zone, which is narrower in case of increased intensity of depletion light.[185] RESOLFT technique is based upon photoswitching instead of stimulated emission, which leads to utilization of much lower light intensities,[185] compared to STED, and the fluorophore requirements generally are in line with those for SMLM methods.[187]

The second broad category of super-resolution methods is based upon imaging of individual fluorophores within the diffraction-limited volume at different time points. Each imaging frame is processed in order to precisely localize the individual fluorophore positions, and the sum of fluorophore localizations in all the recorded frames yields a super-resolved image (Fig. 1.5.2). Positions of isolated emitters can be determined with nanometer or even subnanometer precision by localizing the center of their fluorescence emission images,[188-190] however, two or more molecules in the same diffraction-limited volume create overlapping images and cannot be distinguished, which is the fundamental reason of the diffraction limit in spatial resolution.

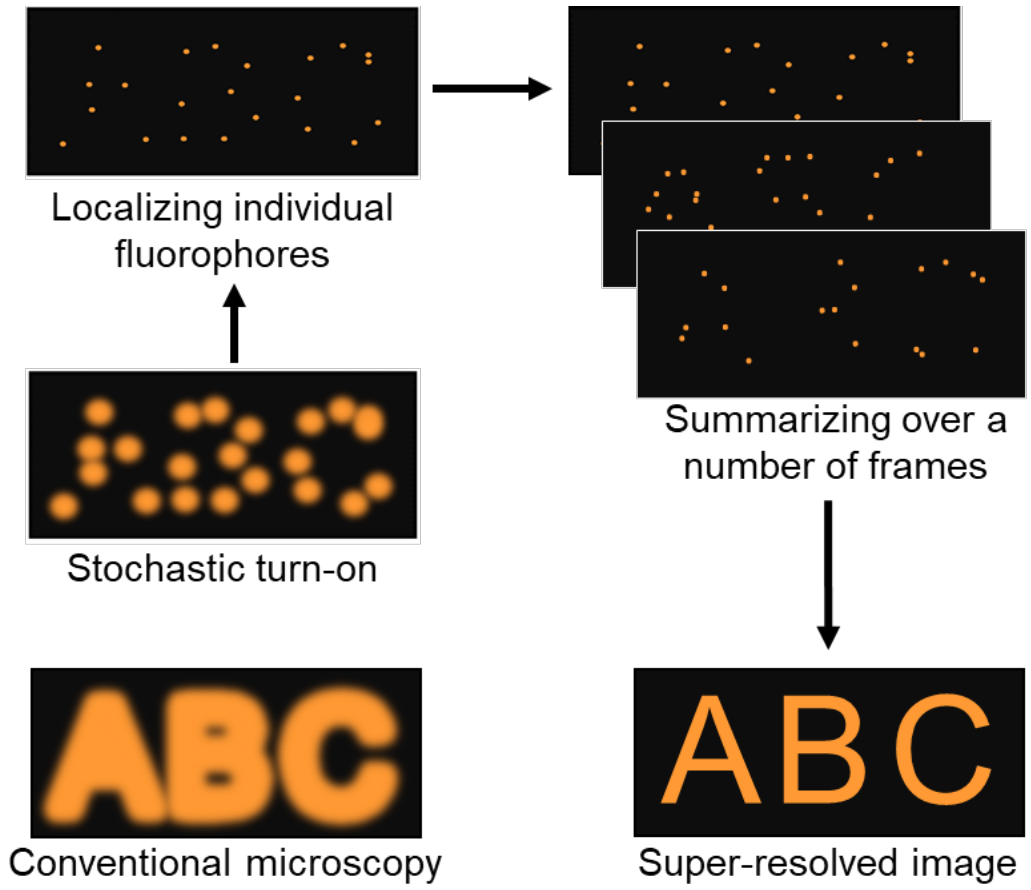

Fig 1.5.2. Principle of achieving super-resolution in SMLM methods

The key difference between the different methods of single molecule localization microscopy (SMLM) lies in the way to achieve a turn-on only for a small fraction of fluorophores at a time. Stochastic optical reconstruction microscopy (STORM)[191, 192] and (fluorescence) photoactivated localization microscopy [(F)PALM],[193] together with related methods,[194, 195

utilize stochastic activation of photoswitchable organic dyes (in STORM) or fluorescent proteins (in PALM).[191-195] This is done in such a way that the image overlapping is minimized and thus the molecules can be localized with high precision. After a short time in emissive state, the molecules are switched to a dark state or photobleached, and a different stochastic subset of fluorophores is imaged and localized, making it possible to obtain a super-resolved image after a sufficient number of iterations.[191-193]

An alternative way to create a stochastic turn-on response is to exploit transient binding of fluorescent probes. Point accumulation for imaging in nanoscale topography (PAINT)[196] method utilizes directly a fluorogenic and/or a solvatochromic response of fluorescence probes. The dyes of special molecular design are capable of transient binding to the target molecule or biomembrane, accompanied by an increase in fluorescence intensity and/or a shift of fluorescence emission maximum, thus creating the desired turn-on behavior.

A combined super-resolution imaging method named MINFLUX was developed by S. Hell and coworkers.[197] MINFLUX exploits stochastic fluorescence turn-on of individual fluorophores coupled with patterned illumination, typically a donut-shaped beam. As a result, it is possible to achieve about 1 nm precision through the detection of local emission maxima[197].

The nature of signal acquisition in SMLM, which uses stochastic turn-on of fluorophore molecules, imposes several key requirements towards the probes which are compatible with this group of methods. First, the fluorophore should be able to switch between emissive and dark states, and the difference in brightness between these states, referred to as on-off contrast ratio, should be substantial. Although the on-off contrast ratios are seldom reported, many of the commonly used SMLM fluorophores possess on-off contrast ratios much greater than 1000:1.[187] Second, the fluorophore should have a fraction of time spent in the bright state, referred to as a duty cycle, to be sufficiently low, regardless if the dye is later photoswitched or bleached irreversibly. For instance, in case there are 50 probe molecules within the diffraction-limited volume the fluorophore should stay less than 2% of its time in a bright state (*i.e.* the duty cycle should be less than 0.02), in order to avoid frequent double or multiple localizations. In approximation, the duty cycle corresponds to the ratio between the rates of turn-on and turn-off processes for both reversible switching and irreversible activation.[187] Additionally, the duty cycle for a given fluorophore, generally, depends on probe chemical environment as well as on illumination conditions. Third, the fluorophores must be bright (and sometimes photostable) enough to allow single molecule detection, that is it is crucial that a molecule emits a large number of photons in turn-on state. The localization uncertainty roughly corresponds to the inverse square root of the number of photons detected.[189, 198, 199] Therefore, from the photophysical point of view an ideal SMLM fluorophore should possess a low duty cycle, a high on-off contrast ratio and a high brightness. Other important criteria include the number of switching cycles and phototoxicity, as well as probe targeting efficiency.

A wide range of fluorescent probes has been utilized in SMLM, including organic dyes, fluorescent proteins, and quantum dots. These fluorophores rely upon diverse switching mechanisms to exhibit turn-on and turn-off behavior. Generally, a choice of probe strongly depends on the method, as due to a large diversity of techniques, used to create the on/off behavior,

signal acquisition and processing, the probe, which is not suitable for one group of methods, might be highly applicable for another.[187]

1.5.2 Probes for super-resolution microscopy based on conventional fluorophores

Conventional fluorophores can be used directly in super-resolution microscopy methods with patterned illumination, while the methods based on stochastic activation require creation of blinking behavior for these dyes. This on-off transition can be induced either by utilization of special buffers, which render most of the fluorophores in solution non-emissive,[200, 201] or by utilization of various caging groups, allowing to activate at a time only a part of the fluorophores present in the sample.

Cyanines

Cyanine dyes are among the most frequently used classes of fluorophores for SMLM,[200, 201] particularly Cy5 and its close structural relatives such as Alexa Fluor 647 (Fig. 1.5.3, A). The reversible photoswitching behavior of Cy5 was first reported Heilemann et al. and Bates et al. in 2005.[200, 201] According to the reported data, Cy5 can be switched to a long-lived non-emissive state after illumination with red light, while the light with shorter wavelength can be used to switch nonfluorescent fluorophore molecules back into emissive state. Alternatively, Cy5 can be switched to fluorescent state by illuminating a Cy3 fluorophore (termed an activator molecule) positioned within 1-2 nm from Cy5. In both cases the photoswitching behavior was obtained in a special buffer solution commonly utilized in single-molecule FRET microscopy, containing a primary thiol, such as β-mercaptoethylamine (MEA) or β-mercaptoethanol (BME) together with enzymatic oxygen-scavenging system.[200, 201] For the first time the photoswitching of Cy5 was used for SMLM in the original STORM paper by Rust et al. in 2006, where the Cy3−Cy5 dye pair was exploited to image circular RecA-coated plasmid DNA.[191] Later it was shown by the same group that also Cy5.5 and Cy7 exhibit good switching properties, and that each of the three fluorophores (Cy5, Cy5.5 and Cy7) can be paired with a number of activator dyes (such as Alexa Fluor 405, Cy2 and Cy3) (Fig. 1.5.3, B), allowing to create a palette of activator-reporter pairs which can be used in multicolour super-resolution microscopy.[202, 203] In 2007 Bock et al. showed that Cy5 could be used for SMLM without an activator fluorophore,[204] this approach, referred to as dSTORM (direct STORM) was later substantially expanded utilizing a number of cyanines and other fluorophores.[205-207]

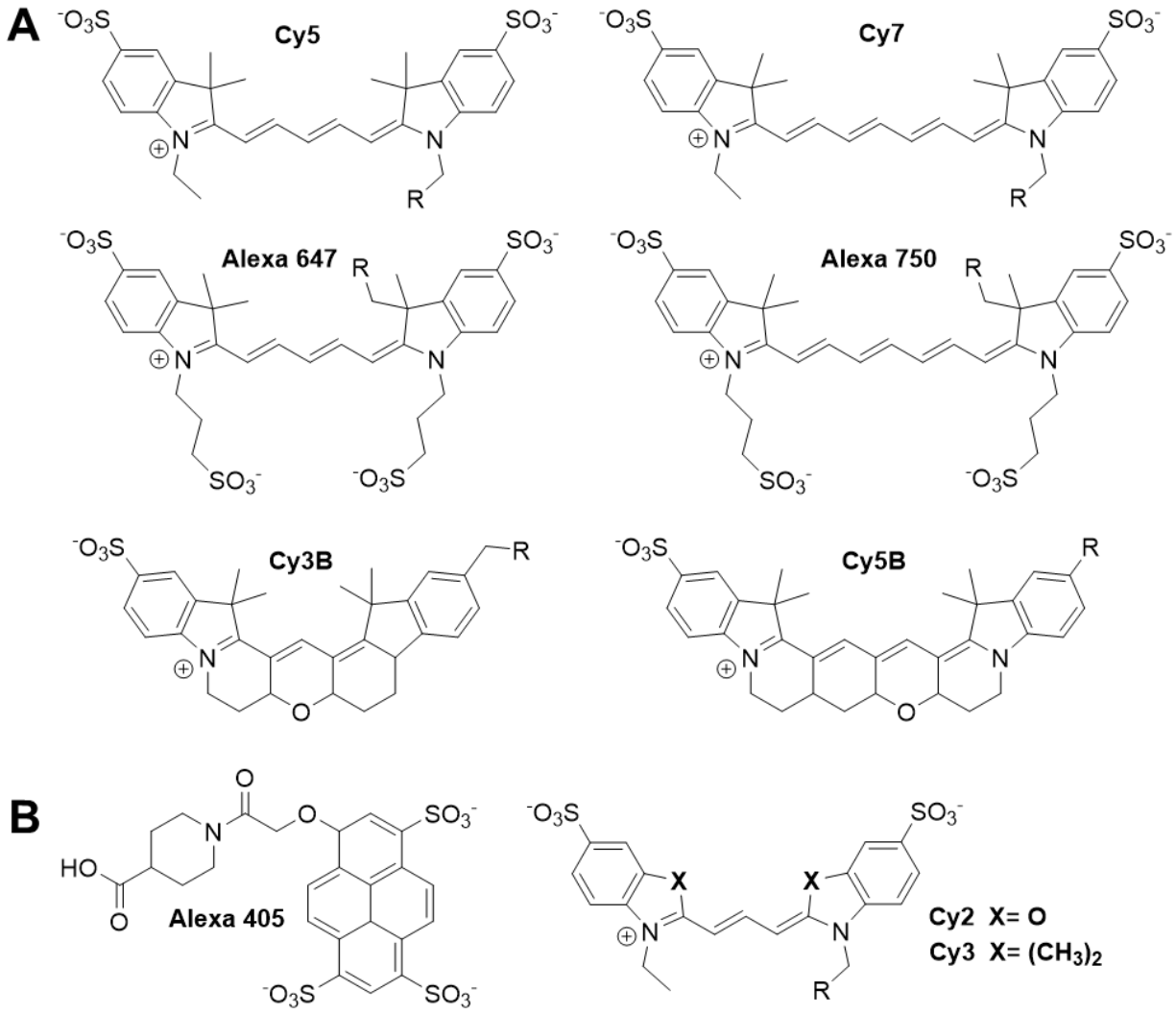

Fig. 1.5.3. Structures of commonly used photoswitchable cyanine dyes (A) and activator molecules (B)

The structure and mechanism of formation of a Cy5 dark state was studied by Dempsey *et al.* using single-molecule imaging and mass spectrometry.[208] It was found that upon illumination with red light a thiolate anion can react covalently with the Cy5 polymethine bridge (most probably with the γ-carbon) (Fig. 1.5.4, A), which is accompanied by a disruption of the conjugation and a shift to the ultraviolet region in absorption,[208] resulting in fluorescence turn-off. It was recently found that reversible interaction with a thiolate is also responsible for an increased photostability of cyanines in thiolate buffer.[209] In addition, Vaughan et al. have found that tris-2-carboxyethylphosphine (TCEP) in capable of reacting reversibly with the γ-carbon of Cy5 polymethine bridge even without illuminating with red light,[210] being additional evidence the γ-carbon is the reaction site for nucleophile agents. Utilization of TCEP to induce photoswitching allowed to perform two-colour imaging using Cy5 and Cy7 (or close structural relatives of Cy5 and Cy7 such as Alexa Fluor 647 and Alexa Fluor 750, correspondingly) due to an about 3-fold enhancement of relatively low photon output of Cy7 compared to thiol strategy.[210]

The fluorophore Cy3 does not photoswitch well in deoxygenated thiol-containing buffer, in contrary to Cy5, Cy5.5, and Cy7.[208, 211] Such a behavior could be caused by a difference in accessibility to the short polymethine bridge of Cy3 or in other photochemical steps. Nevertheless, a version of Cy3 with additional structural rigidity – Cy3B (Fig. 1.5.3, A) was found to exhibit photoswitching behavior in deoxygenated solution regardless of the presence of thiols,[211] implying another photoswitching mechanism, such as formation of a long-lived radical, as in case of some rhodamine fluorophores.[212]

Another strategy to create photoswitching in cyanine dyes exploits the formation of hydrocyanines,[213] rendering the fluorophores non-emissive through chemical reduction, followed by oxidation back into emissive state.[214, 215] Hydrocyanines are typically obtained through a net hydride anion addition to the α carbon atom of the cyanine polymethine bridge (Fig. 1.5.4, B). Vaughan *et al.* have developed a method to perform a "reductive caging", when the cyanines Cy3, Cy3B, Cy5, or Cy5.5 could be *in situ* reduced to hydrocyanines through a brief treatment of a fixed and labeled sample with dilute aqueous $NaBH_4$.[213] After this the formed hydrocyanines are activated in an imaging cocktail, needed to suppress bleaching and blinking. Reductive caging allows to increase greatly (4-20 times) the photon fluxes per localization, though the method activates only ~12−40% of fluorophores and does not provide an improvement in duty cycle over thiol-based strategy.[213] This approach has also been extended to perform multicolour SMLM, using a variety of other cyanine and non-cyanine organic dyes.[216] Recently, a version of Cy5 with additional structural rigidity called Cy5B (Fig. 1.5.3, A) was developed by Michie *et al.*, which possesses a recovery yield of ~38%, exceeding about 6-fold the parent Cy5.[217]

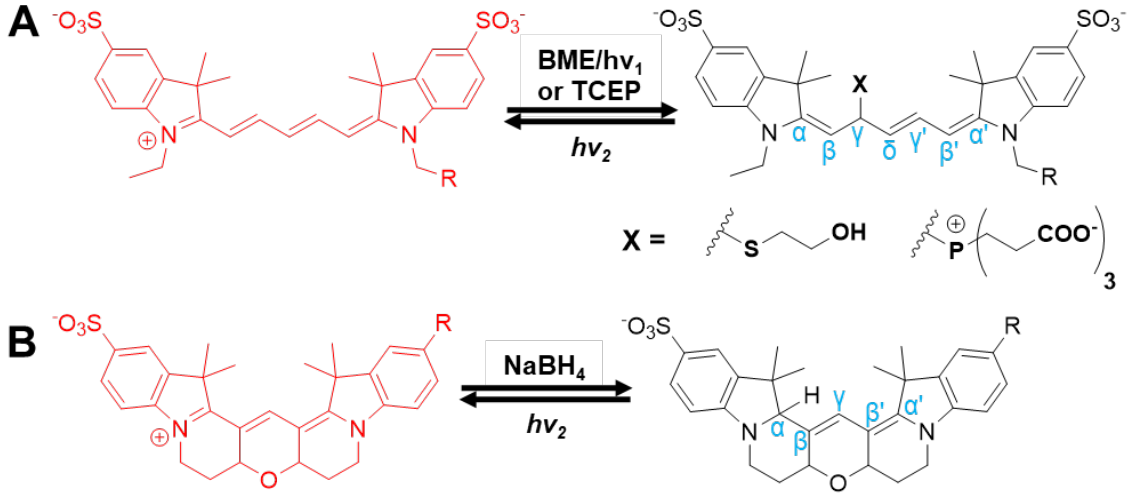

Fig. 1.5.4. Mechanism of photoswitching for Cy5 fluorophore in thiol-containing solution (A) and Cy3B fluorophore in solution with $NaBH_4$ (B).

The cyanine fluorophores Cy3B, Cy5, and Cy7 (together with their close structural relatives, such as Alexa Fluor 647 and Alexa Fluor 750) are among the most heavily used fluorophores in SMLM[211] due to their suitable photoswitching properties (particularly in case of Cy5 and Alexa 647) including high photon count, low duty cycle, and reasonably large number of switching cycles.[187]

Rhodamines

Rhodamine dyes are frequently used for fluorescence microscopy due to their high extinction coefficients coupled with high quantum yields and high photostability. The relatively facile synthesis makes this class of organic dyes a promising candidate for the further development of SMLM probes. Several commercially available rhodamine fluorophores, including ATTO 488, Alexa Fluor 488 and Alexa Fluor 568 (Fig. 1.5.5) exhibit photoswitching behavior in thiol-containing deoxygenated buffers.[205, 207, 211] The brightness of rhodamine dyes can be further enhanced by replacing the N,N-dialkyl groups with 4-membered azetidine rings.[36]

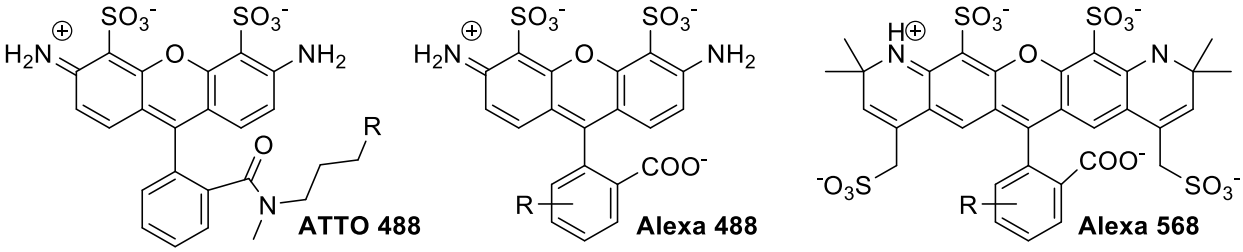

Fig. 1.5.5. Commercially available SMLM-compatible rhodamine dyes.

However, in contrary to cyanine dyes, such as Cy5 and Cy7, many rhodamines are photoswitched to a nonemissive long-lived radical state (Fig. 1.5.6, A) , as evidenced by paramagnetic resonance spectroscopy studies.[212] It is believed that the mechanism of a radical state formation includes the photoreduction of rhodamine triplet state by thiol in solution (Fig. 1.5.6, B).[212]

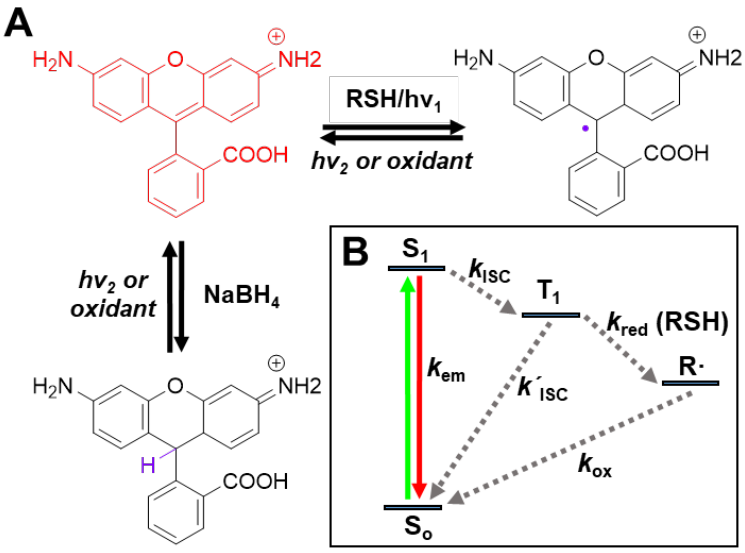

Fig. 1.5.6. Photoswitching of rhodamine fluorophores. Mechanism of reversible rhodamine photoswitching reactions in presence of thiol or sodium borohydride (A). Energy diagram of a photoactivated reaction between rhodamine fluorophore and thiol (B).

Rhodamines are believed to be promising candidates for reductive caging, exhibiting high photon-recovery yields after UV illumination (e.g., 66% for ATTO 488) when compared to cyanine fluorophores (typically 12-40% recovery).[213, 216] During reductive caging the conjugation in rhodamine disrupts upon the net addition of a hydride anion to the central carbon bridge of the xanthene group (Fig. 1.5.6, A), rendering the molecule non-emissive. The hydride can be removed by UV illumination, switching the molecule back into emissive state.

An ability of rhodamines to form spirocycle through the central carbon atom of xanthene ring can be used to create photoactivatable rhodamines via an introduction of special "caging" moieties, which can be removed upon irradiation with a specific wavelength, leading to a transition of the fluorophore into an open emissive form (Fig. 1.5.7).

Diazoketone group was used for caging by Below et al. to create photoactivatable Rhodamine NN dyes.[218] In contrary to spirolactams, the irradiation of non-emissive closed form of Rhodamine NN leads to the cleavage of the caging group after a transition to the open form (Fig. 1.5.7, A).[218] Thus, the uncaged dye molecules remain in the open emissive state until it is photobleached. Diazoketone caging group can be introduced into various rhodamine and carbopyronine fluorophores to create photoactivatable dyes with emission covering a large spectral range.[219, 220]

2-nitrobenzyl derivatives were initially used to create a caged fluoresceines,[221] later expanded for rhodamine probes.[222-225] An improved strategy, used by Wysocki et al., includes an acylation of reduced rhodamine derivatives with 4,5-dimethoxy-2-nitrobenzyl (DMNB) moiety.[226] Upon illumination of caged rhodamines the DMNB moiety is cleaved, leading to the transition of the fluorophore into an emissive form (Fig 1.5.7, B). This approach was expanded to Si-rhodamine,[227] fluorescein,[226] carbofluorescein and carborhodamine[228] dyes. It is possible to introduce two caging groups (*e.g.* Rh_Q8 in Fig. 1.5.7, B), which leads to a possibility to perform the partial uncaging with an associated variation in emission signal.[223, 228, 229]

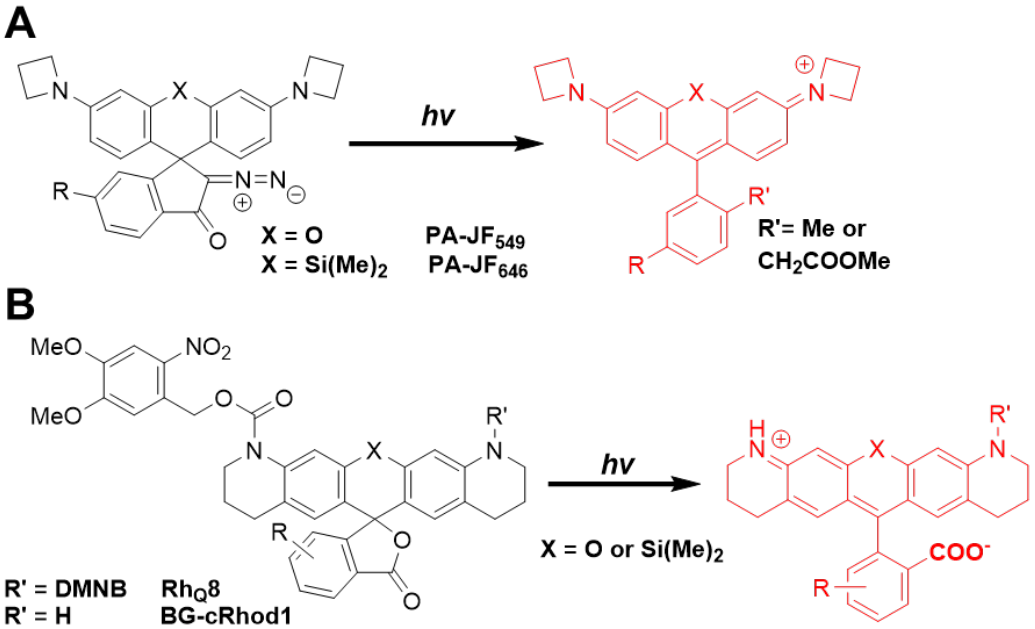

Fig. 1.5.7. Mechanism of photoactivation for rhodamines with diazoketone (A) and 4,5-dimethoxy-2-nitrobenzyl (DMNB) (B) caging groups.

Spiropyrans and oxazine auxochromes

Spiropyrans are a class of photochromic organic dyes, which exhibit an intrinsic on-off switching behavior via a mechanism, similar to spirocyclization in rhodamines. These fluorophores can exist in two forms: a closed spirocyclic form, which is non-emissive; and a highly emissive open merocyanine form (Fig. 1.5.8, A). An illumination with a certain wavelength can shift the equilibrium between the two forms.[230, 231] Thus, upon illumination with visible light the spirocyclic form is obtained through an intramolecular nucleophilic addition, resulting in the disruption of π-conjugation and generation of either a non-fluorescent product[232] or an emissive product with a blue-shifted emission.[233, 234] The fluorescent open form can be obtained by illuminating the non-emissive dye form with UV or blue light, causing a photoelimination of the nucleophile. The equilibrium between the two forms exhibits good reversibility under UV/visible light irradiation and the spiropyrans do not require special fluorescence quenchers or oxygen-free environment to function,[187] which enabled their direct use in SMLM.[235]

Oxazine auxochromes exhibit reversible spirocycle formation, similar to spiropyrans (Fig. 1.5.8, B), accompanied by either fluorescence on/off switching or a large spectroscopic shift.[236-238] The oxazine part of the dye functions as a molecular switch, able to modulate the fluorescence of a grafted fluorophore. The range of fluorophores, which could be introduced into oxazine auxochrome molecular design, include pyrenes, coumarins, fluorenes, BODIPY and cyanines with a predominant closed form for all cases except cyanine fluorophores.[236-240]

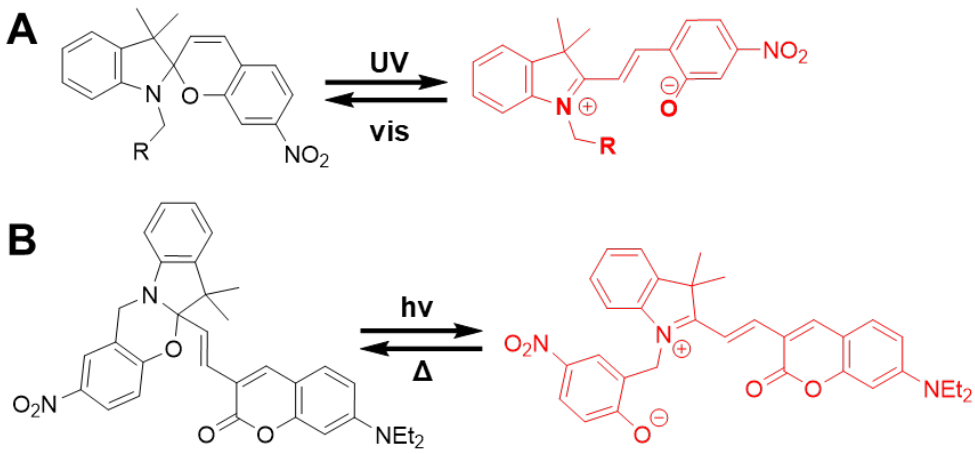

Fig. 1.5.8. Mechanism of photoswitching of spiropyrans (A) and oxazine auxochromes (B).

1,2-diarylethenes

1,2-diarylethene fluorophores are another class of photochromic compounds which undergo photoisomerization reactions between the open and the closed states (Fig. 1.5.9). The open form of the dyes does not absorb light in the visible region, however upon UV irradiation a new C-C bond is formed between the two thiene residues, yielding the closed form of 1,2-diarylethenes, which typically absorbs in the visible region of spectrum and is fluorescent for a number of dye structures.[241-243] The main features of 1,2-diarylethene fluorophores include high fatigue resistance (i.e. large number of switching cycles before degradation), large spectral shift between the two isomers, fast isomerization and good thermal stability.[244-246] These fluorophores can also be utilized as photoswitchable fluorescence quenchers, which is achieved by tethering a second fluorophore with fluorescence emission around 500 nm to 700 nm, such as perylenemonoimide,[247] perylenebisimide,[248] naphthalimide[249] or tetraphenylethene.[250] This spectral range corresponds to the absorption of the closed-ring form of 1,2-diarylethenes, and upon their photoisomerization the fluorescence of external fluorophore can be switched due to intramolecular energy transfer,[250, 251] a behaviour suitable for SMLM.[241, 242]

Changes in molecular design allowed to create 1,2-diarylethene-based fluorophores directly compatible with super-resolved imaging. One example includes an amphiphilic 1,2-dithienylethene probe for cell imaging.[241] Irie *et al*. modified the fluorophore by converting the two thiophene moieties into benzothiophene-1,1-dioxides together with extending the conjugation, which allowed to create diarylethene fluorophores with increased brightness, which can be used in SMLM (Fig. 1.5.9, B).[242, 243] By changing the substituents at 6 and 6' positions of the benzothiophene-1,1-dioxides it became possible to tune the emission wavelength of the dye closed form while retaining high quantum yields and fatigue resistance.[242] A water-soluble hydrophilic 1,2-diarylethene derivative for SMLM was created by Hell and co-workers, basing on a similar molecular design.[243]

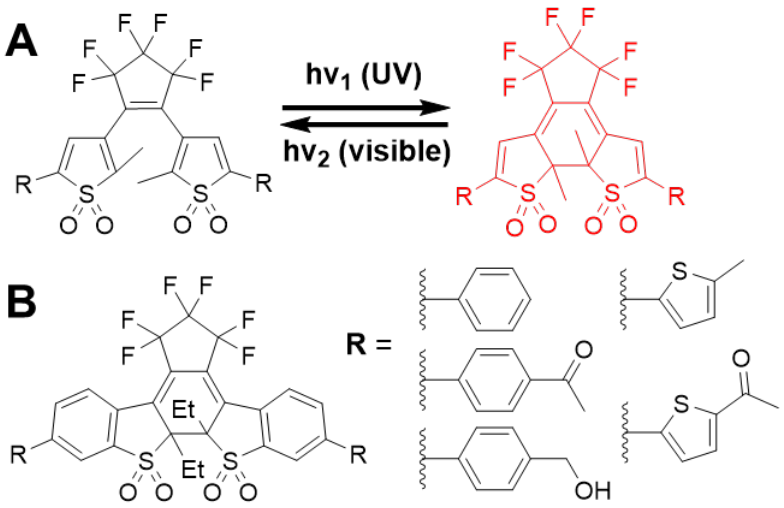

Fig. 1.5.9. Mechanism of photoswitching (A) and structures of 1,2-diarylethene fluorophores (B).

Dicyanodihydrofurans

Fluorophores, based on dicyanodihydrofuran (DCDHF) moiety, possess large extinction coefficients, high quantum yields and good photostability.[252-254] The dicyanodihydrofurans, which are strong electron acceptors, can be linked to an electron donor group, such as amine or hydroxyl, through a conjugated linker, yielding the molecular rotor fluorophores. These fluorophores can be utilized in SMLM using a caging strategy.[187] The push-pull system of dicyanodihydrofurans can be disrupted by replacing the donor amine group with an electron-withdrawing azide moiety, resulting in a non-emissive caged DCDHF fluorophore (Fig. 1.5.10, A). Upon photoactivation the azide group is converted to an amino group through a stabilized aryl nitrene,[255] thus restoring the emission.[256, 257] Similar to DMNB and diazoketone caging groups, the photoactivation of azido-DCDHFs is irreversible. The spectral properties of dicyanodihydrofuran fluorophores can be finely tuned through the changes in the aromatic part of conjugated linker (Fig. 1.5.10, B). Azido-chloroalkane-DCDHF probe was utilized by Lee *et al.* to label Halo-tagged proteins for SMLM imaging of protein distribution.[257]

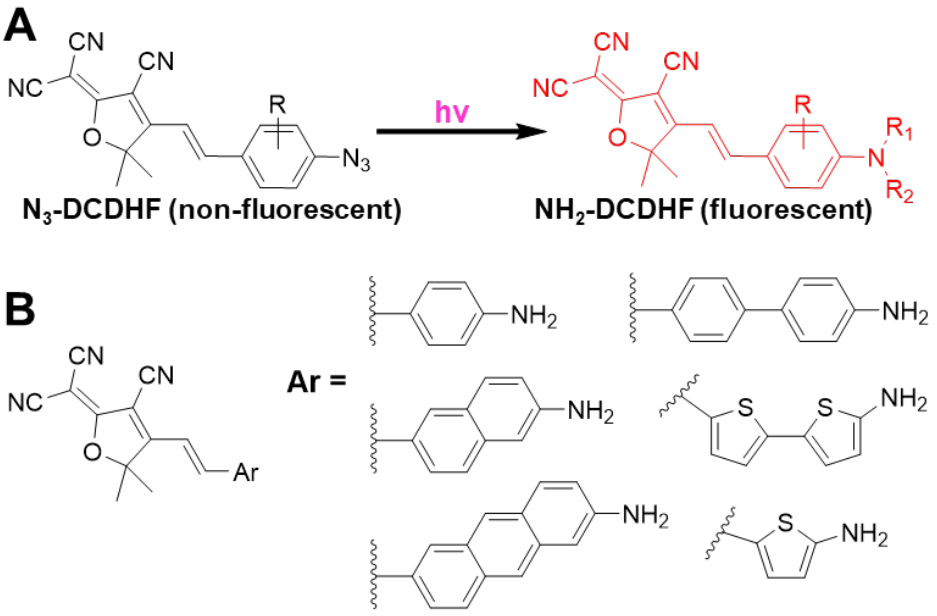

Fig. 1.5.10. Mechanism of photoactivated conversion of caging group in DCDHFs (A). Structures of DCDHF fluorophores (B).

1.5.3 Fluorogenic probes for super-resolution microscopy

Fluorescent probes with fluorogenic response are currently the most frequently used class of dyes used for super-resolution microscopy.[187, 258] The key advantage of using fluorogenic probes is that they are able to improve substantially the imaging contrast in various SRM methods, including STED, SIM and STORM.[259] Additionally, the probes with fluorogenic response are used directly in PAINT to create stochastic blinking.[187]

One of the ways to create probes with fluorogenic response is to exploit tautomeric transition between nonemissive and emissive forms of the same fluorophore. For instance, an ability of rhodamine fluorophores to reversibly form a spiro-ring through the central carbon of the xanthene ring can be used to induce photoswitching (Fig. 1.5.11, A),[33] providing the desired fluorogenic response. An intramolecular nucleophile, such as carboxylate, amide or hydroxyl, is required to form the spiro-ring and make the molecule non-emissive, which results in either dynamic switching between the states (in case of carboxylates and hydroxyls) or a possibility of photoactivation upon illumination with UV light (in case of amides).[260-262] Additionally, the equilibrium between the open and closed forms can be shifted by variations in solvent polarity, pH or concentrations of certain metal ions or small molecules.[8, 32, 263, 264] Is is also possible to tune

the reaction by introducing changes to the electron density of xanthene ring.[265] Alternatively, changing an oxygen atom to dimethylsilyl moiety in Si-rhodamines allowed to create probes undergoing spirocyclization at much higher polarity.[34-36] Si-rhodamines with a carboxylic acid group at the 2-position of the phenyl ring (SiR-carboxyl) (Fig. 1.5.11, B) are mostly in a quenched spirocyclic form in solution, however, the probe becomes *ca* 5 times brighter when a ligand conjugated to the dye binds to a reactive protein tag such as SNAP tag.[34] In this way the background fluorescence is largely decreased; the spirocyclic form also masks the zwitterionic fluorescent form, enhancing the cell permeability of the dye, while the open emissive form possesses the photoswitching properties, needed for SMLM.[34] Changing the nucleophile allows to tune the stability of the closed form: the spirolactams, such as RSA-1 and RSA-2 (Fig. 1.5.11. B), are generally more stable compared to spirolactones.[266] Upon irradiation, the dyes convert into emissive form, after a period of time spontaneously returning back into non-emissive closed form.

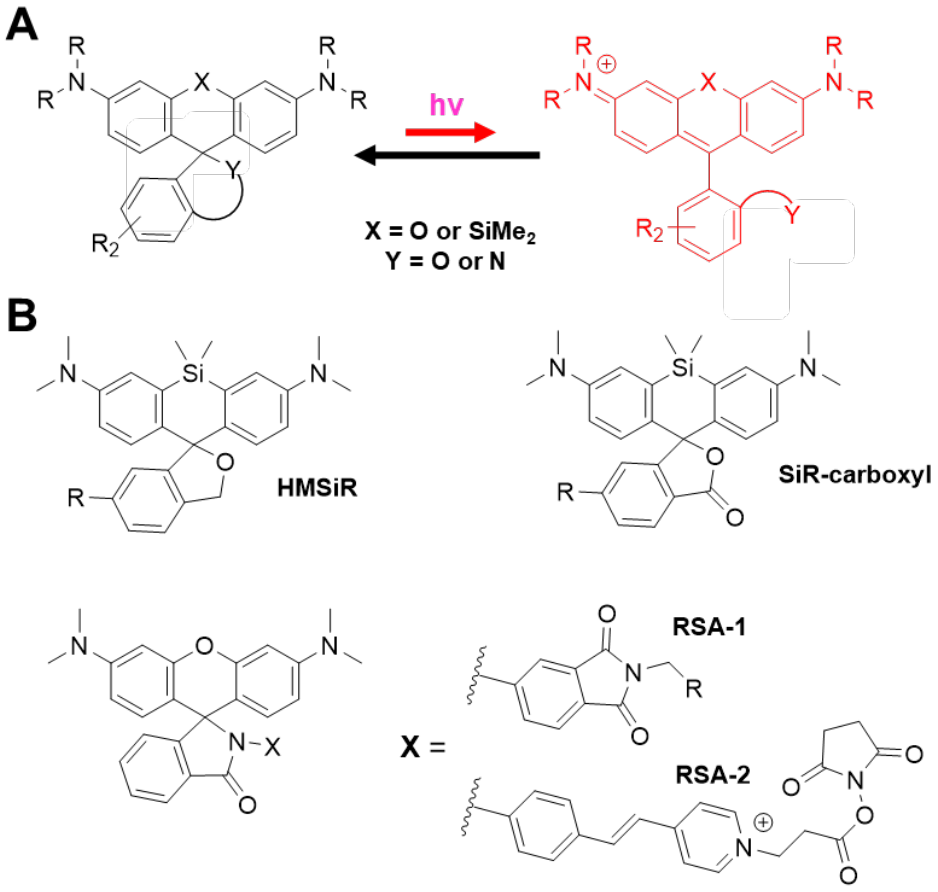

Fig. 1.5.11. Switching mechanism (A) and structures of fluorogenic spirorhodamine dyes used for SMLM

The spectroscopic and photoswitching properties of rhodamine fluorophores were significantly improved by Lavis *et al*: thus, a substitution of two N,N-dialkyl moieties in rhodamines by a four-membered azetidine ring results in substantial improvement of quantum yield values.[36] Further adjustment of the substituents in azetidine rings allowed to finely tune the equilibrium between open and spirocyclic forms of rhodamines.[265] Using this strategy, a series of

novel probes was created (Fig. 1.5.12), possessing enhanced fluorogenic response (21-fold for JF_{646} and 113-fold for JF_{635}), resulting in much higher on-off contrast due to the stabilization of emissive open form upon binding with the Halo-tagged target protein.[265]

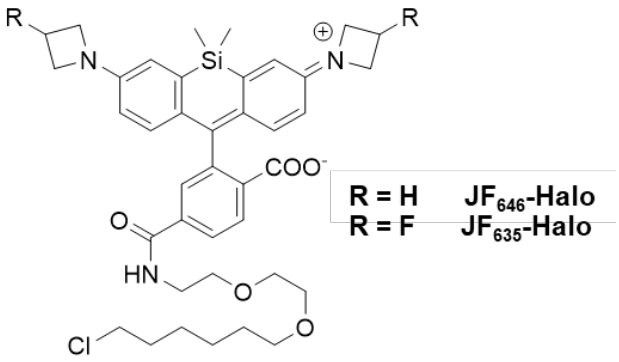

Fig. 1.5.12 Structures of modified Si-rhodamine dyes with enhanced quantum yields.

Another way to create fluorogenic probes implies utilization of intracellular machinery. Thus, bacterial nitroreductases can be applied to reduce non-emissive nitro-DCDHF fluorophores into the highly emissive corresponding amines (Fig. 1.5.13),[187, 267, 268] which was used, as an example, for SMLM of live *B. subtilis*.[267]

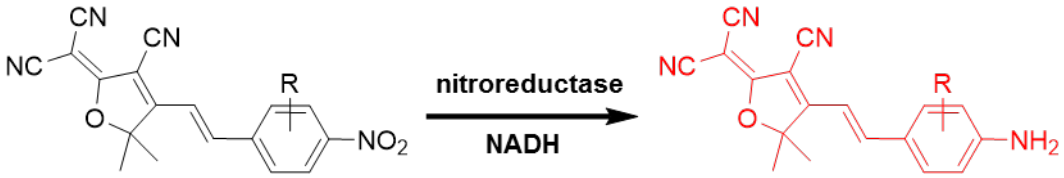

Fig. 1.5.13. Structure of enzyme-activatable fluorogenic DCDHF probes

Another important mechanism, used for the development of fluorogenic response in super-resolved imaging, is the formation of quenched dimers or aggregates. Thus, Nile Red dye has low quantum yields in water due to formation of non-emissive aggregates, however, upon entering the hydrophobic lipid environment the fluorophore becomes highly emissive,[8, 196] which was used to create super-resolved images of POPC LUVs and supported lipid bilayers (Fig. 1.5.14).[196]

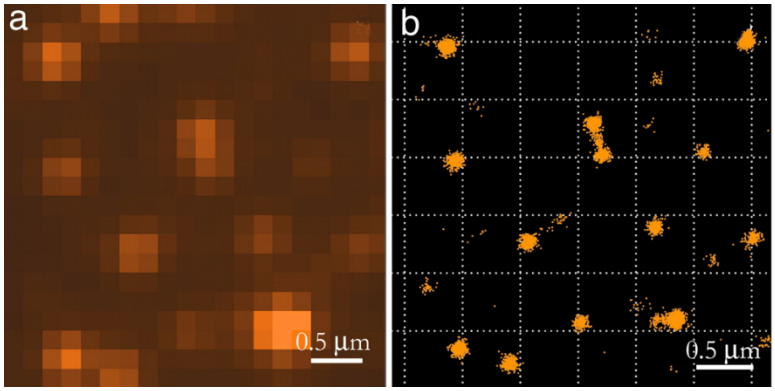

Fig. 1.5.14. Conventional microscopy image (A) and super-resolved PAINT image (B) of lipid vesicles, attached to glass surface and stained with Nile Red.[196]

Another example of this approach is the application of Merocyanine 540 for super-resolved lipid order sensing in supported bilayers (Fig. 1.5.15). This fluorophore (Fig. 1.5.15, A) is able to form dimers when introduced into liquid ordered phase, which is accompanied by a decrease in fluorescence intensity together with a bathochromic emission shift (Fig. 1.5.15, B).[269] Such behavior allows to utilize the fluorophore in PAINT microscopy in order to visualize the different lipid domains in mixed-phase supported lipid bilayers, based on the signal intensity (Fig. 1.5.15, C).[269]

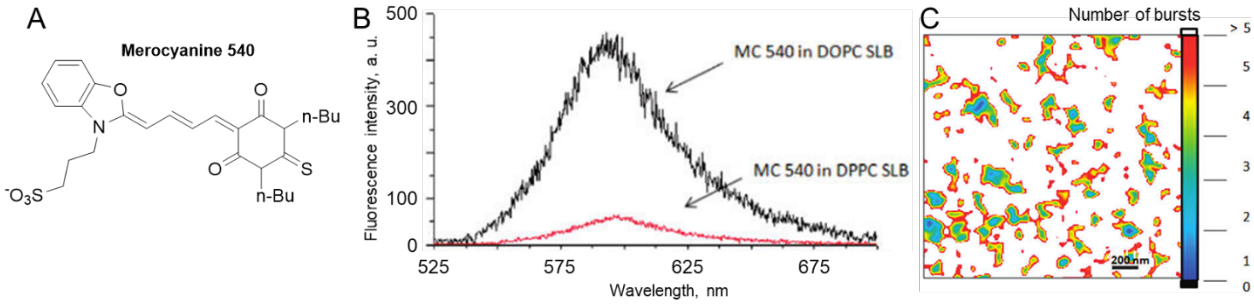

Fig. 1.5.15. Structure of Merocyanine 540 SMLM probe (A). Spectra of Merocyanine 540 in supported lipid bilayers of different composition (B). PAINT microscopy image of Merocyanine 540 in mixed-phase supported lipid bilayers (C). Regions with relatively low number of bursts per localization correspond to the liquid ordered phase. Modified from [269]

1.5.4 Chromogenic probes for super-resolution microscopy

In comparison to fluorogenic probes, the field of chromogenic probes for super-resolution microscopy is still underexplored.[187, 258] Chromogenic response of fluorescent probes can be potentially applied to super-resolution microscopy in several ways:

1) Diminishing the background noise upon choosing the appropriate emission filter;

2) Collecting additional spectral information using environment-sensitive dyes.

Traditionally, the difference in emission maxima of the chromogenic probes in different environment is used to improve the signal-to-noise ratio through utilization of appropriate bandpass filters for signal detection, as in case of filtering off the red-shifted emission of Nile Red in water.[269, 270]

The sensitivity of solvatochromic ICT probes to the lipid order can be used to obtain the information about the parameters of cell membranes combined with super-resolution. Thus, a solvatochromic probe Di-4-AN(F)EPPTEA (Fig. 1.5.16, A) was applied for STED GP imaging to investigate small (~100–200 nm) internal endocytic vesicles located close to the plasma membrane. The lipid order in these vesicles is challenging to determine via the conventional confocal GP images due to the limited spatial resolution of confocal microscopy, therefore the imaging was performed using a multicolour STEP setup. The fluorescence signal was detected at the two channels: ordered channel (520–570 nm, I_1) and disordered channel (620–700 nm, I_2). Using these channels, the super-resolved GP images $(I_1 - I_2)/(I_1 + I_2)$ were created (Fig. 1.5.16, B-D). The improved resolution of the STED mode allowed to determine the lipid order of the endocytic vesicles and to compare it to the lipid order in the plasma membrane. It was found that the vesicular membranes had a significantly lower molecular order ($GP \sim 0.1$) compared to the plasma membrane ($GP > 0.3$) (Fig 1.5.16, C-D), in line with predictions from previous measurements.[91]

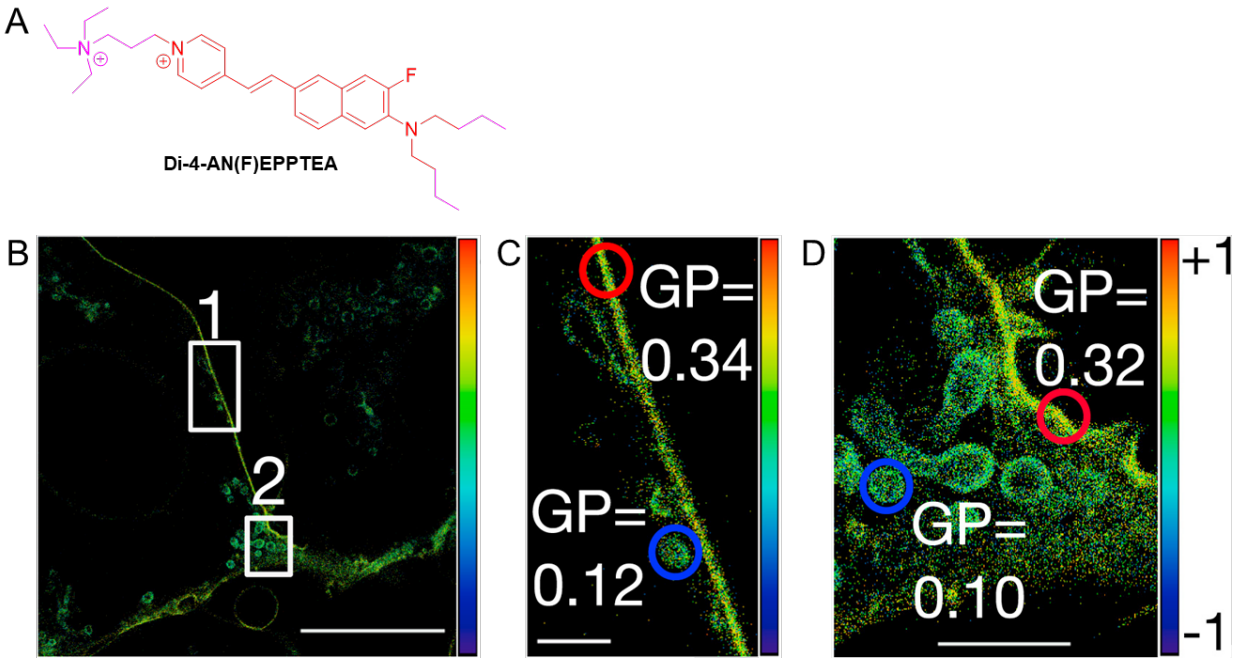

Fig. 1.5.16 STED GP images of the plasma membrane of live CHO cells labeled with Di-4-AN(F)EPPTEA. Structure of Di-4-AN(F)EPPTEA probe (A). Overview STED GP image (B) (scale bars, 10 μm) and close-up STED GP images (C and D) into the marked areas (rectangle 1 (C) and rectangle 2 (D); scale bars, 0.5 μm), highlighting the improved GP determination of internal vesicles of low molecular order (blue circles) in the STED recordings. ($GP = 0.11 \pm 0.09$)

for the vesicles compared to $GP = 0.32 \pm 0.07$ of the plasma membrane (red circles)). Red-to-blue color code: GP values from maximally ordered (red, +1) to maximally disordered (blue, −1). Modified from [271].

A direct utilization of the chromogenic response in super-resolution microscopy became possible with recent implementation of spectrally resolved SRM methods,[272-274] which allowed to obtain the single-molecule spectral information combined with high spatial resolution. In combination with a chromogenic Nile Red, a spectrally resolved PAINT (SR-PAINT) method was utilized to perform surface hydrophobicity mapping,[275] visualize the distinctions between the polarity of plasma membrane and membranes of internal organelles[276] and effect of cholesterol addition and cholera toxin treatment on plasma membrane in live cells.[276]

One of the first examples of spectrally resolved PAINT SRM was performed by *M. Bongiovanni et al.*[275] In this work, solvatochromic Nile Red was used for the surface hydrophobicity mapping in live cells.[275] Notably, the probe allowed to distinguish by colour the differences in hydrophobicity in the LUVs with different lipid composition (Fig. 1.5.17, A), in protein aggregates (Fig. 1.5.17, B) and in plasma membrane of live HEK 293 cells before and after the treatments, which change the level of cholesterol (Fig. 1.5.17, C).[275]

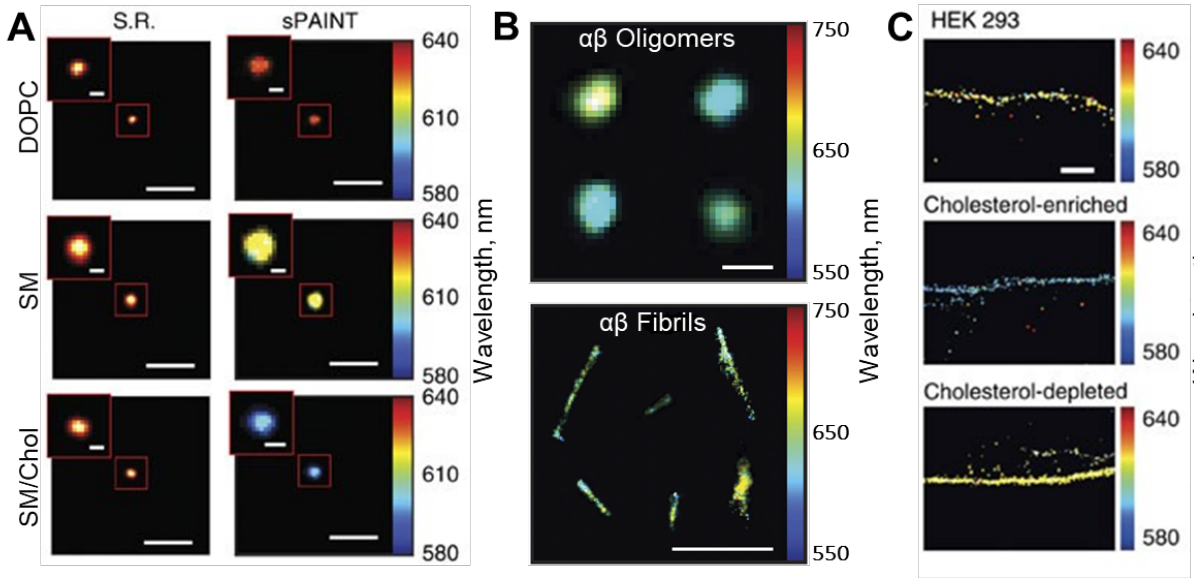

Fig. 1.5.17. Spectrally-resolved PAINT images of LUVs with different lipid composition (A), protein aggregates (B) and live HEK-293 cell plasma membranes (C) using Nile Red. Scale bars:100 nm for αβ oligomers (B) and cell membranes (C); 1 μM for αβ Fibrils (B); 500 nm for panel (A) and 20 nm in zoomed regions in panel A. Adapted from [275].

Further improvement of signal acquisition and processing was performed by Xu and co-workers.[277] The implemented changes in microscopy setup lead to an enhancement in the sensitivity of SR-PAINT, which in turn enabled the visualization of nanoscale heterogeneity of plasma membrane (Fig. 1.5.18, A) and differences between plasma membrane and internal biomembranes (Fig. 1.5.18, B).[276]

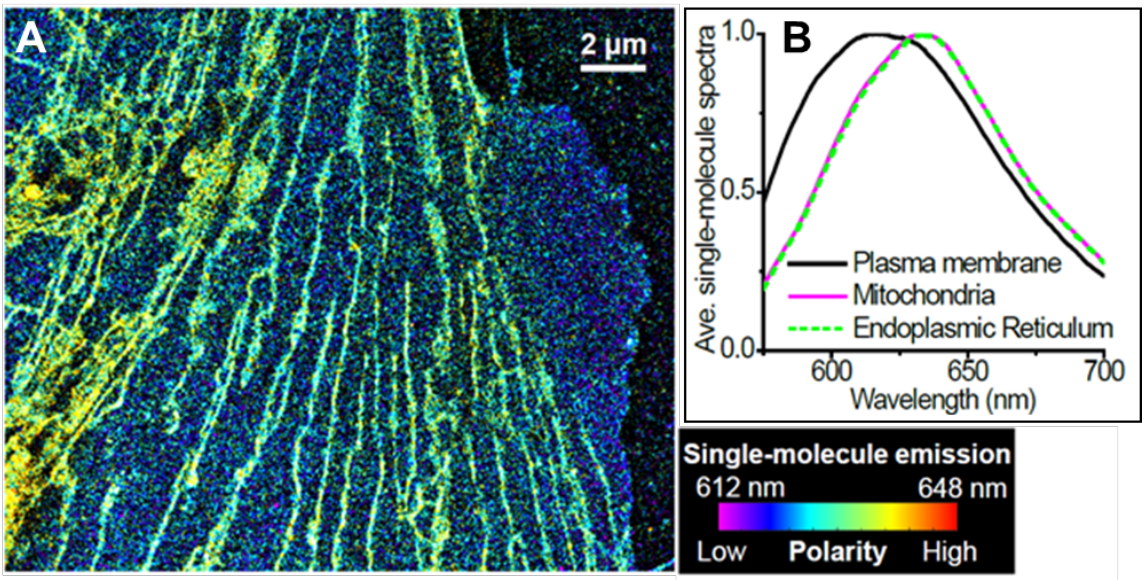

Fig. 1.5.18. SR-PAINT image of a Nile Red-labeled live PtK2 cell (A) and average spectra of single Nile Red molecules from different nanoscale regions in live cells (B). Adapted from[276]

Spectrally-resolved super-resolution microscopy opens new opportunities for probing biological and chemical systems at a single-molecule scale,[277] however, its performance relies on the development of SMLM-compatible environment-sensitive probes.[8, 277]

Aim of my PhD project

As shown in the bibliographical overview above, environment-sensitive fluorescent probes are able to provide important information about many parameters of live cell interior. At the same time, the incorporation of specific targeting groups can ensure probe accumulation in specific cell organelles, thus enabling acquisition of signal only from the regions of interest in live cells. However, the field of solvatochromic organelle-targeted probes remains rather little developed so far.

My PhD project has the following aim:

To design fluorescent environment-sensitive probes of amphiphilic nature able to target specifically different cell membrane structures and report on their biophysical properties.

In order to achieve the aim, we have defined several specific objectives:

1. To achieve more efficient targeting of dyes to plasma membranes;

2. To create a solvatochromic plasma membrane probe, compatible with super-resolution live cell microscopy;

3. To synthesize an array of organelle-targeted fluorescent probes, able to sense polarity and lipid order;

4. To provide membrane probes with chemical reactivity in order to ensure more robust permanent staining.

2. Results and discussion

2.1. Efficient targeting of dyes to plasma membranes

2.1.1. Fluorescent anionic cyanine-based plasma membrane probes for live cell and tissue imaging

Introduction of zwitterionic plasma membrane targeting moieties allowed to significantly improve the probe selectivity and overall image quality for a number of fluorophores.[15, 74, 126, 127] However, for a number of cationic dyes, such as cyanines, the overall charge of the molecule remains positive after modification with zwitterionic targeting groups. This can potentially lead to increased staining of the negatively charged glass surface of microscopy support and increased endocytosis in case of live cell imaging. One of the possible solutions lies in the development of anionic plasma membrane targeting moieties.

3-(alkylammonio)propane-1-sulfonates (Fig. 2.1.1, A, in magenta) were chosen as promising candidates for PM targeting motifs due to their facile synthesis and functionalization. In order to test the performance of anionic targeting groups, we have synthesized a palette consisting of five cyanine dyes with different spectral properties, each bearing two of the new targeting moieties (Fig. 2.1.1, B). The anionic PM-targeting groups were synthesized in one step and then grafted to the corresponding cyanine carboxylic diacids using the common peptide synthesis procedures (Fig. 2.1.1, A-B). This strategy allows to easily vary, if needed, the alkyl chain lengths, resulting in different membrane affinity of a resulting probe.

Due to the amphiphilic nature of the anionic PM-targeting motifs our probes are expected to form non-emissive aggregates in aqueous medium, which would disassemble into emissive molecular form in presence of lipids (Fig. 2.1.1, C), providing a fluorogenic turn-on response, as it was previously observed for zwitterionic probes[15, 126]

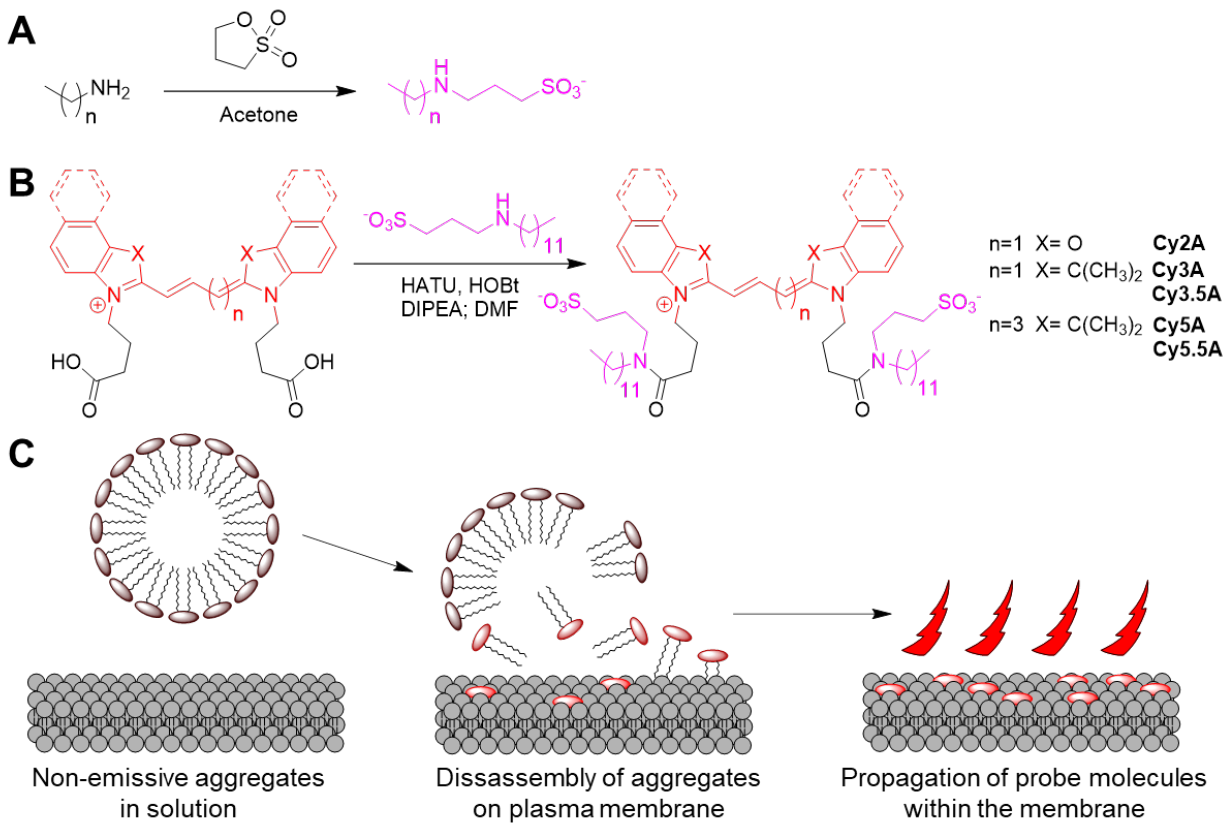

Fig. 2.1.1. Synthesis of anionic PM-targeting motif (A) and anionic cyanine plasma membrane probes (B). Mechanism of the fluorogenic response of the anionic cyanine probes to the presence of plasma membrane (C).

The spectroscopic properties of anionic cyanine probes were tested in organic solvents and large unilamellar vesicles (LUVs) (Fig. 2.1.2). The absorption spectra of the probes in model membranes (DOPC LUVs) (Fig. 2.1.2, A) were narrow and close to the mirror image of the corresponding emission spectra (Fig. 2.1.2, B), indicating no effect of functionalization on the fluorophore emission. Similar results were obtained in organic solvents. On the contrary, the probes exhibited an increase in short-wavelength shoulder in absorption spectra when measured in a phosphate buffer (PB) (Fig. 2.1.2, A), which was also accompanied by a significant decrease in fluorescence intensity (Fig. 2.1.2, B). These results support our expectations concerning the formation of non-emissive H-aggregates[69] in aqueous medium (Fig. 2.1.1, C).

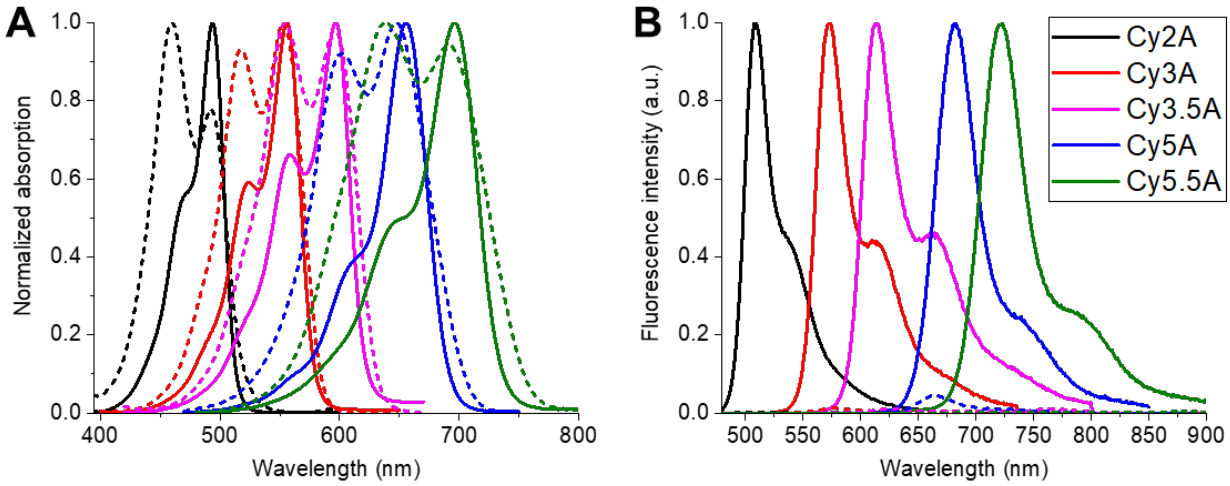

Fig 2.1.2. Normalized absorption (A) and emission (B) spectra of anionic cyanine probes. Solid lines represent the spectra in DOPC, while the corresponding spectra in phosphate buffer are represented in dashed lines. Probe concentration was 1 μM for Cy2A and Cy3 and 0.5 μM for Cy3.5, Cy5 and Cy5.5. Total lipid concentration was 400 μM. Excitation wavelength was 470 nm for Cy2A, 540 nm for Cy3A, 546 nm for Cy3.5A, 601 nm for Cy5A and 623 nm for Cy5.5A.

After that, we used confocal fluorescence microscopy in live KB cells in order to evaluate the performance of the anionic cyanines in cellular imaging when compared with the zwitterionic cyanine probes (Fig. 2.1.3). Live cells were incubated for 10 min at r.t. with 50 nM of probe solution in HBSS and then imaged without a washing step. The samples, labeled with our probes, exhibited much less fluorescence intensity from the glass surface of microscopy support (Fig. 2.1.3, A), while at the same time providing higher signal from cell membranes (Fig. 2.1.3, B), when compared to an analogue with zwitterionic targeting groups. After 1 hour of incubation at r.t. the anionic cyanines exhibit comparable fluorescence intensity from plasma membrane and from inside the cells (Fig. 2.1.3, C), while for zwitterionic cyanines the emission from the internalized dye inside the cells is about 2 times brighter than the signal from plasma membrane and also the overall signal intensity is significantly lower. In line with our expectations, the changes in molecular design, and particularly an introduction of negative charges, allowed to effectively decrease the glass surface staining and cellular internalization, thus improving the overall image quality.

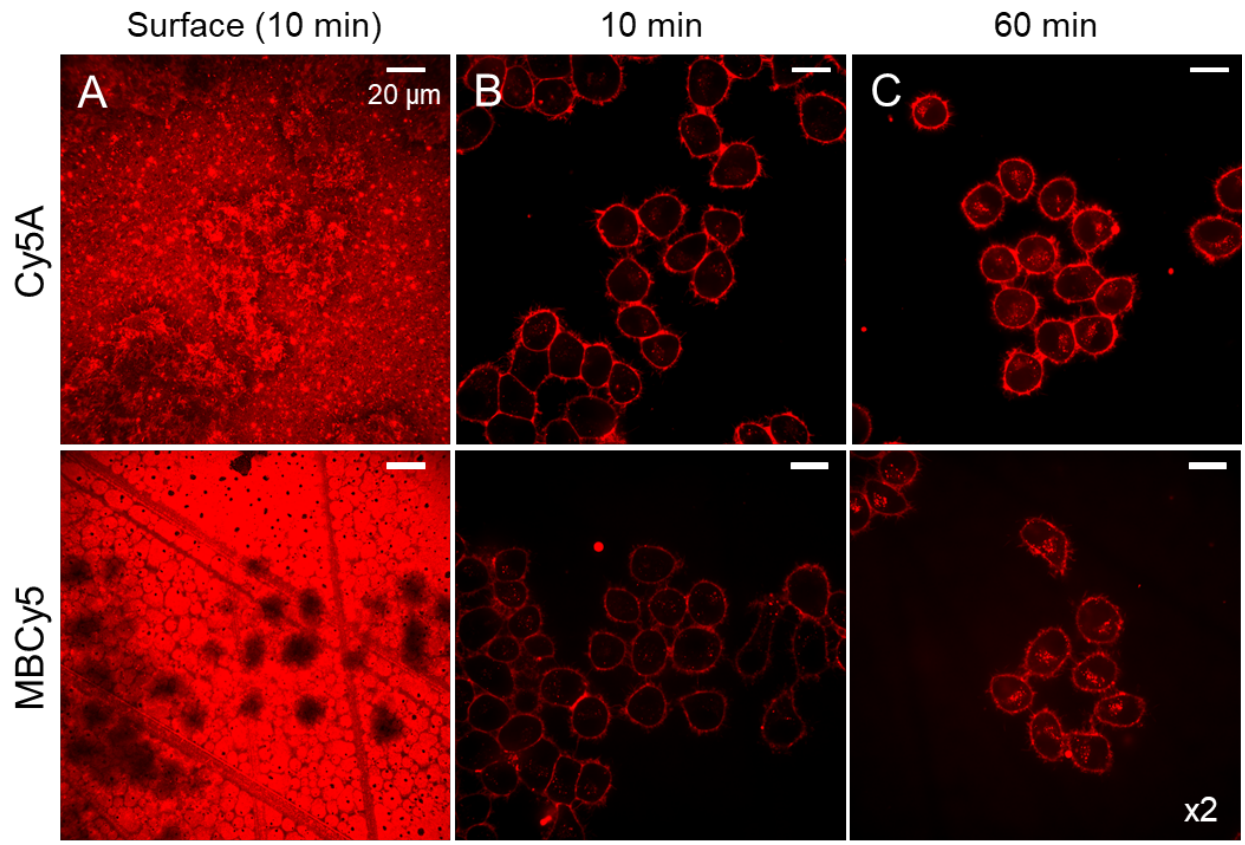

Fig. 2.1.3. Live KB cells stained with Cy5A and MBCy5 in HBSS. Confocal microscopy images focused on the surface of microscopy dish (A) and cells (B) after 10 minutes of incubation at r.t. Confocal microscopy images of cells after 1h of incubation at r.t. Dye concentration 50 nM. Range 503-3052 in panels (A) and (B). Range 808-6165 in panel (C). Excitation wavelength was 638 nm.

Colocalization microscopy experiments in live KB cells (Fig. 2.1.4) revealed that the new probes possess high selectivity towards plasma membrane, while also featuring much less internalization compared to WGA-Alexa 488 conjugate. The differences in relative fluorescence intensities between the different cells on the same image could be possibly explained by the significantly larger size of WGA conjugates when compared to cyanines together with the differences in the binding sites on the PM (WGA binds N-acetyl-D-glucosamine and sialic acid residues,[124] but not the membrane lipids).

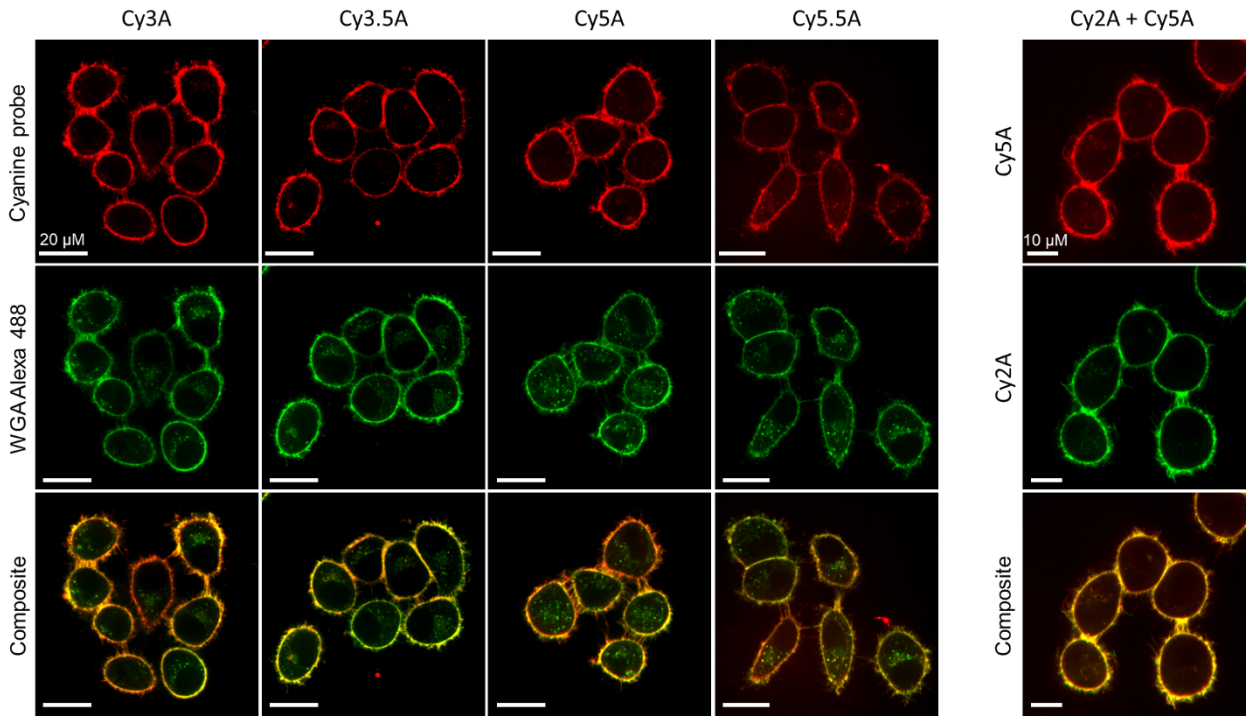

Fig 2.1.3. Colocalization of anionic cyanine probes with commercial WGA-Alexa 488 conjugate in live KB cells. Concentrations of all dyes used were 50 nM. Excitation wavelength was 488 nm for WGA and Cy2A, 532 nm for Cy3A and Cy3.5A, 638 nm for Cy5A and Cy5.5A.

On the next step, anionic cyanines were used to visualize layer II-III pyramidal neurons in a live mouse brain using *in vivo* two-photon excitation (TPE) microscopy (Fig. 2.1.4). A solution, containing the probe Cy3.5A together with Me-β-cyclodextrin, was delivered into the cortex of a mouse utilizing a stereotactic injection (Fig. 2.1.4, A). After 30 minutes from the start of injection, the neurons were imaged through an acute cranial window (Fig. 2.1.4, B). The probe Cy3.5A provided bright and specific staining of the PM in layer II-III pyramidal neurons at 100 μm depth from the brain surface (Fig. 2.1.4, C). The high quality of the obtained images allowed to distinguish neuron soma (Fig. 5, D), dendrites with dendritic spines (Fig. 2.1.4, E) and axons with axonal boutons (Fig. 2.1.4, F). Moreover, the dye showed no sign of photobleaching and did not eliminate from the neuronal membrane after one hour of imaging, thus exhibiting a photostable and robust staining. To the best of our knowledge, this is the first example of *in vivo* neuronal membrane microscopy imaging using a molecular fluorescent probe.

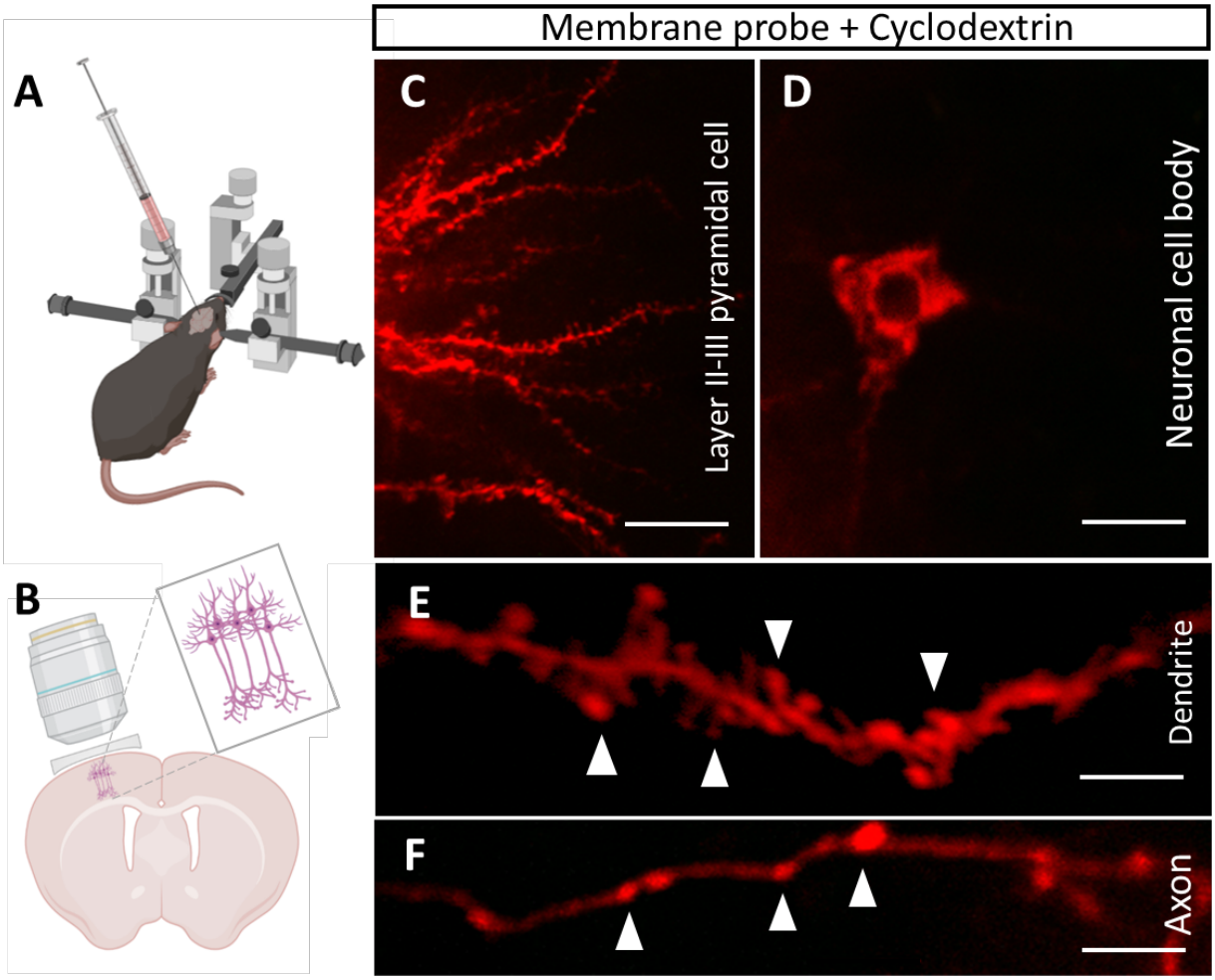

Fig. 2.1.4. In vivo 2-photon microscopy of neurons stained by Cy3.5A probe injected into the brain parenchyma. (A) Stereotactic injection of the probe into the mouse cortex. (B) Intravital imaging of the stained neuronal structures through an acute cranial window. Zoomed insert shows layer II-III pyramidal neurons. (C) Representative micrograph of stained neurites in vivo at 100 µm depth from the brain surface. (D) Representative micrograph of stained pyramidal neuron soma. (E) Representative micrograph of stained single dendrite. White arrows indicate dendritic spines. (F) Representative micrograph of stained single axon. White arrows indicate axonal boutons. Scale bar: (C) – 20 µm; (D) – 10 µm; (E, F) – 5 µm.

Based on these results, a manuscript is being prepared for publication.

2.1.2. Redesigning solvatochromic probe Laurdan for imaging lipid order selectively in cell plasma membranes

Inspired by the results, obtained for negatively charged cyanine-based plasma membrane probes, next we aimed to graft our anionic targeting group to an environment-sensitive dye in order to create a plasma membrane-targeted environment-sensitive probe and verify, whether an addition of anionic targeting group would affect the fluorophore sensitivity.

In the course of the project we totally redesigned a widely used Laurdan probe (Fig. 2.1.5, A).[10, 91, 110, 111] Laurdan, which is based on an environment-sensitive ICT Prodan fluorophore, was chosen due to its several distinctive features:

1) Prodan-based probes are able to sense a number of biophysical parameters in membranes, including polarity,[110] lipid order,[91, 110] mechanical strain,[111] and viscosity;[10]

2) The emission of Prodan in the blue region of visible spectrum makes the probes compatible with a majority of fluorescent proteins in multicolour microscopy imaging applications.

Our probe is expected to sense changes in lipid order in plasma membrane through the changes in its emission colour (Fig. 2.1.5, B), similarly to the parent probe. The synthesis of the probe Pro12A was performed in 4 steps with a total yield of 23 %, using 2-bromonaphthalene as a starting material (Fig. 2.1.5, C).

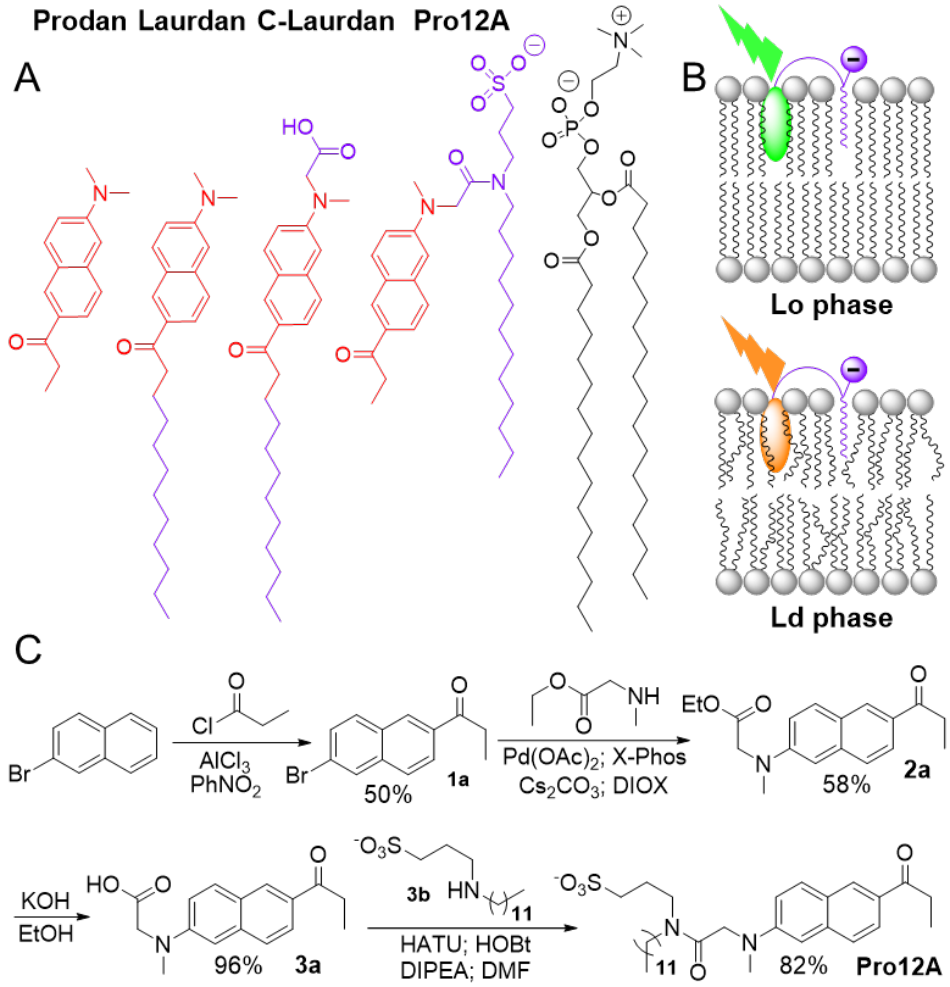

Fig. 2.1.5. Structure of Pro12A, Laurdan and C-Laurdan fluorescent probes (A). Mechanism of the sensing of lipid order by a solvatochromic ICT probe Pro12A (B). Synthetic procedure for anionic Pro12A plasma membrane probe (C).

Next, we assessed the spectroscopic properties of our probe in large unilamellar vesicles (LUVs) (Fig. 2.1.6, A). The experiments reveal that the fluorophore retains the sensitivity towards lipid order after functionalization, showing no sign of fluorophore perturbation after the addition of a targeting group. Moreover, the quantum yields of Pro12A in lipid vesicles exhibit those of Laurdan by 2 to 3-fold, suggesting much faster binding kinetics. Additionally, the localization of Pro12A in membrane was studied using fluorescence quenching (Fig. 2.1.6, B-C). Upon the addition of dodecyl viologen (Fig. 2.1.6, B), which is a fluorescence quencher by PET mechanism,[278] only the probe molecules localized on the outer membrane leaflet are expected to be quenched (Fig. 2.1.6, B). The emission intensity of our probe decreases significantly stronger compared to uncharged Laurdan (Fig. 2.1.6, C). Such a difference suggests that Pro12A stains only the outer leaflet and does not traverse the membrane (Fig. 2.1.6, B). Specific staining of the outer membrane leaflet by Pro12A is expected to increase the probe sensitivity towards lipid order, considering the transversal asymmetry of plasma membrane in live cells.

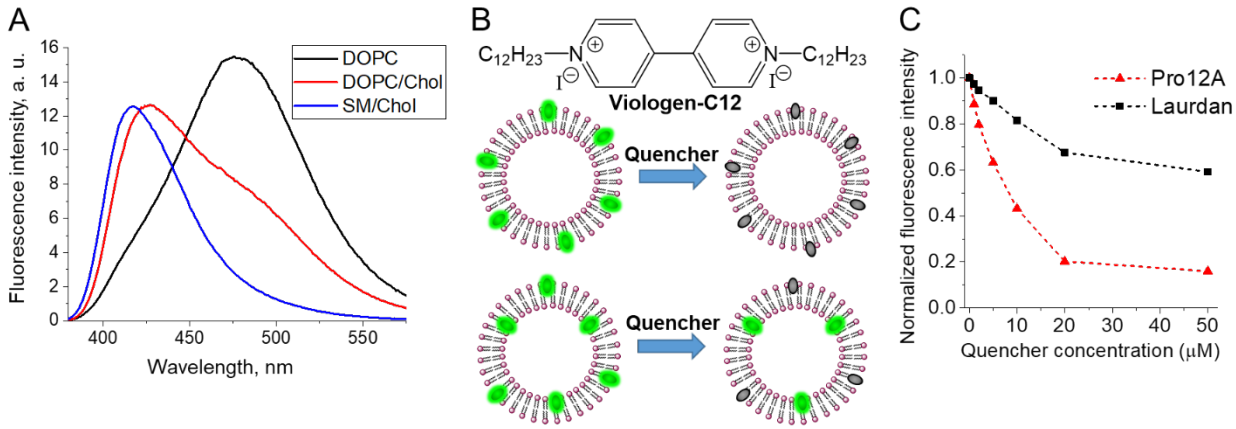

Fig. 2.1.6. Fluorescence emission spectra of ProA12 probe in LUVs of different composition (A); Mechanism of leaflet-dependent fluorescence PET fluorescence quenching by C12-Viologen (B) of Pro12A (middle) and Laurdan (bottom). Normalized fluorescence intensity of Pro12A and Laurdan at different concentrations of added PET quencher (C).

On the next step, we compared the sensitivity to lipid order of Pro12A with Laurdan and C-Laurdan, using phase separated giant plasma membrane vesicles (GPMVs) (Fig. 2.1.7). The obtained generalized polarization (GP) images, together with the corresponding GP values (Fig. 2.1.7, A-B) suggest that Pro12A is more sensitive to the changes in lipid order in GPMVs compared to the two other probes. Moreover, Pro12A displayed almost equal fluorescence signal from the two separated lipid phases (Fig. 2.1.7, C-D). On the contrary, both Laurdan and C-Laurdan exhibited significantly lower fluorescence intensity in Ld phase of GPMVs compared to Lo. Even partitioning of Pro12A between Lo and Ld phases is an important advantage, as it allows acquisition of the signal with high intensities from both lipid domains while distinguishing them by the probe emission colour.

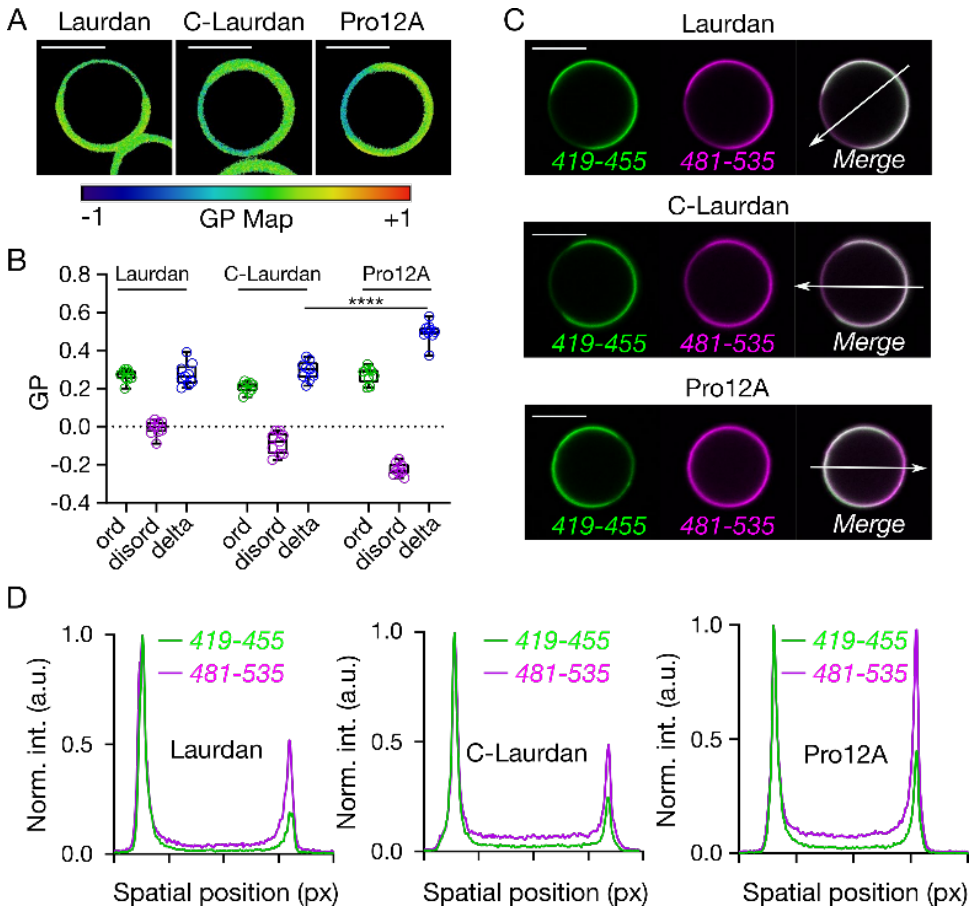

Fig. 2.1.7. Sensitivity of Pro12A, Laurdan and C-Laurdan to lipid order in phase separated GPMVs. GP images of GPMVs doped with Laurdan, C-Laurdan and Pro12A (A). Quantification of GP for the ordered and disordered phases obtained from GPMVs stained with Laurdan, C-Laurdan and Pro12A (B). Fluorescence signal in the ordered vs disordered channel for these three probes (C). Line profiles of fluorescence signal in the ordered and disordered phases and in the ordered and disordered channels (D).

After that, the three probes were compared in terms of internalization. Confocal microscopy imaging of live Chinese Hamster Ovary (CHO) cells, stained with Pro12A, revealed strong fluorescence signal at the plasma membranes and a practically complete absence of the signal inside the cells 15 minutes after the labelling (Fig. 2.1.8, A). In sharp contrast, Laurdan and especially C-Laurdan exhibited significant fluorescence signal inside the cells and thus much less resolved membrane signal (Fig. 2.1.8, B-C). These observations were further supported by plotting the signal intensity (line profile) across the cellular membrane (Fig. 2.1.8, D), revealing that only Pro12A showed nearly zero signal both outside and inside the cells, while C-Laurdan exhibited the strongest intracellular fluorescence. These results further prove that the presence of a membrane-targeting group with a sulphonate and a dodecyl chain provides an effective PM targeting. The observed stronger internalization of C-Laurdan when compared to Laurdan is unexpected and could be possibly explained by a better water solubility of the former probe, leading to a stronger partitioning into cells when used at the same concentration.

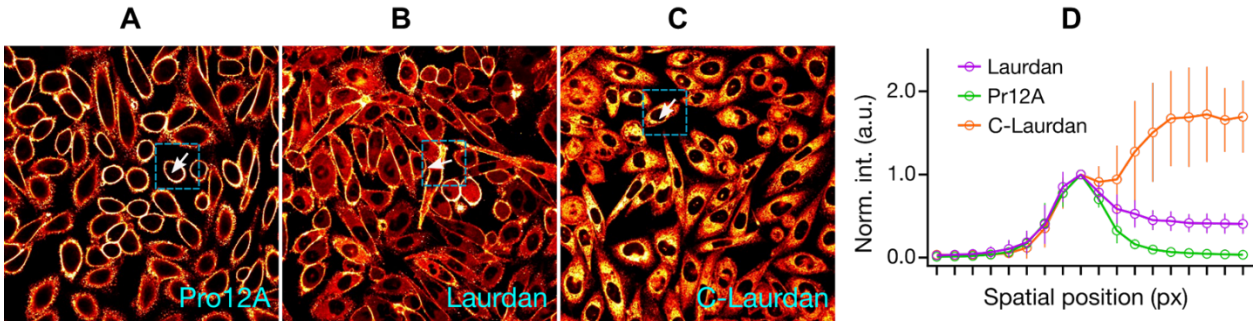

Fig. 2.1.8. Internalization of Pro12A, Laurdan and C-Laurdan in live CHO cells. Confocal microcopy images of cells stained with Pro12A (A), Laurdan (B) and C-Laurdan (C). Fluorescence intensity plots across the cell membranes (D) in the highlighted regions of A-C.

Next, the ability of Pro12A and Laurdan to respond to the changes in cholesterol content in live cell plasma membrane was assessed using cholesterol extraction by methyl-β-cyclodextrin[279] (MCBD) (Fig. 2.1.9). For both probes, the extraction of cholesterol resulted in decreased GP values, which is expected as the lower cholesterol content decreases lipid order.[280] Remarkably, the decrease in the GP values was much stronger for Pro12A when compared to Laurdan (Fig. 2.1.9, A). The observed higher sensitivity towards cholesterol extraction of Pro12A vs Laurdan can be possibly attributed to the differences in the leaflet binding behavior of these two probes (Fig. 2.1.9, B). While the Laurdan is distributed between the both membrane leaflets, the Pro12A is expected to localize only within the outer one, which is also supported by the quenching experiments (Fig. 2.1.6, B-C). Due to the outer leaflet of plasma membrane being richer in sphingomyelin[112, 114] and probably in cholesterol[281] compared to the inner one, cholesterol extraction is expected to induce stronger changes in the lipid order at the outer leaflet. Therefore, Pro12A, which is localized at this leaflet, surpasses Laurdan, which provides an averaged signal from both leaflets.

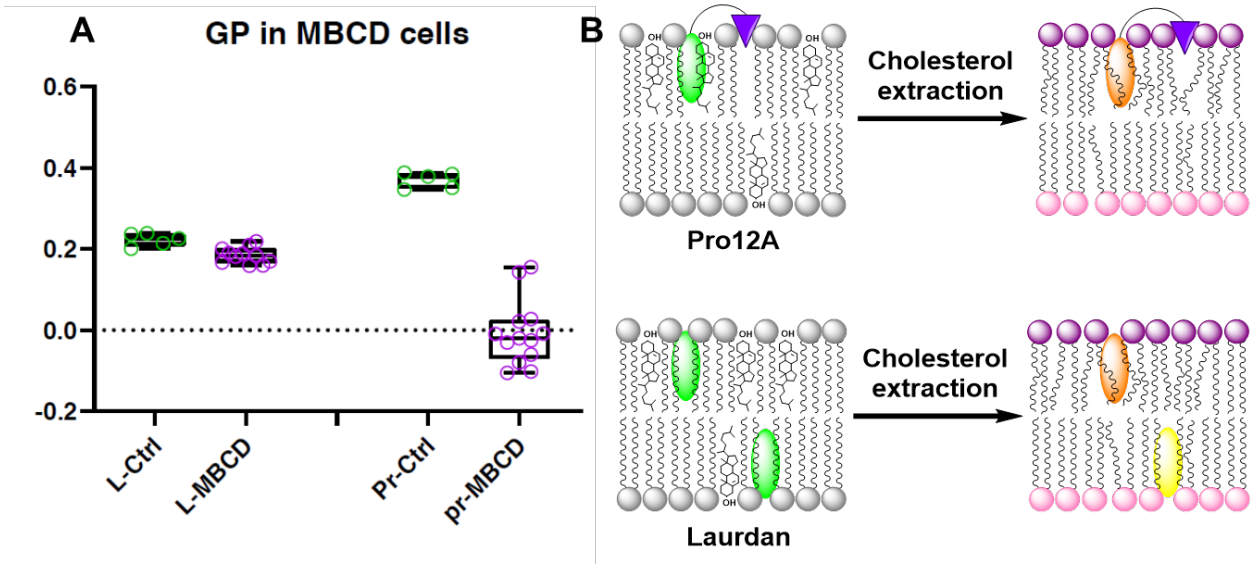

Fig. 2.1.9. Response of Pro12A and Laurdan to methyl-β-cyclodextrin treatment. GP values for the cells, stained with Laurdan and Pro12A, before and after cholesterol extraction with

MBCD (A). Mechanism of sensitivity of Pro12A and Laurdan probes towards cholesterol extraction (B)

Finally, our probe Pro12A has shown an absence of a cross-talk with a number of commonly used orange-red fluorescent proteins and dyes in live cells, proving its applicability for a multicolour fluorescence microscopy imaging.

Spectroscopic experiments in GUVs and GPMVs, as well as the experiments in live cells, were performed in collaboration with Erdinc Sezgin. The results of the project were published in *Analytical Chemistry*, the article is enclosed herewith (Article 1).

analytical chemistry

pubs.acs.org/ac Article

Redesigning Solvatochromic Probe Laurdan for Imaging Lipid Order Selectively in Cell Plasma Membranes

Dmytro I. Danylchuk,[‖] Erdinc Sezgin,[‖] Philippe Chabert, and Andrey S. Klymchenko*

Cite This: *Anal. Chem.* 2020, 92, 14798−14805 Read Online

ACCESS | Metrics & More | Article Recommendations | Supporting Information

ABSTRACT: Imaging of biological membranes by environmentally sensitive solvatochromic probes, such as Laurdan, provides information about the organization of lipids, their ordering, and their uneven distribution. To address a key drawback of Laurdan linked to its rapid internalization and subsequent labeling of internal membranes, we redesigned it by introducing a membrane anchor group based on negatively charged sulfonate and dodecyl chain. The obtained probe, Pro12A, stains exclusively the outer leaflet of lipid bilayers of liposomes, as evidenced by leaflet-specific fluorescence quenching with a viologen derivative, and shows higher fluorescence brightness than Laurdan. Pro12A also exhibits stronger spectral change between liquid-ordered and liquid-disordered phases in model membranes and distinguishes better lipid domains in giant plasma membrane vesicles (GPMVs) than Laurdan. In live cells, it stains exclusively the cell plasma membranes, in contrast to Laurdan and its carboxylate analogue C-Laurdan. Owing to its outer leaflet binding, Pro12A is much more sensitive to cholesterol extraction than Laurdan, which is redistributed within both plasma membrane leaflets and intracellular membranes. Finally, its operating range in the blue spectral region ensures the absence of crosstalk with a number of orange/red fluorescent proteins and dyes. Thus, Pro12A will enable accurate multicolor imaging of lipid organization of cell plasma membranes in the presence of fluorescently tagged proteins of interest, which will open new opportunities in biomembrane research.

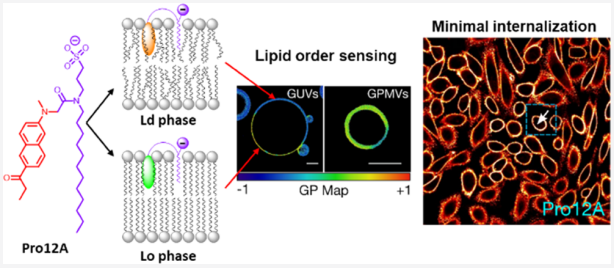

Imaging biological membranes and understanding their lipid ordering using molecular tools, such as fluorescent probes, has attracted significant interest in recent years.[1−5] In particular, fluorescent environment-sensitive probes shed light on different fundamental properties of the biomembranes studied, including microviscosity, tension, polarity, and lipid order.[6]

Microscopic viscosity, essential for the determination of lateral diffusion in biomembranes or in three-dimensional cellular environment, also affects metabolism, enzymology, and protein folding.[7] This parameter can be measured by exploiting the excited-state planarization in dyes termed as molecular rotors.[7−9] Imaging membrane tension opens new opportunities in mechanobiology, with the help of ground-state planarizable probes, so-called flippers.[10,11]

Local membrane polarity, which is a complex parameter combining hydration, presence of dipoles, solvent relaxation, and lipid order,[2,12] can reflect various processes in cells, including apoptosis,[13−15] starvation,[16] and oxidative stress,[16−18] and can distinguish between normal and cancer cells.[19] This parameter is studied by solvatochromic fluorescent dyes.[6]

Lipid order is of high importance for cell signaling, trafficking, and membrane bioactivity.[1,20] Plasma membrane reveals heterogeneity in lipid distribution at both lateral and transversal levels. It is proposed that the interactions between sphingolipids and cholesterol (Chol) lead to the formation of nanoscale domains of higher lipid order.[21,22] These domains are modeled in bilayers of saturated lipids and Chol, forming the so-called liquid ordered (Lo) phase, which is clearly separated from the loosely packed liquid disordered phase (Ld) phase formed by unsaturated lipids.[23−25] It is also known that in healthy cells, the outer leaflet contains mainly sphingomyelin (SM) and phosphatidylcholine, while the inner one is represented by phosphatidylethanolamine and phosphatidylserine,[26,27] which results in higher lipid order at the outer leaflet.[28] Lipid order can be sensed either through monitoring the local viscosity by molecular rotors[29] or lipid packing by mechanosensitive dyes[11] as well as through local polarity using solvatochromic dyes.[6,30,31] Solvatochromic dyes generally detect ordered lipid phases as less polar environments because their tight packing excludes polar water molecules and freezes dipolar relaxation processes.[2,23,32,33]

Received: August 21, 2020
Accepted: September 29, 2020
Published: October 12, 2020

https://dx.doi.org/10.1021/acs.analchem.0c03559
Anal. Chem. 2020, 92, 14798−14805

The examples of solvatochromic dyes, used to sense lipid order, include Prodan[34] and its lipophilic analogues Laurdan[23,35] and C-Laurdan (Figure 1A),[36] di-4-ANEPPDHQ,[35,37] Nile Red,[33,38] and its derivatives (e.g., NR12S, NR12A, and NR4A),[33,39] push−pull pyrenes,[40,41] dioxaborine (DXB-NIR),[16] etc. Among these dyes, Prodan and Laurdan operate in the blue region of the visible spectrum (emission maximum in lipid membranes <500 nm).[23,35] Although this range is generally less attractive for bioimaging, it does not overlap with that of the majority of commonly used fluorescent proteins, which makes them compatible with multilabeling protocols.

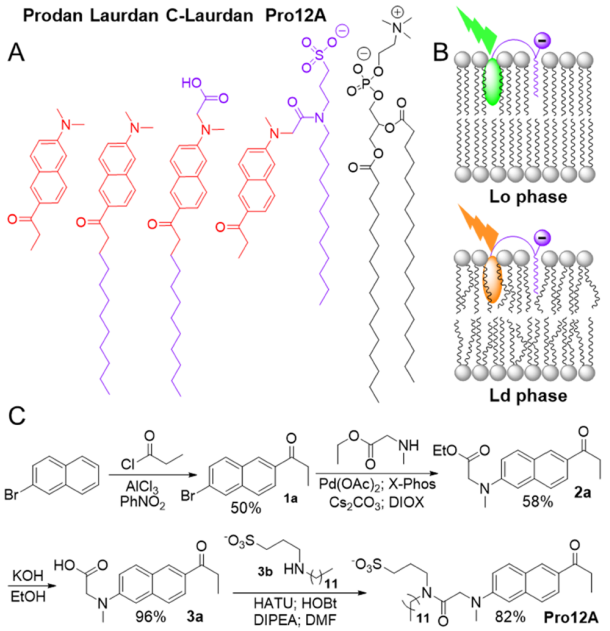

Figure 1. Chemical design (A), sensing principle (B), and synthesis (C) of Pro12A probe for lipid membranes. (A) Part in red highlights Prodan fluorophore in different membrane probes. (B) Schematic presentation of lipid bilayers presenting Lo and Ld phases and the color response of the solvatochromic probe to the changes in the lipid order.

However, the application of Laurdan to live cells is limited due to its fast flip-flop to the inner leaflet and subsequent rapid internalization that leads to staining of intracellular membranes.[35,42] An attempt to prevent internalization of Laurdan by introducing a carboxylate group (C-Laurdan)[36] showed only a moderate improvement because carboxylate may lose its negative charge by reprotonation. This issue can be effectively solved by changing the molecular design of the probe, namely, by introducing membrane anchor groups, bearing an alkyl chain together with a zwitterionic group.[33,43] Our recent study using solvatochromic Nile Red showed that further improvement in the plasma membrane targeting can be achieved by replacing the zwitterionic head group with an anionic sulfonate.[39] We hypothesized that the use of this anionic anchor for Prodan fluorophore could result in an analogue that can specifically target cell plasma membrane with minimal internalization while being sensitive to lipid order and compatible with common fluorescent proteins and dyes used in bioimaging.

The aim of the current work is to create a cell-impermeable Prodan/Laurdan-based fluorescent probe that targets the outer biomembrane leaflet for live-cell imaging of plasma membranes and deciphers their lipid order.

EXPERIMENTAL SECTION

Materials and Characterization of Compounds. All of the reagents were purchased from Sigma-Aldrich or Alfa Aesar or TCI and used as received. MilliQ-water (Millipore) was used in all experiments. The NMR spectra were recorded at 20 °C on a BrukerAvance III 400 MHz spectrometer. The mass spectra were obtained using an Agilent Q-TOF 6520 mass spectrometer. Absorption and emission spectra were recorded on an Edinburgh FS5 spectrofluorometer equipped with a thermostated cell holder. Fluorescence quantum yields were measured using quinine sulfate in 0.5 M sulfuric acid (λ_{ex} = 360 nm, QY_{ref} = 54.6%)[44] as a reference.

Compound **3b** was synthesized according to the known procedures.[45] Synthesis of compounds **1a**−**3a** is based on a synthetic route, similar to the one proposed previously for C-Laurdan.[42]

*1-(6-Bromonaphthalene-2-yl)-propane-1-one (**1a**).* Five grams of 2-bromonaphthalene was dissolved in 25 mL of dry nitrobenzene under an Ar atmosphere and the solution was cooled to 0 °C in an ice bath. After that, 3.56 g (1.1 equiv) of $AlCl_3$ was added portionwise, followed by a dropwise addition of 2.69 g (2.54 mL, 1.2 equiv) of propionyl chloride, then the reaction mixture was stirred at r.t. for 18 h.

After the reaction, the mixture was quenched with distilled water (50 mL) and extracted three times with EtOAc. The organic phases were combined, washed with brine, dried over Na_2SO_4, and concentrated *in vacuo*. The crude product was purified by recrystallization from ethanol. Yield 3.15 g (50%) as a colorless solid. **^{1}H NMR** (400 MHz, $CDCl_3$) δ ppm 8.43 (d, J = 1.0 Hz, 1 H) 8.06 (dd, J = 8.8, 1.8 Hz, 1 H) 8.04 (d, J = 1.5 Hz, 1 H) 7.81 (t, J = 9.2 Hz, 2 H) 7.62 (dd, J = 8.5, 2.0 Hz, 1 H) 3.12 (q, J = 7.3 Hz, 2 H) 1.28 (t, J = 7.2 Hz, 3 H).

*Ethyl 2-[(6-Propanoylnaphthalene-2-yl)methylamino]-acetate (**2a**).* An oven-dried Schlenk flask was evacuated and backfilled with Ar; after that, 2 g of compound **1a** was added together with 137 mg (0.08 equiv) of $Pd(OAc)_2$, 582 mg (0.16 equiv) of XPhos, followed by 9.95 g (4 equiv) of Cs_2CO_3 and 2.34 g (2 equiv) of sarcosine ethyl ester (in form of hydrochloride salt). The Schlenk flask was then capped with a rubber septum, evacuated, and backfilled with Ar three times. After this, anhydrous dioxane (25 mL) was added and the mixture was stirred for 18 h at 100 °C under an Ar atmosphere.

After the reaction, the mixture was filtered through Celite and concentrated *in vacuo*. The crude product was purified by gradient flash column chromatography (SiO_2, heptane:EtOAc 9:1 to 2:8). Yield 1.33 g (58%) as a yellow solid. **^{1}H NMR** (400 MHz, $CDCl_3$) δ ppm 8.33 (d, J = 1.5 Hz, 1 H) 7.94 (dd, J = 8.8, 1.8 Hz, 1 H) 7.80 (d, J = 9.0 Hz, 1 H) 7.65 (d, J = 8.8 Hz, 1 H) 7.10 (dd, J = 9.2, 2.6 Hz, 1 H) 6.89 (d, J = 2.5 Hz, 1 H) 4.17−4.23 (m, 4 H) 3.21 (s, 3 H) 3.08 (q, J = 7.3 Hz, 2 H) 1.27 (t, J = 7.3 Hz, 3 H) 1.25 (t, J = 7.2 Hz, 3 H). **^{13}C NMR** (101 MHz, $CDCl_3$) δ ppm 200.47 ($C_{carbonyl}$) 170.50 ($C_{carboxyl}$) 148.75 (C_{ar}) 137.44 (C_{ar}) 130.95 (C_{ar}) 130.88 (C_{ar}) 129.58 (C_{ar}) 126.42 (C_{ar}) 125.67 (C_{ar}) 124.64 (C_{ar}) 115.75 (C_{ar}) 105.96 (C_{ar}) 61.15 (C_{al}) 54.43 (C_{al}) 39.74 (C_{al}) 31.52 (C_{al}) 14.24 (CH_3) 8.64 (CH_3). **HRMS (ESI)**, ***m/z*** $[M + H]^+$ calcd for $C_{18}H_{22}NO_3^+$, 300.1594; found, 300.1611.

https://dx.doi.org/10.1021/acs.analchem.0c03559
Anal. Chem. 2020, 92, 14798−14805

*N-Methyl-N-(6-propionylnaphthalen-2-yl)glycine (**3a**).* Compound **2a** (1.2 g) was dissolved in 40 mL of a freshly prepared solution of KOH (0.25 M) in EtOH. The reaction mixture was stirred for 2 days at r.t. (control by TLC). After the reaction, the solution was acidified with HCl to pH 2, and the products were extracted with EtOAc three times. The ethyl acetate layers were then combined, dried over Na_2SO_4, and concentrated *in vacuo*. Yield 1.05 g (96%) as a pale yellow solid. **^{1}H NMR** (400 MHz, methanol-d_4) δ ppm 8.41 (d, J = 1.5 Hz, 1 H) 7.89 (dd, J = 8.8, 1.8 Hz, 1 H) 7.86 (d, J = 9.3 Hz, 1 H) 7.67 (d, J = 8.5 Hz, 1 H) 7.20 (dd, J = 9.0, 2.5 Hz, 1 H) 6.96 (d, J = 2.5 Hz, 1 H) 4.29 (s, 2 H) 3.21 (s, 3 H) 3.13 (q, J = 7.3 Hz, 2 H) 1.24 (t, J = 7.3 Hz, 3 H). **^{13}C NMR** (101 MHz, methanol-d_4) δ ppm 203.18 ($C_{carbonyl}$) 174.45 ($C_{carbonyl}$) 150.92 (C_{ar}) 139.32 (C_{ar}) 132.02 (C_{ar}) 131.75 (C_{ar}) 131.30 (C_{ar}) 127.58 (C_{ar}) 127.01 (C_{ar}) 125.34 (C_{ar}) 117.20 (C_{ar}) 106.70 (C_{ar}) 54.75 (C_{al}) 39.92 (C_{al}) 32.44 (C_{al}) 9.19 (CH_3). **HRMS (ESI)**, ***m/z*** $[M + H]^+$ calcd for $C_{16}H_{18}NO_3^+$, 272.1281; found, 272.1296.

*3-(N-Dodecyl-2-(methyl(6-propionylnaphthalen-2-yl)-amino)acetamido)propane-1-sulfonate (**Pro12A**).* 3-(Dodecylamino)propane-1-sulfonate (**3b**, 59.5 mg, 1.05 equiv) and 47.7 mg (65 μL, 2 equiv) of DIPEA were mixed in 2 mL of dry DMF under an Ar atmosphere; after this, the mixture was stirred for 30 min at 50 °C. In a separate flask, 50 mg of carboxylic acid **3a** was dissolved in 2 mL of dry DMF together with 73.7 mg (1.05 equiv) of HATU, 12.5 mg (0.5 equiv) of HOBt and 95.4 mg (129 μL, 4 equiv) of DIPEA. After 5 min, the solution of activated acid was transferred to the flask with amine and the final mixture was stirred for 24 h at 45 °C (control by TLC). After the reaction, the solvent was evaporated *in vacuo* and the crude product was purified by preparative TLC (SiO_2; DCM:MeOH 85:15). Compound **Pro12A**: yield 104 mg (82%) as pale yellow solid (obtained in form of a salt with DIPEA). **^{1}H NMR** (400 MHz, methanol-d_4) δ ppm 8.37 (s, 1 H) 7.86 (ddd, J = 8.8, 3.2, 1.7 Hz, 1 H) 7.81 (dd, J = 9.0, 2.5 Hz, 1 H) 7.63 (dd, J = 8.8, 5.5 Hz, 1 H) 7.13 (td, J = 9.4, 2.5 Hz, 1 H) 6.88 (t, J = 3.0 Hz, 1 H) 4.43 (d, J = 31.6 Hz, 2 H) 3.54 (dt, J = 41.9, 8.0 Hz, 2 H) 3.34−3.42 (m, 2 H) 3.13−3.21 (m, 5 H) 2.79−2.96 (m, 2 H) 1.99−2.21 (m, 2 H) 1.51−1.73 (m, 2 H) 1.18−1.31 (m, 21 H) 0.85−0.90 (m, 3 H). **^{13}C NMR** (101 MHz, methanol-d_4) δ ppm 203.00 (d, J = 5.8 Hz, $C_{carboxyl}$) 171.44 ($C_{carboxyl}$) 151.27 (d, J = 15.8 Hz, C_{ar}) 139.34 (C_{ar}) 139.30 (C_{ar}) 131.96 (d, J = 10.2 Hz, C_{ar}) 131.55 (d, J = 13.3 Hz, C_{ar}) 131.32 (C_{ar}) 127.53 (d, J = 3.3 Hz, C_{ar}) 126.84 (d, J = 8.5 Hz, C_{ar}) 125.31 (d, J = 12.4 Hz, C_{ar}) 117.37 (d, J = 10.2 Hz, C_{ar}) 106.62 (C_{ar}) 55.96 (C_{al}) 54.97 (d, J = 12.0 Hz, C_{al}) 47.13 (d, J = 18.7 Hz, C_{al}) 40.13 (d, J = 22.6 Hz, C_{al}) 33.20 (C_{al}) 32.41 (C_{al}) 30.82−30.96 (m, C_{al}) 30.58−30.66 (m, C_{al}) 30.01 (C_{al}) 28.86 (C_{al}) 28.15 (d, J = 7.9 Hz, C_{al}) 25.68 (C_{al}) 23.86 (C_{al}) 14.58 (C_{al}) 13.28 (CH_3) 9.22 (CH_3). **HRMS (ESI)**, ***m/z***: $[M+2Na]^+$ calcd for $C_{31}H_{47}N_2O_5SNa_2$, 605.3011; found, 605.3015.

Preparation of Large Unilamellar Vesicles (LUVs). All types of LUVs used were prepared by the following procedure. A stock solution of the corresponding lipid(s) in chloroform was placed into a round-neck flask, after which the solvent was evaporated *in vacuo* and phosphate buffer (20 mM, pH 7.4) was added. After all the solid was dissolved, a suspension of multilamellar vesicles was extruded using a Lipex Biomembranes extruder (Vancouver, Canada). The size of the filters was first 0.2 μm (7 passages) and thereafter 0.1 μm (10 passages). This generates monodisperse LUVs with a mean diameter of 0.12 μm as measured with a Malvern Zetamaster 300 (Malvern, U.K.). The phospholipid:cholesterol molar ratio in the case of DOPC/Chol and SM/Chol was 1:0.9. LUVs were labeled by the addition of the DMSO stock solution of the probes to a final concentration of 2 μM, unless indicated, and incubation for 5 min.

Fluorescence Quenching Experiment. Solutions of Pro12A and Laurdan in DOPC LUVs (1 μM of dye for 500 μM total lipid concentration) were made by adding concentrated dye stock solution in DMSO to LUVs, followed by vortexing the mixture. In the case of Pro12A, the mixture was incubated for 15 min at RT. To ensure the complete binding and disaggregation of Laurdan, brief heating to 40 °C was done, followed by another vortexing and slow cooling over 2 h. Then, Viologen-C12 was added (from DMSO stock solution) to a given concentration and fluorescence spectra were measured after 15 min of incubation.

Preparation of Giant Unilamellar Vesicles (GUVs). GUVs were prepared by electroformation. Lipid stock (DOPC:SM:Chol 2:2:1) was spread onto two parallel platinum wires attached to a custom-built Teflon-coated chamber and left briefly to evaporate the solvent. Wires were passed under nitrogen gas before submersion in 300 mM sucrose. Ten hertz AC current was applied for 1 h to trigger vesicles swelling at 70 °C, followed by 2 Hz for 30 min with slow cooling.

Preparation of Giant Plasma Membrane Vesicles (GPMVs). GPMVs were prepared as previously described.[46] Briefly, the cells seeded out on a 60 mm Petri dish (≈70% confluent) were washed with GPMV buffer (150 mM NaCl, 10 mM Hepes, 2 mM $CaCl_2$, pH 7.4) twice. Two milliliters of GPMV buffer was added to the cells. Twenty-five millimolar PFA and 20 mM DTT (final concentrations) were added in the GPMV buffer. The cells were incubated for 2 h at 37 °C. Then, GPMVs were collected by pipetting out the supernatant. GUVs and GPMVs were labeled by adding Pro12A (or Laurdan and C-Laurdan) with a final concentration of 50 nM.

Cell Lines, Culture Conditions, and Treatment. The CHO cells were maintained in DMEM-F12 medium supplemented with 10% FBS medium and 1% L-glutamine. The cells were transfected with the plasmids using Lipofectamine 3000 as described in the manufacturer's protocol.

Fluorescence Microscopy. All imaging was done at room temperature (21−23 °C). Samples were imaged with a Zeiss LSM 780 confocal microscope. Spectral imaging was done as described before.[47] Cells were incubated with Pro12A (or Laurdan and C-Laurdan) with a final concentration of 0.8 μM in PBS for 5 min. After the labeling, the cells were washed once and the imaging was performed in L15 medium. Pro12A, Laurdan, and C-Laurdan were excited with 405 nm and emission collected between 410 and 600 nm.

RESULTS AND DISCUSSION

The probe Pro12A was designed based on solvatochromic fluorophore Prodan (parent analogue of Laurdan)[34] and the anionic plasma membrane targeting moiety (Figure 1A). The latter is composed of lipophilic dodecyl chain and anionic sulfonate, which ensures effective high-affinity binding to cell plasma membranes.[39] The solvatochromic dye is expected to sense changes in lipid order in the plasma membrane by changing its emission color (Figure 1B): shifting its emission to the longer wavelengths (e.g., from green to orange) from apolar dehydrated Lo phase to polar hydrated Ld phase.[2]

https://dx.doi.org/10.1021/acs.analchem.0c03559
Anal. Chem. 2020, 92, 14798−14805

Taking into account that charged carboxylate did not decrease the sensitivity of C-Laurdan to lipid order compared to parent Laurdan,[36] we functionalized this fluorophore at the dialkylamino side. The synthesis was performed in four steps starting from 2-bromonaphthalene (Figure 1C). In the final step, the key intermediate, a Prodan-bearing carboxylate group (**3a**), was coupled to the anchor amine (**3b**), affording the final probe Pro12A in a relatively good yield. The structure of new compounds was confirmed by NMR and mass spectroscopy (SI Figures S1−S9).

Absorption and fluorescence spectroscopy of Pro12A in organic solvents showed that it preserved the solvatochromism of parent Laurdan (Table S1, Figure 2A, SI Figure S10C,D).

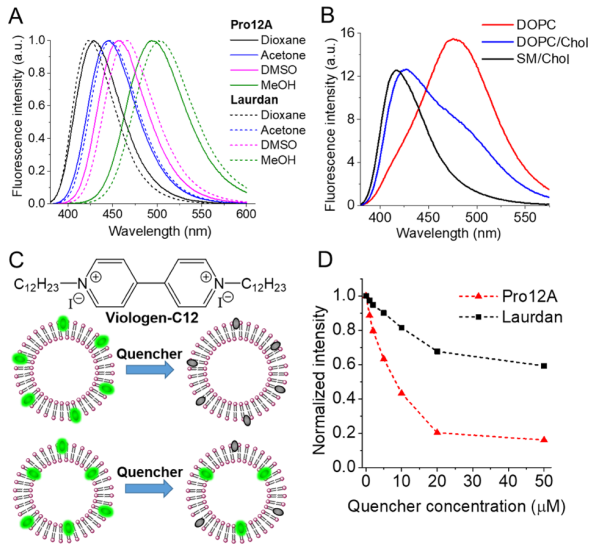

Figure 2. Spectroscopy experiments in solvents and lipid vesicles. (A) Normalized fluorescence spectra of Pro12A and Laurdan in solvents of different polarities. (B) Fluorescence spectra of Pro12A in LUVs of different compositions. Probe concentration was systematically 2 μM. Total lipid concentration for all vesicles was 1 mM. (C) Chemical structure of Viologen-C12 and scheme of surface quenching by Viologen-C12 of the probes located at the outer bilayer leaflet (upper panel) and both leaflets (lower panel). (D) Fluorescence quenching of Pro12A and Laurdan in DOPC LUVs with increasing concentrations of Viologen-C12. The intensity was recorded at the maximum of probe emission: 476 nm (Pro12A) and 493 nm (Laurdan). Probe and lipid concentrations were 1 and 500 μM, respectively. Twenty millimolar phosphate buffer (pH 7.4) was used for all LUVs. λ_{ex} = 360 nm in all cases.

Indeed, similarly to Laurdan, Pro12A displayed a red shift in fluorescence spectra with an increase in the solvent polarity. Large unilamellar vesicles (LUVs) with different phospholipid compositions were then used as model membranes, presenting the Ld phase in case of unsaturated lipid DOPC with or without cholesterol and the Lo phase for a mixture of sphingomyelin (SM) and cholesterol. The emission band of Pro12A in the Lo phase (Figures 2B and S10A,B) was strongly blue-shifted with respect to that of the Ld phase without cholesterol, in line with that for Laurdan and other solvatochromic dyes.[39,48] Interestingly, the value of the blue shift from the Ld (DOPC) to Lo (SM/Chol) phase was slightly larger for Pro12A compared to Laurdan (59 vs 53 nm, see Table S1). Similar to Laurdan, the Pro12A probe can also sense the presence of cholesterol in DOPC vesicles (Table S1) so that the resulting spectrum is intermediate between those in SM/Chol and DOPC LUVs (Figure 2B). The absorption maximum of Pro12A in LUVs was systematically red-shifted (372−379 nm) compared to that of Laurdan (356−358 nm), making it more suitable for excitation with common violet light sources (395 nm LED or 405 nm laser). Moreover, the new probe in LUVs exhibited two- to threefold larger fluorescence quantum yield (QY) values compared to Laurdan (Table S1). This drastic difference is probably linked to the more efficient membrane binding of Pro12A. The amphiphilic nature of our probe, induced by the charged sulfonate group, renders its better solubilization in water and further transfer to lipid membranes, whereas a highly hydrophobic Laurdan could partially precipitate in an aqueous buffer before reaching the lipid membrane. Fluorescence intensity of Pro12A in the buffer increased linearly with concentration until 0.5 μM, followed by the decrease of the slope of the titration curve (SI Figure S11). This observation suggests the presence of critical micellar concentration (CMC ∼ 0.5 μM) for Pro12A, above which the dye molecules undergo self-quenching. The latter is useful for decreasing the background fluorescence of the free probes in a solution, similar to other amphiphilic membrane probes.[33,39,43]

The probe added to the bulk solution is expected to bind first to the outer membrane leaflet and remain there if it does not undergo a flip-flop.[33] To verify the localization of Pro12A at the outer membrane leaflet, we used fluorescence quenching by photoinduced electron transfer (PET)[49] with a specially designed amphiphilic dodecyl viologen (Viologen-C12; Figure 2C). Due to their highly electron-deficient nature, viologens are efficient PET quenchers,[50−52] while dodecyl chains should provide the quencher with high affinity to lipid membranes. As the PET process requires close dye-quencher proximity,[53] only the dye at the outer leaflet is expected to be effectively quenched by Viologen-C12 (Figure 2C). Fluorescence intensity of Pro12A in DOPC LUVs dropped rapidly with the increase in Viologen-C12 concentration, reaching 84% quenching at 50 μM concentration, whereas only 41% quenching was observed for Laurdan (Figures 2D and S10E,F). The shape of the curves with the saturation behavior at higher quencher concentrations was similar for both probes, indicating that the binding mode of Viologen-C12 is similar for both probes, and the difference in the quenching efficiency is linked to different availability of the probe to the quencher. We can conclude that Pro12A is much more exposed to the quencher, probably because it is localized at the outer leaflet, in contrast to Laurdan that can diffuse freely through the membrane to the inner leaflet. Thus, the use of an anchor group favors one-leaflet binding, as it is expected to inhibit the flip-flop between the leaflets.

Next, we tested Pro12A in phase-separated membrane systems. In microscopy experiments with phase-separated giant unilamellar vesicles (GUVs) and giant plasma membrane vesicles (GPMVs),[46] Pro12A was able to distinguish the domains with different lipid orders (Figure 3). Spectroscopic scans of the vesicles labeled by Pro12A revealed different intensity variations as a function of the wavelength (Figure 3A). The reconstructed spectra for each region in GUVs revealed a strong band shift (Figure 3B), with band positions corresponding to those in Lo and Ld phases of LUVs (Figure 2B). The spectral change in GPMVs was similar (Figure 3C), but its amplitude was smaller as expected, given the packing of the domains is less different compared to GUVs.[54] Then, ratiometric imaging using generalized polarization (GP) index

https://dx.doi.org/10.1021/acs.analchem.0c03559
Anal. Chem. 2020, 92, 14798−14805

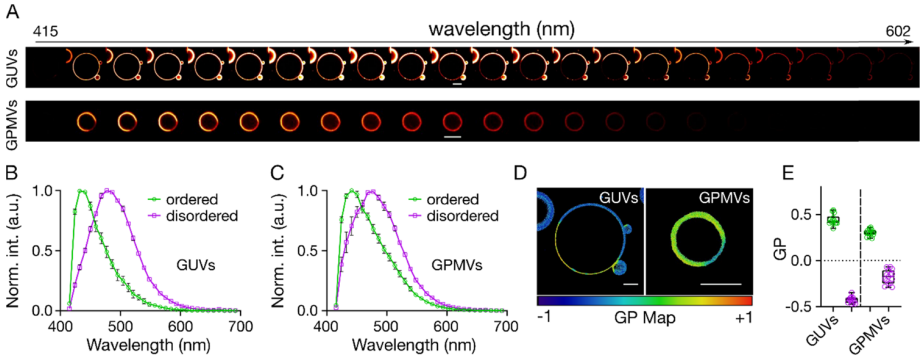

Figure 3. Spectra of Pro12A in phase-separated GUVs and GPMVs. (A) Montage of spectral images obtained with spectral detector (each image is one channel with 8.9 nm wavelength intervals) for Pro12A-doped GUVs and GPMVs. (B, C) Reconstruction of the spectra from the spectral images for (B) GUVs and (C) GPMVs. (D) GP images of the phase-separated GUVs and GPMVs. (E) GP values obtained from the phase-separated GUVs and GPMVs. Scale bars are 10 μm.

showed that Pro12A can clearly distinguish Lo and Ld phases in GUVs and GPMVs (Figure 3D). The GP analysis suggested a stronger difference in the lipid order for GUVs compared to that for GPMVs (Figure 3E), in line with the previous data.[54] GUVs are prepared from pure synthetic lipids and therefore present "pure" Lo and Ld phases with the largest variation of the lipid order. On the other hand, GPMVs are native membranes with a complex mixture of lipids and proteins, where changes in the lipid order are expected to be subtler, as suggested by other studies, including those using Laurdan.[47,55]

In the next step, we compared Pro12A with Laurdan and C-Laurdan probes in phase-separated GPMVs (Figure 4) in terms of the sensitivity to the lipid order. GP images and the obtained values (Figure 4A,B) suggested that Pro12A is more sensitive to changes in the lipid order in GPMVs compared to its counterparts. Additionally, Pro12A displayed almost equal fluorescence signal from the two separated lipid phases (Figure 4C,D). By contrast, Laurdan and C-Laurdan showed significantly lower signal in the Ld phase of GPMVs compared to Lo, in line with previous reports.[47,55] Even partitioning of Pro12A between Lo and Ld phases is another important advantage because it allows recording good signal from both domains while distinguishing them by emission color.

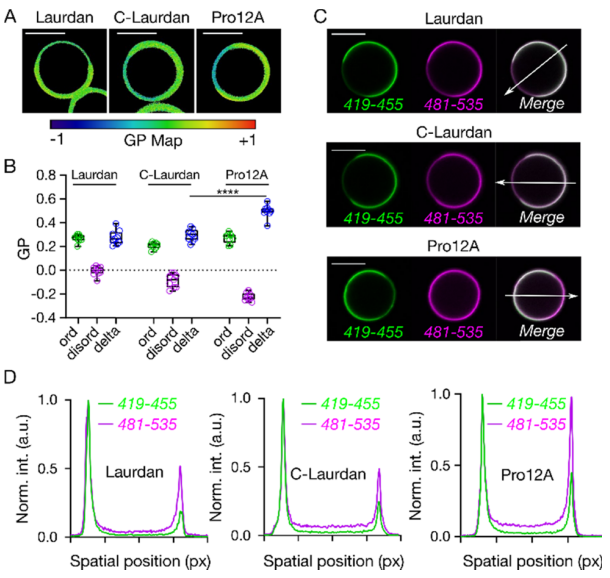

Figure 4. Sensitivity of Pro12A, Laurdan, and C-Laurdan to lipid packing in the phase-separated GPMVs. (A) GP images of GPMVs doped with Laurdan, C-Laurdan, and Pro12A. (B) Quantification of GP for the ordered and disordered phases obtained from GPMVs stained with Laurdan, C-Laurdan, and Pro12A. (C) Fluorescence signal in the ordered vs disordered channel for these three probes. (D) Line profiles of fluorescence signal in the ordered and disordered phases and in the ordered and disordered channels.

Next, we compared these three probes in terms of internalization. Confocal imaging of live Chinese hamster ovary (CHO) cells stained with Pro12A showed a strong fluorescence signal at the plasma membranes and practically complete absence of the signal inside the cells 15 min after the labeling (Figure 5A). In sharp contrast, Laurdan and especially C-Laurdan showed significant fluorescence signal inside the cells and thus much less resolved membrane signal (Figure 5B,C). These observations were further supported by plotting the signal intensity (line profile) across the cellular membrane (Figure 5D), revealing that only Pro12A showed nearly zero signal both outside and inside the cells, while C-Laurdan showed the strongest intracellular fluorescence. Thus, the presence of the membrane anchor with the sulfonate group and dodecyl chain ensures effective plasma membrane targeting of the dye. The observed stronger internalization of C-Laurdan compared to Laurdan is unexpected and it could be explained by its better water solubility and thus stronger partitioning into cells when used at the same concentration.

After that, the ability of Pro12A and Laurdan to respond to changes in the cholesterol content in the live-cell plasma membrane was tested using cholesterol extraction by methyl-β-cyclodextrin[56] (MCBD) (Figure 5E). For both probes, cholesterol extraction decreased the GP values, which is expected because a lower cholesterol content decreases the lipid order.[35] Remarkably, Pro12A displayed a much stronger decrease in the GP values compared to Laurdan (Figure 5E). The observed higher sensitivity of Pro12A vs Laurdan to cholesterol extraction is probably related to the differences in the leaflet binding behavior of these two probes. Laurdan is distributed between both membrane leaflets, while Pro12A is expected to localize only at the outer one, which is supported by our quenching experiments (Figure 2C,D). As the outer leaflet of the plasma membrane is richer in sphingomyelin[26,28] and probably in cholesterol[57] than the inner one, cholesterol extraction should produce stronger changes in the lipid order at the outer leaflet. Therefore, Pro12A localized at this leaflet

https://dx.doi.org/10.1021/acs.analchem.0c03559
Anal. Chem. 2020, 92, 14798−14805

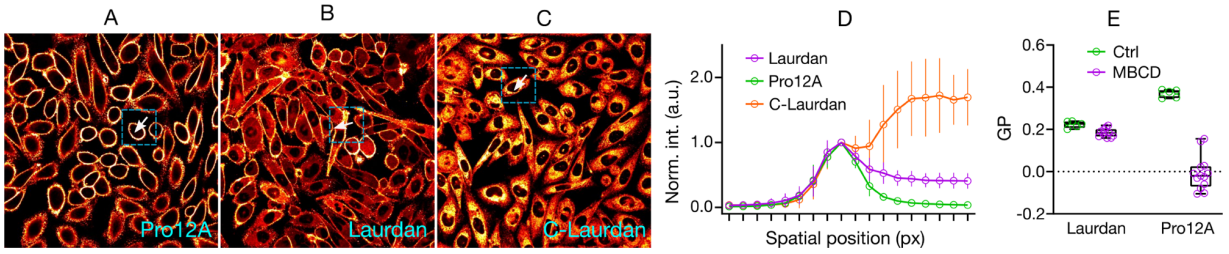

Figure 5. Localization of Pro12A, Laurdan, and C-Laurdan in live cells. Confocal microscopy images of CHO cells stained with Pro12A (A), Laurdan (B), and C-Laurdan (C). Fluorescence intensity plots across the cell membranes (D) in the highlighted regions of A–C. Response of Pro12A and Laurdan to methyl-β-cyclodextrin treatment (E).

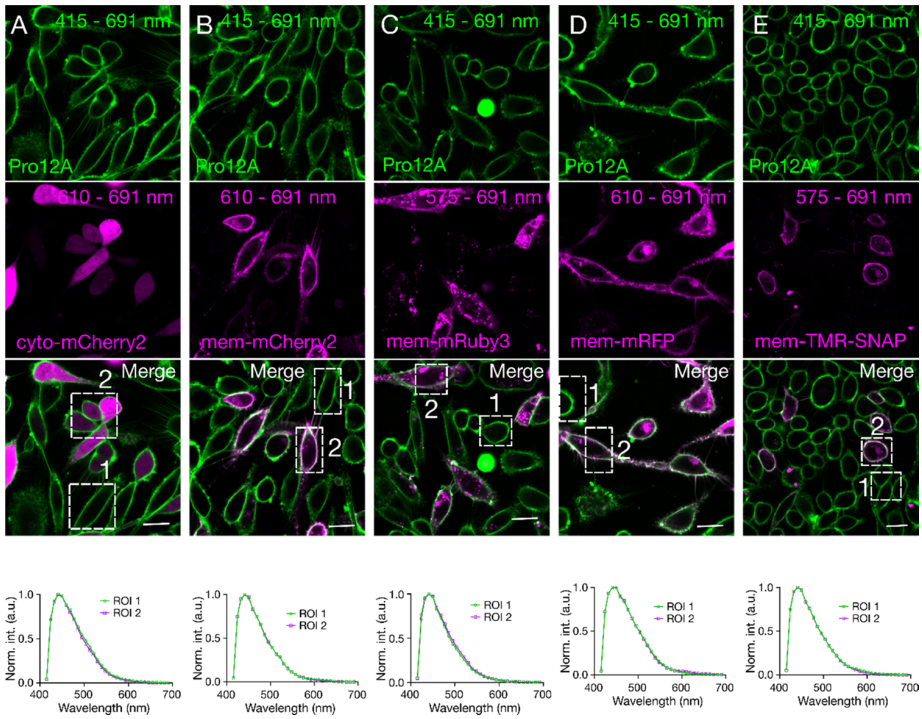

Figure 6. Application of Pro12A in combination with fluorescent proteins. Images of cells labeled with Pro12A and transfected with (A) cytosolic mCherry2; (B) membrane-anchored mCherry2; (C) membrane-anchored mRuby3; (D) membrane-anchored mRFP; and (E) membrane-anchored TMR. Top panels are images and bottom panels are intensity profiles of the regions marked in the corresponding images. Two separate regions of interest (ROIs) are selected; in ROI 1, there is only Pro12A signal (no protein), while in ROI 2, there are both protein and Pro12A signals. Two ROIs possess identical spectra, showing no effect of these fluorescent proteins on Pro12A spectrum. Scale bars: 10 μm.

surpasses Laurdan, which provides an averaged signal from both leaflets.

Finally, the compatibility of Pro12A with the commonly used fluorescent proteins or dyes was examined using fluorescence microscopy in live CHO cells (Figure 6). mCherry2 localized in the cytosol (Figure 6A) and membrane (Figure 6B), membrane-localized mRuby (Figure 6C), mRFP (Figure 6D), and TMR-SNAP (Figure 6E) were imaged in cells co-stained with Pro12A using respective detection channels. It was found that the emission spectrum of Pro12A in cells acquired by a microscope does not alter in the case of all these co-staining conditions (Figure 6A–E), which signifies an absence of signal leakage and high compatibility of ProA12 with all the fluorescent proteins and dyes studied.

CONCLUSIONS

To develop a universal tool for monitoring lipid organization of cell plasma membranes, compatible with common fluorescent proteins, we addressed the fundamental drawback of a well-known solvatochromic probe Laurdan for sensing lipid order, related to its internalization and inefficient plasma membrane labeling. We redesigned Laurdan by grafting an anchor group composed of sulfonate charged group and dodecyl alkyl chain. The new probe Pro12A showed a two- to threefold higher fluorescence quantum yields in lipid membranes compared to Laurdan, because of more effective partitioning from the aqueous medium. It also shows higher sensitivity to lipid order in both model lipid vesicles and membranes derived from cells, probably because of more defined localization in lipid membranes imposed by the anchor group. Finally, in contrast to Laurdan, Pro12A binds exclusively the outer membrane leaflet and stains selectively

https://dx.doi.org/10.1021/acs.analchem.0c03559
Anal. Chem. 2020, 92, 14798–14805

cell plasma membranes without detectable internalization. Due to this specific outer leaflet targeting, the sensitivity of ProA12 to cholesterol extraction from plasma membranes of live cells is much higher compared to that of Laurdan. Its application in combination with commonly used orange/red fluorescent proteins and dyes revealed an absence of signal crosstalk, allowing for accurate and unbiased multicolor cellular microscopy. This probe reinforces the toolkit of available solvatochromic membrane probes, opening new possibilities for biomembrane imaging in live cells.

■ ASSOCIATED CONTENT

Supporting Information

The Supporting Information is available free of charge at https://pubs.acs.org/doi/10.1021/acs.analchem.0c03559.

It describes the probe synthesis and characterization and additional spectroscopy data, as well as additional experimental data (PDF)

■ AUTHOR INFORMATION

Corresponding Author

Andrey S. Klymchenko − *Laboratoire de Bioimagerie et Pathologies, UMR 7021 CNRS, Université de Strasbourg, 67401 Illkirch, France;* orcid.org/0000-0002-2423-830X; Email: andrey.klymchenko@unistra.fr

Authors

Dmytro I. Danylchuk − *Laboratoire de Bioimagerie et Pathologies, UMR 7021 CNRS, Université de Strasbourg, 67401 Illkirch, France*

Erdinc Sezgin − *MRC Human Immunology Unit, Weatherall Institute of Molecular Medicine, University of Oxford, Oxford OX3 9DS, U.K.; Science for Life Laboratory, Department of Women's and Children's Health, Karolinska Institutet, 17177 Stockholm, Sweden;* orcid.org/0000-0002-4915-388X

Philippe Chabert − *Laboratoire de Bioimagerie et Pathologies, UMR 7021 CNRS, Université de Strasbourg, 67401 Illkirch, France*

Complete contact information is available at: https://pubs.acs.org/10.1021/acs.analchem.0c03559

Author Contributions

[‖]D.I.D. and E.S. contributed equally. The manuscript was written through contributions of all authors. All authors have given approval to the final version of the manuscript.

Notes

The authors declare no competing financial interest.

■ ACKNOWLEDGMENTS

This work was supported by the European Research Council ERC Consolidator grant BrightSens 648528 and ED222 of the University of Strasbourg. E.S. is supported by SciLifeLab fellow program.

■ REFERENCES

(1) Sezgin, E.; Levental, I.; Mayor, S.; Eggeling, C. *Nat. Rev. Mol. Cell Biol.* **2017**, *18*, 361−374.

(2) Klymchenko, A. S.; Kreder, R. *Chem. Biol.* **2014**, *21*, 97−113.

(3) Wang, H. M.; Feng, Z. Q. Q.; Del Signore, S. J.; Rodal, A. A.; Xu, B. *J. Am. Chem. Soc.* **2018**, *140*, 3505−3509.

(4) Bumpus, T. W.; Baskin, J. M. *Trends Biochem. Sci.* **2018**, *43*, 970−983.

(5) Stone, M. B.; Shelby, S. A.; Veatch, S. L. *Chem. Rev.* **2017**, *117*, 7457−7477.

(6) Klymchenko, A. S. *Acc. Chem. Res.* **2017**, *50*, 366−375.

(7) Chambers, J. E.; Kubankova, M.; Huber, R. G.; Lopez-Duarte, I.; Avezov, E.; Bond, P. J.; Marciniak, S. J.; Kuimova, M. K. *ACS Nano* **2018**, *12*, 4398−4407.

(8) Su, D. D.; Teoh, C. L.; Wang, L.; Liu, X. G.; Chang, Y. T. *Chem. Soc. Rev.* **2017**, *46*, 4833−4844.

(9) Sherin, P. S.; Lopez-Duarte, I.; Dent, M. R.; Kubankova, M.; Vysniauskas, A.; Bull, J. A.; Reshetnikova, E. S.; Klymchenko, A. S.; Tsentalovich, Y. P.; Kuimova, M. K. *Chem. Sci.* **2017**, *8*, 3523−3528.

(10) Colom, A.; Derivery, E.; Soleimanpour, S.; Tomba, C.; Dal Molin, M.; Sakai, N.; Gonzalez-Gaitan, M.; Matile, S.; Roux, A. *Nat. Chem.* **2018**, *10*, 1118−1125.

(11) Dal Molin, M.; Verolet, Q.; Colom, A.; Letrun, R.; Derivery, E.; Gonzalez-Gaitan, M.; Vauthey, E.; Roux, A.; Sakai, N.; Matile, S. *J. Am. Chem. Soc.* **2015**, *137*, 568−571.

(12) Demchenko, A. P.; Mely, Y.; Duportail, G.; Klymchenko, A. S. *Biophys. J.* **2009**, *96*, 3461−3470.

(13) Shynkar, V. V.; Klymchenko, A. S.; Kunzelmann, C.; Duportail, G.; Muller, C. D.; Demchenko, A. P.; Freyssinet, J. M.; Mely, Y. *J. Am. Chem. Soc.* **2007**, *129*, 2187−2193.

(14) Kreder, R.; Pyrshev, K. A.; Darwich, Z.; Kucherak, O. A.; Mely, Y.; Klymchenko, A. S. *ACS Chem. Biol.* **2015**, *10*, 1435−1442.

(15) Liu, C.; Tian, M. G.; Lin, W. Y. *J. Mater. Chem. B* **2020**, *8*, 752−757.

(16) Ashoka, A. H.; Ashokkumar, P.; Kovtun, Y. P.; Klymchenko, A. S. *J. Phys. Chem. Lett.* **2019**, *10*, 2414−2421.

(17) Han, X. Y.; Wang, R.; Song, X. Y.; Yu, F. B.; Lv, C. J.; Chen, L. X. *Biomaterials* **2018**, *156*, 134−146.

(18) de la Haba, C.; Palacio, J. R.; Martinez, P.; Morros, A. *Biochim. Biophys. Acta, Biomembr.* **2013**, *1828*, 357−364.

(19) Jiang, N.; Fan, J. L.; Xu, F.; Peng, X. J.; Mu, H. Y.; Wang, J. Y.; Xiong, X. Q. *Angew. Chem., Int. Ed.* **2015**, *54*, 2510−2514.

(20) Lingwood, D.; Simons, K. *Science* **2010**, *327*, 46−50.

(21) Simons, K.; Ikonen, E. *Nature* **1997**, *387*, 569−572.

(22) Brown, D. A.; London, E. *J. Biol. Chem.* **2000**, *275*, 17221−17224.

(23) Dietrich, C.; Bagatolli, L. A.; Volovyk, Z. N.; Thompson, N. L.; Levi, M.; Jacobson, K.; Gratton, E. *Biophys. J.* **2001**, *80*, 1417−1428.

(24) Veatch, S. L.; Keller, S. L. *Biophys. J.* **2003**, *85*, 3074−3083.

(25) Baumgart, T.; Hess, S. T.; Webb, W. W. *Nature* **2003**, *425*, 821−824.

(26) Zwaal, R. F. A.; Schroit, A. J. *Blood* **1997**, *89*, 1121−1132.

(27) Murate, M.; Abe, M.; Kasahara, K.; Iwabuchi, K.; Umeda, M.; Kobayashi, T. *J. Cell Sci.* **2015**, *128*, 1627−1638.

(28) Lorent, J. H.; Levental, K. R.; Ganesan, L.; Rivera-Longsworth, G.; Sezgin, E.; Doktorova, M.; Lyman, E.; Levental, I. *Nat. Chem. Biol.* **2020**, *16*, 644−652.

(29) Wu, Y. L.; Stefl, M.; Olzynska, A.; Hof, M.; Yahioglu, G.; Yip, P.; Casey, D. R.; Ces, O.; Humpolickova, J.; Kuimova, M. K. *Phys. Chem. Chem. Phys.* **2013**, *15*, 14986−14993.

(30) Amaro, M.; Reina, F.; Hof, M.; Eggeling, C.; Sezgin, E. *J. Phys. D: Appl. Phys.* **2017**, *50*, No. 134004.

(31) Zhang, Y. L.; Frangos, J. A.; Chachisvilis, M. *Biochem. Biophys. Res. Commun.* **2006**, *347*, 838−841.

(32) Bagatolli, L. A. *Biochim. Biophys. Acta, Biomembr.* **2006**, *1758*, 1541−1556.

(33) Kucherak, O. A.; Oncul, S.; Darwich, Z.; Yushchenko, D. A.; Arntz, Y.; Didier, P.; Mely, Y.; Klymchenko, A. S. *J. Am. Chem. Soc.* **2010**, *132*, 4907−4916.

(34) Weber, G.; Farris, F. J. *Biochemistry* **1979**, *18*, 3075−3078.

(35) Owen, D. M.; Rentero, C.; Magenau, A.; Abu-Siniyeh, A.; Gaus, K. *Nat. Protoc.* **2012**, *7*, 24−35.

(36) Kim, H. M.; Choo, H. J.; Jung, S. Y.; Ko, Y. G.; Park, W. H.; Jeon, S. J.; Kim, C. H.; Joo, T.; Cho, B. R. *ChemBioChem* **2007**, *8*, 553−559.

(37) Jin, L.; Millard, A. C.; Wuskell, J. P.; Dong, X. M.; Wu, D. Q.; Clark, H. A.; Loew, L. M. *Biophys. J.* **2006**, *90*, 2563−2575.

(38) Bongiovanni, M. N.; Godet, J.; Horrocks, M. H.; Tosatto, L.; Carr, A. R.; Wirthensohn, D. C.; Ranasinghe, R. T.; Lee, J. E.; Ponjavic, A.; Fritz, J. V.; Dobson, C. M.; Klenerman, D.; Lee, S. F. *Nat. Commun.* **2016**, *7*, No. 13544.
(39) Danylchuk, D. I.; Moon, S.; Xu, K.; Klymchenko, A. S. *Angew. Chem., Int. Ed.* **2019**, *58*, 14920−14924.
(40) Niko, Y.; Didier, P.; Mely, Y.; Konishi, G.; Klymchenko, A. S. *Sci. Rep.* **2016**, *6*, No. 18870.
(41) Valanciunaite, J.; Kempf, E.; Seki, H.; Danylchuk, D. I.; Peyriéras, N.; Niko, Y.; Klymchenko, A. S. *Anal. Chem.* **2020**, *92*, 6512−6520.
(42) Mazeres, S.; Joly, E.; Lopez, A.; Tardin, C. *F1000Res* **2014**, *3*, 172.
(43) Collot, M.; Ashokkumar, P.; Anton, H.; Boutant, E.; Faklaris, O.; Galli, T.; Mély, Y.; Danglot, L.; Klymchenko, A. S. *Cell Chem. Biol.* **2019**, 600−614.
(44) Brouwer, A. M. *Pure Appl. Chem.* **2011**, *83*, 2213−2228.
(45) Sakai, K.; Kaji, M.; Takamatsu, Y.; Tsuchiya, K.; Torigoe, K.; Tsubone, K.; Yoshimura, T.; Esumi, K.; Sakai, H.; Abe, M. *Colloids Surf., A* **2009**, *333*, 26−31.
(46) Sezgin, E.; Kaiser, H. J.; Baumgart, T.; Schwille, P.; Simons, K.; Levental, I. *Nat. Protoc.* **2012**, *7*, 1042−1051.
(47) Sezgin, E.; Waithe, D.; Bernardino de la Serna, J.; Eggeling, C. *ChemPhysChem* **2015**, *16*, 1387−1394.
(48) Sezgin, E.; Gutmann, T.; Buhl, T.; Dirkx, R.; Grzybek, M.; Coskun, U.; Solimena, M.; Simons, K.; Levental, I.; Schwille, P. *PLoS One* **2015**, *10*, No. e0123930.
(49) Daly, B.; Ling, J.; de Silva, A. P. *Chem. Soc. Rev.* **2015**, *44*, 4203−4211.
(50) Dalvi-Malhotra, J.; Chen, L. *J. Phys. Chem. B* **2005**, *109*, 3873−3878.
(51) Sun, L.-c.; Yang, Y.-f.; He, J.-j.; Shen, T. *Dyes Pigm.* **1995**, *28*, 275−279.
(52) Liu, J.-X.; Zhou, Q.-F.; Xu, H.-J. *Chin. J. Chem.* **2010**, *11*, 120−125.
(53) Pantazis, A.; Westerberg, K.; Althoff, T.; Abramson, J.; Olcese, R. *Nat. Commun.* **2018**, *9*, No. 4738.
(54) Sezgin, E.; Levental, I.; Grzybek, M.; Schwarzmann, G.; Mueller, V.; Honigmann, A.; Belov, V. N.; Eggeling, C.; Coskun, U.; Simons, K.; Schwille, P. *Biochim. Biophys. Acta, Biomembr.* **2012**, *1818*, 1777−1784.
(55) Kaiser, H. J.; Lingwood, D.; Levental, I.; Sampaio, J. L.; Kalvodova, L.; Rajendran, L.; Simons, K. *Proc. Natl. Acad. Sci. U.S.A.* **2009**, *106*, 16645−16650.
(56) Zidovetzki, R.; Levitan, I. *Biochim. Biophys. Acta, Biomembr.* **2007**, *1768*, 1311−1324.
(57) Liu, S.-L.; Sheng, R.; Jung, J. H.; Wang, L.; Stec, E.; O'Connor, M. J.; Song, S.; Bikkavilli, R. K.; Winn, R. A.; Lee, D.; Baek, K.; Ueda, K.; Levitan, I.; Kim, K.-P.; Cho, W. *Nat. Chem. Biol.* **2017**, *13*, 268−274.

https://dx.doi.org/10.1021/acs.analchem.0c03559
Anal. Chem. 2020, 92, 14798−14805

Supporting information

Redesigning solvatochromic probe Laurdan for imaging lipid order selectively in cell plasma membranes

Dmytro I. Danylchuk,[1‡] Erdinc Sezgin,[2, 3‡] Philippe Chabert[1] and Andrey S. Klymchenko[1*]

[1] Laboratoire de Bioimagerie et Pathologies, UMR 7021 CNRS, Université de Strasbourg, 74 route du Rhin, 67401, Illkirch, France
[2] MRC Human Immunology Unit, Weatherall Institute of Molecular Medicine, University of Oxford, Headley Way, Oxford OX3 9DS, UK
[3] Science for Life Laboratory, Department of Women's and Children's Health, Karolinska Institutet, Stockholm, Sweden
*E-mail: andrey.klymchenko@unistra.fr
‡These authors contributed equally to the work.

EXPERIMENTAL

Synthesis of quencher dodecyl viologen (Viologen-C12). (Adapted from[1])

1-Dodecyl-4-(1-dodecylpyridin-1-ium-4-yl)pyridin-1-ium iodide. 0.63 g of 4,4`-bipyridine were dissolved in 20 mL of dry acetonitrile together with 3.59 g (3 mL, 3 equiv.) of n-dodecyl iodide. The reaction mixture was refluxed for 20h (control by TLC). After the reaction the mixture was diluted twice with diethyl ether and the solids were filtered off and washed with Et_2O on a glass filter. The crude product was recrystallized from EtOH:H_2O 1:1 mixture. Yield 2.45 g (81%) as lustrous reddish crystals. **^{1}H NMR** (400 MHz, DMSO-d_6) δ ppm 9.38 (d, *J*=6.5 Hz, 4 H) 8.78 (d, *J*=6.5 Hz, 4 H) 4.68 (t, *J*=7.4 Hz, 4 H) 1.97 (br t, *J*=6.3 Hz, 4 H) 1.34 - 1.19 (m, 36 H) 0.85 (t, *J*=6.8 Hz, 6 H).

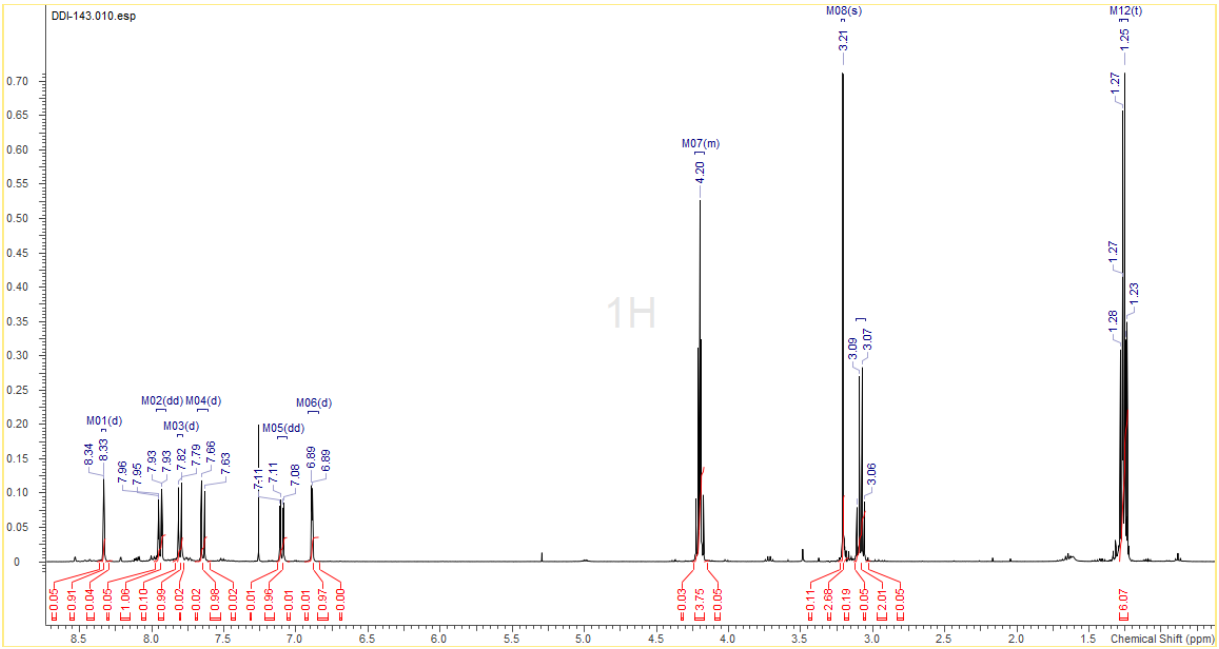

Figure S1. ^{1}H NMR spectrum of **2a** in $CDCl_3$.

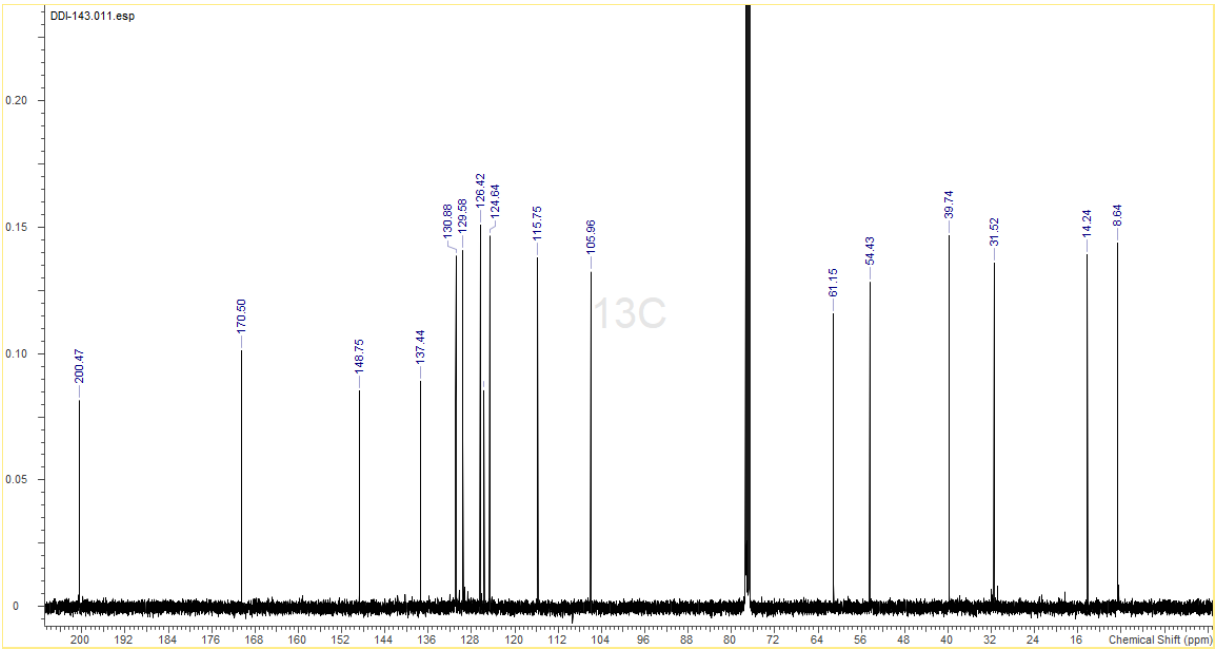

Figure S2. ^{13}C NMR spectrum of **2a** in $CDCl_3$.

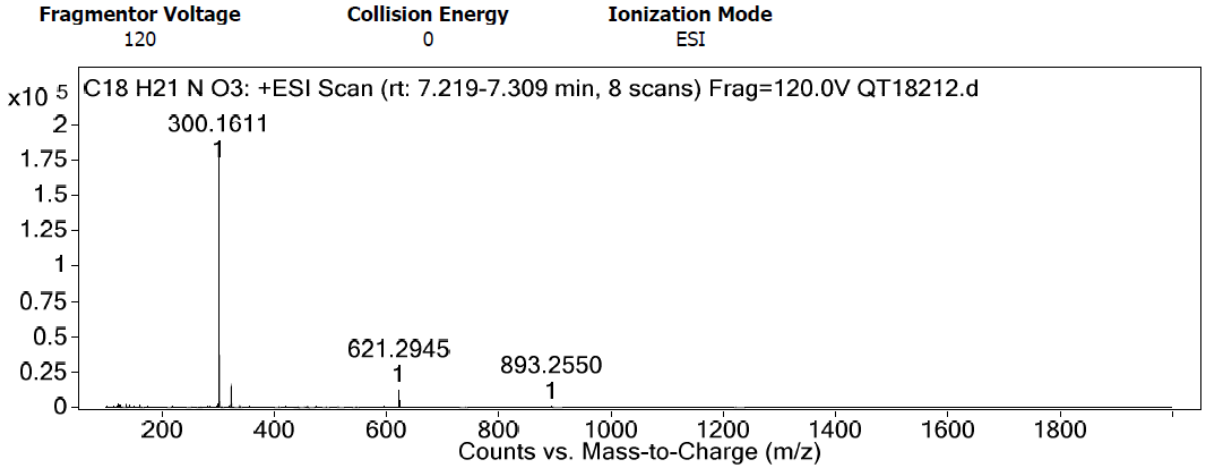

Figure S3. HRMS (ESI+) of **2a**.

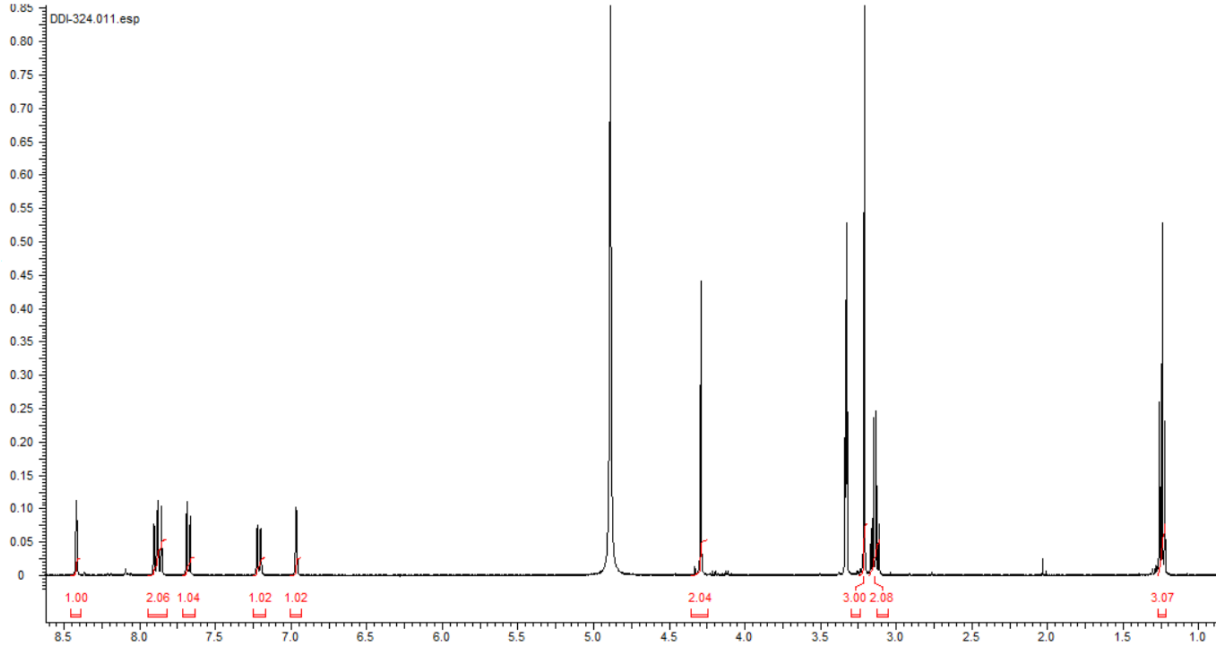

Figure S4. ^{1}H NMR spectrum of **3a** in CD_3OD.

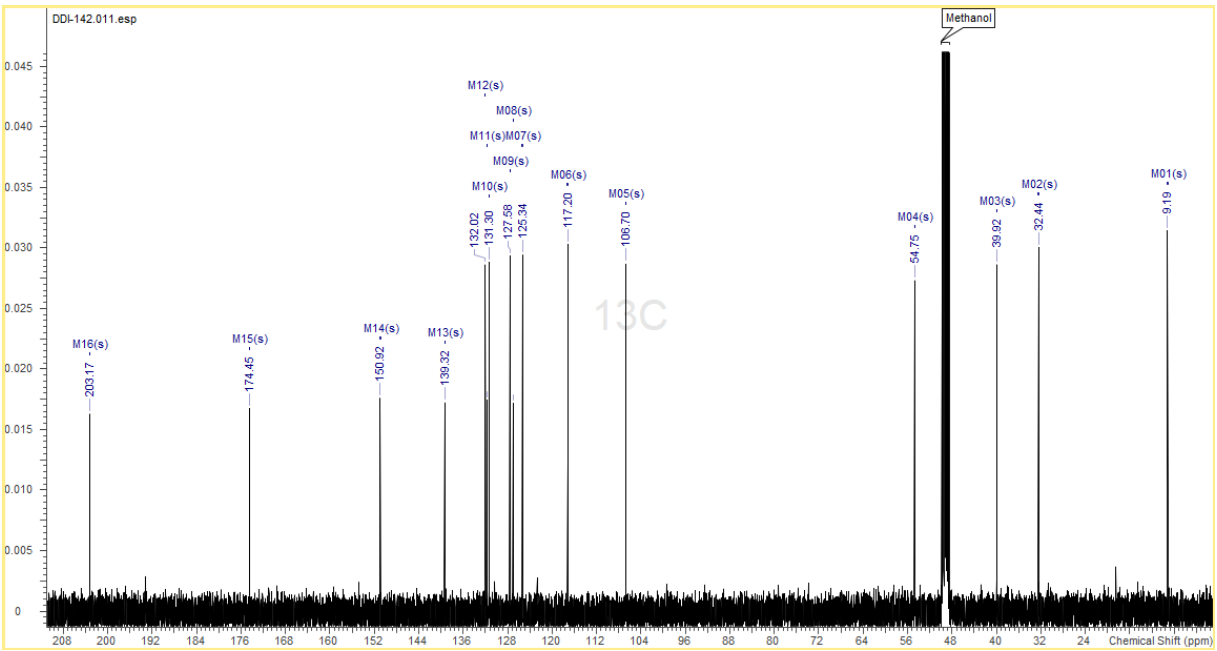

Figure S5. ^{13}C NMR spectrum of **3a** in CD_3OD.

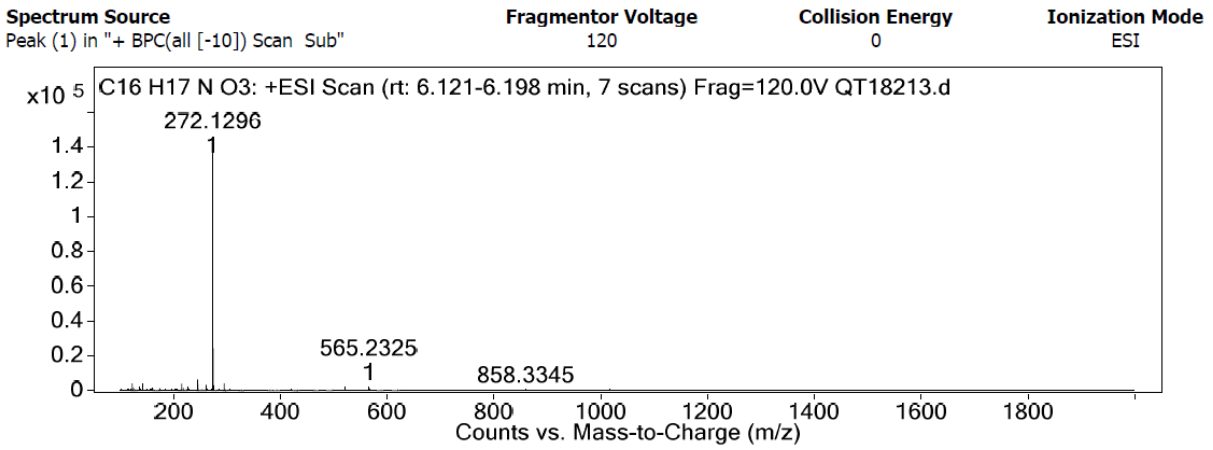

Figure S6. HRMS (ESI+) of **3a**.

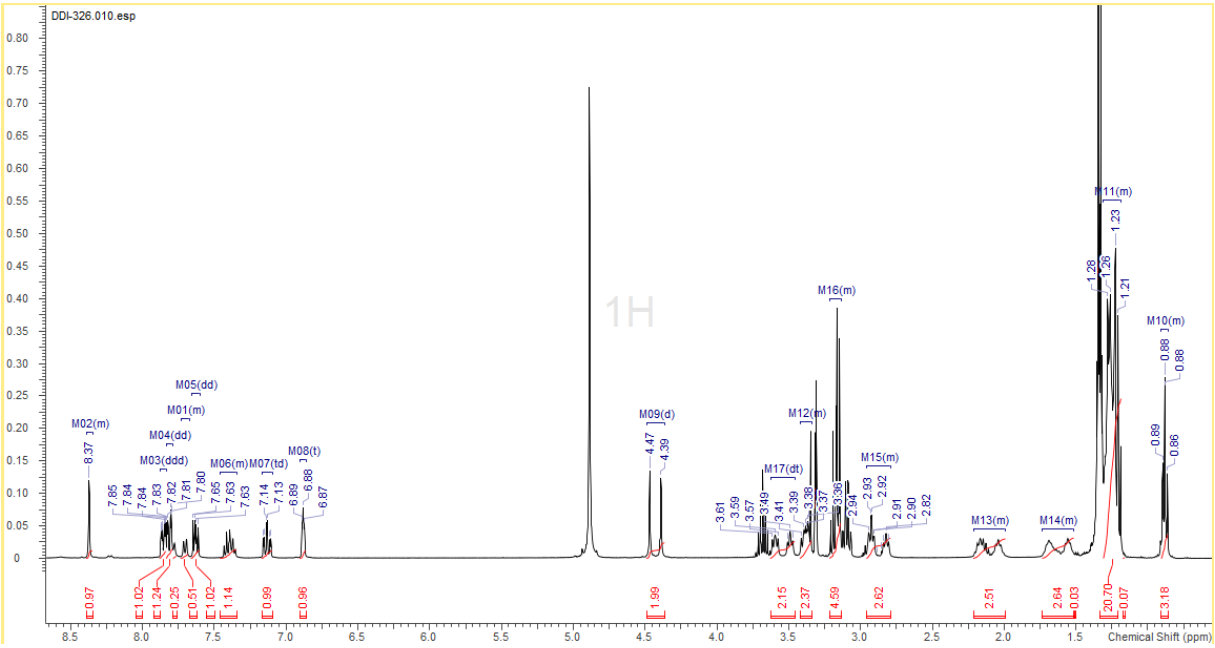

Figure S7. ^{1}H NMR spectrum of **Pro12A** in CD_3OD.

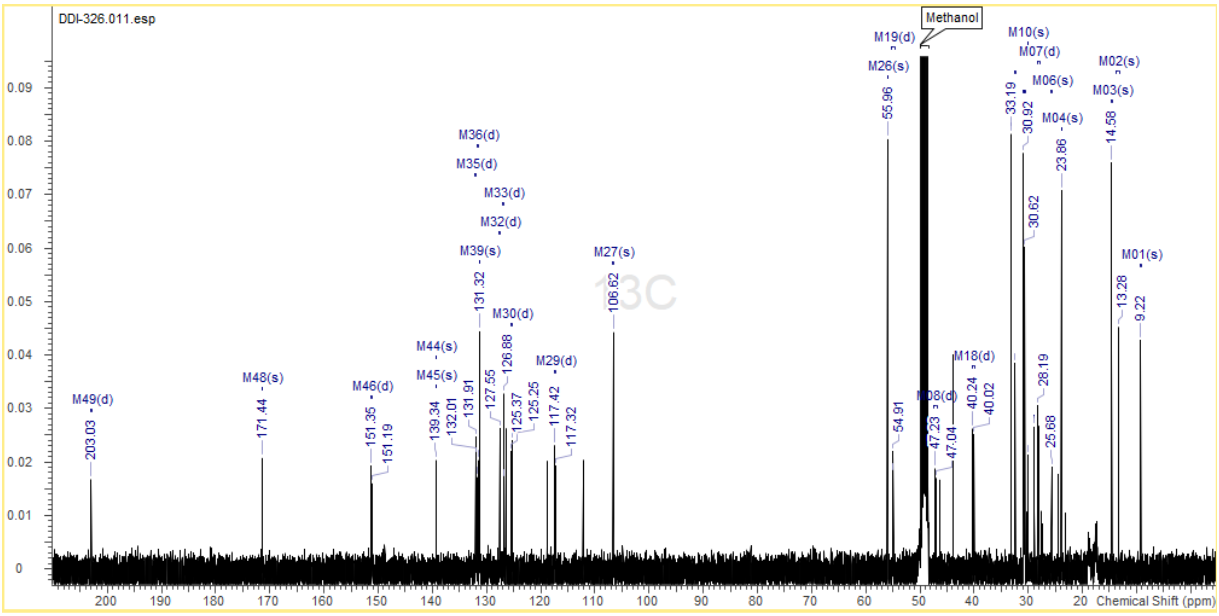

Figure S8. ^{13}C NMR spectrum of **Pro12A** in CD_3OD.

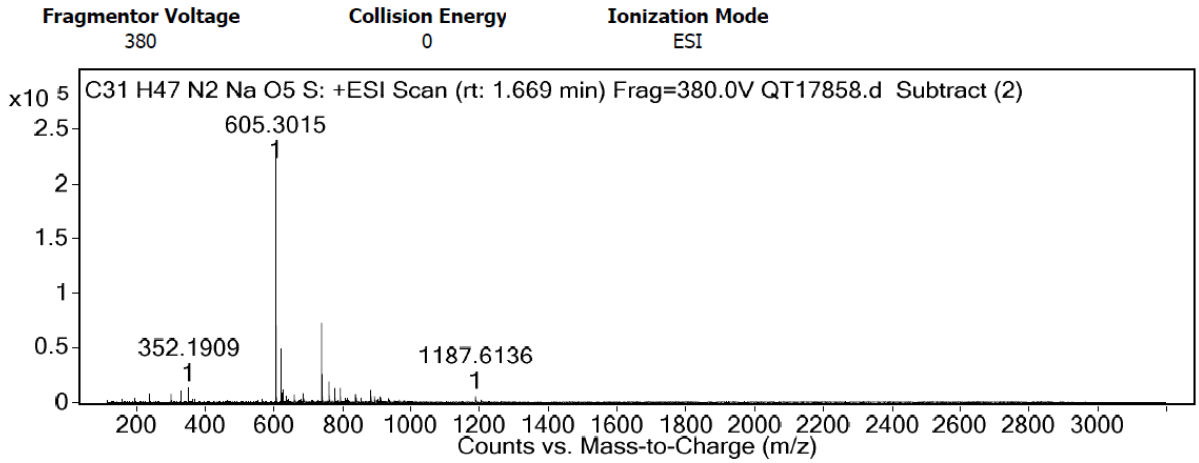

Figure S9. HRMS (ESI+) of **Pro12A**.

RESULTS

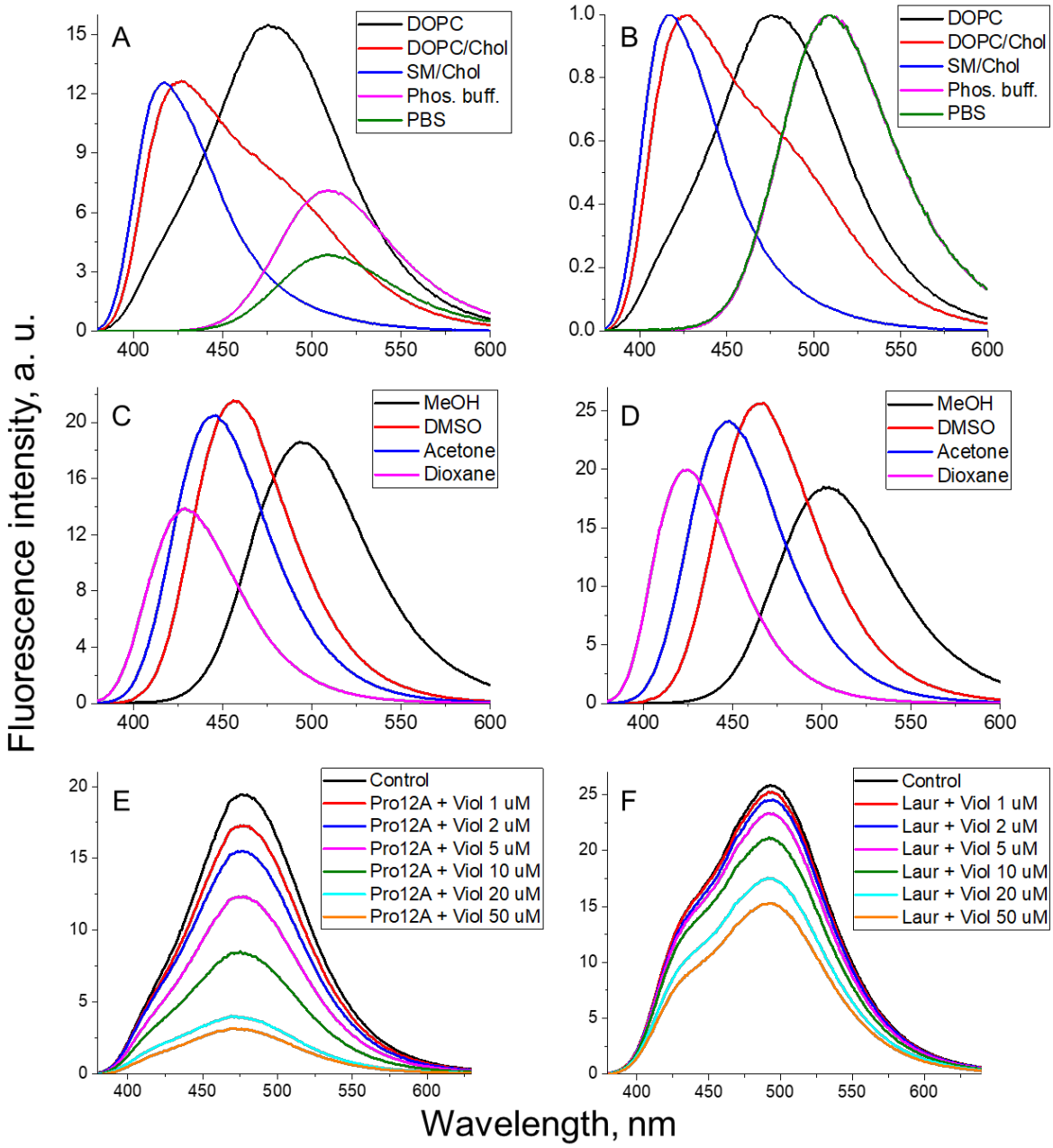

Figure S10. Fluorescence emission spectra of Pro12A in solvents and lipid vesicles of different composition: raw data (A) and normalized spectra (B); spectra of Pro12A (C) and Laurdan (D) in different solvents. Emission spectra of Pro12A (E) and Laurdan (F) in DOPC LUVs upon addition of different concentrations of dodecyl viologen. Probe concentration was 2 μM for (A-D) and 1 μM for (E-F). λ_{ex} = 360 nm in all cases. Total lipid concentration was 1 mM for all vesicles in (A-B) and 500 μM for (E-F).

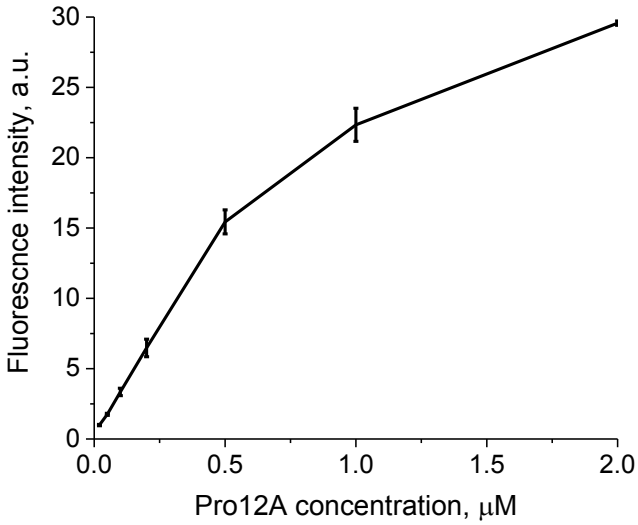

Figure S11. Fluorescence emission intensity of Pro12A at different concentrations in PBS. Excitation wavelength was 360 nm. The fluorescence intensity was recorded at the emission maximum. A deviation from the linear intensity increase is observed around 0.5 μM, indicating that around this concentration the dye starts forming micelles (critical micellar concentration), which leads to self-quenching.

Table S1. Fluorescence properties of probes in liposomes of different composition and organic solvents.[a]

Solvent or medium	Probe					
	Pro12A			Laurdan		
	λ_{abs}, nm	λ_{em}, nm	QY, %	λ_{abs}, nm	λ_{em}, nm	QY, %
DOPC	372	476	54.4	356[c]	488[c]	25[c]
DOPC/Chol	374	427	69.6	358[c]	439[c]	21[c]
SM/Chol	379	417	51.5	357[c]	435[c]	19[c]
PB[b]	371	509	25.2	-	-	-
PBS	369	509	12.5	-	-	-
Dioxane	349	429	42.9	348	425	38.8
Acetone	354	446	55.9	350	448	45.5
DMSO	359	456	54.5	359	467	67.9
MeOH	359	493	55.5	363	501	43.1

[a] Probe concentrations were 2 μM. For liposomes total lipid concentration was 1 mM. Data for Laurdan in PB and PBS is not presented due to its insufficient solubility in aqueous media. Fluorescence quantum yields were measured using quinine sulfate in 0.5 M sulfuric acid (λ_{ex}= 360 nm, QY_{ref} = 54.6%)[2] as a reference.
[b] PB – 20 mM phosphate buffer, pH 7.4.
[c] Data taken from.[3]

REFERENCES

(1) Grenier, M. C.; Davis, R. W.; Wilson-Henjum, K. L.; LaDow, J. E.; Black, J. W.; Caran, K. L.; Seifert, K.; Minbiole, K. P. The antibacterial activity of 4,4'-bipyridinium amphiphiles with conventional, bicephalic and gemini architectures. *Bioorg. Med. Chem. Lett.* **2012**, *22*, 4055-4058.
(2) Brouwer, A. M. Standards for photoluminescence quantum yield measurements in solution (IUPAC Technical Report). *Pure Appl. Chem.* **2011**, *83*, 2213-2228.
(3) Niko, Y.; Didier, P.; Mely, Y.; Konishi, G.; Klymchenko, A. S. Bright and photostable push-pull pyrene dye visualizes lipid order variation between plasma and intracellular membranes. *Sci. Rep.* **2016**, *6*, 18870.

2.2. Development of solvatochromic plasma membrane probes, compatible with super-resolution live cell microscopy

During the next part of our research we aimed to create a plasma membrane-targeted solvatochromic probe for super-resolution microscopy. Nile Red fluorophore system was chosen as the basis for functionalization as the parent Nile Red dye being successfully utilized in spectrally resolved PAINT with live cells.[275, 276]

In order to increase the photostability of our Nile Red probes, we decided to develop a functionalization strategy using the N-alkyl chain of Nile Red. We hypothesized that an introduction of phenolic oxygen, previously used for design of membrane probe NR12S (Fig. 2.2.1, A),[15] might be responsible for a decrease in its photostability compared to the parent unsubstituted dye.

To design a probe with ON/OFF behavior, we have decided to decrease the length of alkyl chain in the targeting group (Fig. 2.2.1, A), which could provide low-affinity reversible binding to the lipid membrane (Fig. 2.2.1, B). As a result, two probes were created: NR12A with high affinity to membranes for conventional microscopy, and NR4A, a low-affinity probe for PAINT SMLM (Fig. 2.2.1, A-B).

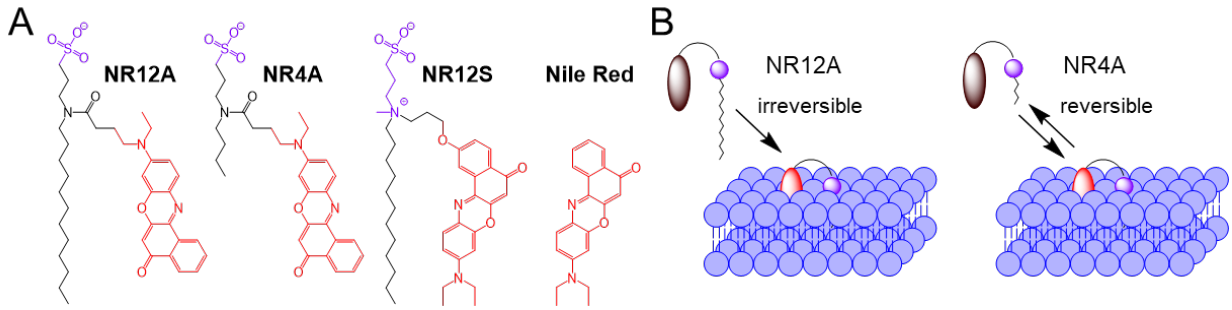

Fig. 2.2.1. Structure (A) and mechanism of membrane binding (B) of NR12A and NR4A.

The synthesis of the Nile Red probes was performed in 6 steps with overall yield of 2 % (NR12A) and 3 % (NR4A), using m-amizidine as a starting material (Fig. 2.2.2). The overall yield could be possibly improved by changing the purification procedure for a key intermediate 5a.

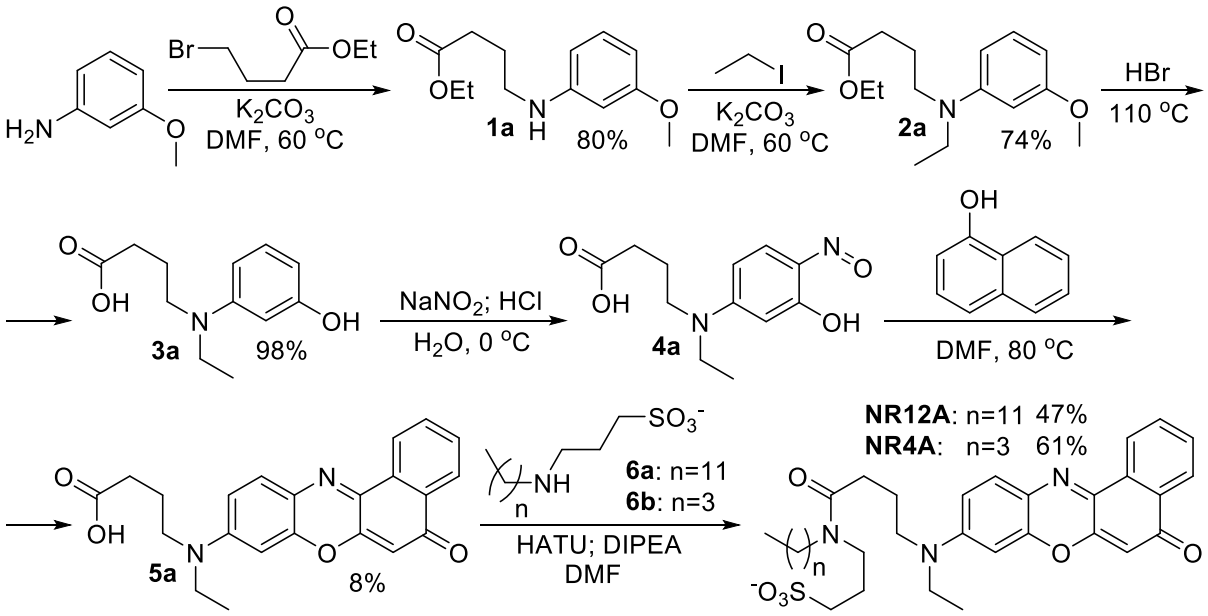

Fig. 2.2.2. Synthesis schemes of Nile Red solvatochromic plasma membrane probes.

Spectroscopic experiments in large unilamellar vesicles (LUVs) of varied composition showed that the functionalization did not perturb the fluorophore properties. Fluorescence spectra of both NR4A and NR12A exhibited a blue shift of around 45-50 nm in Lo phase vesicles, composed of sphingomyelin/cholesterol (SM/Chol), compared to Ld phase vesicles, made of dioleoylphosphatidylcholine (DOPC) (Fig. 2.2.3, A). This behavior is similar to NR12S[15] and parent Nile Red and reflects lower local polarity/hydration in the Lo phase. The fluorescence of NR12A in phosphate buffer was negligible (Fig. 2.2.3, A), indicating the formation of self-quenched aggregates in water. On the contrary, the probe NR4A exhibited a non-negligible red-shifted fluorescence (Fig. 2.2.3, A), similarly to parent Nile Red, suggesting that NR4A is well dissolved and does not form aggregates in water.

Ratiometric microscopy imaging revealed that both new probes are able to distinguish between the domains with different lipid order in giant unilamellar vesicles (GUVs) (Fig. 2.2.3, B). The fluorescence emission was collected at two different channels: I_1 (550-600 nm) and I_2 (600-650 nm), which were used to generate ratiometric (I_1/I_2) microscopy images. Notably, the probe NR12A and NR4A showed higher sensitivity towards the differences in lipid order in the different domains compared to NR12S (Fig. 2.2.3, B), possibly due to an improved probe localization in the bilayer.

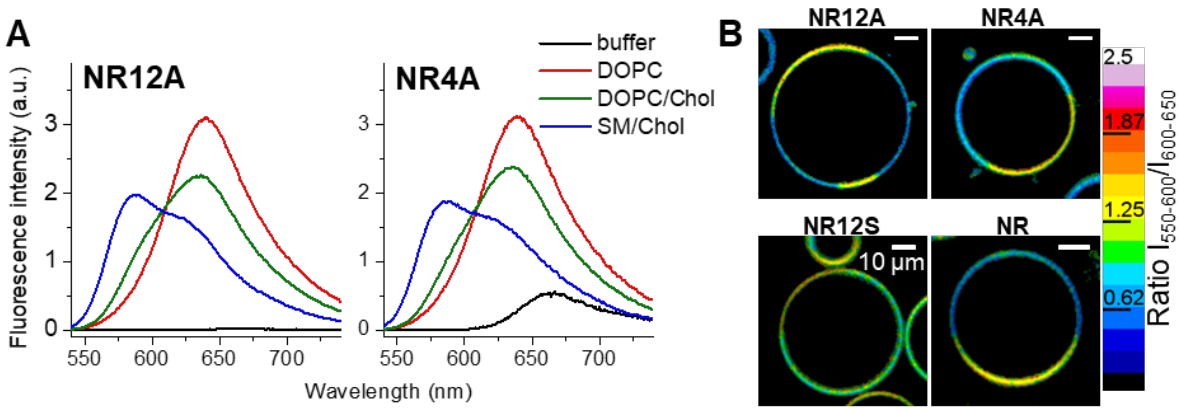

Fig. 2.2.3. Solvatochromic Nile Red probes sensing differences in lipid order in model membranes. Fluorescence emission spectra of Nile Red probes (2 µM) in LUVs of different composition (A). Total phospholipid concentration was 1 mM. Excitation wavelength was 520 nm. All the spectra were corrected via dividing by absorbance at the excitation wavelength. Ratiometric confocal microscopy images of mixed lipid phase GUVs (DOPC:Sph:Chol 1:1:0.7) stained with NR12A, NR4A, NR12S, and Nile Red (B). Excitation wavelength was 488 nm. Probe concentration was systematically 200 nM.

Both probes showed an increase in fluorescence intensity (fluorogenic response) upon binding to the LUVs composed of DOPC, however there was a strong variation in the titration curves (Fig. 2.2.4, A). The affinity of NR12A to the LUVs was much higher compared to parent Nile Red, displaying rapid intensity growth followed by a plateau at higher concentrations. On the contrary, NR4A showed only a moderate fluorescence intensity increase in response to higher concentrations of LUVs, weaker than the unsubstituted Nile Red. These results confirm that we have developed a high-affinity (NR12A) and a low-affinity (NR4A) lipid membrane binders.

The photostability of our probes was checked in DOPC LUVs against NR12S and unsubstituted Nile Red (Fig. 2.2.4, B). Both probes exhibited higher photostability compared to the parent Nile Red and the NR12S probe, confirming our hypothesis that an introduction of the phenolic oxygen has a detrimental effect on the photostability of Nile Red fluorophore. Remarkably, probe NR4A displayed virtually no fluorescence intensity decrease upon continuous illumination, further evidencing the reversible character of its binding.

Single-molecule microscopy experiments with the probes in supported DOPC lipid bilayers showed that NR4A and Nile Red, which are the weak binders, exhibited large number of single-molecule turn-on events that lasted well through $>10^4$ frames (Fig. 2.2.4, C), thanks to the continuous probe exchange between the solution and the membrane. In contrast, the strong binders NR12A and NR12S showed few turn-on events (Fig. 2.2.4, C), probably because most of the molecules, being quasi-irreversibly bound to the membrane, photobleached before single-molecule images could be recorded.

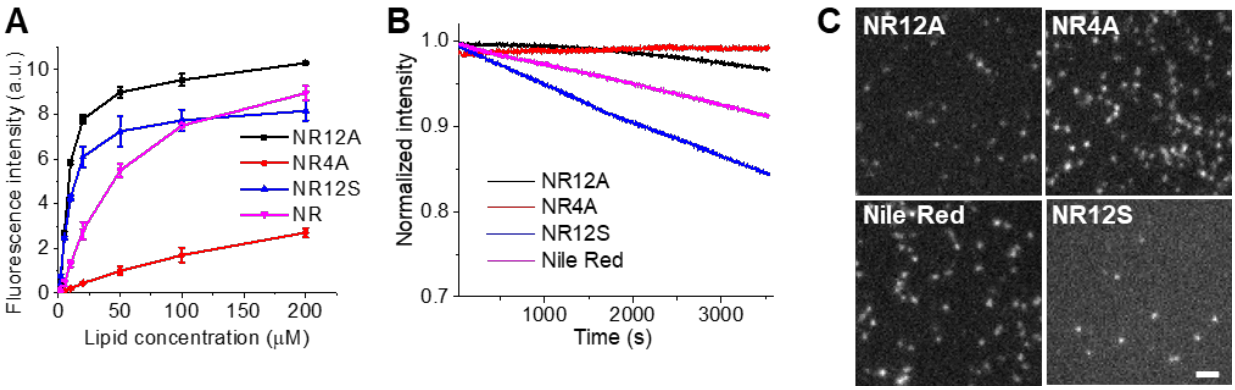

Fig. 2.2.4. Titration of the four membrane probes (100 nM) with increasing concentrations of DOPC LUVs: fluorescence intensity at 620 nm vs. lipid concentration (A). Fluorescence intensity of the different probes (400 nM) under continuous illumination vs. time in DOPC liposomes (200 μM) (B). Excitation and emission wavelengths were 540 and 620 nm, respectively. Typical single-molecule raw images of the four probes in DOPC supported bilayers (C). The images were recorded at 9 ms integration time (110 frames per second), probe concentration was 10 nM in all cases.

On the next step, the Nile Red probes were incubated with live HeLa cells and imaged using confocal fluorescence microscopy (Fig. 2.2.5). Both probes NR4A and NR12A stained exclusively the plasma membrane, while the unsubstituted Nile Red underwent rapid internalization, which resulted in indiscriminate staining of all cell lipid components (Fig. 2.2.5, A). Additionally, NR12A yielded >2-fold brighter fluorescence intensity compared to zwitterionic NR12S probe. The signal from NR4A was >10-fold lower than for NR12A, in line with the previous results suggesting its weak affinity to biomembranes. Photobleaching experiments further proved that both new probes are more photostable compared to NR12S, supporting the usefulness of the designed functionalization strategy (Fig. 2.2.5, B). Notably, only NR4A revealed no sign of photobleaching after continuous illumination (Fig. 2.2.5, B), which confirmed that the probe binds to cell membranes in a reversible manner, so that the bleached probe species are quickly replaced by intact ones, being in line with the requirements for PAINT. On the other hand, the high brightness and PM specificity of NR12A makes it suitable for conventional microscopy techniques, such as 3D z-stacked confocal imaging (2.2.5, C).

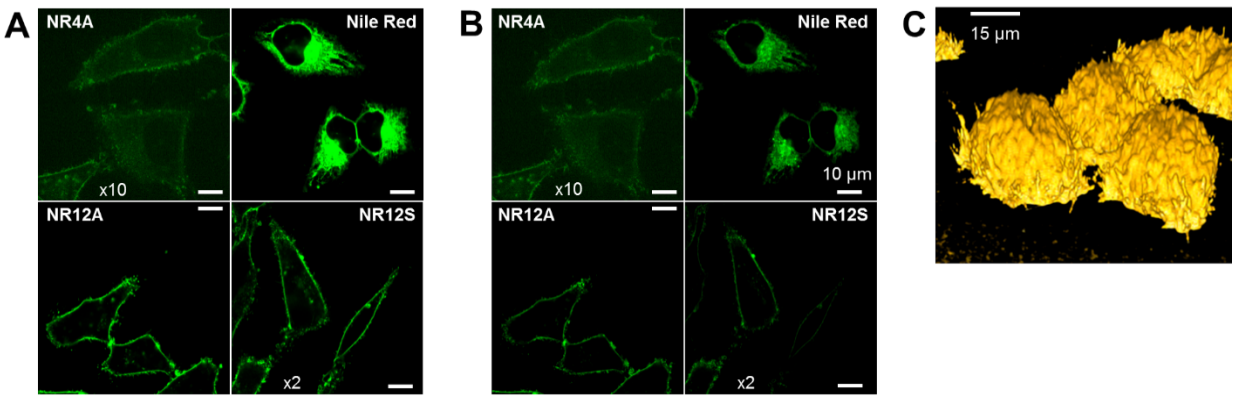

Fig. 2.2.5. Live cell microscopy imaging with Nile Red probes. Spinning disk confocal microscopy images of HeLa cells stained with NR4A, NR12A, Nile Red and NR12S before illumination (A) and immediately after (B) 60 seconds of illumination with 550 nm light at 3.14 $W \cdot cm^{-2}$. 3D-stacked confocal image of live KB cells stained with NR12A (C). Dye concentration was 20 nM in all cases.

3D PAINT super-resolution imaging of live cells was performed using NR4A, NR12S and Nile Red (Fig.2.2.6). In case of NR4A with reversible binding, the quality of the image was high due to the high counts of single molecules over 5×10^4 imaging frames. In contrast, the signal from NR12S was low because of low counts of single molecules due to strong binding and lower photostability, together resulting in a very dim reconstructed PAINT image. Though the quality of the final image in case of Nile Red was decent, the probe strongly labelled the internal membranes in a cell, in line with previous microscopy data (Fig. 2.2.5, A).

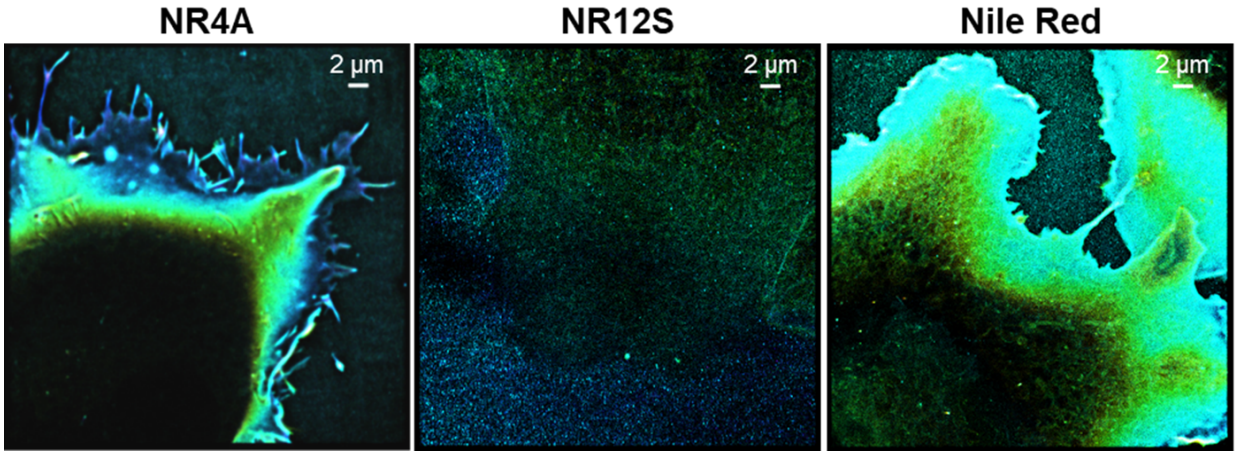

Fig. 2.2.6. Zoom-out views of 3D PAINT images of COS-7 cells with NR4A, NR12S, and Nile Red. Probe concentration was 10 nM for NR4A and Nile Red and 20 nM for NR12S.

Due to the high plasma membrane specificity of NR4A together with its high performance in PAINT it became possible to visualize the rich nanoscale structural features of the plasma membrane (Fig. 2.2.7). 3D PAINT microscopy in live HeLa cells showed numerous outward curves of the PM, including: mildly bulging sites that raised up ~100 nm in height over ~1 µm lateral distances (Fig. 2.2.7, B-C); tube-like protrusions with higher curvatures (~100 nm radius; Fig. 2.2.7, B and D); and tall protrusions above the limit of the working z range (>400 nm above the focal plane), so that they appear dark at the center (Fig. 2.2.7, B and E). A characteristic feature of these nanoscale protrusions was their highly dynamic character, resulting is significant structural changes within the time scale of 1 minute. Additionally, the PM also featured pit-like invaginations with the size *ca* 150-200 nm (Fig. 2.2.7, B and F), which dynamically (in the timescale of minutes) moved inside the cell (Fig. 2.2.7, G).

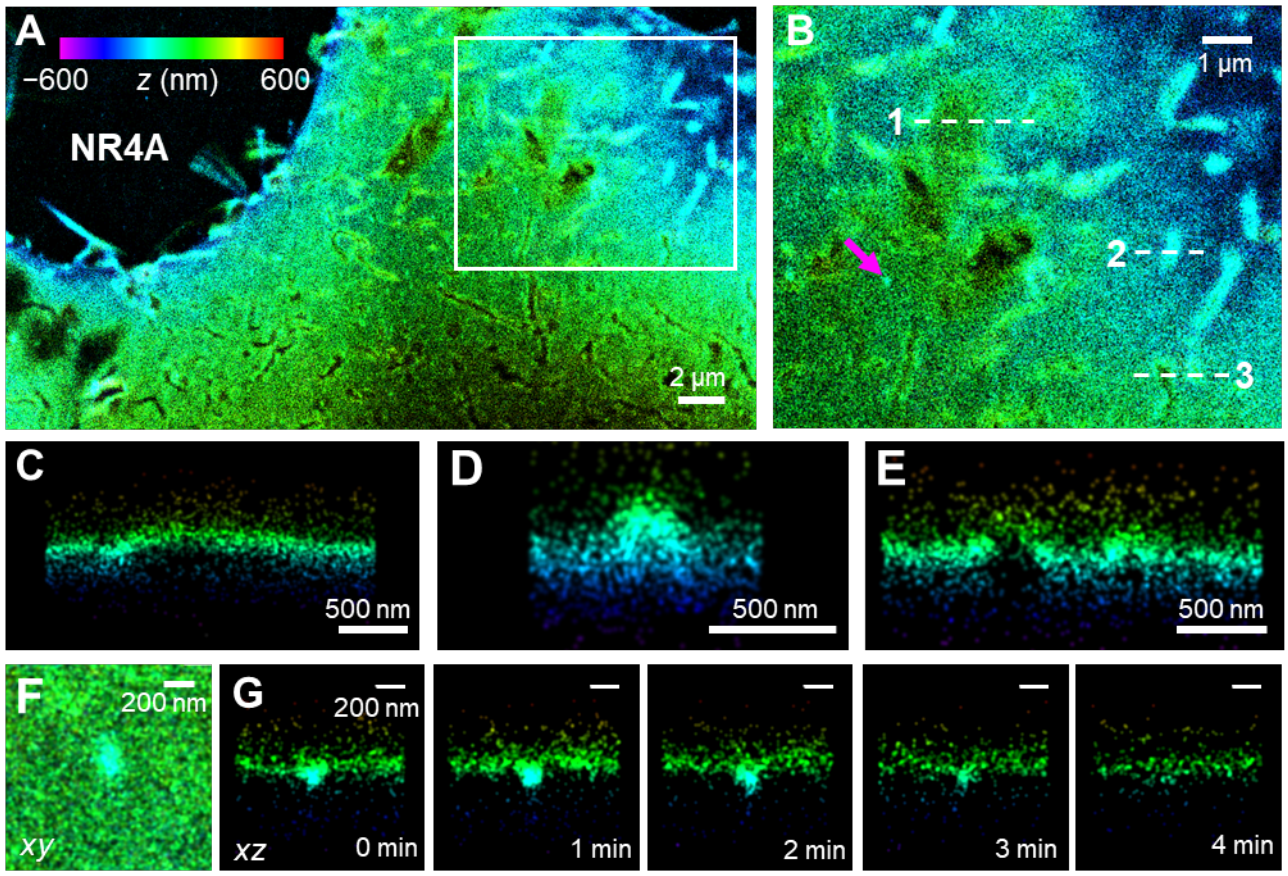

Fig. 2.2.7. Probe NR4A used for super-resolution live cell membrane imaging. (A) 3D PAINT image of the top plasma membrane of a HeLa cell stained by NR4A; (B) Zoom-in image of the white box in (A); (C-D) Virtual cross sections in the xz plane along lines 1-3 in (B), respectively; (F) Zoom-in image in-plane (xy) and (G) a time series of the vertical (xz) images of the endocytosis site marked by the magenta arrow in the image (B). All 3D PAINT images are rendered with color to present the depth (z) information (the colour scale bar is represented in (A)).

On the next stage we utilized environment-sensitive behaviour of NR4A to study the nanoscale distribution of lipid order in plasma membrane. During a spectrally resolved PAINT experiment a super-localized position of every single molecule of NR4A was measured together with its fluorescence spectrum. The calculated intensity-weighted average of the emission wavelengths of each probe molecule, *i.e.* its spectral mean, can be presented in pseudo-colour and allows to describe the local lipid order with nanoscopic precision.[276] In live COS-7 cells, stained with NR4A, the obtained pseudocolour varied from blue to cyan (Fig. 2.2.8, A-B) with the corresponding averaged single-molecule spectra of NR4A peaked at ~610 nm (Fig. 2.2.8, D-E). Remarkably, both the tube-like nanoscale protrusions (Fig. 2.2.8, A) and invaginations (Fig. 2.2.8, B) of the PM cause a bathochromic shift in the local spectral mean (Fig. 2.2.8, D-E), indicating a lower lipid order in the regions of increased membrane curvature. The relation between the membrane curvature formation and the lipid composition is also suggested in the recent works.[282, 283] Upon the chemical fixation the probe NR4A was able to enter the cell through a compromised plasma membrane, staining the intracellular membrane structures (Fig. 2.2.8, C) with a distinct

~20 nm bathochromic shift in emission (Fig. 2.2.8, F). This result indicates lower lipid order of the organelle membranes compared to PM.

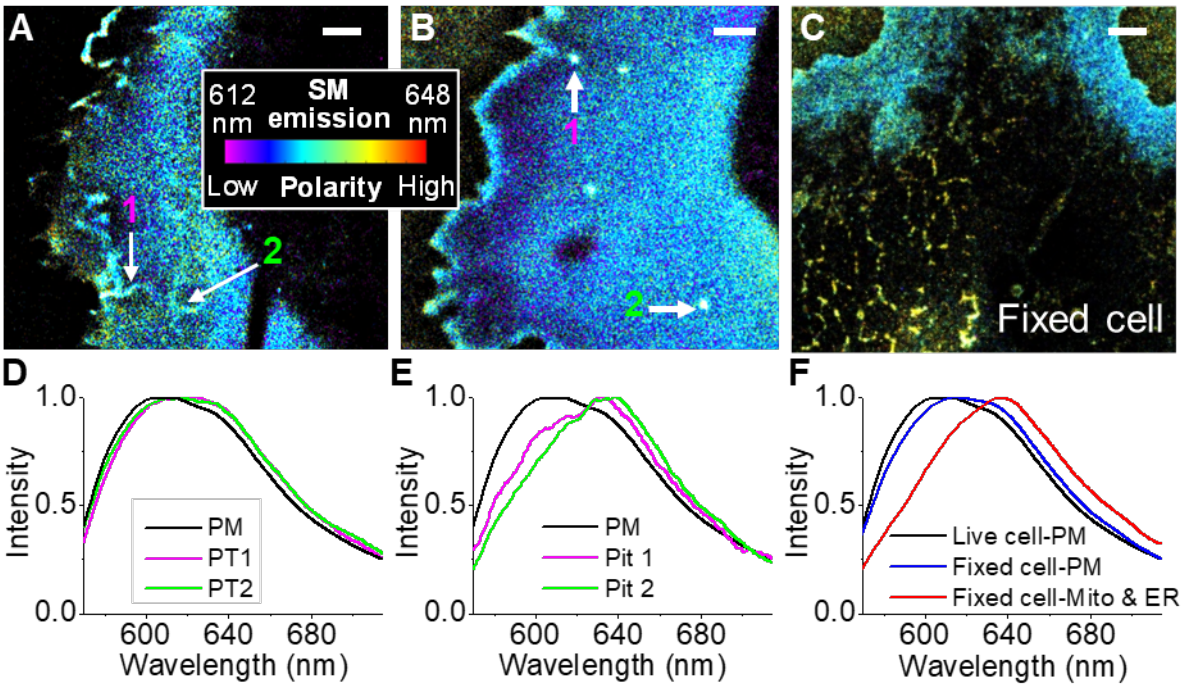

Fig. 2.2.8. Nanoscopic mapping of lipid order in cell membranes with NR4A. (A, B) Spectrally resolved PAINT images of the plasma membrane of live COS-7 cells, stained with NR4A The colour represents a single-molecule spectral mean (coded by the colour scale bar). (C) Spectrally resolved PAINT images of the plasma membrane of fixed COS-7 cells with NR4A, revealing staining for both the plasma membrane and internal membranes. (D) Averaged single-molecule spectra for the smooth parts of the plasma membrane (black) compared with the ones for the tube-like protrusions pointed to by the two arrows in (A) (magenta and green). (E) Averaged single-molecule spectra for the smooth parts of the plasma membrane (black) compared with the ones for the tube-like protrusions pointed to by the two arrows in (B) (magenta and green). (F) Averaged single-molecule spectra for the plasma membrane of live (black) and fixed (blue) COS-7 cells, compared with the ones for the internal membranes of fixed COS-7 cells (red).

Single-molecule experiments and super-resolution microscopy was performed in collaboration with the team of Ke Xu. The results of the project were published in *Angewandte Chemie international edition*, the article is enclosed herewith (Article 2).

A Journal of the Gesellschaft Deutscher Chemiker

Angewandte International Edition Chemie

GDCh

www.angewandte.org

Accepted Article

Title: Tailor-made switchable solvatochromic probes for live-cell super-resolution imaging of plasma membrane organization

Authors: Dmytro I. Danylchuk, Seonah Moon, Ke Xu, and Andrey S Klymchenko

To be cited as: *Angew. Chem. Int. Ed.* 10.1002/anie.201907690
Angew. Chem. 10.1002/ange.201907690

Link to VoR: http://dx.doi.org/10.1002/anie.201907690
http://dx.doi.org/10.1002/ange.201907690

WILEY-VCH

10.1002/anie.201907690

WILEY-VCH

COMMUNICATION

Tailor-made switchable solvatochromic probes for live-cell super-resolution imaging of plasma membrane organization

Dmytro I. Danylchuk,[a]‡ Seonah Moon,[b], [c]‡ Ke Xu,[b], [c]* Andrey S. Klymchenko[a]*

Abstract: Visualization of the nanoscale organization of cell membranes remains challenging because of the lack of appropriate fluorescent probes. Here, we introduce a new design concept for super-resolution microscopy probes that combines specific membrane targeting, ON/OFF switching, and environment sensing functions. In this design, we propose a functionalization strategy for solvatochromic dye Nile Red that improves its photostability. The dye is grafted to a newly developed membrane-targeting moiety composed of a sulfonate group and an alkyl chain of varied lengths, which ensures high brightness and lipid-order sensitivity of the probes and tunes their binding/unbinding-induced ON/OFF switching required for single-molecule localization microscopy. While the long-chain probe with strong membrane binding, NR12A, is suitable for conventional microscopy, the short-chain probe NR4A, due to the reversible binding, enables first nanoscale cartography of the lipid order exclusively at the surface of live cells. The latter probe reveals in plasma membranes the presence of nanoscopic protrusions and invaginations of lower lipid order, suggesting a subtle connection between membrane morphology and lipid organization.

The complex nature of cell plasma membranes raised intensive research in the last decades, stimulated by the hypothesis of membrane microdomains (lipid rafts).[1] In model membranes, these domains are identified in terms of lipid order,[2] where liquid-ordered phases (Lo) rich in sphingomyelin and cholesterol “swim” in a pool of disordered phase (Ld) formed by unsaturated lipids. The challenge to visualize lipid domains in cells is linked to their highly dynamic nature, nanoscopic size, and non-flat geometry of plasma membranes with protrusions and invaginations.[3]

One approach to visualize membrane organization is fluorescent labeling of lipids, such as sphingomyelin[4] and ceramide,[5] but labeling may alter properties of lipids.[6] Another approach is to label proteins that specifically target sphingolipids,[7] although the effect of these large molecules on lipid order is still unclear. New possibilities are offered by the environment-sensitive probes,[8] sensitive to polarity (solvatochromic dyes), viscosity (molecular rotors),[9] and membrane tension (flippers).[10] The emission color of solvatochromic probes, like Laurdan,[2b] di-4-ANEPPDHQ,[11] and Nile Red,[12] directly reflects the lipid order, because it is linked with the local polarity and hydration, so that Lo and Ld phases can be distinguished in model membranes. Previously, based on Nile Red, we designed probe NR12S that reports lipid order selectively at the outer leaflet of cell plasma membranes[12]. Due to its high brightness and capacity to work at nanomolar concentrations, it became a common tool to study transmembrane asymmetry,[13] apoptosis,[14] maturation of endosomes,[15] membrane potential,[16] lipid trafficking,[17] etc.[8] The current challenge is to adapt this type of probes for super-resolution microscopy.[18]

Super-resolution microscopy, including single-molecule localization microscopy (SMLM), is making a revolution in the structural and functional characterization at the subcellular level.[3, 19] Numerous efforts have been made to develop fluorescent probes for super-resolution techniques,[20] where ON/OFF switching, required by SMLM, was implemented through photo-switching,[7a, 21] isomerization,[22] transient binding of dyes[23] and proteins[24] to the membrane, and DNA hybridization.[25] A largely underexplored direction, which can open a new dimension in SMLM, is to implement sensing function into this type of probes. It became possible with recently introduced spectrally resolved PAINT (SR-PAINT) for super-resolution imaging of biomembranes.[26] It exploits solvatochromic dye Nile Red, which (i) lights-up upon reversible binding to biomembranes[23a] and (ii) changes its emission color in response to the lipid order[6a, 8, 12, 26a, 26b]. However, this dye is not plasma membrane specific, as it binds all lipid components of cells. Here, based on Nile Red fluorophore, we designed the first probe combining together plasma membrane specificity, controlled ON/OFF switching, and sensing functions, which enabled imaging of both nanoscale morphology and lipid order in biomembranes.

To develop probes for SR-PAINT, we fundamentally changed the design strategy vs the original NR12S (Fig. 1a). First, we inverted the position of Nile Red modification and thus removed phenolic oxygen from the dye (NR12A and NR4A), which was hypothesized to cause lower photostability. Second, we propose here a new membrane-targeting moiety based on an anionic sulfonate head group and a lipophilic alkyl chain of varied lengths. We reasoned that dyes with long alkyl chains (NR12A and NR12S) should label plasma membranes quasi-irreversibly (Fig. 1b), which is suitable for conventional fluorescence microscopy. By contrast, a short alkyl chain (in NR4A) may enable reversible labeling (Fig. 1c) and thus the desired ON/OFF switching required for PAINT.[23a] Compounds NR12A and NR4A were thus synthesized in six steps starting from m-anizidine (Fig. S1).

In organic solvents of varying polarity, the absorption and emission characteristics of NR4A and NR12A were close to Nile Red (Fig. S2, Table S1), indicating that the functionalization did not perturb the fluorophore properties. All studied probes showed fluorescence intensity increase (fluorogenic response) on binding to large unilamellar vesicles (LUVs) composed of DOPC, but the titration curves varied strongly (Fig. 1d). NR12A showed significantly higher affinity to LUVs than the parent Nile Red, displaying rapid intensity growth followed by a plateau at higher concentrations, similarly to NR12S. In sharp contrast, NR4A displayed a slow increase in the fluorescence intensity with liposomes concentration, even weaker than the parent Nile Red. These results confirmed that we obtained a weak (NR4A) and a strong (NR12A) binders of lipid membranes.

[a] D. I. Danylchuk; Dr. A. S. Klymchenko
Laboratoire de Bioimagerie et Pathologies, UMR 7021 CNRS
Université de Strasbourg, 74 route du Rhin, 67401, Illkirch, France
E-mail: andrey.klymchenko@unistra.fr
[b] S. Moon; Dr. K. Xu
Department of Chemistry, University of California, Berkeley
University of California, Berkeley, California, 94720, United States
E-mail: xuk@berkeley.edu
[c] S. Moon; Dr. K. Xu
Chan Zuckerberg Biohub, San Francisco, CA 94158, United States

‡These authors contributed equally.

10.1002/anie.201907690

WILEY-VCH

COMMUNICATION

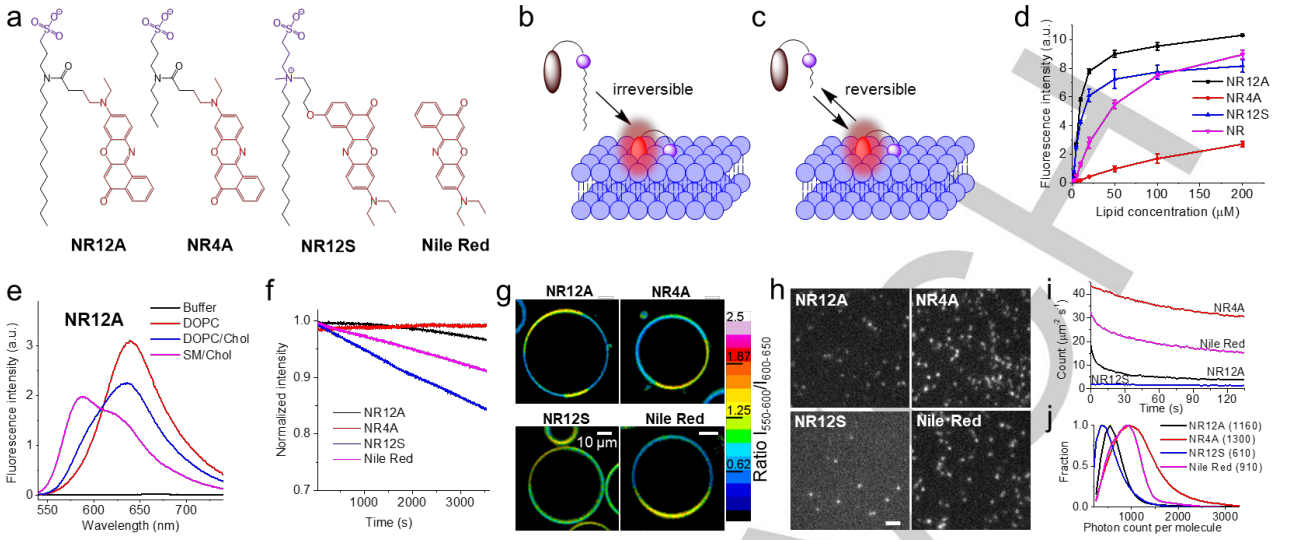

Figure 1. Design of probes and their characterization in model membranes. (a) Chemical structures of NR12A and NR4A as well as the previously reported NR12S and Nile Red. (b,c) Design concept of the fluorogenic probes that irreversibly (b) or reversibly (c) bind to biomembranes due to the presence of long or short hydrophobic chains, respectively. (d) Titration of the four membrane probes (100 nM) with increasing concentrations of lipid vesicles: fluorescence intensity at 620 nm vs. lipid concentration. Errors are s.d.m. (n = 3). (e) Fluorescence spectra of NR12A (2 μM) in buffer (20 mM phosphate buffer, pH 7.4) and liposomes (LUVs) of different lipid composition (1 mM lipids). Excitation wavelength was 520 nm. All the spectra were corrected via dividing by absorbance at the excitation wavelength. (f) Fluorescence intensity of the different probes (400 nM) under continuous illumination vs. time in DOPC liposomes (200 μM). Excitation and emission wavelengths were 540 and 620 nm, respectively. (g) Ratiometric confocal microscopy of giant vesicles composed of DOPC/SM/Chol, 1/1/0.7, stained with NR12A, NR4A, NR12S, or Nile Red (200 nM). (h) Typical single-molecule raw images recorded at 9 ms integration time (110 frames per second) in DOPC supported bilayers, for the four probes (10 nM). (i) Time-dependent counts of single molecules detected per μm^2 per second for the four probes over the full camera view. (j) Distribution of single-molecule brightness of probes in DOPC supported bilayers, expressed in terms of photon count after 50% splitting to the imaging channel. The average value for each probe is given in the legend.

Fluorescence spectra of both NR4A and NR12A (Fig. 1e, S3) exhibited blue shift by about 45-50 nm in Lo phase vesicles, composed of sphingomyelin/cholesterol (SM/Chol), compared to Ld phase vesicles, made of dioleoylphosphatidylcholine (DOPC). This behavior is similar to NR12S,[12] Nile Red (Fig. S3), and other solvatochromic probes,[2b, 11] reflecting lower local polarity/hydration in the Lo phase.[6a] Remarkably, the intensity ratio of blue to red part of emission band for both new probes was more sensitive than NR12S to lipid order (from Ld to Lo phase it increased 5.9-, 4.9- and 2.9-fold for NR4A, NR12A and NR12S, respectively), as their emission bands were narrower (Table S2). In phosphate buffer, NR12A displayed blue-shifted absorption compared to Nile Red (Table S1) and negligible fluorescence (Fig. 1e), similarly to NR12S, indicating that the NR12A forms self-quenched aggregates in water. By contrast, NR4A showed red-shifted absorption (Table S1) and non-negligible fluorescence (Fig. 1e), similarly to Nile Red, suggesting that NR4A is well dissolved and does not aggregate in water. Importantly, NR12A and NR4A displayed high fluorescence quantum yields in LUVs (39-53%, Table S1). Moreover, in DOPC LUVs they were significantly more photostable than NR12S (Fig. 1f), confirming our hypothesis on the negative effect of the phenolic oxygen on the photostability of Nile Red fluorophore. In giant unilamellar vesicles (GUVs), using two-color confocal microscopy, NR12A and NR4A provided excellent contrast between Lo phase, characterized by high intensity ratio $I_{550\text{-}600}/I_{600\text{-}650}$ (in yellow, Fig. 1g, S4), and Ld phase with low $I_{550\text{-}600}/I_{600\text{-}650}$ (in blue). The ratio changes between the two phases were higher than that of NR12S (pseudo-color change from yellow to green), in line with the spectral data in LUVs.

Single-molecule microscopy of the probes in supported DOPC lipid bilayers showed that the weak binders, NR4A and Nile Red, exhibited large number of single-molecule turn-on events that lasted well through $>10^4$ frames (Fig. 1hi, Movie S1), thanks to the continuous probe exchange between the solution and the membrane. By contrast, the strong binders, NR12A and NR12S, showed few turn-on events (Fig. 1hi), probably because most molecules were quasi-irreversibly bound to the membrane and then photobleached before single-molecule images could be recorded. Remarkably, single-molecule brightness histograms further showed that NR4A surpassed all other probes, including Nile Red, by the number of photons collected per molecule (Fig. 1j), in line with our photostability data in solution (Fig. 1f). Finally, single-molecule spectroscopy confirmed sensitivity of NR4A to lipid order in membranes (Fig. S5).

Next, the probes were incubated with HeLa cells and imaged using fluorescence microscopy (Fig. 2a). In contrast to Nile Red, showing intracellular fluorescence, NR12A exclusively stained the plasma membranes, being >2-fold brighter than NR12S. NR4A also showed specific staining for plasma membranes, but the signal was >10-fold lower, in line with its weak affinity to biomembranes. Among studied dyes only NR4A showed no signs of photobleaching (Fig. S6), which confirmed that it binds reversibly to cell membranes, so that bleached probe species are quickly replaced by intact ones, as required by PAINT.[23a] Overall, NR12A appears as a significantly improved analog of NR12S for conventional imaging, which enables, for instance, obtaining high-quality three-dimensional (3D) confocal imaging of membrane surface (Fig. 2b). Meanwhile, NR4A, for its reversible binding capability, appears promising for PAINT. NR4A is also attractive for stimulated emission depletion microscopy,[19a] because exchangeable probes solve the problem of photobleaching.[27]

10.1002/anie.201907690

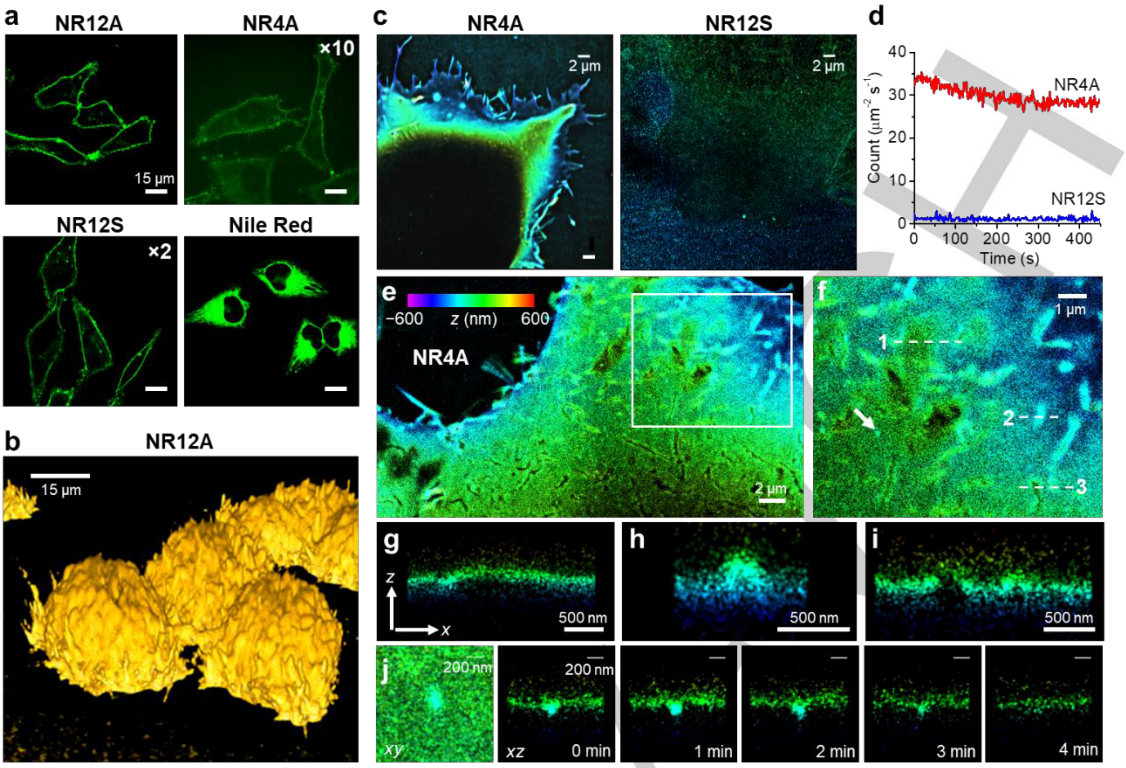

Figure 2. Cellular studies show NR12A and NR4A as superior probes for conventional and super-resolution microscopy, respectively. (a) Spinning disk confocal microscopy images of HeLa cells stained with NR12A, NR4A, NR12S, and Nile Red (20 nM) after 10 min incubation at r.t. (b) A 3D stacked image of KB cells stained with NR12A. (c) Zoom-out views of 3D PAINT results of COS-7 cells with NR4A (10 nM) and NR12S (20 nM). (d) Time-dependent counts of single molecules detected per μm^2 per second for the two probes in representative regions: 5×10^4 frames were recorded for >450 s at 110 frames per second. (e) 3D PAINT image of the top plasma membrane of a HeLa cell stained by NR4A. (f) Zoom-in of the white box in (e). (g-i) Virtual cross sections in the *xz* plane along lines 1-3 in (f). (j) Zoom-in in-plane (*xy*) image, and a time series of the vertical (*xz*) images of the endocytosis site marked by the arrow in (f). All 3D PAINT images are rendered with color to present the depth (*z*) information [color scale bar in (e)].

We then performed 3D PAINT super-resolution imaging of live cells. With 10 nM dye in the imaging medium, NR4A reversibly bound to the plasma membrane, thus achieving high counts of single molecules over 5×10^4 frames (Fig. 2d), as in supported bilayers (Fig. 1h), hence good PAINT images within 1 min acquisition (Fig. 2ce and Fig. S7). In contrast, NR12S performed poorly with low counts of single molecules (Fig. 2d), and so resulted in very dim final PAINT images (Fig. 2c). Although Nile Red also allowed decent image quality, it strongly labeled internal membranes (Fig. S8), consistent with confocal data (Fig. 2a) and previous PAINT results.[26b] We also examined CM-DiI and DiD, two common plasma membrane probes for SMLM,[28] and found both to nonspecifically label internal membranes in live cells (Fig. S8).

Owing to its high specificity, NR4A helps unveil rich nanoscale structural features of the plasma membrane (Fig. 2e-j). For HeLa cells, 3D PAINT showed numerous outward curves of the plasma membrane, including mildly bulging sites that raised up ~100 nm in height over ~1 μm lateral distances (Fig. 2fg), tube-like protrusions with higher curvatures (~100 nm radius; Fig. 2fh), as well as tall protrusions above the limit of our working z range (>400 nm above the focal plane), so that they appear dark at the center (Fig. 2fi). The observed nanoscale protrusions of the plasma membrane were highly dynamic, showing significant structural changes on the time scale of 1 minute (Fig. S8). Meanwhile, we also noted 150-200 nm-sized, pit-like invagination structures that dynamically moved into the cell on the time scale of minutes (Fig. 2j and Fig. S7), indicative of endocytosis. Similar membrane features were also observed in COS-7 cells (Fig S9).

We next exploited solvatochromism of NR4A to examine the nanoscale distribution of local chemical polarity in plasma membranes, reflecting lipid order. To this end, we performed SR-PAINT, where the fluorescence spectrum of every single molecule of NR4A was measured together with its super-localized position.[26b, 29] The obtained spectral mean, calculated as the intensity-weighted average of the emission wavelengths of each probe molecule and presented in pseudo-color, allowed us to describe local lipid order with nanometer-scale spatial resolution and minute-scale temporal resolution[26b]. In live COS-7 cells, NR4A showed a variation of pseudo-color from blue to cyan (Fig. 3ab), with the averaged single-molecule spectra peaked at ~610 nm (Fig. 3d), similar to that of Nile Red in the plasma membrane.[26b] Interestingly, upon chemical fixation, NR4A became cell permeable and so labeled internal organelle membranes with a distinct ~20 nm redshift (Fig. 3cf), similar to the results obtained earlier with Nile Red,[26b] indicating lower lipid order for the organelle membranes.

The high specificity of NR4A to the plasma membrane in live cells enabled nanoscale cartography of lipid order of cell surface, which has been a challenge so far as Nile Red exhibits strong background from internal membranes. Remarkably, for the tube-like nanoscale protrusions, in cyan pseudo-color, the locally averaged single-molecule spectra showed a ~4 nm redshift when compared to smooth parts of the plasma membrane,

10.1002/anie.201907690

predominantly in blue (Fig. 3ad). This difference indicates slightly reduced local lipid order, possibly related to the dynamic structural changes of these protrusions under forces. More drastically, a strong redshift of ~20 nm, i.e., even lower lipid order, was observed for the ~200 nm-sized membrane pits (Fig. 3be), assigned above to endocytosis sites (Fig. 2j). Recent works[30] suggest that membrane curvature formation is closely related to the lipid composition. Our results above provide direct evidence of decreased local packing orders for the highly curved structures in the plasma membrane. In view of lipid rafts hypothesis,[1] our work suggests that nanoscopic domains of low lipid order can originate from protrusions and extensions at the cell surface.

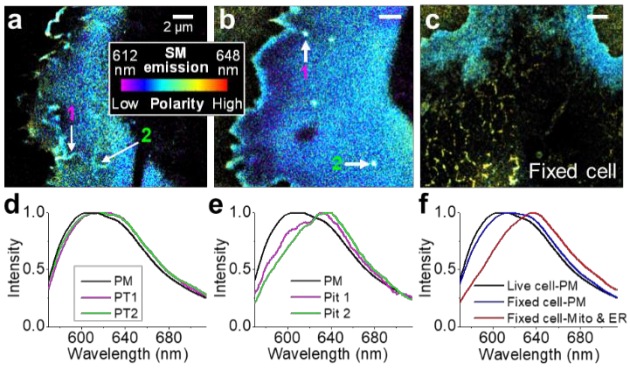

Figure 3. Nanoscopic mapping of lipid order in cell membranes with NR4A. (a,b) SR-PAINT with NR4A for the plasma membrane of live COS-7 cells. Color represents single-molecule spectral mean (color scale bar). (c) NR4A SR-PAINT for a fixed COS-7 cell, showing staining for both the plasma membrane and internal membranes. (d) Averaged single-molecule spectra at smooth parts of the plasma membrane (black) vs. at the tube-like protrusions pointed to by the two arrows in (a) (magenta and green). (e) Averaged single-molecule spectra at smooth parts of the plasma membrane (black) vs. at the cluster structures pointed to by the two arrows in (b) (magenta and green). (f) Averaged single-molecule spectra at the plasma membrane of live (black) and fixed (blue) COS-7 cells, vs. at the internal membranes of fixed COS-7 cells (red).

Thus, we introduce the concept of a fluorescent probe for super-resolution microscopy that combines target specificity, ON/OFF switching, and polarity sensing. It was realized based on solvatochromic dye Nile Red and a newly introduced low-affinity membrane binder that ensures reversible bind/unbinding events and targets specifically cell plasma membranes. The developed probe (NR4A) revealed lipid order heterogeneity at the cell surface and its connection to nanoscale membrane topology.

Acknowledgements

This work was supported by the European Research Council ERC Consolidator grant BrightSens 648528 and the National Science Foundation (CHE-1554717). K.X. is a Chan Zuckerberg Biohub investigator. S.M. acknowledges support from a Samsung Scholarship. Bohdan Wasylyk is acknowledged for providing the KB cells.

Keywords: Fluorescent probes • solvatochromism • membranes • super-resolution microscopy • lipid order

[1] a) D. Lingwood, K. Simons, *Science* **2010**, *327*, 46; b) E. Sezgin, I. Levental, S. Mayor, C. Eggeling, *Nat. Rev. Mol. Cell Biol.* **2017**, *18*, 361.

[2] a) T. Baumgart, S. T. Hess, W. W. Webb, *Nature* **2003**, *425*, 821; b) C. Dietrich, L. A. Bagatolli, Z. N. Volovyk, N. L. Thompson, M. Levi, K. Jacobson, E. Gratton, *Biophys. J.* **2001**, *80*, 1417.

[3] M. B. Stone, S. A. Shelby, S. L. Veatch, *Chem. Rev.* **2017**, *117*, 7457.

[4] M. Kinoshita, K. G. Suzuki, N. Matsumori, M. Takada, H. Ano, K. Morigaki, M. Abe, A. Makino, T. Kobayashi, K. M. Hirosawa, T. K. Fujiwara, A. Kusumi, M. Murata, *J. Cell. Biol.* **2017**, *216*, 1183.

[5] A. Burgert, J. Schlegel, J. Becam, S. Doose, E. Bieberich, A. Schubert-Unkmeir, M. Sauer, *Angew. Chem. Int. Ed. Engl.* **2017**, *56*, 6131.

[6] a) A. S. Klymchenko, R. Kreder, *Chem. Biol.* **2014**, *21*, 97; b) E. Sezgin, I. Levental, M. Grzybek, G. Schwarzmann, V. Mueller, A. Honigmann, V. N. Belov, C. Eggeling, U. Coskun, K. Simons, P. Schwille, *Biochim. Biophys. Acta-Biomembr.* **2012**, *1818*, 1777.

[7] a) H. Mizuno, M. Abe, P. Dedecker, A. Makino, S. Rocha, Y. Ohno-Iwashita, J. Hofkens, T. Kobayashi, A. Miyawaki, *Chemical Science* **2011**, *2*, 1548; b) F. Hullin-Matsuda, M. Murate, T. Kobayashi, *Chem. Phys. Lipids* **2018**, *216*, 132.

[8] A. S. Klymchenko, *Acc. Chem. Res.* **2017**, *50*, 366.

[9] J. E. Chambers, M. Kubankova, R. G. Huber, I. Lopez-Duarte, E. Avezov, P. J. Bond, S. J. Marciniak, M. K. Kuimova, *ACS Nano* **2018**, *12*, 4398.

[10] A. Colom, E. Derivery, S. Soleimanpour, C. Tomba, M. Dal Molin, N. Sakai, M. Gonzalez-Gaitan, S. Matile, A. Roux, *Nat. Chem.* **2018**, *10*, 1118.

[11] L. Jin, A. C. Millard, J. P. Wuskell, X. M. Dong, D. Q. Wu, H. A. Clark, L. M. Loew, *Biophys. J.* **2006**, *90*, 2563.

[12] O. A. Kucherak, S. Oncul, Z. Darwich, D. A. Yushchenko, Y. Arntz, P. Didier, Y. Mely, A. S. Klymchenko, *J. Am. Chem. Soc.* **2010**, *132*, 4907.

[13] S. Chiantia, P. Schwille, A. S. Klymchenko, E. London, *Biophys J* **2011**, *100*, L1.

[14] R. Kreder, K. A. Pyrshev, Z. Darwich, O. A. Kucherak, Y. Mely, A. S. Klymchenko, *ACS chemical biology* **2015**, *10*, 1435.

[15] Z. Darwich, A. S. Klymchenko, D. Dujardin, Y. Mely, *Rsc Advances* **2014**, *4*, 8481.

[16] M. Sundukova, E. Prifti, A. Bucci, K. Kirillova, J. Serrao, L. Reymond, M. Umebayashi, R. Hovius, H. Riezman, K. Johnsson, P. A. Heppenstall, *Angew. Chem. Int. Ed.* **2019**, *58*, 2341.

[17] a) J. Kim, A. Singh, M. Del Poeta, D. A. Brown, E. London, *J. Cell Sci.* **2017**, *130*, 2682; b) D. B. Iaea, F. R. Maxfield, *PloS one* **2017**, *12*, e0188041.

[18] E. Sezgin, F. Schneider, V. Zilles, I. Urbancic, E. Garcia, D. Waithe, A. S. Klymchenko, C. Eggeling, *Biophys. J.* **2017**, *113*, 1321.

[19] a) S. J. Sahl, S. W. Hell, S. Jakobs, *Nat. Rev. Mol. Cell Biol.* **2017**, *18*, 685; b) Y. M. Sigal, R. Zhou, X. Zhuang, *Science* **2018**, *361*, 880.

[20] a) J. B. Grimm, B. P. English, J. J. Chen, J. P. Slaughter, Z. J. Zhang, A. Revyakin, R. Patel, J. J. Macklin, D. Normanno, R. H. Singer, T. Lionnet, L. D. Lavis, *Nat. Methods* **2015**, *12*, 244; b) H. L. Li, J. C. Vaughan, *Chem. Rev.* **2018**, *118*, 9412; c) L. Wang, M. S. Frei, A. Salim, K. Johnsson, *J. Am. Chem. Soc.* **2018**, *141*, 2770; d) G. T. Dempsey, J. C. Vaughan, K. H. Chen, M. Bates, X. W. Zhuang, *Nat. Methods* **2011**, *8*, 1027.

[21] a) M. J. Rust, M. Bates, X. W. Zhuang, *Nat. Methods* **2006**, *3*, 793; b) S. Habuchi, R. Ando, P. Dedecker, W. Verheijen, H. Mizuno, A. Miyawaki, J. Hofkens, *Proc. Natl. Acad. Sci. U. S. A.* **2005**, *102*, 9511.

[22] S. N. Uno, M. Kamiya, T. Yoshihara, K. Sugawara, K. Okabe, M. C. Tarhan, H. Fujita, T. Funatsu, Y. Okada, S. Tobita, Y. Urano, *Nature Chemistry* **2014**, *6*, 681.

[23] a) A. Sharonov, R. M. Hochstrasser, *Proc. Natl. Acad. Sci. U. S. A.* **2006**, *103*, 18911; b) C. K. Spahn, M. Glaesmann, J. B. Grimm, A. X. Ayala, L. D. Lavis, M. Heilemann, *Sci. Rep.* **2018**, *8*, 14768.

[24] S. Rocha, J. A. Hutchison, K. Peneva, A. Herrmann, K. Müllen, M. Skjøt, C. I. Jørgensen, A. Svendsen, F. C. De Schryver, J. Hofkens, H. Uji-i, *ChemPhysChem* **2009**, *10*, 151.

[25] R. Jungmann, M. S. Avendano, M. J. Dai, J. B. Woehrstein, S. S. Agasti, Z. Feiger, A. Rodal, P. Yin, *Nat. Methods* **2016**, *13*, 439.

[26] a) M. N. Bongiovanni, J. Godet, M. H. Horrocks, L. Tosatto, A. R. Carr, D. C. Wirthensohn, R. T. Ranasinghe, J. E. Lee, A. Ponjavic, J. V. Fritz, C. M. Dobson, D. Klenerman, S. F. Lee, *Nat. Commun.* **2016**, *7*, 13544; b) S. Moon, R. Yan, S. J. Kenny, Y. Shyu, L. M. Xiang, W. Li, K. Xu, *J. Am. Chem. Soc.* **2017**, *139*, 10944; c) R. Yan, S. Moon, S. J. Kenny, K. Xu, *Acc. Chem. Res.* **2018**, *51*, 697.

[27] C. Spahn, J. B. Grimm, L. D. Lavis, M. Lampe, M. Heilemann, *Nano Letters* **2019**, *19*, 500.

[28] S. H. Shim, C. Xia, G. Zhong, H. P. Babcock, J. C. Vaughan, B. Huang, X. Wang, C. Xu, G. Bi, X. Zhuang, *Proc. Natl. Acad. Sci. U. S. A.* **2012**, *109*, 13978.

[29] Z. Zhang, S. J. Kenny, M. Hauser, W. Li, K. Xu, *Nature Methods* **2015**, *12*, 935.

[30] a) S. Vanni, H. Hirose, H. Barelli, B. Antonny, R. Gautier, *Nature communications* **2014**, *5*, 4916; b) M. Pinot, S. Vanni, S. Pagnotta, S. Lacas-Gervais, L.-A. Payet, T. Ferreira, R. Gautier, B. Goud, B. Antonny, H. Barelli, *Science* **2014**, *345*, 693.

10.1002/anie.201907690

WILEY-VCH

Entry for the Table of Contents

COMMUNICATION

Targeting, switching and sensing were combined together in one fluorescent probe to achieve nanoscale cartography of cell plasma membranes. The proposed design is based on a new functionalization strategy of solvatochromic dye Nile Red, sensitive to lipid order, and a special membrane-targeting moiety that controls binding/unbinding-induced ON/OFF switching for super-resolution microscopy.

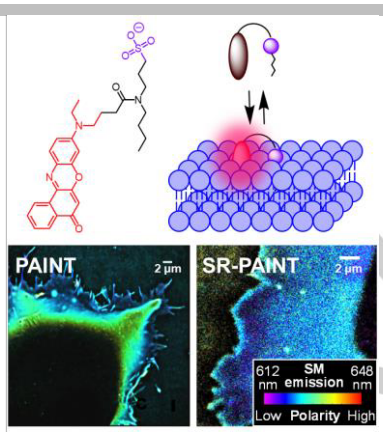

Dmytro I. Danylchuk, Seonah Moon, Ke Xu, Andrey S. Klymchenko**

Page No. – Page No.

Tailor-made switchable solvatochromic probes for live-cell super-resolution imaging of plasma membrane organization

Angewandte
Eine Zeitschrift der Gesellschaft Deutscher Chemiker
Chemie

Supporting Information

Switchable Solvatochromic Probes for Live-Cell Super-resolution Imaging of Plasma Membrane Organization

Dmytro I. Danylchuk[+], Seonah Moon[+], Ke Xu, and Andrey S. Klymchenko**

anie_201907690_sm_miscellaneous_information.pdf
anie_201907690_sm_Movie_S1.avi

Supporting information

Materials and Methods

Synthesis and characterization of probes. General methods and materials. All the reagents were purchased from Sigma-Aldrich or Alfa Aesar or TCI and used as received. MilliQ-water (Millipore) was used in all experiments. NMR spectra were recorded at 20ºC on a BrukerAvance III 400 spectrometer. Mass spectra were obtained using an Agilent Q-TOF 6520 mass spectrometer. Absorption and emission spectra were recorded on an Edinburgh FS5 spectrofluorometer equipped with a thermostated cell compartment. Fluorescence quantum yields were measured using Nile Red (NR) in methanol (λ_{ex}= 520 nm, QY_{ref} = 38%[1] as a reference.

Ethyl 4-((3-methoxyphenyl)amino)butanoate (1a). 5 g of m-anisidine were mixed with 12.34 g (2.2 eq.) of freshly ground K_2CO_3 and 1.35 g (0.2 eq.) of KI in 40 ml of dry DMF, after that 7.93 g of ethyl 4-bromobytanoate was added and the mixture was stirred at 60 °C for 6h (control by TLC) under Ar atmosphere. After the reaction the solvent was evaporated *in vacuo*, the solid residue was dissolved in Et_2O and washed with water and brine. The organic phase was dried over Na_2SO_4 and the solvent was evaporated *in vacuo*. The crude product was purified by column chromatography (SiO_2; Hept:EtOAc 3:1, dry deposit on celite). The product is to be kept under Ar atmosphere due to oxidation. Compound **1a**: yield 7.69g (79.8 %) as colourless oil. **^{1}H NMR (400 MHz, $CDCl_3$) δ ppm** 1.23 – 1.30 (td, *J*=7.0, 1.0 Hz, 3 H) 1.95 (quin, *J*=7.0 Hz, 2 H) 2.43 (t, *J*=7.3 Hz, 2 H) 3.17 (t, *J*=7.0 Hz, 2 H) 3.78 (s, 3 H) 4.15 (q, *J*=7.3 Hz, 2 H) 6.17 (t, *J*=2.4 Hz, 1 H) 6.23 (ddd, *J*=8.1, 2.4, 0.8 Hz, 1 H) 6.27 (ddd, *J*=8.1, 2.4, 0.8 Hz, 1 H) 7.08 (t, *J*=8.1 Hz, 1 H). **MS (ESI), *m/z*:** $[M+H]^+$ calcd for $C_{13}H_{20}NO_3^+$, 238.14; found, 238.14.

Ethyl 4-(ethyl(3-methoxyphenyl)amino)butanoate (2a). 7.68 g of compound **1a** were mixed with 15.17 g (7.82 mL, 3 eq.) of ethyl iodide and 11.18 g (3 eq.) of freshly ground K_2CO_3 in 40 mL of dry DMF. The reaction was stirred at 50 °C for 20h (control by TLC) under Ar atmosphere. After the reaction, the solvent was evaporated *in vacuo*, the solid residue was dissolved in DCM and washed with water and brine. The organic phase was dried over Na_2SO_4 and the solvent was evaporated *in vacuo*. The crude product was purified by column chromatography (SiO_2; Hept:EtOAc 4:1, dry deposit on celite). The product is to be kept under Ar atmosphere due to oxidation. Compound **2a**: yield 6.31g (73.5 %) as colourless oil. **^{1}H NMR (400 MHz, $CDCl_3$) δ ppm** 1.16 (t, *J*=7.0 Hz, 3 H) 1.28 (t, *J*=7.2 Hz, 3 H) 1.93 (quin, *J*=7.3 Hz, 2 H) 2.36 (t, *J*=7.3 Hz, 2 H) 3.28 - 3.33 (m, 2 H) 3.36 (q, *J*=7.0 Hz, 2 H) 3.81 (s, 3 H)

4.16 (q, *J*=7.0 Hz, 2 H) 6.22 - 6.30 (m, 2 H) 6.33 – 6.36 (m, 1 H) 7.13 (t, *J*=8.0 Hz, 1 H). **MS (ESI), *m/z*:** $[M+H]^+$ calcd for $C_{15}H_{24}NO_3^+$, 266.17; found, 266.17.

4-(ethyl(3-hydroxyphenyl)amino)butanoic acid (3a). 5.46 g of compound **2a** were mixed with 40 mL of $HBr_{(conc)}$ and the mixture was refluxed for 8h (control by TLC). After the reaction the solvent was evaporated *in vacuo*, followed by heating to 100 °C under high vacuum for 3h to evaporate the traces of solvent. Compound **3a**: yield 5.60 g (98.0 %) as a colourless solid. **^{1}H NMR (400 MHz, Methanol-*d*$_4$) δ ppm** 1.16 (t, *J*=7.3 Hz, 3 H) 1.51 - 1.76 (m, 1 H) 1.76 - 2.03 (m, 1 H) 2.34 - 2.47 (m, 2 H) 3.60 - 3.70 (m, 5 H) 6.99 (dd, *J*=8.0, 2.3 Hz, 1 H) 7.03 (q, *J*=2.3 Hz, 1 H) 7.04 (dt, *J*=4.5, 1.0 Hz, 1 H) 7.06 (dt, *J*=4.5, 1.0 Hz, 1 H) 7.44 (t, *J*=8.0 Hz, 1 H). **MS (ESI), *m/z*:** $[M]^+$ calcd for $C_{12}H_{17}NO_3^+$, 223.12; found, 223.12.

General procedure for 3-(alkylammonio)propane-1-sulfonate (6a and 6b), adapted from elsewhere.[2] 4g of corresponding alkylamine were mixed with 1.2 eq. of 1,3-propanesultone in 30 mL of dry acetone. The reaction was refluxed under Ar atmosphere for 24h. After the reaction, the crude product was filtered off, washed 2 times with acetone and recrystallized from ethanol.
Compound **6a**: yield 4.58 g (69.2 %) as a white solid. **^{1}H NMR (400 MHz, DMSO-d$_6$ (60 °C)) δ ppm** 0.88 (t, J=6.8 Hz, 3 H) 1.24 - 1.35 (m, 18 H) 1.57 (quin, J=7.6 Hz, 2 H) 1.97 (quin, J=6.4 Hz, 2 H) 2.66 (t, J=6.4 Hz, 2 H) 2.88 (t, J=7.3 Hz, 2 H) 3.06 (t, J=6.4 Hz, 2 H). **MS (ESI), m/z:** $[M]^+$ calcd for $C_{15}H_{32}NO_3S^-$, 306.21; found, 306.21. Compound **6b**: yield 6.56 g (61.4 %) as a white solid. **^{1}H NMR (400 MHz, DMSO-d$_6$) δ ppm** δ ppm 0.89 (t, J=7.3 Hz, 3 H) 1.33 (sxt, J=7.4 Hz, 2 H) 1.49 - 1.58 (m, 2 H) 1.93 (quin, J=6.8 Hz, 2 H) 2.62 (t, J=6.7 Hz, 2 H) 2.88 (t, J=7.7 Hz, 2 H) 3.04 (t, J=6.8 Hz, 2 H) **MS (ESI), m/z:** $[M]^+$ calcd for $C_{15}H_{32}NO_3S^-$, 194.09; found, 194.08.

4-(ethyl-5-oxo-5*H*-benzo[a]phenoxazin-9-yl)amino)butanoic acid (5a). 2.87 g of 4-(ethyl(3-hydroxyphenyl)amino)butanoic acid (**3a**) were dissolved in 10 mL of water together with 2 mL of $HCl_{(conc)}$ at r.t. After this the mixture was cooled to 0 °C and a solution of 1.33 g (1.1 eq.) of $NaNO_2$ in 10 mL of water was added dropwise at 0 °C. The reaction mixture was stirred for 1.5h at 0 °C, after which the water was removed by liophilization. The product, 4-(ethyl(3-hydroxy-4-nitrosophenyl)amino)butanoic acid (**4a**), was used for the next step without further purification.
3.24 g of compound **4a** were mixed with 2.78 g (1.5 eq.) of 1-naphtol and 15 ml of dry DMF. The mixture was stirred at 80 °C for 5h. After the reaction the solvent was evaporated in vacuo, and the residues were dissolved in DCM and filtered through SiO_2. After this, the solvent was evaporated in vacuo. In order to purify the compound, a methyl ester of compound **5a** was formed by an addition of 1.54 g (0.94 mL) of $SOCl_2$ dropwise to the solution of the crude **5a** in 40 mL of MeOH at 0 °C. After 1h of stirring at 0 °C, the mixture was stirred for 20h at r.t., afterwards the solvent was evaporated in vacuo. The methyl ester of **5a** was purified by column chromatography (SiO_2; Hept:EtOAc 1:1, dry deposit on celite). **^{1}H NMR (400 MHz, CDCl$_3$) δ ppm** 1.26 (t, *J*=7.0 Hz, 3 H) (quin, *J*=7.4 Hz, 2 H) 2.38 - 2.47 (m, 2 H) 3.39 - 3.52 (m, 4 H) 3.73 (s, 3 H) 6.39 (s, 1 H) 6.50 (d, *J*=2.8 Hz, 1 H) 6.69 (dd, *J*=9.0, 2.8 Hz, 1 H) 7.61 (d, *J*=9.0 Hz, 1 H) 7.65 (td, *J*=7.8, 1.4 Hz, 1 H) 7.74 (dt, *J*=7.8, 1.40 Hz, 1 H) 8.30 (dd, *J*=7.8, 1.3 Hz, 1 H) 8.65 (dd, *J*=7.9, 0.9 Hz, 1 H). **MS (ESI), *m/z*:** $[M+Na]^+$ calcd for $C_{22}H_{20}N_2O_4$, 413.16; found, 413.15.
On the next step, 370 mg of methyl ester of **5a** were dissolved in 15 mL of 20% $HCl_{(aq)}$ and the mixture was stirred for 15h at 90 °C (control by TLC). After the reaction the solvent was removed *in vacuo* and the solid residue was twice washed with water on a filter. Compound **5a**: overall yield 345 mg (7.7 %) as dark red solid. **^{1}H NMR (400 MHz, DMSO-*d*$_6$) δ ppm** 1.16 (t, *J*=6.9 Hz, 3 H) 1.81 (quin, *J*=7.5 Hz,

2 H) 2.35 (t, *J*=7.3 Hz, 2 H) 3.44 (quin, *J*=7.5 Hz, 2 H) 3.52 (t, *J*=6.9 Hz, 2 H) 6.32 (s, 1 H) 6.76 (s, 1 H) 6.91 (d, *J*=9.4 Hz, 1 H) 7.63 (d, *J*=8.5 Hz, 1 H) 7.72 (t, *J*=7.5 Hz, 1 H) 7.81 (t, *J*=7.5 Hz, 1 H) 8.13 (d, *J*=7.8 Hz, 1 H) 8.56 (d, *J*=7.8 Hz, 1 H). **^{13}C NMR (101 MHz, DMSO-*d*$_6$) δ** 12.73 (CH_3) 22.75 (C_{al}) 31.04 (C_{al}) 41.28 (C_{al}) 45.45 (C_{al}) 49.81 (C_{al}) 78.58 (C_{al}) 96.77 (C_{ar}) 104.87 (C_{ar}) 111.19 (C_{ar}) 123.86 (C_{ar}) 124.23 (C_{ar}) 125.18 (C_{ar}) 125.47 (C_{ar}) 130.44 (C_{ar}) 131.45 (C_{ar}) 132.05 (C_{ar}) 132.08 (C_{ar}) 135.43 (C_{ar}) 146.95 (C_{ar}) 174.66 (C_{ar}) 182.03 (C_{ar}) 192.67 (s, COOH) 217.84 (s, 1 C_{ar}). **MS (ESI), *m/z*:** $[M+Na]^+$ calcd for $C_{22}H_{20}N_2O_4Na$, 399.14; found, 399.13.

General procedure for 3-(N-alkyl-4(ethyl(5-oxo-5*H*-benzo[a]phenoxazin-9-yl)amino)butanamido)propane-1-sulfonate (NR12A and NR4A). 30 mg of compound **5a** were dissolved in 2 mL of dry DMF together with 32.9 mg (1.05 eq.) of HATU and 20.6 mg (28 µL, 2 eq.) of DIPEA. After 5 minutes, a solution of 1.05 eq. of the corresponding 3-(alkylammonio)propane-1-sulfonate (**6a** or **6b**) and 20.6 mg (28 µL, 2 eq.) of DIPEA in 2 mL of dry DMF was added and the mixture was stirred for 24h at r.t. under Ar atmosphere (control by TLC). After the reaction the solvent was evaporated *in vacuo* and the crude product was purified by gradient column chromatography (SiO_2; DCM:MeOH 88:12 to DCM:MeOH 85:15 for **NR12A** and DCM:MeOH 85:15 to DCM:MeOH 82:18 for **NR4A**). Compound **NR12A**: yield 29.9 mg (47.2 %) as dark red solid. **^{1}H NMR (400 MHz, Methanol-*d*$_4$) δ ppm** 0.81 - 0.92 (m, 3 H) 1.11 - 1.33 (m, 19 H) 1.34 - 1.40 (m, 4 H) 1.47 - 1.62 (m, 2 H) 1.91 - 2.00 (m, 2 H) 2.00 - 2.10 (m, 2 H) 2.41 - 2.58 (m, 2 H) 2.78 - 2.89 (m, 2 H) 3.36 - 3.58 (m, 6 H) 6.23 (s, 1 H) 6.55 (dd, *J*=8.8, 2.5 Hz, 1 H) 6.83 (ddd, *J*=12.0, 9.3, 2.5 Hz, 1 H) 7.50 (d, *J*=9.3 Hz, 1 H) 7.57 - 7.66 (m, 1 H) 7.66 - 7.76 (m, 1 H) 8.13 (d, *J*=7.8 Hz, 1 H) 8.53 (d, *J*=7.8 Hz, 1 H). **^{13}C NMR (101 MHz, Methanol-*d*$_4$) δ ppm** 15.29 (CH_3) 15.71 (CH_3) 16.99 (C_{al}) 19.91 (C_{al}) 21.32 (C_{al}) 26.24 (C_{al}) 26.70 (C_{al}) 27.12 (C_{al}) 28.22 (C_{al}) 32.98 (C_{al}) 33.08 (C_{al}) 33.15 (C_{al}) 33.27 (C_{al}) 35.58 (C_{al}) 46.38 (C_{al}) 58.42 (C_{al}) 99.98 (C_{ar}) 108.04 (C_{ar}) 114.78 (C_{ar}) 127.40 (C_{ar}) 128.84 (C_{ar}) 129.18 (C_{ar}) 133.36 (C_{ar}) 135.02 (C_{ar}) 135.21 (C_{ar}) 135.96 (C_{ar}) 141.93 (C_{ar}) 150.61 (C_{ar}) 155.78 (C_{ar}) 156.50 (C_{ar}) 176.93 (C_{ar}) 187.84 (C_{ar}). **MS (ESI), *m/z*:** $[M]^-$ calcd for $C_{37}H_{50}N_3O_6S^-$, 664.34; found, 664.34. Compound **NR4A**: yield 32.8 mg (60.5 %) as dark red solid. **^{1}H NMR (400 MHz, Methanol-*d*$_4$) δ ppm** 0.96 (dt, *J*=9.1, 7.4 Hz, 3 H) 1.21 (t, *J*=7.0 Hz, 3 H) 1.30 - 1.41 (m, 4 H) 1.51 - 1.61 (m, 2 H) 1.82 - 1.97 (m, 2 H) 1.97 - 2.12 (m, 2 H) 2.39 - 2.57 (m, 2 H) 2.79 - 2.89 (m, 2 H) 3.34 - 3.57 (m, 6 H) 6.11 (d, *J*=2.0 Hz, 1 H) 6.42 (dd, *J*=9.2, 2.7 Hz, 1 H) 6.72 (td, *J*=8.8, 2.7 Hz, 1 H) 7.37 (dd, *J*=9.2, 3.4 Hz, 1 H) 7.52 - 7.59 (m, 1 H) 7.64 (td, *J*=7.5, 1.3 Hz, 1 H) 8.05 (dd, *J*=7.8, 1.00 Hz, 1 H) 8.38 - 8.44 (m, 1 H) **^{13}C NMR (101 MHz, Methanol-*d*$_4$) δ** 15.39 (CH_3) 15.73 (CH_3) 16.83 (C_{al}) 19.92 (C_{al}) 21.36 (C_{al}) 26.67 (C_{al}) 27.18 (C_{al}) 28.24 (C_{al}) 33.27 (C_{al}) 34.70 (C_{al}) 46.39 (C_{al}) 58.42 (C_{al}) 99.86 (C_{ar}) 107.95 (C_{ar}) 114.70 (C_{ar}) 127.32 (C_{ar}) 128.76 (C_{ar}) 129.08 (C_{ar}) 133.27 (C_{ar}) 134.93 (C_{ar}) 135.14 (C_{ar}) 135.84 (C_{ar}) 141.79 (C_{ar}) 150.44 (C_{ar}) 155.62 (C_{ar}) 156.32 (C_{ar}) 176.84 (C_{ar}) 187.68 (C_{ar}). **MS (ESI), *m/z*:** $[M]^+$ calcd for $C_{29}H_{34}N_3O_6S^-$, 552.22; found, 552.21.

Preparation of liposomes. All types of LUVs used were prepared by the following procedure. A stock solution of corresponding lipid(s) in chloroform was placed into a round-neck flask, after which the solvent was evaporated in vacuo and phosphate buffer (20 mM, pH 7.4) was added. After all the solid was dissolved a suspension of multilamellar vesicles was extruded by using a Lipex Biomembranes extruder (Vancouver, Canada). The size of the filters was first 0.2 µm (7 passages) and thereafter 0.1 µm (10 passages). This generates monodisperse LUVs with a mean diameter of 0.12 µm as measured with a

Malvern Zetamaster 300 (Malvern, U.K.). Phospholipid:Cholesterol molar ratio in case of DOPC/Chol and Sphing/Chol was 1:0.9.

Preparation of giant unilamellar vesicles (GUVs). GUVs were prepared by electroformation in a home-built liquid cell (University of Odense, Denmark), using previously described procedure.[3] A 0.1 mM solution of lipids in chloroform was deposited on the platinum wires of the chamber, and the solvent was evaporated under vacuum for 30 min. The chamber, thermostatted at 55 °C, was filled with a 300 mM sucrose solution, and a 2-V, 10-Hz alternating electric current was applied to this capacitor-like configuration for *ca.* 2 h. Then, a 50 μL aliquot of the obtained stock solution of GUVs in sucrose (cooled down to room temperature) was added to 200 μL of 300 mM glucose solution containing 200 nM of the probe (obtained by adding corresponding dye stock solution in DMSO to glucose solution, final DMSO concentration <0.32%) to give the final suspension of stained GUVs used in microscopy experiments.

Preparation of supported lipid bilayers. Supported lipid bilayers were prepared by vesicle fusion of small unilamellar vesicles (SUVs) in a similar fashion as the previous work.[4] Briefly, 1,2-dioleoyl-sn-glycero-3-phosphocholine (DOPC) and sphingomyelin were purchased from Avanti Polar Lipids (850375C, 860062C). Cholesterol was purchased from Sigma (C8667). Each lipid was separately dissolved in chloroform. To prepare DOPC SUVs, the DOPC stock solution was transferred to a pre-cleaned round-bottom flask, and chloroform was evaporated under nitrogen flow. For ternary mixture SUVs, the lipid solutions were mixed in a pre-cleaned round-bottom flask at the designated ratios, and chloroform was evaporated under nitrogen flow. The lipid cake was rehydrated with ~60 ^{o}C milli-Q water to the concentration of ~2 mg/mL, then sonicated at ~60 ^{o}C for ~40 min until clear SUV suspension was formed. To form a supported lipid bilayer, the SUV suspension and buffer solution (150 mM NaCl, 10 mM HEPES, 3 mM $CaCl_2$) were gently added to a pre-cleaned, hydrophilic coverslip at 1:4 ratio. The coverslip was incubated at ~60 ^{o}C for ~15 min, and then was thoroughly rinsed with Dulbecco's Phosphate Buffered Saline (DPBS). The lipid bilayer was imaged with 10 nM NR12A, NR4A, NR12S, or Nile Red in DPBS.

Cell Lines, Culture Conditions, and Treatment. HeLa cells (ATCC CCL-2) and KB ATCC CCL-17) cells were grown in Dulbecco`s Modified Eagle Medium (DMEM, Gibco Invitrogen), supplemented with 10% fetal bovine serum (FBS, Lonza), 1% l-Glutamine (Sigma Aldrich) and 1% antibiotic solution (penicillin-streptomycin, Gibco-Invitrogen) at 37 °C in a humidified 5% CO_2 atmosphere. Cells were seeded onto a chambered coverglass (IBiDi) at a density of 5×10^4 cells/well 24 h before the microscopy measurement. For conventional microscopy experiments, the attached HeLa cells in ABIDI dishes were washed twice with warm Dulbecco`s Phosphate buffered saline (DPBS, Dominique Dutscher), after that 1 mL of 20 nM dye solution in DPBS was added and the cells were incubated for 10 min. at r.t. Concentrations used for photobleaching experiments were 20 nM for NR4A, NR12S, and NR; 7 nM for NR12A. For super-resolution measurements, COS-7 (ATCC CRL-1651) and HeLa (ATCC CCL-2) cells were maintained in DMEM supplemented with 10% FBS in 5% CO_2 at 37 ^{o}C. For imaging, cells were plated on 18-mm #1.5 glass coverslips. When cells reached ~50% confluency after 24~48 hr, the coverslip was mounted on a metal holder (CSC-18; Bioscience Tools) in the imaging media (L15 with 20 mM HEPES). Cells were imaged with 10 nM NR4A or Nile Red, or 20 nM NR12S in the imaging media at room temperature. For fixed cell experiments, cells were fixed in 3% paraformaldehyde + 0.1%

glutaraldehyde in DPBS for 20 min at room temperature. After fixation, the sample was treated with freshly prepared 0.1% $NaBH_4$ in DPBS for 5 min, and thoroughly washed with DPBS three times.

Fluorescence microscopy. Cellular imaging of cells was performed using Nikon Ti-E inverted microscope, equipped with CFI Plan Apo ×60 oil (NA = 1.4) objective, X-Light spinning disk module (CREST Optics) (in case of confocal imaging) and a Hamamatsu Orca Flash 4 sCMOS camera with a bandpass filter 593 ± 20 nm (Semrock FF01-593/40-25). The excitation in confocal mode was provided by a 532 nm diode laser (OXXIUS). The exposure time in confocal mode was set to 500 ms per image frame. For photobleaching experiments and widefield imaging, the excitation was provided by light emitting diode (SpectraX) at 550 nm. The 550-nm light power was set to 4.33 mW at the sample level. The diameter of the wide-field illumination spot was 420 μm, according to a photobleaching test, so that the power density used at 550 nm was 3.14 $W \cdot cm^{-2}$. The exposure time in widefield mode was set to 500 ms per image frame. Photobleaching tests were performed by illuminating the samples continuously over 60 seconds in widefield mode, followed by imaging immediately after the illumination and after incubation for 10 min at r.t. All the images were recorded using NIS Elements and then processed using Fiji software.
Confocal imaging of GUVs was performed on a Leica TSC SPE confocal microscope with HXC PL APO 63x/1.40 OIL CS objective. The excitation light was provided by a 488 nm laser while the fluorescence was detected at two spectral ranges: 550–600 nm ($I_{550-600}$) and 600–650 nm ($I_{600-650}$) in a sequential mode with rapid alternation of the detection wavelengths to minimize drift effect. Then, an average of 4 to 5 images in each channel was used. All the detection parameters at each channel were kept constant, while the laser excitation power was adjusted to achieve good signal for each sample. The laser power settings (% of maximal intensity) were: 30% for DOPC GUVs with all probes, 10% for SM/Chol and DOPC/SM/Chol GUVs with NR12A, NR12S and Nile Red and 100% for SM/Chol and DOPC/SM/Chol GUVs with NR4A. The ratiometric images were generated by using special macros under ImageJ (developed by Romain Vauchelles) that divides the image of the $I_{550-600}$ channel by that of the $I_{600-650}$ channel. For each pixel, a pseudo-color scale is used for coding the ratio, while the intensity is defined by the integral intensity recorded for both channels at the corresponding pixel.

3D-PAINT and SR-PAINT super-resolution microscopy. 3D-PAINT and SR-PAINT imaging were performed with a home-built setup based on a Nikon Ti-E inverted fluorescence microscope, as previously described.[4] Briefly, a 561-nm laser (Coherent) was coupled to the back focal plane of an oil-immersion objective lens (Nikon CFI Plan Apochromat lambda 100x, NA1.45). A translational stage shifted the laser to the edge of the objective, thus illuminating ~1 μm into the sample at a typical power density of ~2 kW/cm^2. For 3D-PAINT, emission was filtered by a bandpass filter (ET605/70m, Chroma), and passed through a cylindrical lens (f = 1000 mm) to achieve astigmatism for axial localization.[5] Final image was projected onto an EM-CCD camera (iXon Ultra 897, Andor), which operated at 110 frames per second for 256x256 pixels for ~50,000 frames, or 200 frames per second for 256x128 pixels for ~100,000 frames. For SR-PAINT, emission was filtered with a long-pass filter (ET575lp, Chroma) and a short-pass filter (FF01-758/SP, Semrock), and cropped at the image plane of the microscope camera port to a width of ~4 mm. The cropped intermediate image was collimated by an achromatic lens (f = 80 mm), and was split into two paths at a 50:50 beam splitter (BSW10, Thorlabs). In Path 1, emission was

focused by an achromatic lens (f = 75 mm) onto one-half of an EM-CCD camera. In Path 2, emission was dispersed by an equilateral calcium fluoride prism (PS863, Thorlabs) before being focused by an achromatic lens (f = 60 mm) onto the other half of the same camera. Wavelength calibration was performed using fluorescent beads and narrow bandpass filters, as previously described.[6] The acquired single-molecule data were analyzed as described previously,[4,6] with time sequences of PAINT images generated using single-molecule data accumulated every ~1 min.

Supporting figures

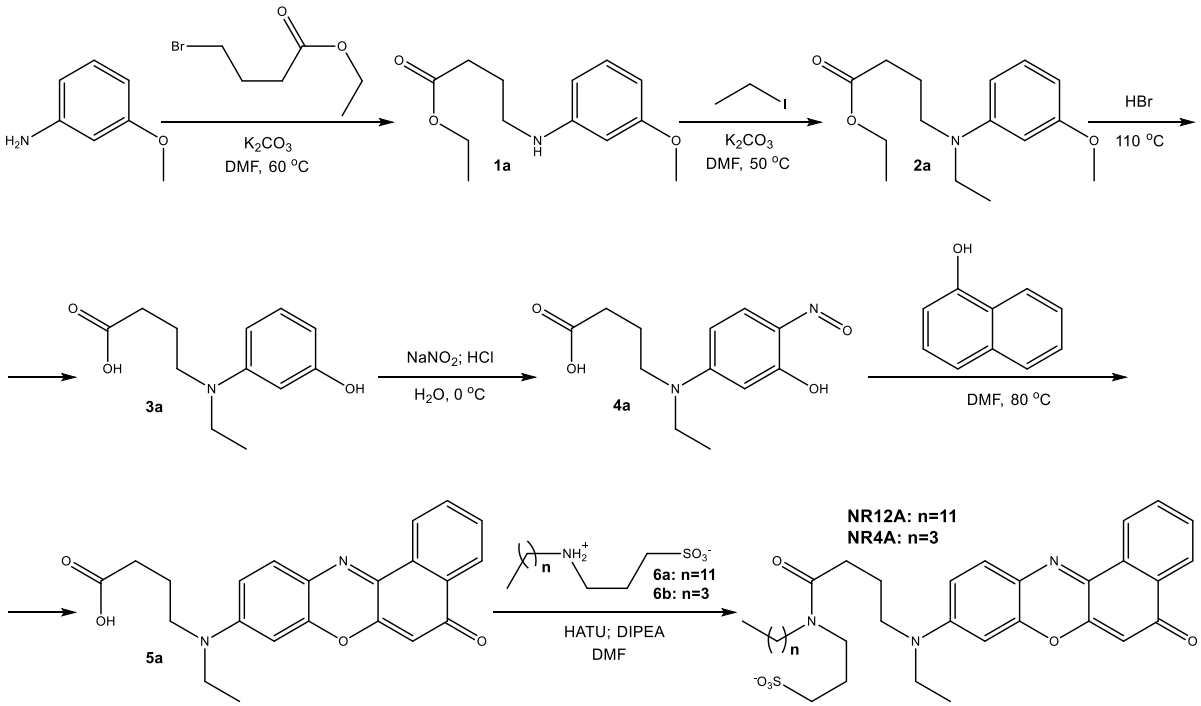

Fig. S1. Synthesis scheme for NR12A and NR4A membrane probes.

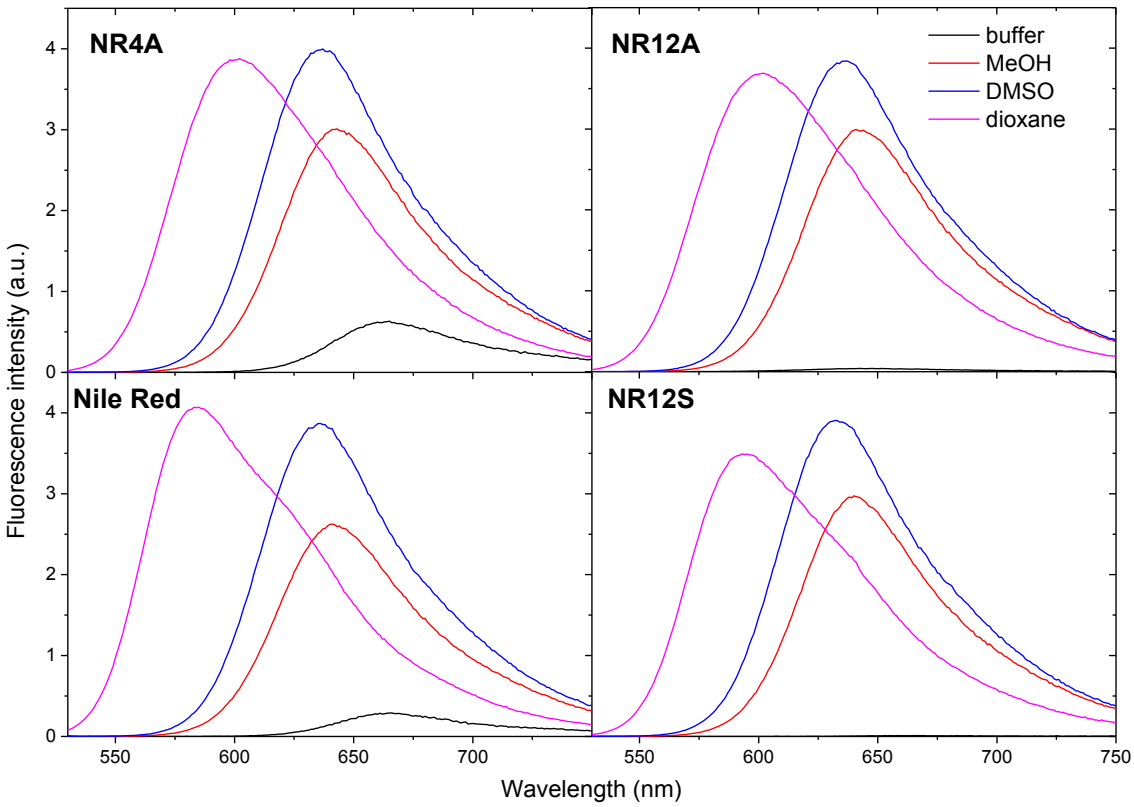

Fig. S2. Fluorescence emission spectra of membrane probes NR4A, NR12A, Nile Red, and NR12S in different solvents. Probe concentration 2 μM. Excitation wavelength was 520 nm. All the spectra were corrected via dividing by absorbance at the excitation wavelength.

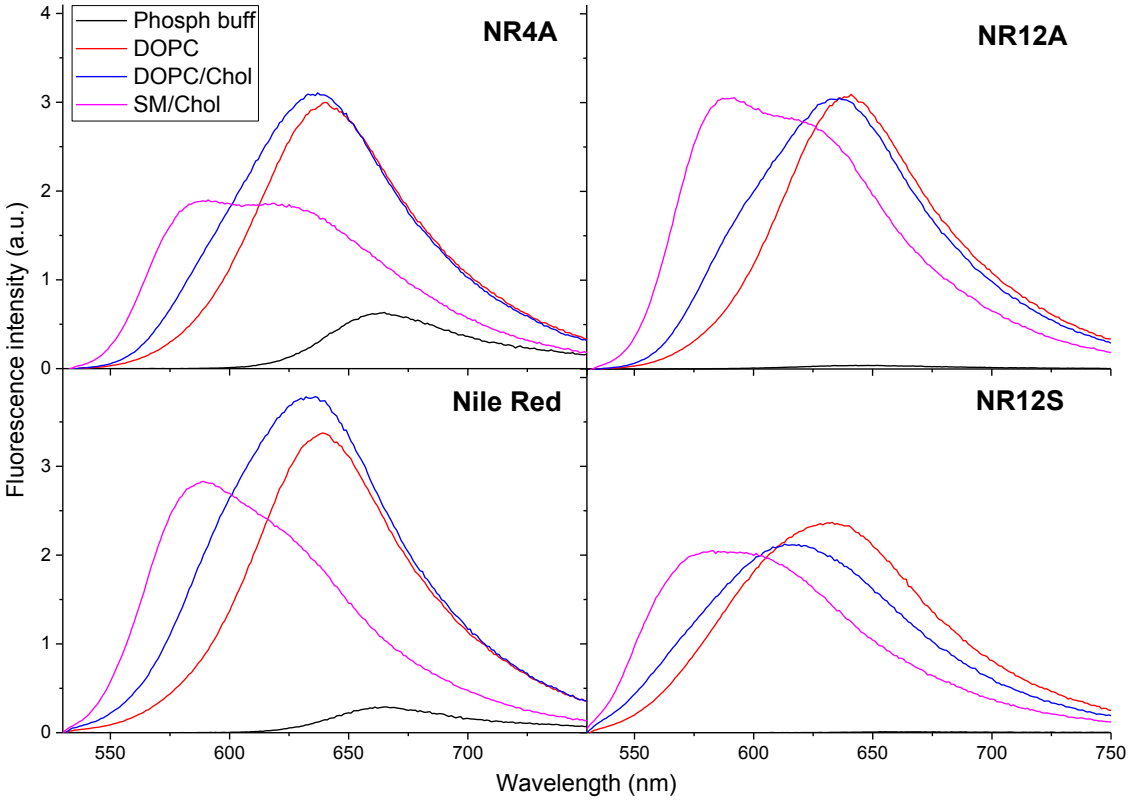

Fig. S3. Fluorescence emission spectra of membrane probes NR4A, NR12A, Nile Red, and NR12S in phosphate buffer and liposomes (LUVs) of different composition. Probe concentration 2 μM, lipid concentration 200 μM (in 20 mM phosphate buffer, pH 7.4). Excitation wavelength was 520 nm. All the spectra were corrected via dividing by absorbance at the excitation wavelength.

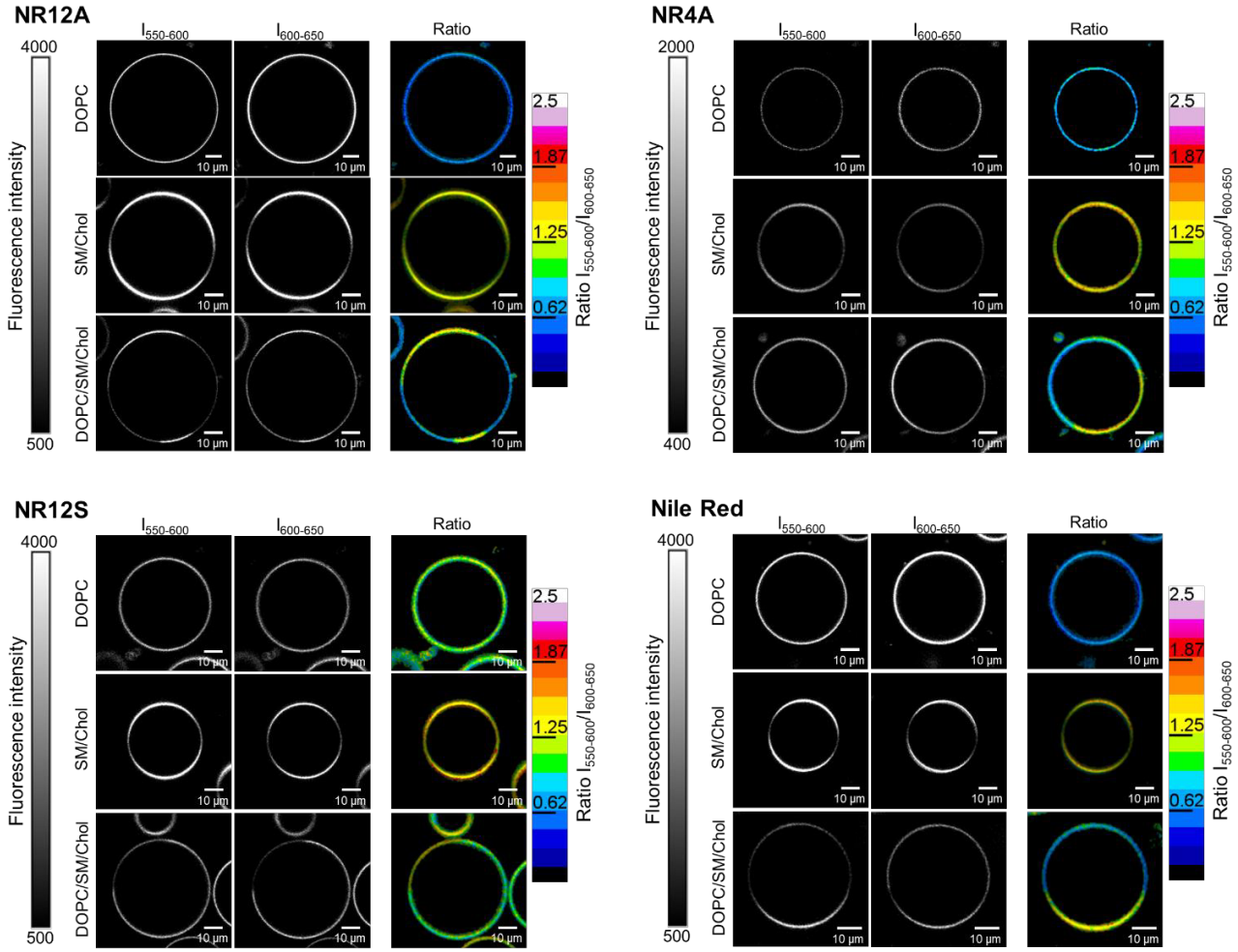

Fig. S4. Confocal microscopy images of giant vesicles (GUVs) of different compositions (DOPC; SM/Chol, 2/1; and DOPC/SM/Chol, 1/1/0.7) stained with NR12A, NR4A, NR12S, and Nile Red. Probe concentration was 200 nM (in 300 mM glucose solution). Excitation wavelength was 488 nm. Ratiometric images were created by dividing the intensity of $I_{550\text{-}600}$ channel by that of the $I_{600\text{-}650}$ channel for each pixel. The laser power settings (% of maximal intensity) were: 30% for DOPC GUVs with all probes, 10% for SM/Chol and DOPC/SM/Chol GUVs with NR12A, NR12S and Nile Red, and 100% for SM/Chol and DOPC/SM/Chol GUVs with NR4A.

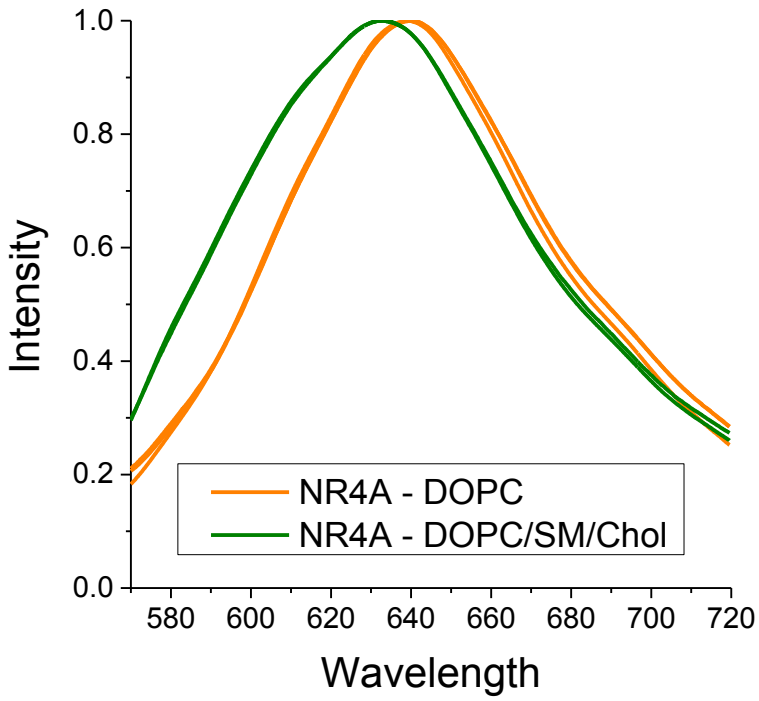

Fig. S5. Single-molecule spectroscopy results for NR4A (10 nM) in supported lipid bilayers. Averaged single-molecule spectra of NR4A on the DOPC bilayer (orange) and the bilayer composed of ternary lipid mixture (green).

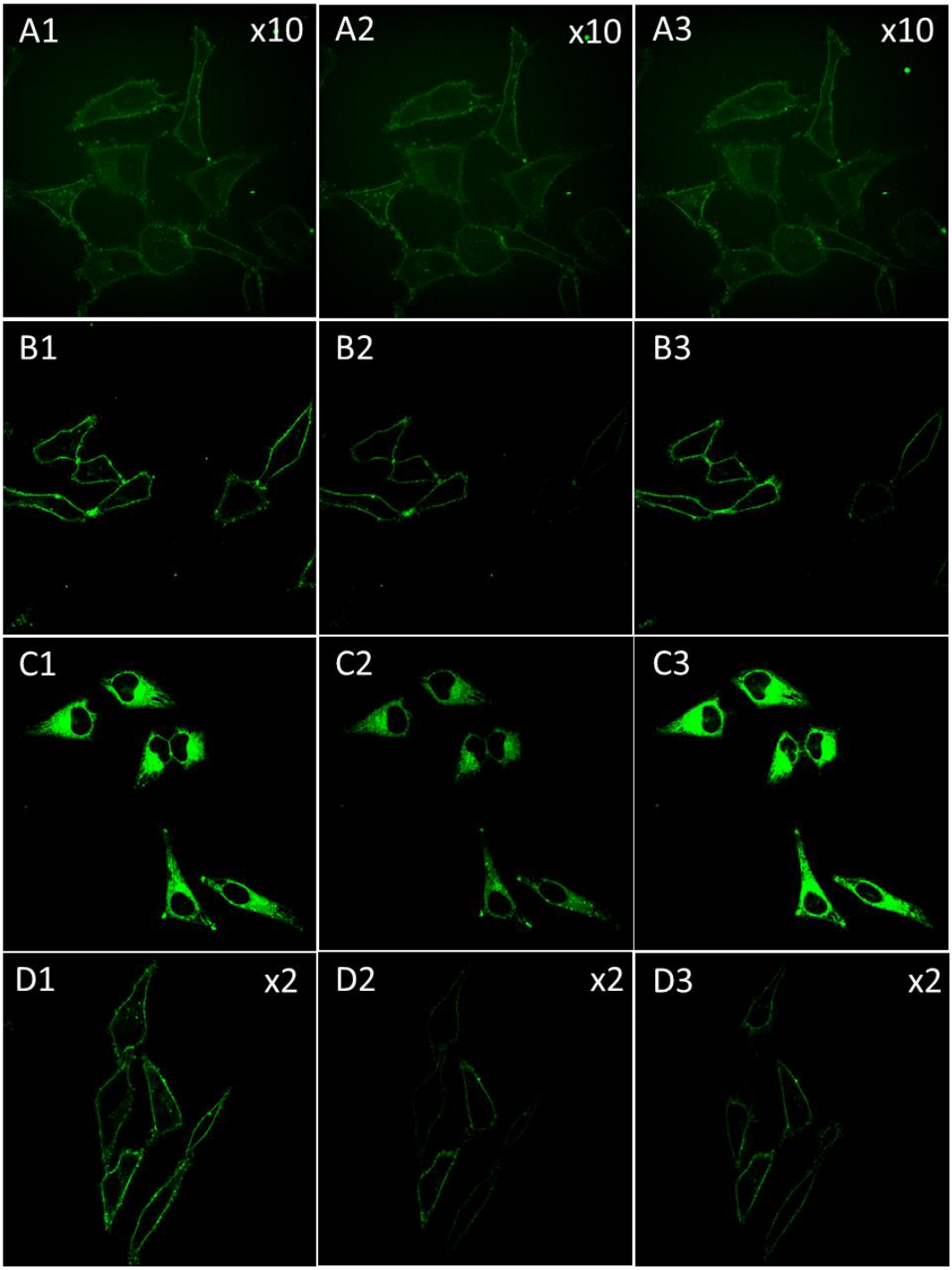

Fig. S6. Spinning disk confocal microscopy images of HeLa cells stained with NR4A, NR12A, Nile Red and NR12S before illumination (A1, B1, C1, D1), immediately after 60 seconds of illumination with 550 nm light at 3.14 $W \cdot cm^{-2}$ (A2, B2, C2 and D2, correspondingly), and after illumination followed by 10 min of incubation at r. t. (A3, B3, C3 and D3, correspondingly). Dye concentration 20 nM.

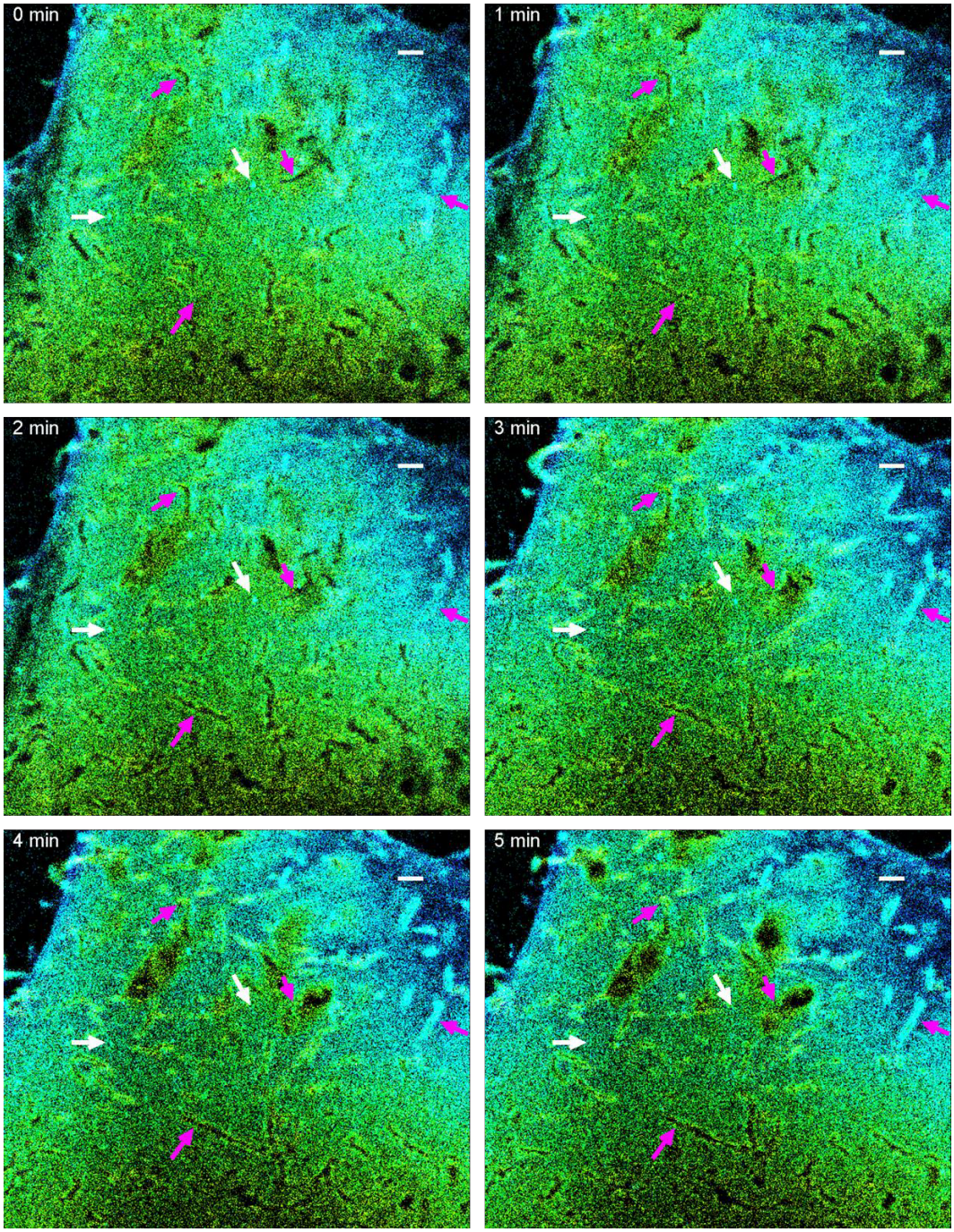

Fig. S7. (a) A time sequence of the 3D-PAINT data for the NR4A-stained plasma membrane of the HeLa cell shown in Fig. 2e-j, presented for single-molecule images accumulated every 1 min. Scale bar: 1 µm. Magenta arrows point to notable structural changes in the observed nanoscale protrusions. White arrows point to two apparent endocytosis sites that moved into the cell during the recording timeframe.

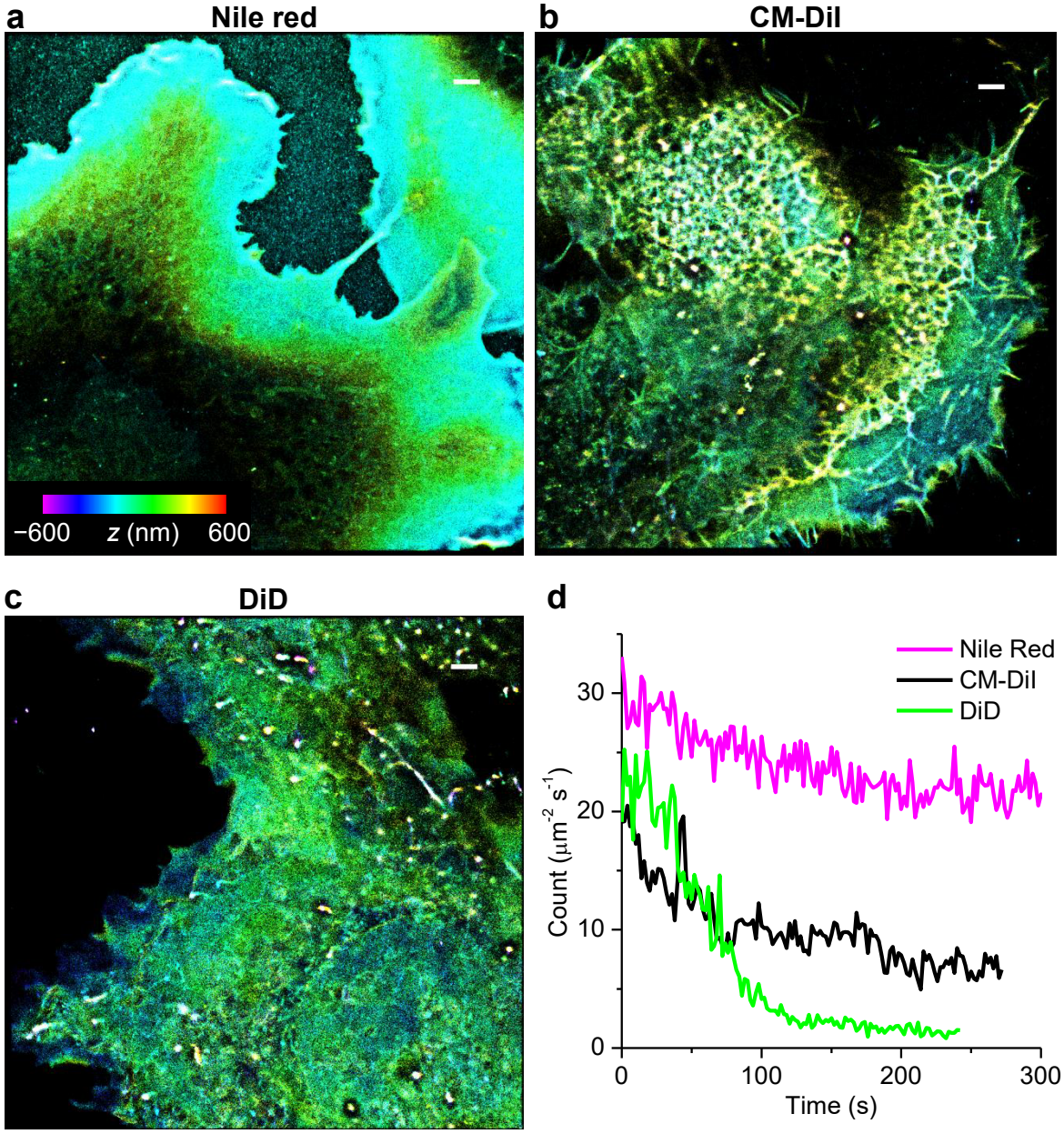

Fig. S8. 3D-SMLM images of live COS-7 cells stained with Nile Red (a), CM-DiI (b), and DiD (c). (a) Nile Red imaging was done by including 10 nM of the probe in the imaging media (L15 with 20 mM HEPES). (b,c) CM-DiI and DiD imaging was done by incubating the cells in 10 μM of the probes for 20 min, and then the probes were washed out. The imaging buffer contained an oxygen scavenger and 25 mM cysteamine to assist photoswitching. During imaging, a 405 nm laser was applied at ~0-1 W/cm^2 to photoswitch dark molecules to the emitting state. All three probes permeated the plasma membrane and stained internal structures including ER, mitochondrial, and nuclear membranes. (d) Time-dependent counts of single molecules detected per μm^2 per second for the three probes. Single-molecule images were recorded at 110 frames per second. This showed that DiD did not photoswitch well under this condition.

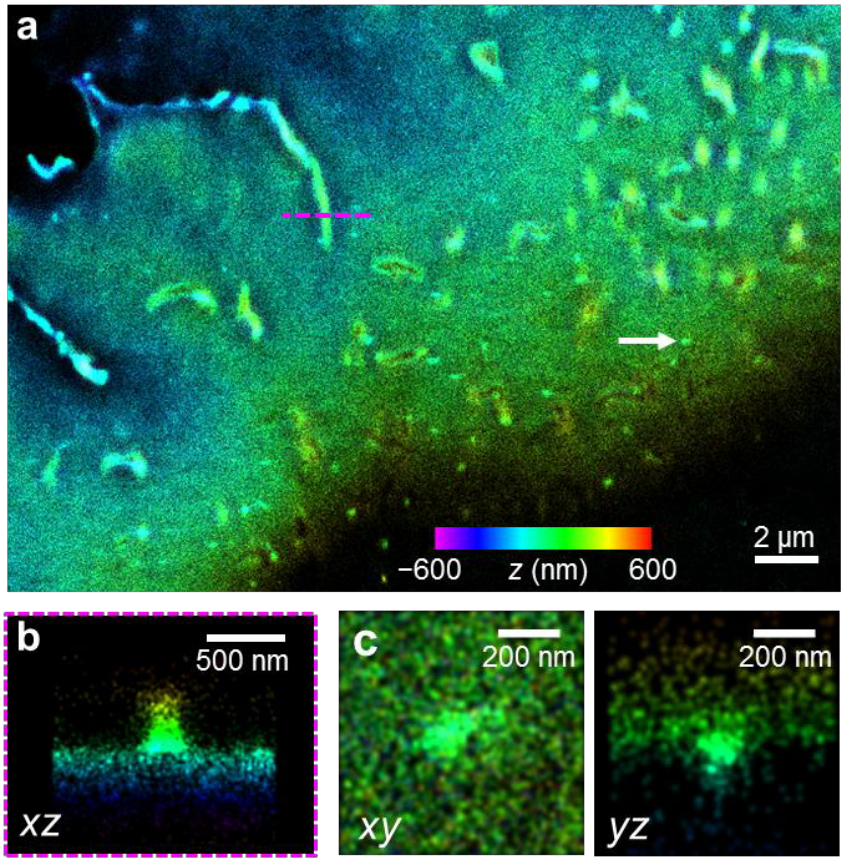

Fig S9. (a) Zoom-in 3D PAINT image of the top plasma membrane of a COS-7 cell stained by NR4A at 10 nM. (b) Virtual cross-section in the *xz* plane along the magenta dash line in (a). (c) Zoom-in in-plane (*xy*) and vertical (*yz*) images of the endocytosis site marked by the white arrow.

Supporting tables

Table S1. Absorption and emission band maxima and quantum yield values for membrane probes in solvents and lipid vesicles.

Solvent or medium	Probe name											
	NR12A			NR4A			Nile Red			NR12S		
	λ_{max} Abs	λ_{max} Em	QY (%)	λ_{max} Abs	λ_{max} Em	QY (%)	λ_{max} Abs	λ_{max} Em	QY (%)	λ_{max} Abs	λ_{max} Em	QY (%)
DOPC LUVs	552	641	51.1±1.3	552	640	53.0±3.3	549	639	55.4±2.4	530	633	47.6±2.1
DOPC/Chol LUVs	551	636	47.1±0.7	553	637	47.7±3.1	554	636	71.4±7.8	526	613	44.6±4.6
SM/Chol LUVs	546	592	39.4±5.4	552	591	41.4±2.3	541	589	52.0±5.1	510	583	42.7±4.6
PBS	537	648	0.096±0.018	586	665	10.1±2.3	586	666	4.7±0.7	521	655	0.097±0.025
MeOH	553	641	44.2±0.8	549	643	45.0±2.5	551	641	38.0±1.3	553	640	43.8±1.0
DMSO	555	637	71.1±2.5	553	637	75.0±2.6	550	336	71.1±2.5	550	633	74.2±2.6
Dioxane	526	602	69.8±2.4	526	602	74.6±2.6	520	585	74.1±2.6	520	593	67.8±2.3

[a] Probe concentration was 2 μM. Total phospholipid concentration for all liposomes was 200 μM (phosphate buffer 20 mM, pH 7.4). Excitation wavelength was 520 nm. Errors are standard deviation of the mean (n = 3).

Table S2. Ratios between fluorescence intensities at 640 nm and 591 nm (for NR12A, NR4A, Nile Red) or 633 nm and 583 nm (for NR12S) and full width at half maximum values for membrane probes in lipid vesicles of different composition.[a]

	NR12A	**NR4A**	**Nile Red**	**NR12S**
	$\mathbf{I_{591}/I_{640}}$	$\mathbf{I_{591}/I_{640}}$	$\mathbf{I_{591}/I_{640}}$	$\mathbf{I_{583}/I_{633}}$
DOPC	0.253±0.003	0.261±0.012	0.276±0.008	0.500±0.015
DOPC/Chol	0.552±0.015	0.490±0.026	0.565±0.022	0.758±0.029
SM/Chol	1.48±0.02	1.27±0.14	1.55±0.10	1.44±0.09
	FWHM (nm)	**FWHM** (nm)	**FWHM** (nm)	**FWHM** (nm)
DOPC	76.8±0.2	77.5±0.1	76.8±0.1	99.5±0.2
DOPC/Chol	90.3±0.4	87.5±0.9	90.9±0.7	104.0±0.8
SM/Chol	91.5±4.5	102.8±8.2	89.9±5.8	100.3±6.5

[a]Errors are standard deviation of the mean (n = 3).

Supporting Movie

Movie S1. Time-laps recordings for 1 s of single-molecule raw images (110 frames per second) taken in DOPC supported bilayers with 10 nM of NR12A, NR4A, NR12S or Nile Red in DPBS. Scale bars: 2 μm.

References

[1] M. L. Deda, M. Ghedini, I. Aiello, T. Pugliese, F. Barigelletti, G. Accorsi, *J. Organomet. Chem.* **2005**, *690*, 857.

[2] K. Sakai, M. Kaji, Y. Takamatsu, K. Tsuchiya, K. Torigoe, K. Tsubone, T. Yoshimura, K. Esumi, H. Sakai, M. Abe, *Colloid Surf. A-Physicochem. Eng. Asp.* **2009**, *333*, 26.

[3] O. A. Kucherak, S. Oncul, Z. Darwich, D. A. Yushchenko, Y. Arntz, P. Didier, Y. Mely, A. S. Klymchenko, *J. Am. Chem. Soc.* **2010**, *132*, 4907.

[4] S. Moon, R. Yan, S. J. Kenny, Y. Shyu, L. M. Xiang, W. Li, K. Xu, *J. Am. Chem. Soc.* **2017**, *139*, 10944.

[5] B. Huang, W. Wang, M. Bates, X. Zhuang, *Science* **2008**, *319*, 810.

[6] Z. Y. Zhang, S. J. Kenny, M. Hauser, W. Li, K. Xu, *Nat. Methods* **2015**, *12*, 935.

2.3. Development of solvatochromic organelle-targeted probes, sensitive towards polarity and lipid order

On the next step, we decided to create an array of organelle-targeted environment-sensitive Nile Red probes by tethering our improved Nile Red acid to the moieties which ensure probe selective accumulation in: lysosomes, mitochondria, ER, Golgi apparatus, lipid droplets and plasma membrane (Fig. 2.3.1, A).

Our probes are expected to sense oxidative stress (due to an increase of polarity of biomembranes, caused by lipid peroxidation[284]) and hyperosmotic shock (due to a drop in the lipid order in organelle membranes, associated with changes in their geometry[285] during mechanical deformation) (Fig. 2.3.1, B). Owing to their selective organelle accumulation, the Nile Red probes are presumed to provide a possibility to compare the organelle membrane polarity in intact live cells, as well as the organelle-specific response to external chemical or physical stimuli.

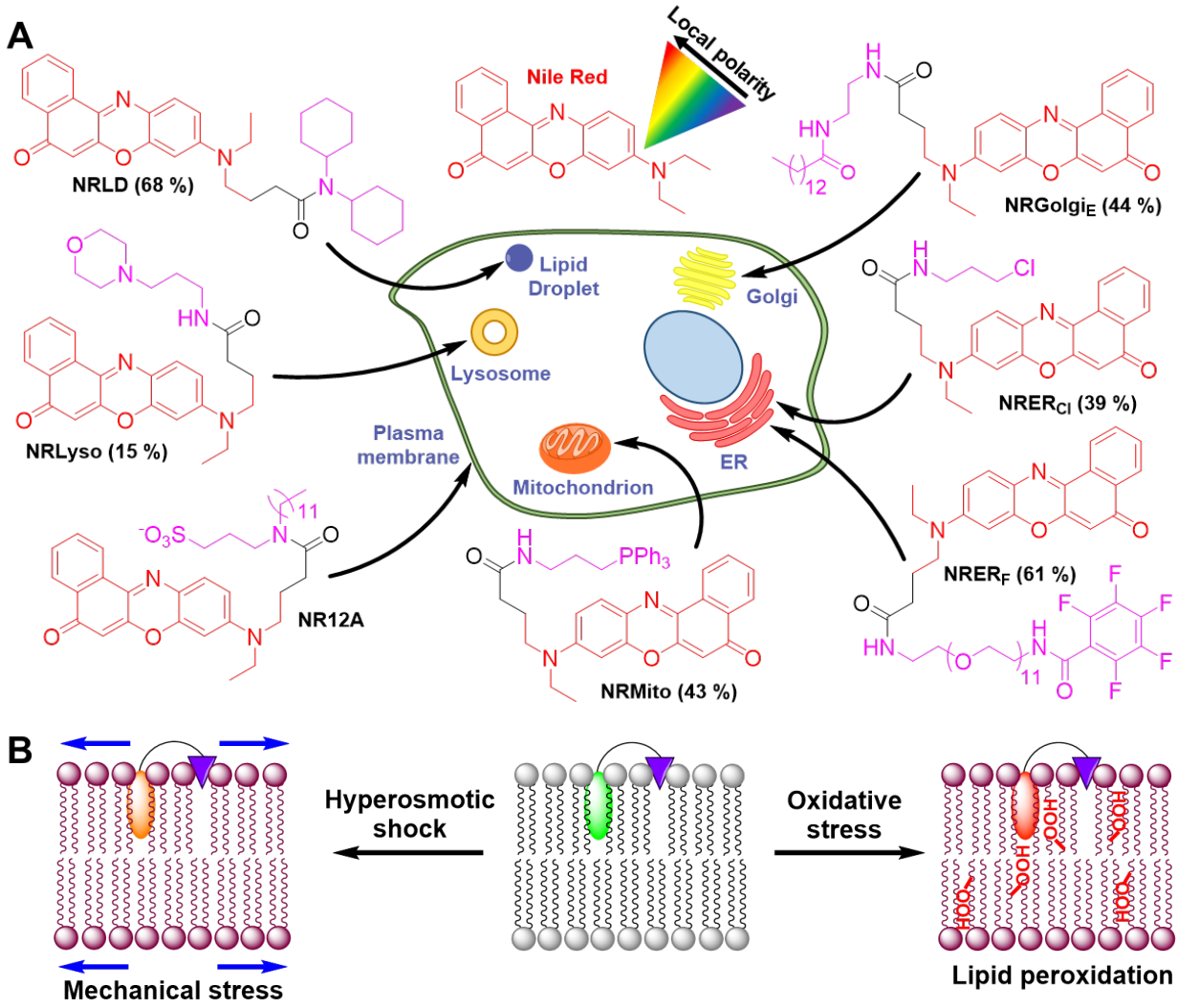

Fig. 2.3.1. Design of organelle-targeted Nile Red probes (A). Mechanism of sensing of the external stimuli by solvatochromic Nile Red probes (B).

In total, six new probes were synthesized with moderate to high yields through the modification of Nile Red fluorophore N-alkyl chain (Fig. 2.3.2). On the last step, the Nile Red acid derivative (**1**) was tethered to the corresponding primary or secondary amines through peptide coupling protocol (Fig. 2.3.2).

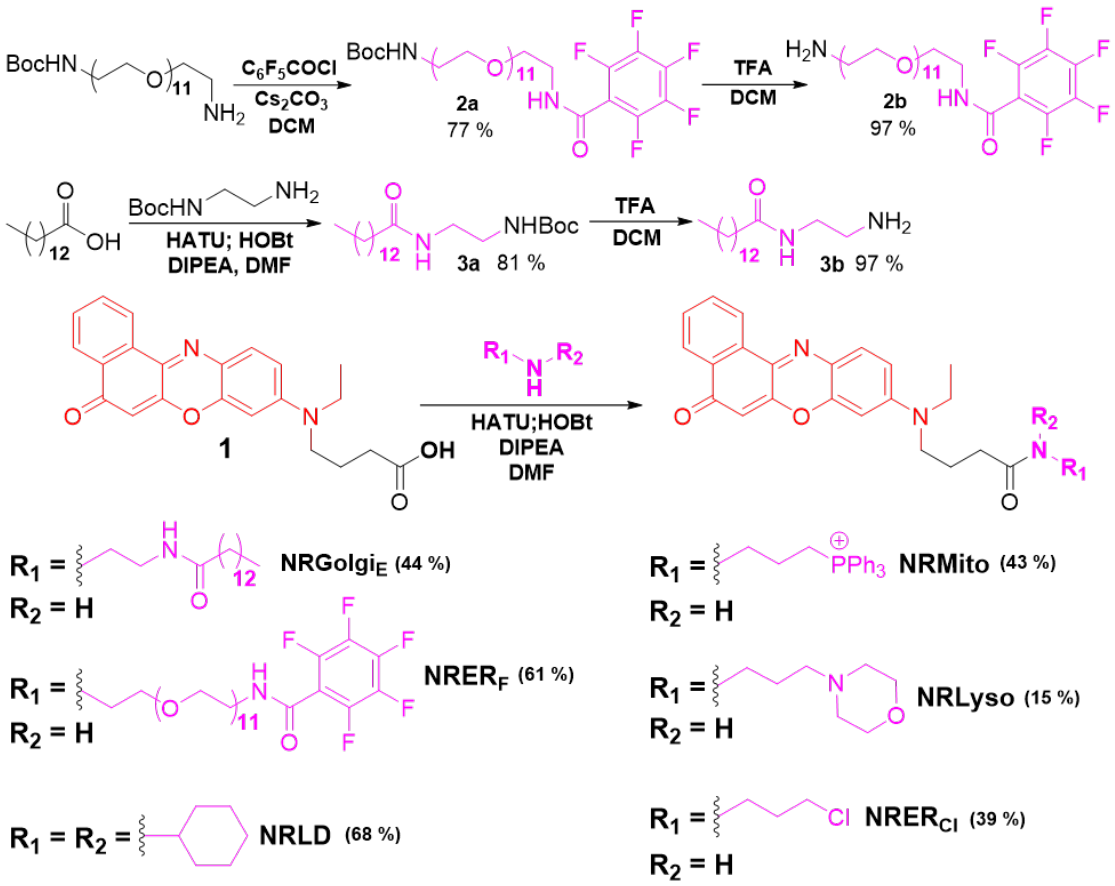

Fig. 2.3.2. Synthesis of organelle-targeted Nile Red probes (A).

All of our new probes, when studied in organic solvents of different polarity, showed high fluorescence quantum yields and the solvatochromic shifts similar to those of a parent Nile Red fluorophore, evidencing that the fluorophore system is not perturbed after functionalization. During spectroscopy experiments in LUVs with different lipid compositions all Nile Red organelle probes have shown an increase in fluorescence quantum yields in DOPC together with a blue shifted emission around 640-650 nm when compared with phosphate buffer (Fig. 2.3.3). These results indicate that all our probes partition well into Ld lipid phase, which they sense as a less polar environment compared to the buffer. In the presence of cholesterol, a further blue shift was systematically observed (Fig. 2.3.3), indicating that Nile Red probes possess some sensitivity to the expulsion of water molecules form the lipid membrane, produced by cholesterol. In SM/Chol LUVs the hypsochromic shifts were much stronger, 40-60 nm more when compared to DOPC, signalizing that our probes preserve an ability to detect much less polar/hydrated environment in the tightly packed Lo phase (Fig. 2.3.3). The exceptions from this behavior were in case of $NRER_F$ and, to a lesser extent, NRMito: these Nile Red probes showed a strong contribution of red-shifted emission from the aqueous medium of the buffer together with a short-wavelength shoulder, which corresponded to the Lo phase (Fig. 2.3.3). These results evidence that the probes are mostly excluded from the tightly packed Lo phase, possibly due to an increased polarity and/or bulkiness of their targeting moieties. However, a presence of the blue-shifted shoulder suggests that a fraction of the probe can still partition into the lipid vesicles and report on the low polarity of the Lo phase interior. In general, the developed Nile Red probes are capable

of binding the lipid membranes and distinguish between Lo and Ld phases, though some probes, such as $NRER_F$ and NRMito, show lower affinity towards the Lo phase.

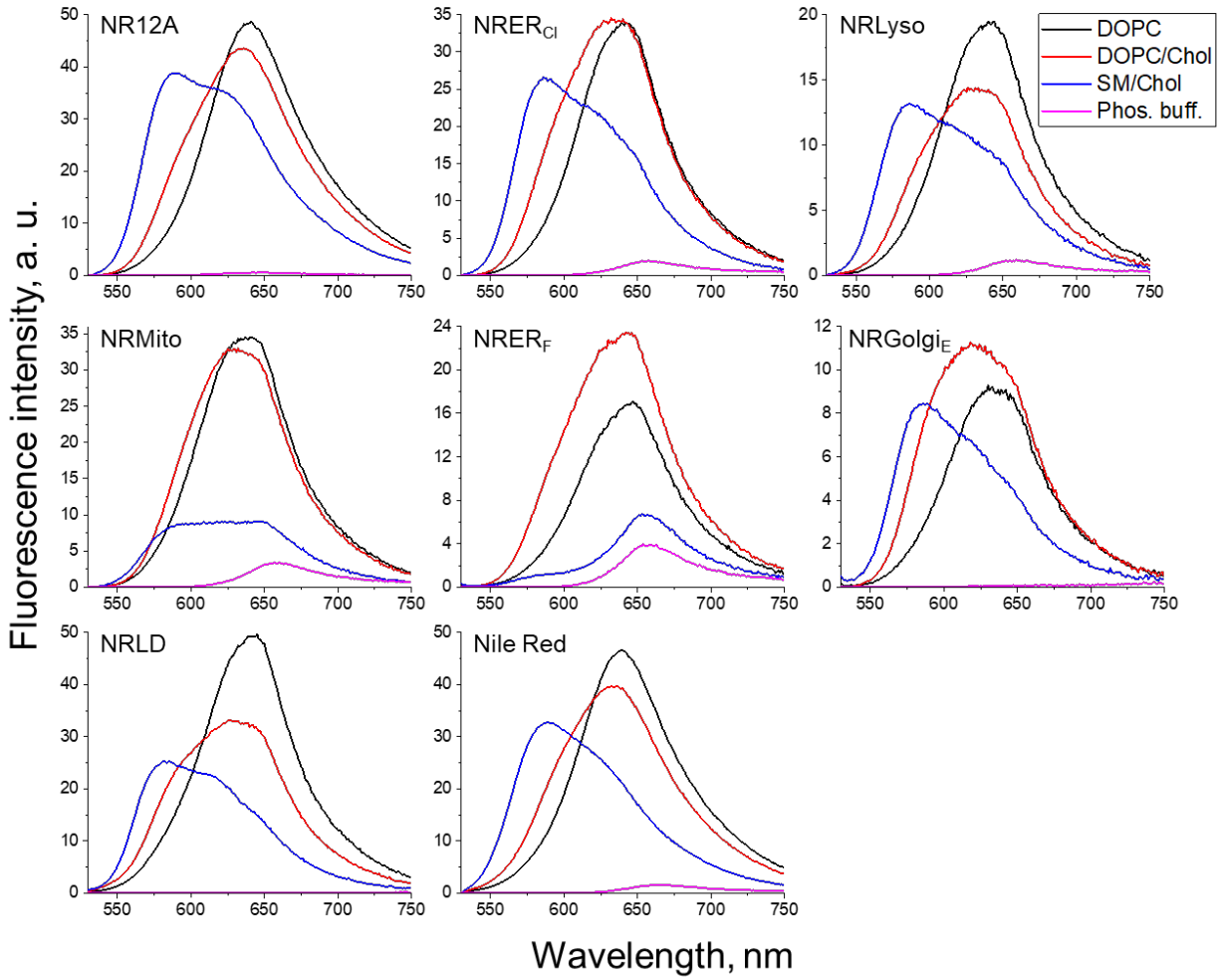

Fig. 2.3.3 Fluorescence emission spectra of the probes NR12A, $NRER_{Cl}$, NRlyso, NRMito, $NRER_F$, $NRGolgi_E$, NRLD and unsubstituted Nile Red in lipid vesicles (LUVs) of different composition. Probe concentration was systematically 2 μM. Total lipid concentration was 1 mM. Excitation wavelength was 520 nm.

Next, we assessed the efficiency of the organelle targeting during the colocalization microscopy experiments in live KB and HeLa cells. All of our probes exhibit significant colocalization with the corresponding commercial organelle markers in live KB cells (Fig. 2.3.4.), showing the Pearson`s correlation coefficient values within the range from 0.89 to 0.96 (except $NRGolgi_E$) in live KB cells. Remarkably, the probe NRLyso exhibited even higher selectivity in both cell lines when compared to commercial LysoTracker Green, which can be concluded from the lower background noise in the images (Fig. 2.3.4, E). Moreover, our probe NRLD showed higher selectivity towards lipid droplets in HeLa cells compared to the parent Nile Red dye, probably owing to an increased hydrophobicity and bulkiness of dicyclohexylamino group.

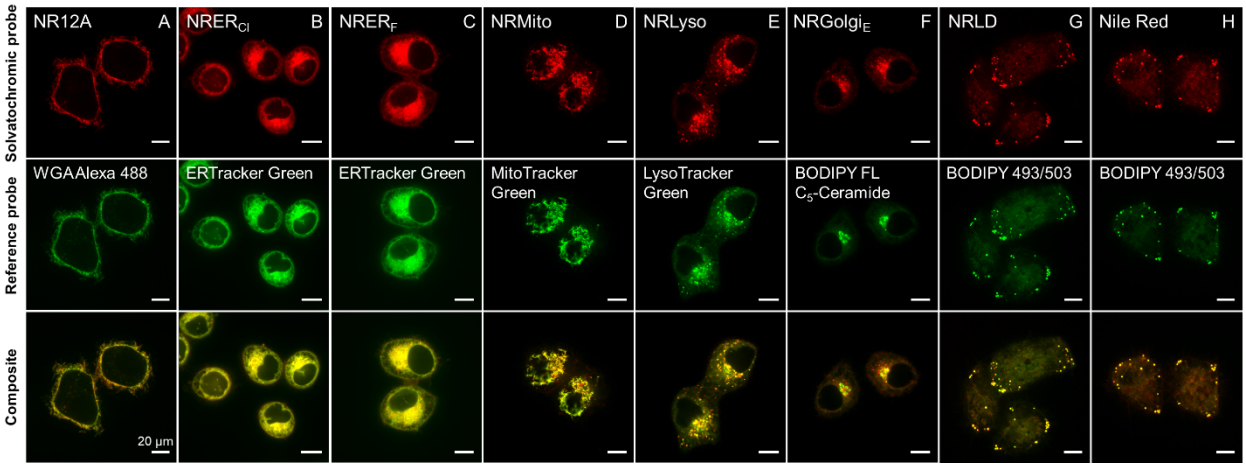

Fig. 2.3.4. Colocalization microscopy imaging of live KB cells stained with organelle-targeted Nile Red probes and commercial organelle-targeted probes. Probe concentration: 20 nM for NR12A; 50 nM for NRMito, NRLyso, NRLD, NRERCl; 200 nM for NRERF; 2.5 μM (in form of BSA-conjugate) for NRGolgiE.

On the next step, the ratiometric microscopy imaging was used to test the performance of the solvatochromic organelle probes in live cells. The fluorescence emission was collected at two different channels: I_1 (550-600 nm) and I_2 (600-650 nm), which were then used to create the ratiometric (I_1/I_2) microscopy images. Prior to the analysis of the images in live cells, all of the probes were calibrated in the model lipid membranes (LUVs of different compositions, representing Lo and Ld phases). Ratiometric microscopy images of LUVs exhibited a drastic change in the in the pseudo-colour, evidencing an increase in the (I_1/I_2) ratio for the probes in the Lo compared to Ld (Fig. 2.3.5, A). The magnitude of this change, judging from the pseudo-colour (Fig. 2.3.5, A) and from the difference in the average ratio values (Fig. 2.3.6, A), was the highest in case of NR12A and the lowest for $NRER_F$, being in line with the results of the spectroscopy experiments in LUVs (Fig. 2.3.3). The results of ratiometric microscopy revealed significant variation of pseudo-colour between different organelles (Fig. 2.3.5, B), reflecting the differences in their local membrane polarity. According to the obtained data, mitochondria and ER are having the most polar interior (orange pseudo-colour), while the lipid droplets (blue-violet) and PM (blue-green) are sensed as regions with significantly lower local polarity. In order to be able to interpret these differences in local polarity changes in terms of lipid order, we analyzed the distribution of the ratio in live cells and compared it with the distributions obtained for each probe from the calibration images in LUVs (Fig. 2.3.5, C). Moreover, we introduce a lipid order parameter (LOP) ($LOP = (R-R_{DOPC})/(R_{SM/Chol}-R_{DOPC})$), this parameter approaches 0 and 1, when the (I_1/I_2) ratio (R) is close to the corresponding value in Ld (R_{DOPC}) and Lo ($R_{SM/Chol}$) phase in LUVs, respectively (Fig. 2.3.6, B). According to the performed analysis, the highest level of lipid order was observed in plasma membranes, being close to that in SM/Chol, in line with literature.[15, 91, 286] In case of all intracellular organelles the observed LOP values were significantly lower compared to PM and decreased in the following order: $NRMito \sim NRER_{Cl} > NRLyso > NRGolgi_E > NRER_F$. Notably, the reported local lipid order differs greatly in case of the two probes accumulating in the endoplasmic reticulum ($NRER_{Cl}$ and $NRER_F$), which could be explained by the distinct

localizations of the two probes in lipid membranes inside the ER, in line with the results of the experiments in model membranes. In case of a lipid droplet marker, the LOP analysis was not applied, as the lipid composition of LDs is different from the one in Lo or Ld phases of lipid bilayers. This fact also explains the observed much lower polarity of lipid droplets.

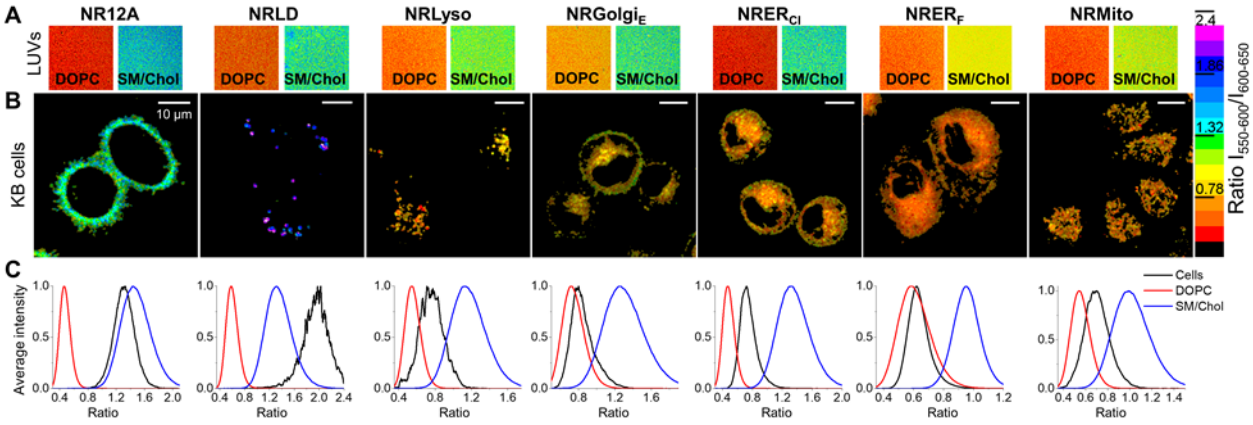

Fig. 2.3.5. Nile Red solvatochromic probes reveal differences in polarity and lipid order within the organelles in live KB cells. Ratiometric microscopy images in LUVs (A) and live cells (B) with the corresponding average intensity histograms (C). Probe concentration 20 nM for NR12A; 50 nM for NRMito, NRLyso, NRLD, NRER$_{Cl}$; 200 nM for NRER$_F$; 5 μM (in form of BSA-conjugate) for NRGolgi$_E$.

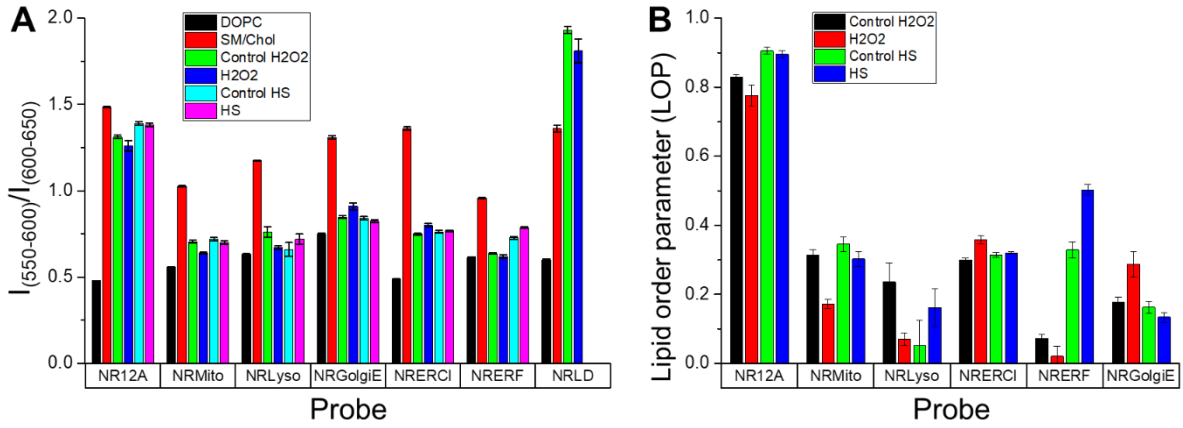

Fig. 2.3.6. Weighted arithmetic mean values of fluorescence intensities ratio $I_{(550-600)}/I_{(600-650)}$ (A) and Lipid order parameter (LOP) values (B) calculated from ratiometric microscopy images of Nile Red organelle probes in LUVs and KB cells under various conditions.

When the cells are exposed to the action of hydrogen peroxide, they are in conditions of oxidative stress, and the polarity of organelle membranes is expected to change as a consequence of lipid peroxidation.[287] The (I_1/I_2) ratio, which reflects the local polarity, altered to different degrees within the different organelles studied, with the most pronounced difference observed in case of LDs, lipid droplets and mitochondria (Fig. 2.3.6 and Fig. 2.3.7). In case of lipid droplets, the high magnitude of response to the oxidative stress is in line with literature data[288] and could

be attributed to the high content of easily oxidizable unsaturated lipids. The observed significant change in polarity in lysosomes could be possibly explained by the fact that the interior of these organelles derives from the extracellular medium and therefore the lysosomes are highly susceptible to the action of H_2O_2, added to the medium. The heterogeneity of lysosomal polarity values increased under oxidative stress (i. e. the broadening of distribution of the intensity ratio was observed, Fig. 2.3.7, C), in line with the literature data.[289] In case of mitochondria the high level of response correlates with the literature data concerning high sensitivity of these organelles to the action of oxidative stress, which is directly linked to apoptosis and aging.[290, 291] The PM, on the other hand, exhibits lower level of response, probably due to a high content of saturated lipids, which are less prone to peroxidation. Surprisingly, $NRER_{Cl}$ and especially $NRGolgi_E$ showed a decrease in polarity after the cells were subjected to oxidative stress. For $NRGolgi_E$, this unexpected polarity decrease could be related to an increase in the fraction of saturated lipids and cholesterol in Golgi due to an oxidative stress. In addition, the oxidative stress seems to affect the localization of the probes in cells, thus, the intensity of some of the probes increased significantly after the treatment with H_2O_2. Overall, the induction of oxidative stress resulted in the significant alternations of polarity/lipid order in the membranes of the whole cell with the strong variations in the response within the different organelles.

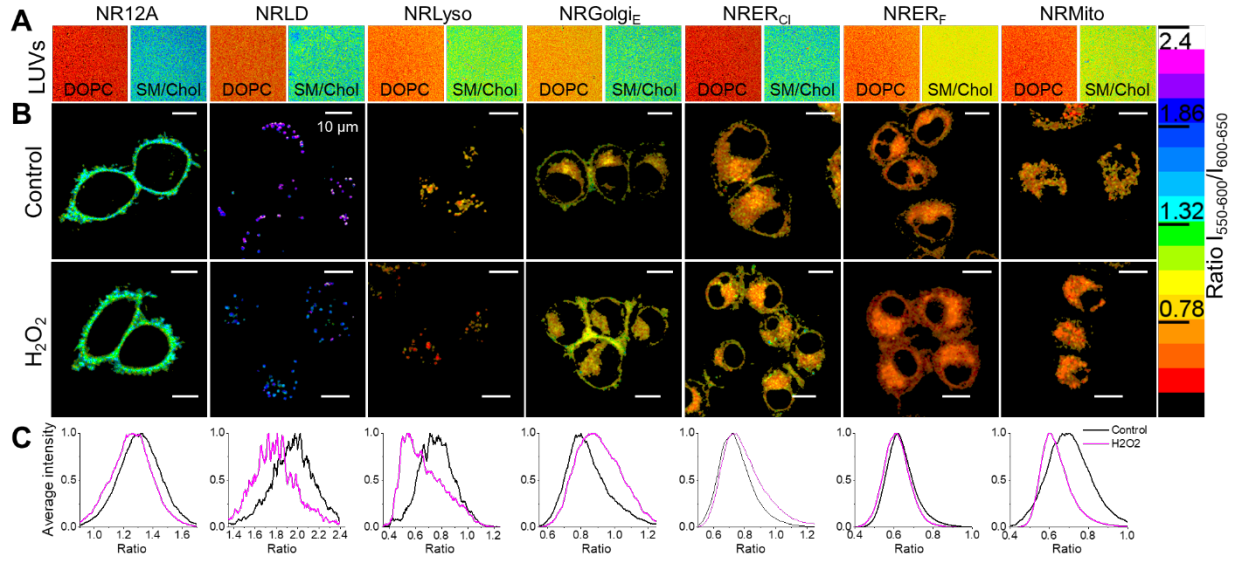

Fig. 2.3.7. Response of live KB cells to oxidative stress imaged by Nile Red organelle probes. Ratiometric microscopy images in LUVs (A) and live cells (B) with the corresponding average intensity histograms (C). Probe concentration was 20 nM for NR12A; 50 nM for NRMito, NRLyso, NRLD, $NRER_{Cl}$; 200 nM for $NRER_F$; 5 μM (in form of BSA-conjugate) for $NRGolgi_E$.

Mechanobiology is a rapidly growing research field with covers several aspects, notably tumor growth,[292] cell development,[293] and collective cellular behavior.[294] Currently, an intensive research is performed concerning the development of the tools to monitor mechanical stress at the level of organelles. [38, 46, 51]

A simple way to induce mechanical stress is to change the osmolality of cellular medium, *e.g.* a hyperosmotic stress induction is accompanied by changes in lipid order and cell

morphology.[38, 46] Here, the effect of hyperosmotic stress on the organelles of live KB cells was studied using the Nile Red organelle probes by monitoring the changes in polarity and lipid order (Fig. 2.3.8). Upon the induction of hyperosmotic stress, the plasma membrane underwent a change in morphology, which resulted in a jagged pattern together with an appearance of less ordered (more polar) regions in the innermost parts of the PM. This result is in line with the previous data (see section 2.2) and could be possibly explained by a decrease in the lipid order for the membrane regions, undergoing the largest displacement during the shrinking of the cell. The innermost parts of the PM seem to undergo more deformation, probably by stretching, compared to the extremities, where the possible shrinkage is limited, presumably due to the presence of rigid cytoskeleton filaments. In general, the local polarity increase (Fig. 2.3.6, A) and a decrease in LOP values (Fig. 2.3.6, B) for plasma membrane in hyperosmotic conditions correlated with the decrease in the lipid order, observed by a mechanoselective PM-targeted flipper probe.[38, 46] In addition to the plasma membrane, an increase in polarity was also observed for mitochondria and Golgi apparatus, while lysosomes and ER exhibited a decrease in polarity (Fig. 2.3.8, B, C). In case of mitochondria, the observed drop in LOP values and an increase in polarity correlate well with a decrease in the microviscosity and the lipid order, observed by mitochondria-targeted molecular rotor[51] and flipper[46] probes, respectively. Moreover, it is in line with a recent result, obtained with a mitochondria-targeted solvatochromic probe.[295] Notably, the decrease in lysosomal polarity together with an an increased LOP value (Fig. 2.3.8, B-C and Fig 2.3.6, B) could be possibly attributed to the shrinkage of lysosomes, which leads to induction of higher lipid order at the inner leaflet of lysosomes, at the place of the localization of NRLyso. It should be noted that the variations of the intensity ratio of the probes in plasma membranes, lysosomes and ER (for $NRER_F$) were observed varied within the nontreated cells of different cell culture passages (cells in Fig. 2.3.8 are ~8 passages older than those in Fig. 2.3.7). This rather peculiar effect requires a dedicated study in order to verify whether the cell aging can affect the polarity of these biomembranes. Different response towards the hyperosmotic stress was also observed in case of the two ER-targeted probes: while the (I_1/I_2) ratio did not change for $NRER_{Cl}$, the probe $NRER_F$ reported a pronounced decrease in the local polarity (Fig. 2.3.8, Fig. 2.3.6). Such a difference could possibly be explained by a higher sensitivity of a polar and bulky PEGylated targeting moiety in case of $NRER_F$ to the changes in the ER morphology and/or in the salt concentration during hyperosmotic stress. According to the data of the spectroscopy experiments in LUVs, the probe $NRER_F$ is partially excluded from the membrane (Fig. 2.3.3), and the compaction of the endoplasmic reticulum during the cell shrinkage could induce a deeper insertion of the Nile Red moiety into the membranes inside the ER. The obtained result is in line with a reported microviscosity increase sensed with an ER-targeted molecular rotor,[51] though an ER-targeted flipper probe exhibited some decrease in the lipid order in similar conditions.[46] On the other hand, the membrane polarity in the endoplasmic reticulum does not seem to be directly affected by the hyperosmotic stress, as evidenced by an absence of any changes in the ratio for a well-inserted ER probe $NRER_{Cl}$. Overall, an induction of mechanical stress in cells resulted in significantly different responses within the organelles, probably due to different geometry and lipid composition of their membranes, as well as different localization of the probes within the leaflets of lipid bilayer together with a varied degree of the fluorophore insertion.

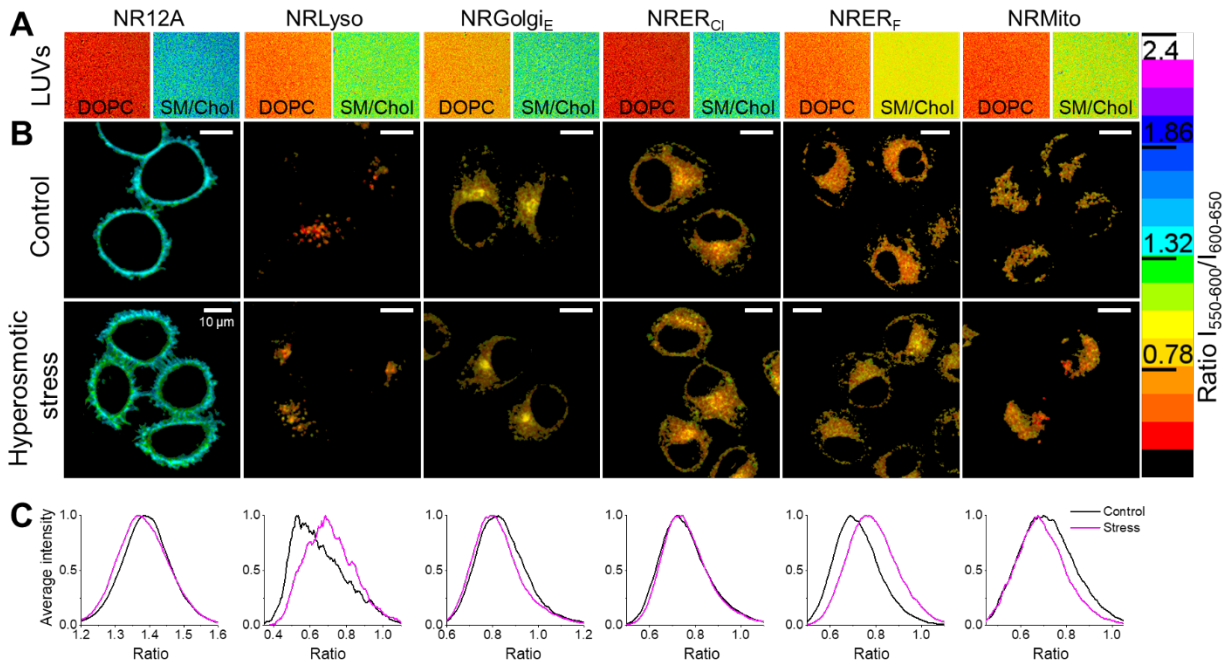

Fig. 2.3.8. Response of live KB cells to hyperosmotic shock imaged by solvatochromic organelle probes. Ratiometric microscopy images in LUVs (A) and live cells (B) with the corresponding average intensity histograms (C). Probe concentration: 20 nM for NR12A; 50 nM for NRMito, NRLyso, NRER$_{Cl}$,; 200 nM for NRER$_F$; 5 μM (in form of BSA-conjugate) for NRGolgi$_E$.

The results of the project were submitted for publication.

2.4. Development of reactive plasma membrane probes

The concept of reactive plasma membrane probes involves development of functionalized fluorophore molecules, which are able to target plasma membrane with consequent reaction with the PM proteins or added linker molecules. After the reaction the probes are expected to be immobilized on the plasma membrane, which would lead to long-term and wash-resistant staining. In principle, it can be done using either irreversible covalent binding or reversible dynamic bonds, in the latter case rendering the staining environment-sensitive.

2.4.1 Reactive probes based on bivalent reactive amphiphiles

One of the possible approaches to create the reactive probes exploits the reversible formation of hydrazone bonds between the corresponding hydrazides and carbonyl compounds (Fig. 2.4.1). A characteristic feature of the reaction between a hydrazide and a carbonyl compound (typically an aldehyde or a ketone) is that its velocity and the equilibrium between the product and the reagents can be shifted depending on the pH. [296-298] Thus, at the pH values *ca* 5-6 the equilibrium is shifted towards the product formation,[297] however, at lower values it is possible to hydrolyze the formed hydrazone adduct. Additional tuning of the pH sensitivity could be possibly achieved by varying the electron density of the carbonyl compound.

The concept of the reactive fluorescent probes, based on hydrazone chemistry, includes the two components: functionalized cyanine dyes, bearing two hydrazide moieties, and special bivalent reactive amphiphiles, bearing two carbonyl groups and two membrane-targeting motifs (Fig. 2.4.1). We expect that the cyanine hydrazides to form hydrazone bonds with the bivalent amphiphiles on cell plasma membrane, which would lead to dye oligo- or polymerization, resulting in long-term fixation of the cyanines on cell surface. At the same time, due to an intrinsic sensitivity towards the pH we expect this “coating” to disassemble at low pH, giving rise to a pH-sensitive reversible staining.

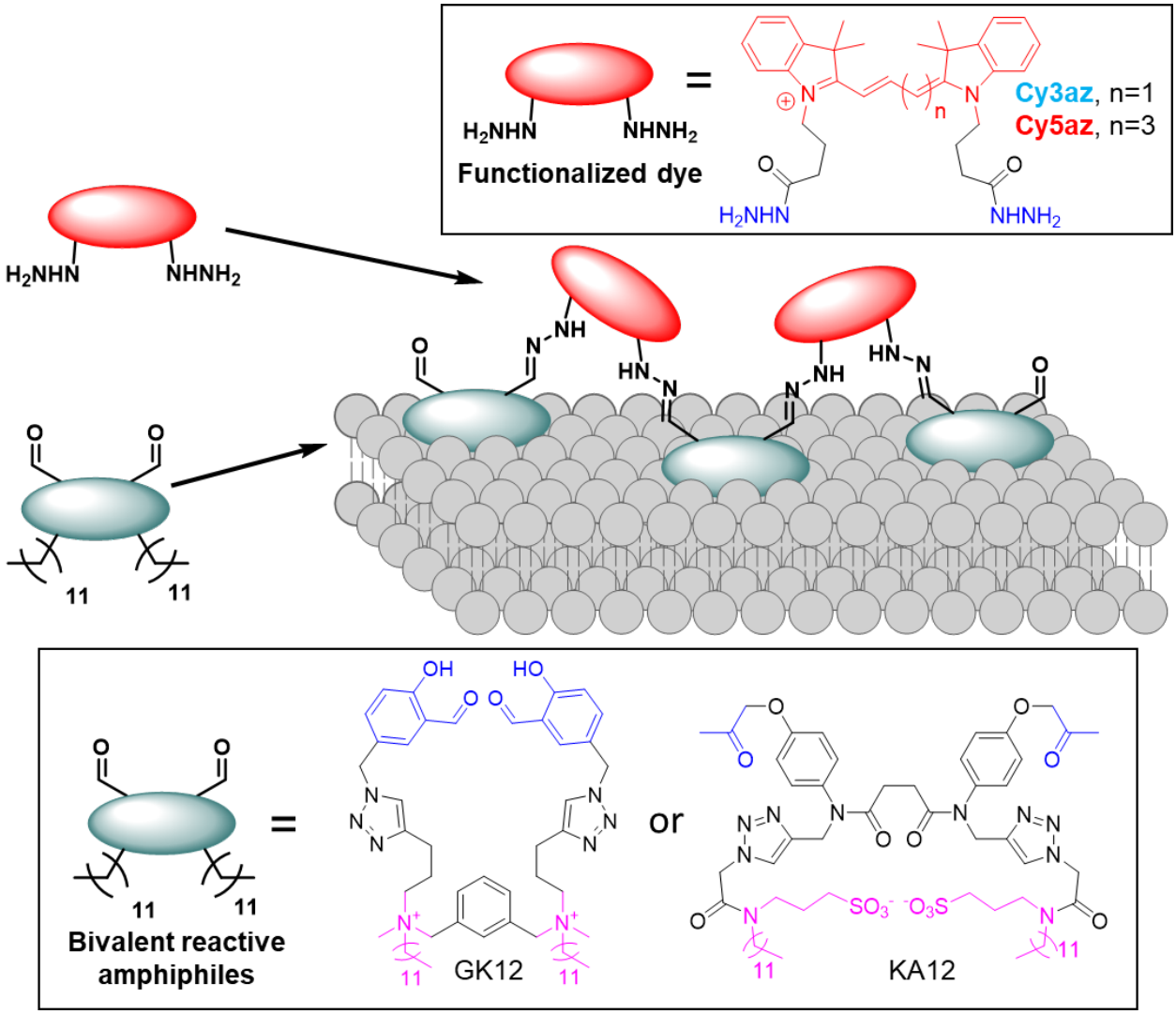

Fig. 2.4.1. Concept and structures of the reactive probes, based on cyanine hydrazides and bivalent reactive amphiphiles. Fluorophore moieties are highlighted in red, PM-targeting groups – in magenta, reactive groups – in blue.

In order to tune the working pH range, we decided to synthesize several bivalent amphiphiles with different reactivity of carbonyl groups. Compound GK12 was designed using two dodecyl chains together with two quaternary ammonium fragments to ensure efficient plasma membrane targeting (Fig. 2.4.1). o-hydroxybenzaldehyde was chosen as carbonyl component due to an ability of a neighbouring hydroxyl group to stabilize the formed hydrazone, leading to accelerated reaction with hydrazines at neutral pH.[299] The synthesis of amphiphile GK12 was performed in 5 steps starting from N-methyldodecyl amine with the overall yield of 9 % (Fig 2.4.2).

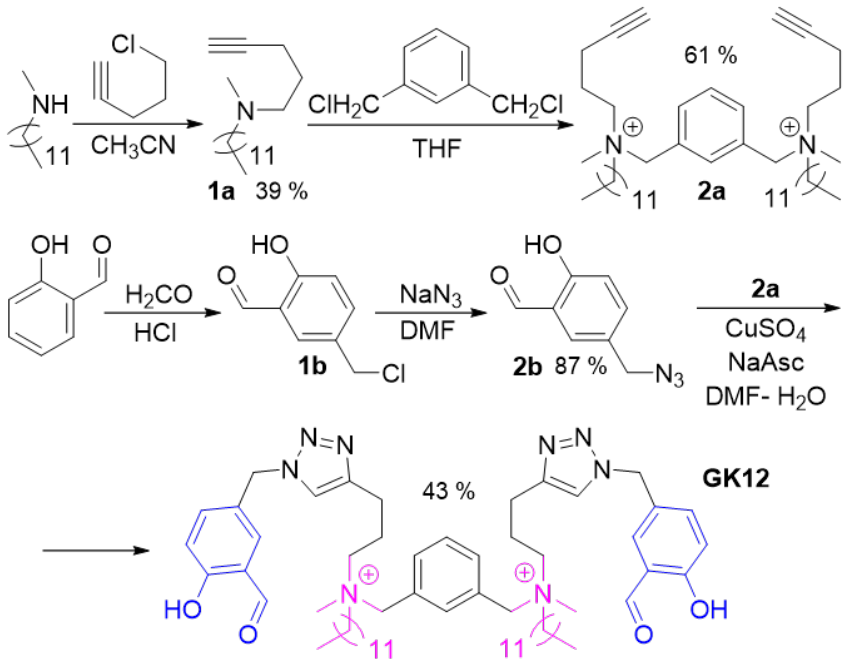

Fig. 2.4.2. Synthesis of bivalent reactive amphiphile GK12. PM-targeting groups are highlighted in magenta, reactive groups – in blue.

Compound KA12 was designed using two anionic plasma membrane-targeting moieties (Fig. 2.4.1). Two aliphatic ketone groups were chosen as carbonyl fragments. The synthesis of amphiphile KA12 was performed in 7 steps starting from N-Boc-4-aminophenol with the overall yield of 2 % (Fig. 2.4.3). A possible improvement in overall yield could be achieved by improving the synthetic procedure for the fragment 6b.

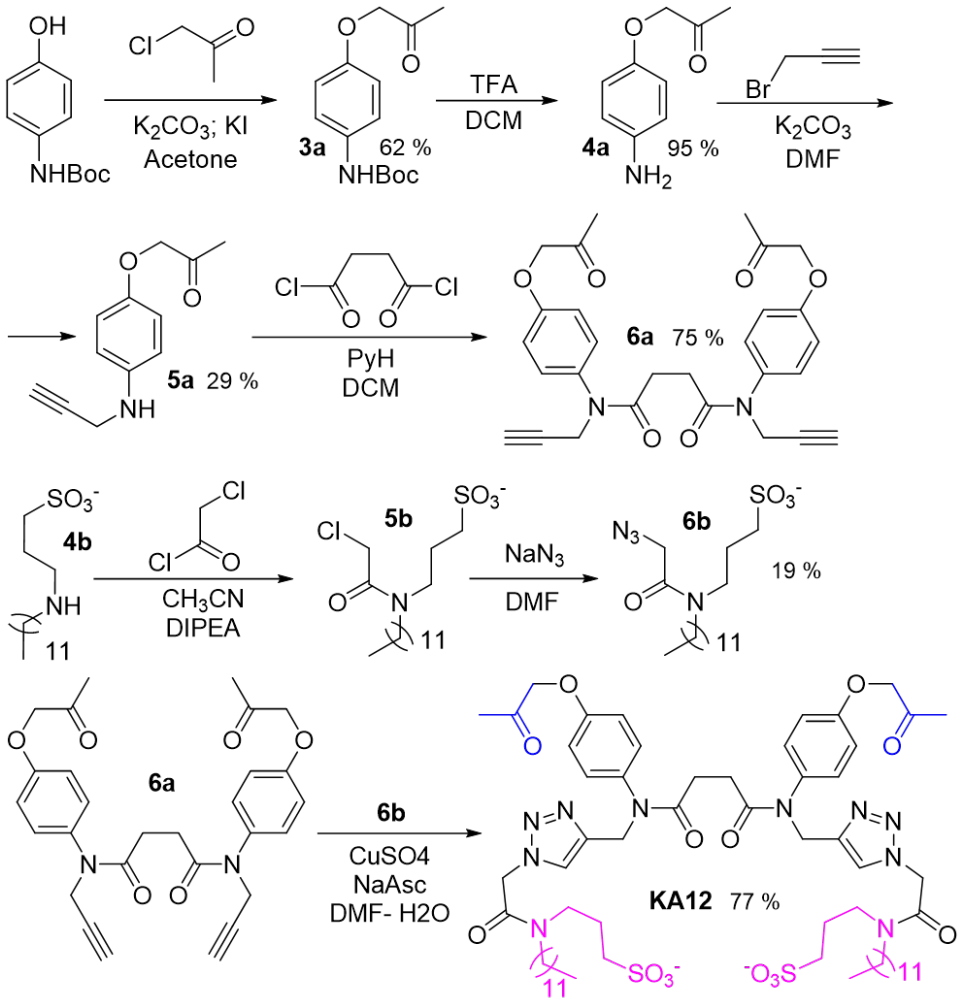

Fig. 2.4.3. Synthesis of bivalent reactive amphiphile KA12. PM-targeting groups are highlighted in magenta, reactive groups – in blue.

Cyanine dihydrazides were synthesized from the corresponding cyanine diacids in good yields, using peptide synthesis protocol (Fig. 2.4.4, A). Spectroscopy experiments showed, that the fluorophore absorption and emission maxima were not affected by functionalization and are close to parent fluorophore spectra (Fig. 2.4.4, B). Moreover, a presence of a significant spectral overlap between Cy3 emission and Cy5 absorption allows to use Cy3az and Cy5az as an efficient FRET pair. The observed QY values in acetate buffer (pH 4) were 4.9 % for Cy3az and 22.4 % for Cy5az, respectively.

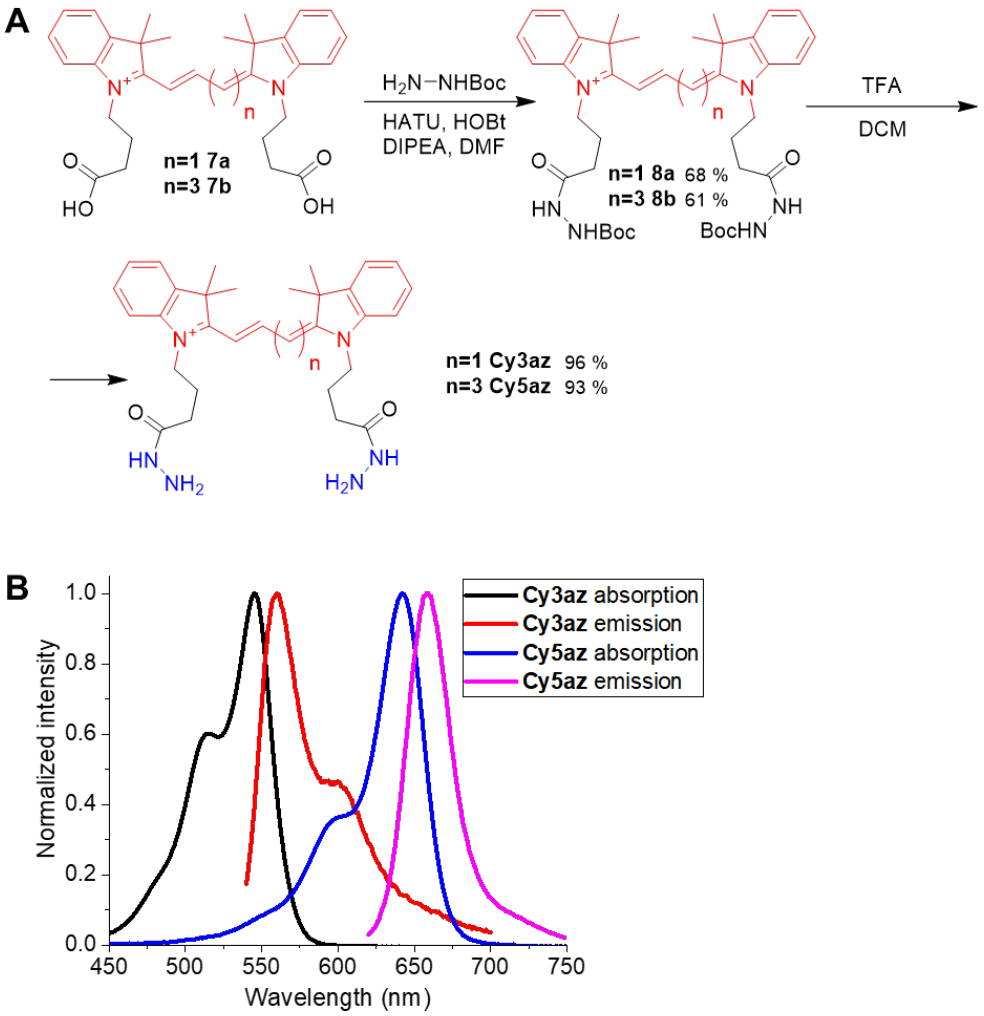

Fig. 2.4.4. Synthesis of cyanine dihydrazides Cy3az and Cy5az (A) Normalized absorption and emission spectra of Cy3az and Cy5az dyes in pH 4 acetate buffer (B). Excitation wavelength was 520 nm for Cy3az and 600 nm for Cy5az.

On the next step, we tested the ability of the synthesized bivalent amphiphiles to polymerize the cyanine dihydrazides on a membrane. DOPC LUVs were chosen as a model membrane system. The reaction of nanoconjugate formation was monitored using FRET approach, using a mixture of Cy3az as a donor and Cy5az as an acceptor (molar ratio 10:1). Due to the high sensitivity of FRET process towards the interfluorophore distance, the energy transfer does not occur between Cy3 and Cy5 in solution. However, upon the formation of nanostructures the fluorophores are confined within a close proximity, and the fluorescence of Cy5 acceptor can be detected upon exciting the Cy3 donor dye (Fig. 2.4.5, A).

As evidenced by the spectroscopy results, an addition of negatively charged amphiphile KA12 to a solution of positively charged Cy3az and Cy5az in the absence of liposomes resulted in fluorescence quenching, presumably due to aggregation, caused by the electrostatic interactions (Fig. 2.4.5, B). However, in presence of both DOPC LUVs and KA12 the brightness of Cy5 increased, evidencing nanostructure formation. The maximum FRET efficiency (I_{Cy5az}/I_{Cy3az}) was observed in case of 10:1 ratio between the concentration of bivalent amphiphile and the total

phospholipid concentration (Fig. 2.4.5, B). In case of a large excess of DOPC (100-fold), a sharp increase in donor emission was observed, possibly due to an increase in available membrane surface, leading to a more loose bivalent amphiphile distribution and, consequently, larger average interfluorophore distance. In line with our expectations, no FRET was observed in case of cyanine dyes in solution without bivalent amphiphile. In case of GK12 amphiphile, no reaction was observed.

Next, we assessed the pH-sensitivity of hydrazone bonds in the formed nanostructures. This was performed by diluting the hydrazone nanostructures into MES buffers (1/100) with different pH values (Fig. 2.4.5, C). After 1 hour of incubation, a significant decrease in emission intensity of Cy5 was observed in buffers with pH values below 6, indicating the disassembly of hydrazone bonds in acidic conditions, while at pH 7 the nanostructures remained stable after dilution. Notably, the disassembly was also accompanied by a hypsochromic shift of Cy5 emission (Fig. 2.4.5, C).

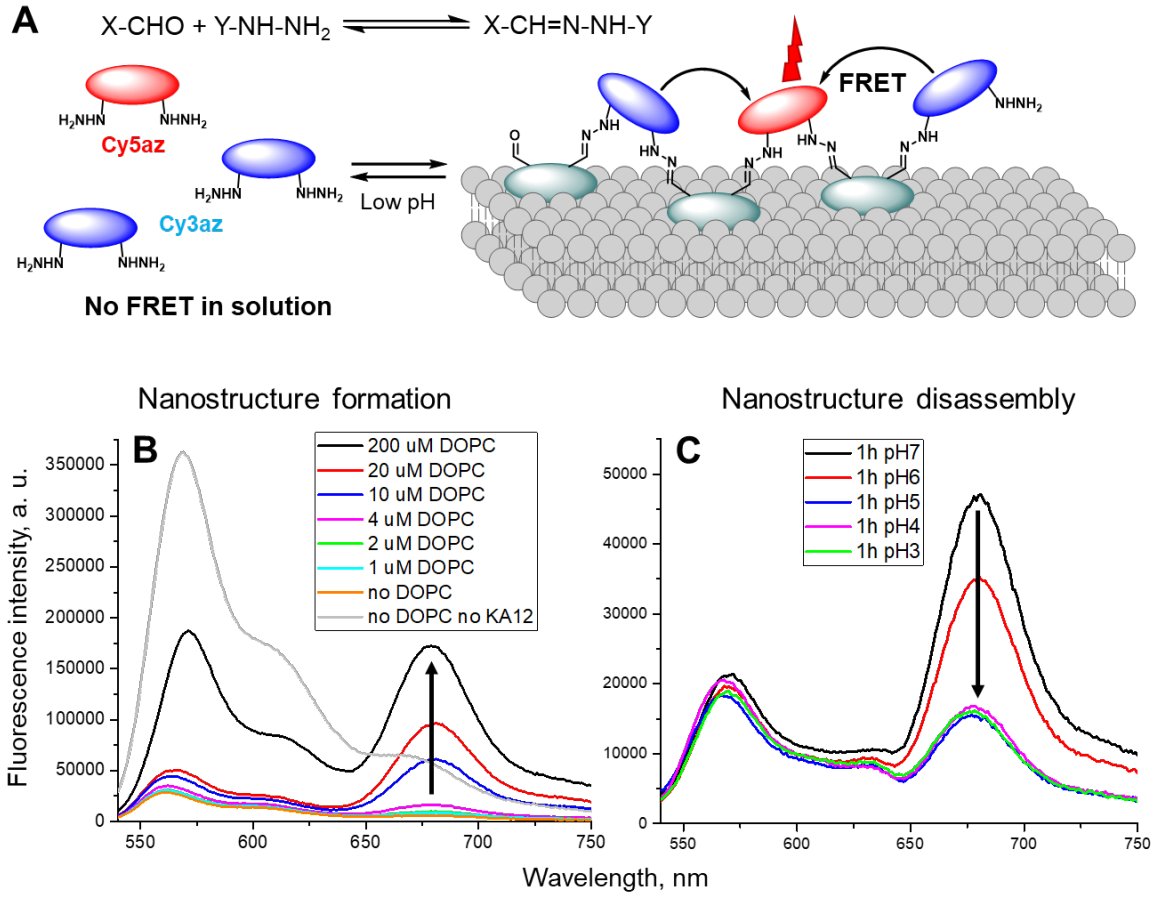

Fig. 2.4.5. (A) Concept of the FRET-based detection of the reversible formation of nanoconjugates on the surface of model membranes. (B) Fluorescence emission spectra of Cy3az + Cy5az (10:1) dye pair after 1h of incubation with KA12 and DOPC liposomes with different total lipid concentrations in MES buffer (pH 7). The concentration of KA12 was 2 µM. Total dye concentration (Cy3az:Cy5az 10:1) was 2 µM. Excitation wavelength was 520 nm. (C) Fluorescence emission spectra of nanoconjugates, diluted 1/100 into MES buffer with different

pH values, after 1h of incubation. The nanoconjugates were originally formed by incubating 2 μM of KA12 with cyanine dihydrazides (Cy3az:Cy5az 10:1, total concentration 2 μM) and DOPC liposomes (total lipid concentration 20 μM) in MES buffer (pH 7) for 24h. Excitation wavelength was 520 nm.

After the initial proof of reactivity in model membranes, the amphiphile KA12 was tested in live HeLa cells (Fig. 2.4.6). Upon the addition of bivalent amphiphile the fluorescence intensity of both Cy3az donor and Cy5az acceptor increased, indicating that the two dyes are in close proximity. However, the interpretation of the results is hindered by rapid dye internalization, leading to cyanine accumulation inside the cells (Fig. 2.4.6), possibly due to a positive molecular charge of cyanine dihydrazides.

One of the possible solutions to circumvent the rapid dye internalization issue lies in creation of cell-impermeable cyanines with improved molecular design, which are retained on the membrane long enough for the reaction to proceed.

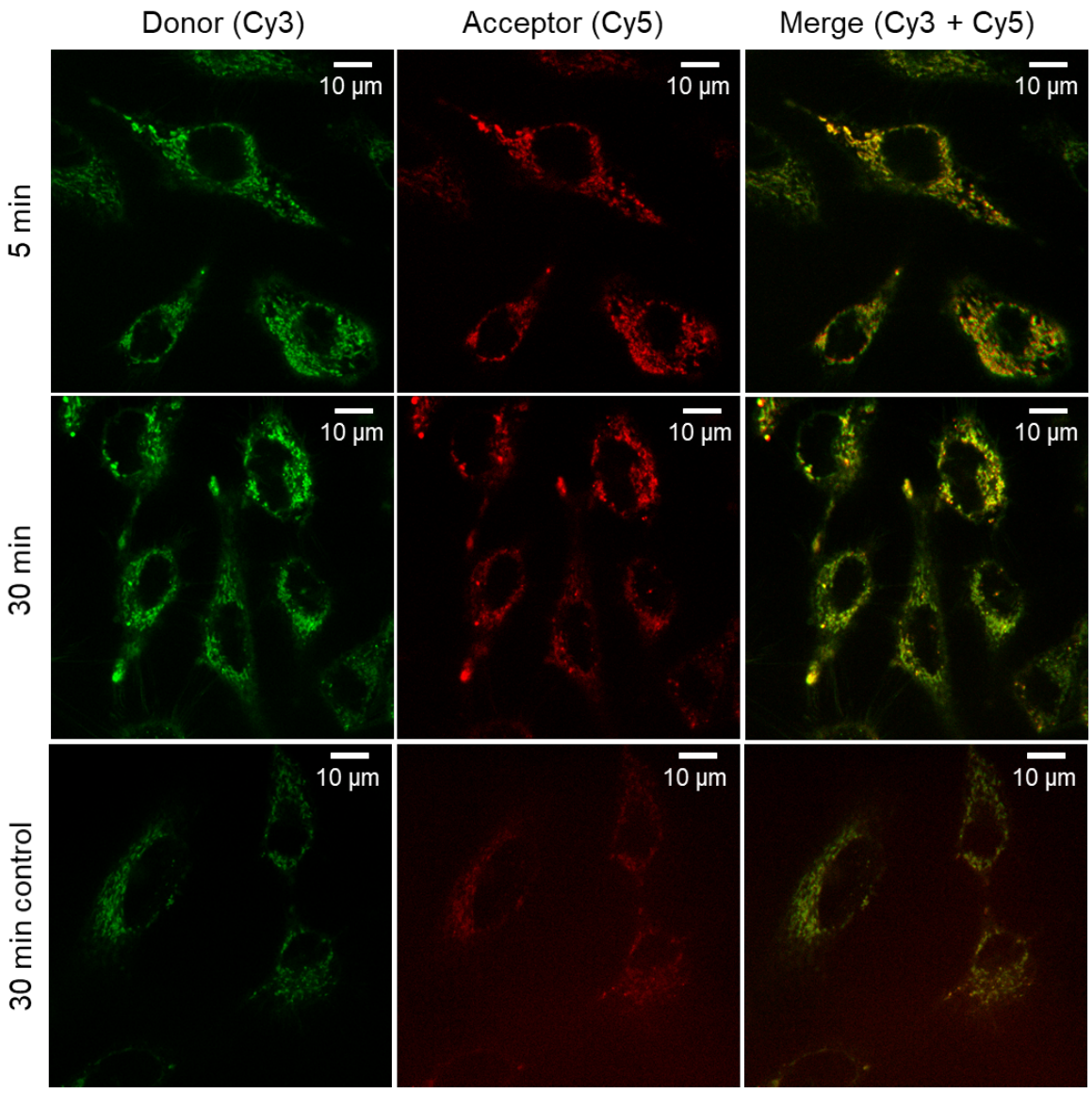

Fig. 2.4.6. Confocal fluorescence microscopy images of live HeLa cells, preincubated with KA12 (1 μM) for 5 minutes and stained with Cy3az and Cy5az mixture (10:1, total dye concentration 1 μM) in MES saline isotonic buffer (pH 6).

2.4.2. Reactive probes based on functionalized membrane-targeted cyanines

The second approach lies in development of PM-targeted fluorescent probes, bearing the moieties, which are reactive towards functional groups, present in the membrane proteins, namely amines and thiols (Fig. 2.4.7, A). In this case, a covalent attachment of the fluorophore to membrane proteins is expected to result to long-term and persistent plasma membrane staining. We have chosen the cyanines with two zwitterionic plasma-membrane targeting groups as the basis for the design of reactive membrane probes, due to their high performance in cellular applications.[126] The design of our probes includes two chloroacetyl groups (in case of Cy3ZCl) or two maleimide groups (in case of Cy3ZM) (Fig. 2.4.7, B). Maleimide residues and chloroacetyl groups are reactive towards sulfhydryl groups of cysteine residues[300] and, to a lesser extent, towards amino groups.

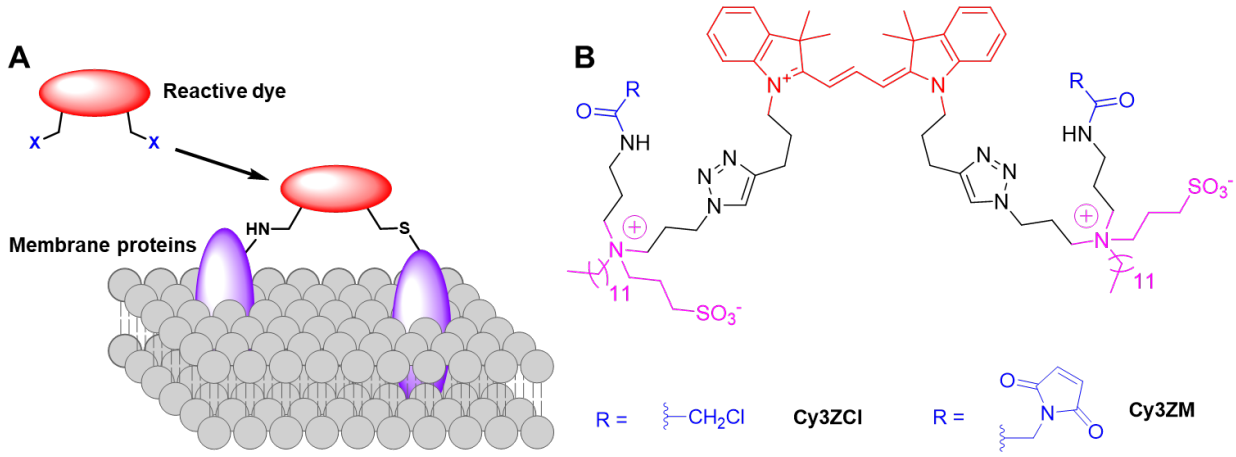

Fig. 2.4.7. Concept of persistent membrane staining by reactive probes (A). Design of zwitterionic reactive cyanines (B). Fluorophore moiety is highlighted in red, PM-targeting groups – in magenta, reactive groups – in blue.

The synthesis of the reactive probes was performed in 3 steps starting from cyanine dialkyne and quaternized ammonia compound (both starting building blocks kindly provided by Dr. Mayeul Collot) with the overall yield of 21 % (For Cy3ZM) and 22 % (for Cy3ZCl) (Fig. 2.4.8).

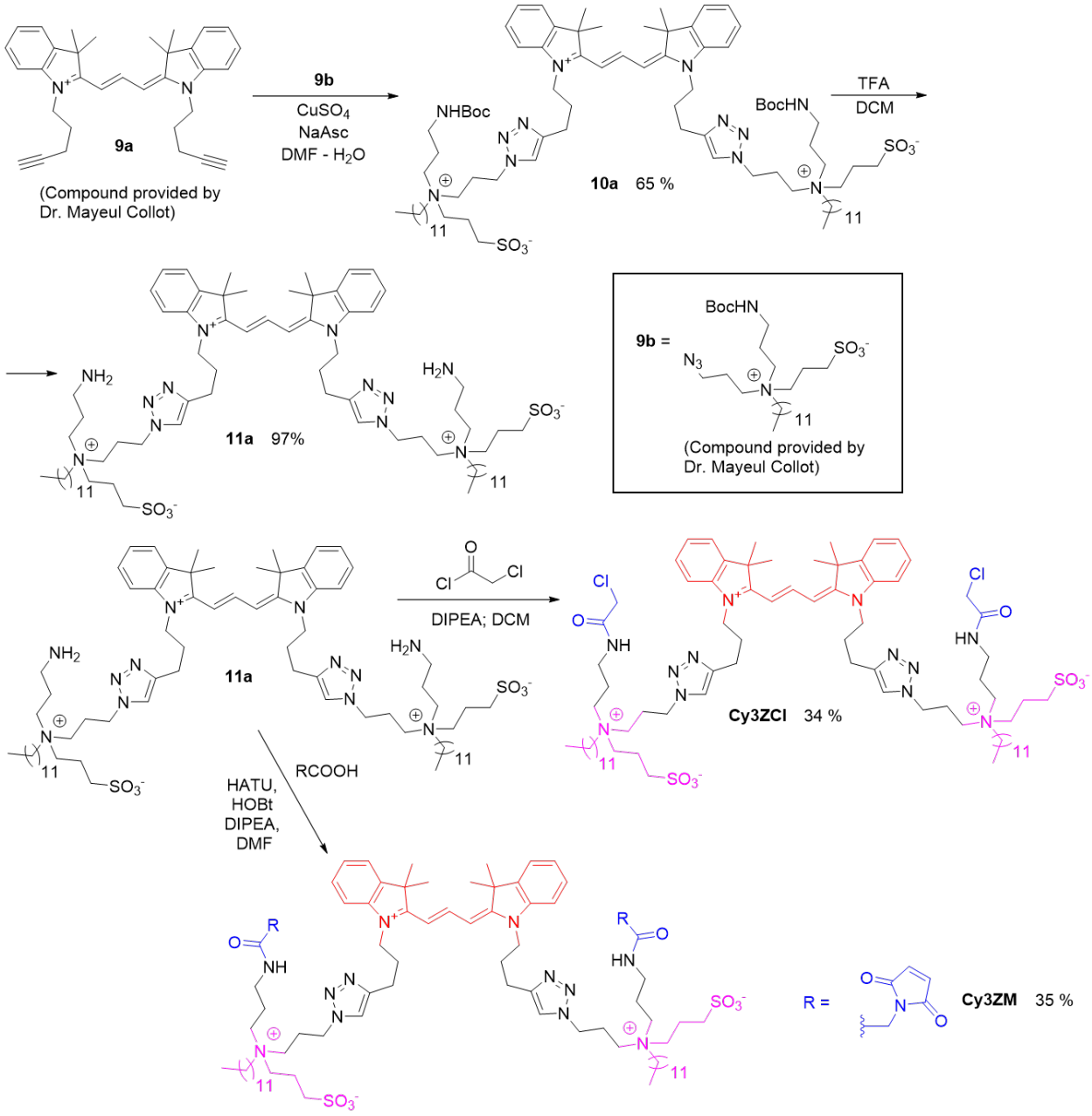

Fig. 2.4.8. Synthesis of zwitterionic reactive cyanine probes. Fluorophore moieties are highlighted in red, PM-targeting groups – in magenta, reactive groups – in blue.

Next, the obtained probes were directly tested in live HeLa cells in order to assess their performance in cellular microscopy (Fig. 2.4.9). The probe Cy3ZM showed preferential staining of the glass surface of microscopy support, probably due to an incorporation of relatively bulky and apolar maleimide groups in molecular design. Probe Cy3ZCl exhibited weak support surface staining, however practically all the fluorescence signal was observed inside the cells in case of both probes (Fig. 2.4.9, lower panel), suggesting rapid internalization. In both cases, the probable reason for the impaired probe performance could be the overall positive charge of the molecules, enhancing the electrostatic interactions with the negatively charged glass surface and accelerating the internalization.

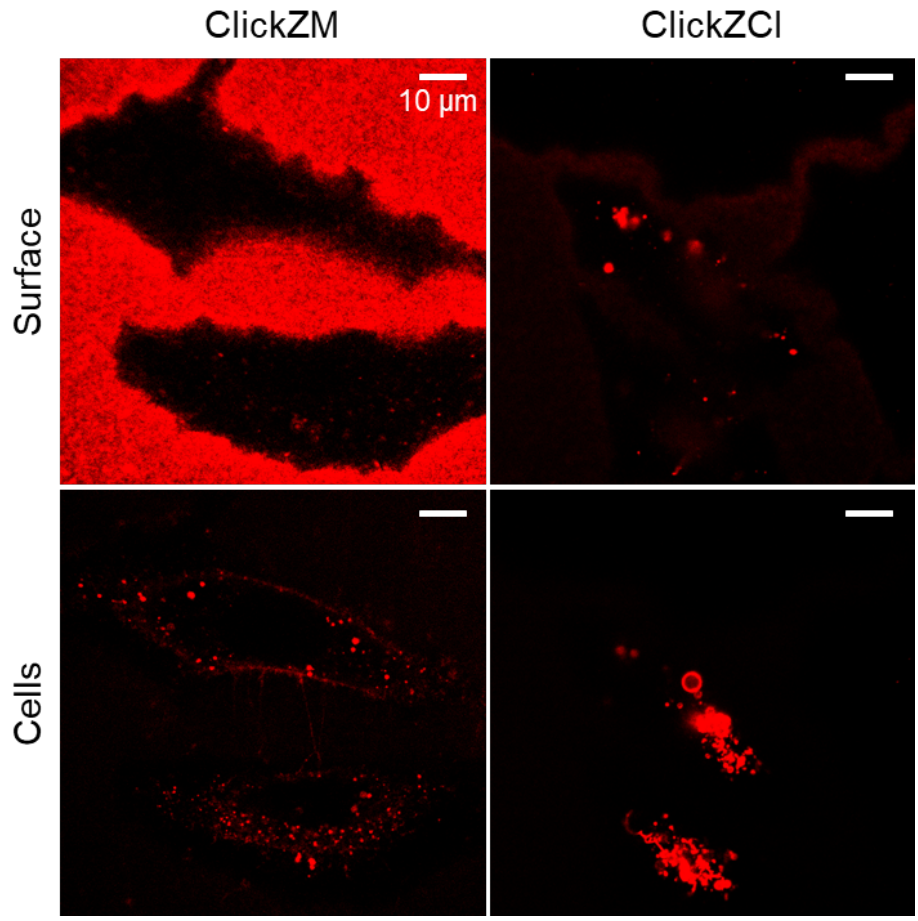

Fig. 2.4.9. Confocal microscopy images of live HeLa cells, stained with reactive zwitterionic cyanine probes (50 nM in HBSS, incubation time 10 min). The images in the upper row are focused on the surface of microscopy support, the ones in the lower row are focused on cells.

Due to the found drawbacks of zwitterionic PM cyanines, we decided to improve the probe design via introducing the negatively charged sulphonates with long alkyl chains. This strategy changes the overall probe charge to -1, and in case of non-reactive cyanine dyes it allowed to considerably decrease both the support surface staining and internalization (see section 2.1.1). The design of anionic reactive fluorescent probes features two chloroacetyl (for Cy3ClA) or two p-bromomethylphenyl (for Cy3BrA) groups (Fig. 2.4.10) to ensure the reactivity towards sulfhydryl or amine residues in proteins.

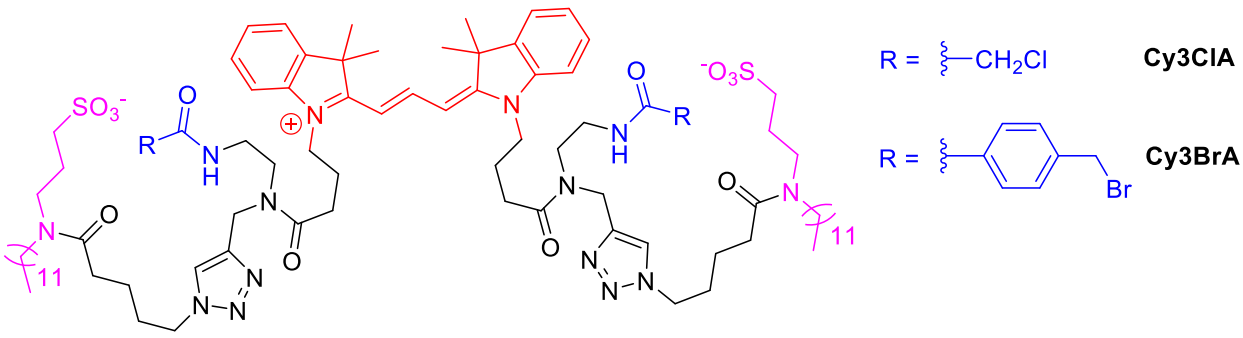

Fig. 2.4.10. Design of reactive anionic PM-targeted cyanines. Fluorophore moiety is highlighted in red, targeting motifs – in magenta, reactive groups – in blue.

The synthesis of anionic reactive probes was performed in 5 steps stating from cyanine diacid with an overall yield of 15 % (for Cy3ClA) or 11 % (for Cy3BrA) (Fig. 2.4.11). Usage of Cu-catalysed azide-alkyne cycloaddition for grafting the anionic targeting moieties allowed to increase the overall reaction yields.

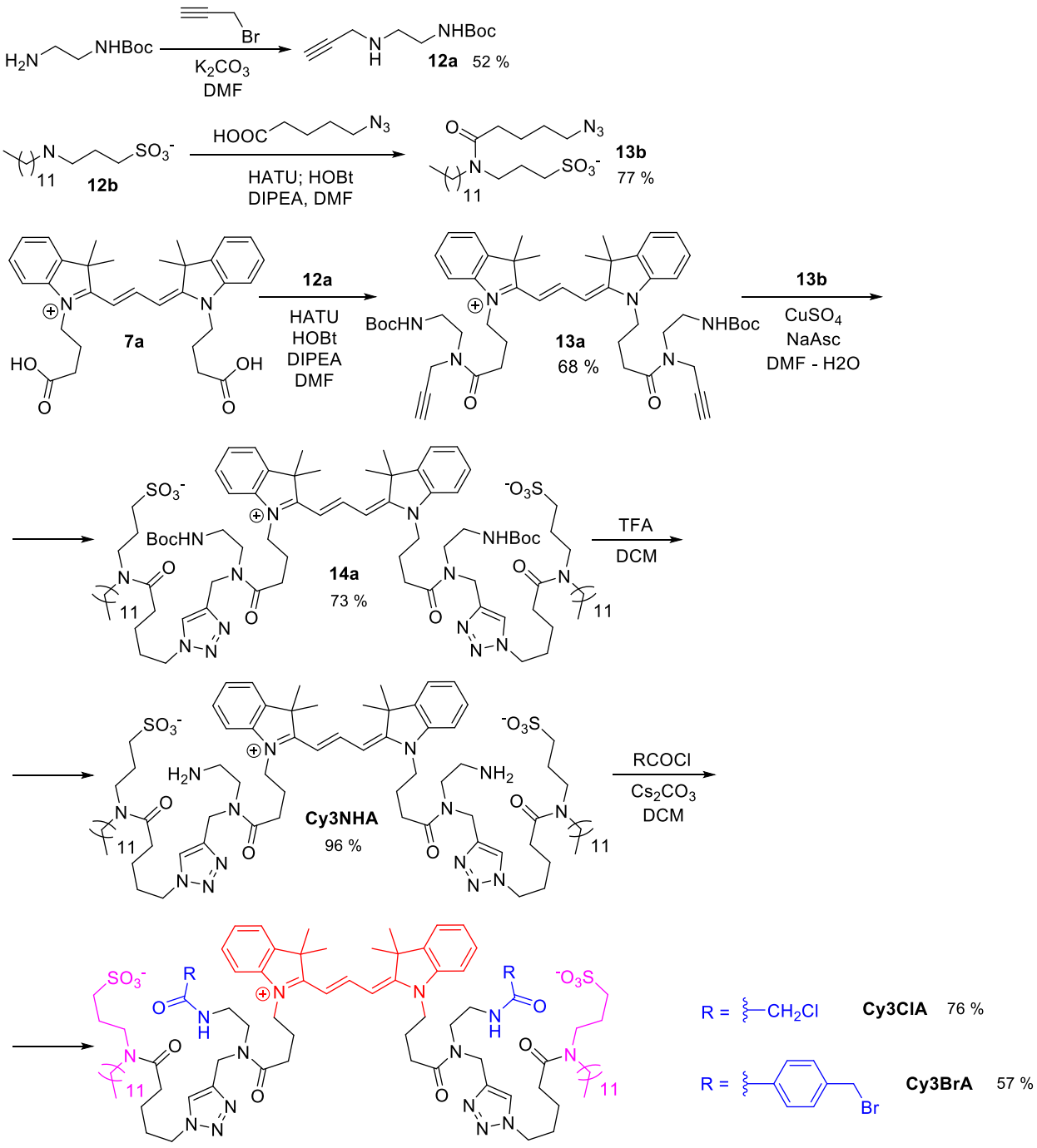

Fig. 2.4.11. Synthesis of reactive anionic PM-targeted cyanines. Fluorophore is highlighted in red, targeting motifs – in magenta, reactive groups – in blue.

On the next step, the performance of the two anionic probes was tested in live KB cells (Fig. 2.4.12). First, the cells were incubated with reactive or non-reactive probes (Fig. 2.4.12, A) for 10 minutes, which was followed by microscopy imaging (Fig. 2.4.12, B). Both Cy3ClA and Cy3BrA showed the preferential staining of the PM, though the image brightness in case of Cy3BrA was lower, possibly due to increased aggregation, induced by bulky reactive motifs. After the first round of microscopy imaging the cells were incubated for 30 min in complete growth medium and imaged again in order to assess the persistence and durability of the staining by

reactive probes (Fig. 2.4.12, C). In comparison with a non-reactive probe Cy3A, both probes showed an increased signal intensity from inside the cell (especially in case of Cy3ClA), however the signal from the plasma membrane was negligible. A possible explanation of this result might include non-optimised experimental conditions, as the cysteine residues are prone to form non-reactive disulfide species, and the amino residues in proteins are protonated at pH of 7.4.

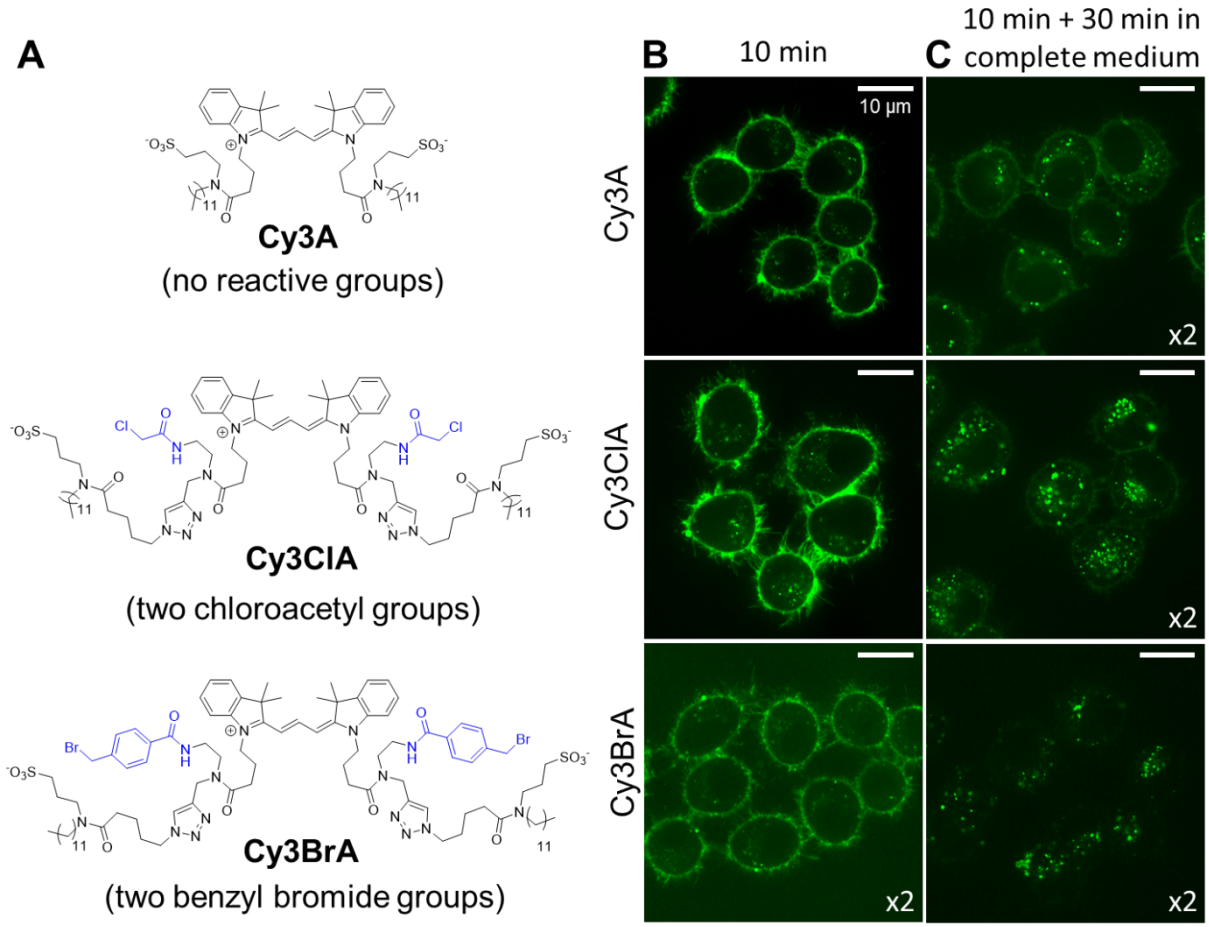

Fig. 2.4.12. Structures of anionic PM-targeted cyanines with and without reactive groups (A). Reactive groups are highlighted in blue. Confocal microscopy images of live KB cells, treated with anionic cyanine probe solution in HBSS (pH 7.4) for 10 minutes, before (B) and after (C) incubation in complete growth medium. Probe concentration was 50 nM. Excitation wavelength was 532 nm.

In order to exclude the effect of pH and disulfide formation on the PM staining by reactive cyanine probes, we repeated the previous experiment with the cells, pretreated with TCEP (tris(2-carboxyethyl)phosphine) (Fig. 2.4.13, A). Due to the strong reductive properties of TCEP all the disulfides are reduced to the corresponding sulfhydryl groups, eligible for the reaction with our probes. The both probes showed preferential internalization, and the overall signal intensity in case of Cy3BrA after the incubation decreased in comparison with a previous experiment (Fig. 2.4.12).

Addition of reactive cyanines at pH 8.4 (Fig. 2.4.13, B) did not affect the staining profiles when compared with previous staining conditions, though the overall signal intensity increased in case of Cy3ClA probe.

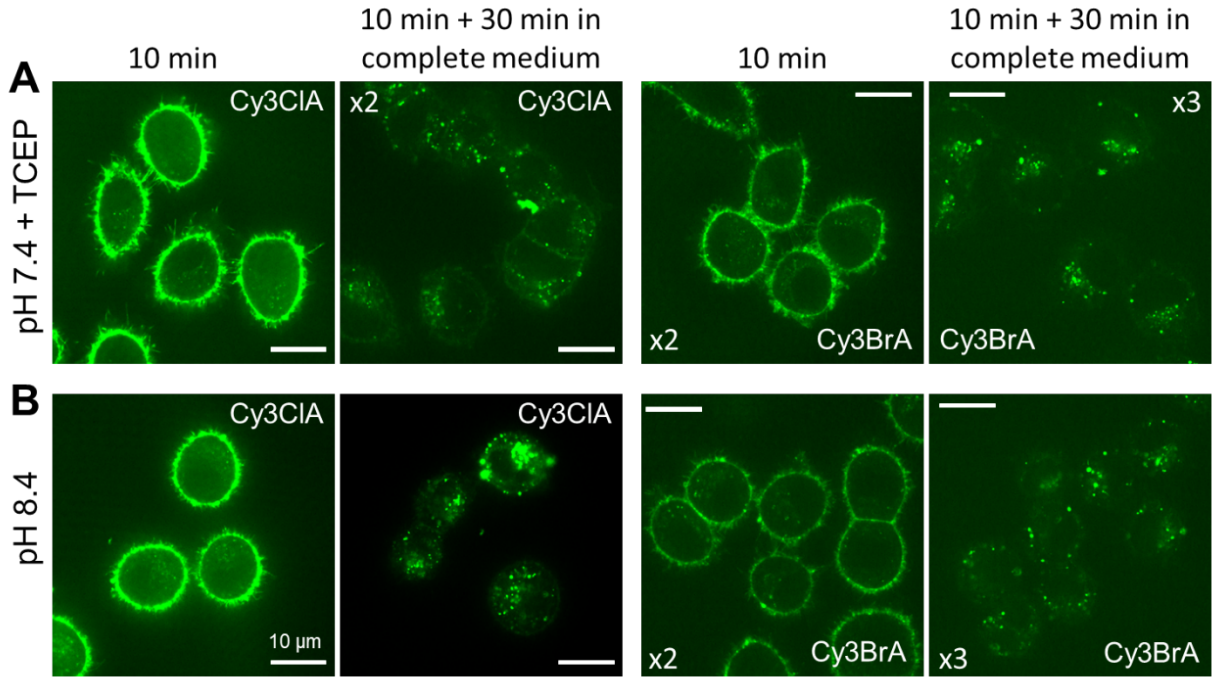

Fig. 2.4.13. Confocal fluorescence microscopy images of live KB cells, stained with anionic cyanine probes with: TCEP at pH 7.4 (A) or without TCEP at pH 8.4 (B), before and after incubation in complete growth medium. Probe concentration was 50 nM. Excitation wavelength was 532 nm.

The observed low probe reactivity could be possibly attributed to either the slow reaction kinetics or the low accessibility of the reactive groups. A possible solution includes further changes in the probe molecular design via an introduction of longer linker groups with varied polarity between the fluorophore and the reactive moieties.

Conclusions and perspectives

My PhD project was dedicated to the creation of targeted environment-sensitive fluorescent probes. Several key steps were accomplished in the course of the study.

During the first part of the project, we focused on the development of more efficient plasma membrane targeting moieties. 3-(alkylammonio)propane-1-sulfonates were chosen, due to their facile synthesis and functionalization, as promising candidates for the negatively charged PM targeting motifs, needed for designing the PM probes with selective and persistent staining. In order to test the performance of these targeting motifs, we have synthesized a palette consisting of five cyanine dyes with different spectral properties, each bearing two of the new targeting moieties. Due to the amphiphilic character of the 3-(dodecylammonio)propane-1-sulfonates, the synthesized probes were also expected to form non-fluorescent aggregates in aqueous medium and disassemble into highly emissive solubilized molecular form in presence of lipid membranes, providing a fluorogenic response.

Spectroscopy experiments in organic solvents and LUVs showed that the fluorophore properties were not perturbed by functionalization. Moreover, our probes featured high QY values in liposomes but were poorly emissive in aqueous medium, in line with the expectations. The probe aggregation in water was further proved by absorption spectra with an appearance of a characteristic short-wavelength shoulder.

The anionic cyanine probes also featured much less staining of the glass surface of the support together with much slower internalization in live cell microscopy imaging when compared with the cyanine probes with zwitterionic targeting groups. During colocalization microscopy experiments in live KB cells our probes also showed high plasma membrane selectivity together with slow internalization. In addition, anionic cyanines were successfully applied for *in vivo* TPE microscopy imaging of layer II-III pyramidal neurons in a live mouse brain. Our probe allowed to clearly distinguish neuron soma, dendrites with dendritic spines and axons with axonal boutons. To the best of our knowledge, this is the first example of *in vivo* neuronal membrane microscopy imaging using a molecular fluorescent probe.

Overall, during this part of the project we proved the utility of 3-(alkylammonio)propane-1-sulfonates as PM-targeting groups and synthesized an array of cyanine PM probes, covering a spectral range of 500-750 nm and possessing high brightness, selectivity and persistence of staining, high signal-to-noise ratio and compatibility with cellular and *in vivo* imaging.

Next, inspired by the results obtained for the anionic cyanine probes, we decided to graft the new plasma membrane-targeting moiety to a solvatochromic dye in order to create an environment-sensitive PM-targeted probe, capable of sensing the lipid order. We totally redesigned a widely used Laurdan probe, using the anionic anchor group. The resulting probe Pro12A was expected to address a fundamental drawback of Laurdan, related to the rapid probe internalization and inefficient plasma membrane labelling.

In the spectroscopy experiments in LUVs with different lipid composition Pro12A showed higher sensitivity towards the lipid order compared with the parent Laurdan probe, possibly due

to a more defined fluorophore localization in lipid membranes, imposed by our anchor group. Our probe also exhibited 2-3-fold higher fluorescence quantum yields in lipid membranes and much faster binding kinetics in comparison with Laurdan. Moreover, the fluorescence quenching experiments suggested that Pro12A binds exclusively the outer membrane leaflet. Experiments in GUVs and GPMVs supported the results in LUVs, evidencing high sensitivity of our probe to the lipid order. In addition, the probe featured more even partitioning between the Lo and Ld lipid phases.

The microscopy experiments in live cells have shown a practically absent internalization of Pro12A together with the sensitivity to the cholesterol extraction from the PM of live cells being much higher compared to that of Laurdan. In addition, our probe exhibited no fluorescence signal cross-talk with a number of commonly used orange/red fluorescent proteins and dyes, proving its high potential in multicolor cellular microscopy.

Overall, we developed an environment-sensitive plasma membrane-targeted probe, which features high sensitivity towards lipid order and high QY values in model membranes, stains exclusively the outer membrane leaflet, does not readily internalize and can be readily used in multicolour live cell fluorescence imaging.

During the next part of the project we aimed at the creation of a solvatochromic PM-targeted probe, suitable for super-resolution microscopy. Starting from a Nile Red fluorophore system, we introduced a new functionalization strategy with the purpose of increasing the dye photostability. In order to create a reversible membrane binding, necessary for PAINT super-resolution imaging, we decided to vary the length of the alkyl chain in the targeting motif. Thus, we synthesized two new probes: NR12A with strong binding, suitable for conventional microscopy, and low affinity probe NR4A, undergoing reversible binding-controlled ON/OFF switching, suitable for super-resolution microscopy.

The probe NR4A allowed to visualize highly dynamic nanoscale protrusions and invaginations of plasma membrane in live cells during 3D PAINT super-resolution imaging. The observed nanoscopic invaginations, exhibiting a minute-scale movement inside the cell, were suggested to be endocytic pits.

In addition, spectrally-resolved PAINT imaging revealed that the regions of plasma membrane with increased curvature possess lower local lipid order, which might indicate a connection between the membrane geometry and lipid organization. SR-PAINT with NR4A in fixed cells allowed to label the internal organelle membranes in addition to PM, the obtained data reveals lower lipid order in the organelle membranes.

Overall, we synthesized two environment-sensitive Nile Red plasma membrane-targeted probes with high brightness and photostability. The probes NR12A and NR4A exhibit superior performance in conventional microscopy and super-resolution PAINT imaging, respectively. The results of spectrally-resolved PAINT microscopy suggest a subtle connection between the lipid order and membrane geometry.

On the next step we synthesized an array of organelle-targeted solvatochromic fluorescent probes based on Nile Red. These probes were expected to accumulate selectively in given

organelles, such as mitochondria, lysosomes, Golgi, ER and lipid droplets, while also being able to sense the polarity and lipid order. The design of these new probes includes the modified Nile Red fluorophore, used for plasma membrane probe synthesis, which was grafted to the corresponding chemical organelle-targeting groups.

Spectroscopy studies in organic solvents and LUVs indicate that the fluorophore properties are not perturbed by functionalization. All the organelle probes studied exhibit an increase in QY values upon binding to model lipid membranes. Notably, the probes $NRER_F$ and NRMito are partially excluded from liquid ordered phase in LUVs, possibly due to bulky and/or polar targeting moieties.

The Nile Red organelle probes showed high organelle selectivity in live HeLa and KB cells, as evidenced by colocalization microscopy experiments with commercial organelle markers. Notably, lysosomal probe NRLyso exhibited higher organelle selectivity when compared to the corresponding commercial organelle marker. Our probe NRLD also featured higher selectivity towards lipid droplets when compared to an unsubstituted Nile Red dye, proving the efficiency of a dicyclohexyl targeting group.

Next, a ratiometric microscopy imaging in live KB cells was performed in order to test the ability of solvatochromic organelle probes to sense the differences in local polarity and lipid order. Prior to cellular imaging, all the probes were calibrated using LUVs of different lipid composition under the microscope. The calibration results revealed that the probe NR12A having the highest sensitivity towards the lipid order and polarity in lipid vesicles, and the probe $NRER_F$ – the lowest, in line with the spectroscopy results in LUVs. Using the obtained intensity ratio values for the model membranes with Lo and Ld phase, we developed a methodology to convert the observed ratiometric microscopy results into a quantitative lipid order parameter. This approach made it possible to compare directly the lipid order in biomembranes of the different organelles, which exhibit the following trend: plasma membrane >> mitochondria ~ ER (with $NRER_{Cl}$) > lysosomes > Golgi apparatus > ER (with $NRER_F$).

After that, we tested the capacity of Nile Red probes to sense the changes in organelle polarity associated with oxidative stress. Upon treatment with H_2O_2 the polarity of biomembranes is expected to increase due to lipid peroxidation, with the magnitude of this effect being dependent on the membrane lipid composition. According to the obtained results, lipid droplets, lysosomes and mitochondria showed the highest response level towards oxidative stress.

Solvatochromic organelle probes were also able to sense the differences in response between different organelles under hyperosmotic stress conditions, with ER, lysosomes, and mitochondria being the most sensitive. Notably, plasma membrane exhibited an increase in heterogeneity with an appearance of domains with lower lipid order in the inner parts of the PM, presumably within the regions of the highest membrane geometry disruption. The changes observed in organelles under mechanical stress are generally in line with the literature data, obtained using viscosity-sensitive molecular rotors and mechanosensitive flippers, though certain differences were observed as well.

Interestingly, the observed ER polarity and the level of sensitivity towards oxidative and hyperosmotic stress varied between the two ER-targeted Nile Red probes. Supposedly, the

difference in probe behavior can be attributed to the increased bulkiness and polarity of the targeting group in case of $NEER_F$ when compared to $NRER_{Cl}$.

Overall, we synthesized an array of solvatochromic Nile Red probes with selective organelle accumulation. Our probes feature high brightness and polarity/lipid order sensing properties coupled with good organelle-targeting efficiency. The organelle probes revealed differences in polarity and lipid order, as well as varied level of response towards external stimuli, within the different organelles. Moreover, we introduced an approach for a quantitative comparison of lipid order in organelles.

Another part of my PhD project was dedicated to the development of reactive plasma membrane probes with the purpose of achieving persistent and long-term staining.

One of the approaches included the formation of hydrazones from the functionalized cyanine dihydrazides on the membrane, using the specially designed PM-targeted amphiphiles with carbonyl groups. Two amphiphiles with different carbonyl moieties and PM-targeting groups were synthesized, together with a pair of cyanine dihydrazides (based on Cy3 and Cy5), in order to monitor the hydrazone formation at the membrane surface by FRET. Among the two amphiphiles synthesized, the compound KA12 showed the formation of nanostructures in LUVs upon addition of Cy3 and Cy5 hydrazides, as observed during the spectroscopy experiments in model membranes. Moreover, the formed nanostructures exhibited pH-responsive disassembly upon dilution. During live cell microscopy experiments, however the reaction between the amphiphile KA12 and cyanine dihydrazides was hindered by rapid dye internalization.

The second approach towards creating reactive plasma membrane probes lies in synthesizing the probes with special reactive groups, which are able to bind covalently to membrane proteins. The first generation of reactive cyanines featured zwitterionic targeting groups comprised of two probes. The synthesized compounds have shown a preferential staining of the glass surface of microscopy support and rapid internalization during live cell imaging. As a solution, a second generation of reactive cyanines was synthesized, this time using negatively charged 3-(dodecylammonio)propane-1-sulfonates for targeting the PM. The two created probes have shown preferential plasma membrane staining in live cell microscopy experiments, however the staining by the reactive probes was not persistent, resulting in probe internalization and/or washing after incubation with complete growth medium. The observed behaviour might be attributed to the insufficient accessibility of the targeting moieties and/or slow reaction kinetics.

In general, we introduced a new anionic plasma membrane-targeted moiety for creating the plasma membrane probes with enhanced optical properties. Moreover, we have developed a number of membrane-targeting probes, based on conventional fluorophores (cyanines) and environment-sensitive fluorophores (Prodan and Nile Red). Additionally, we have also synthesized an environment-sensitive Nile Red plasma membrane-specific probe, compatible with super-resolution microscopy, and an array of organelle-targeted environment-sensitive Nile Red probes. The developed probes possess high potential for applications in bioimaging, cell biology, biophysics or mechanobiology.

Further improvement of plasma membrane-targeted probes can be potentially performed using fluorophore dimers due to their high brightness and intrinsic environment-sensitive fluorogenic behaviour. The latter can also be potentially applied for creating the high-performant PM probes for ultrafast super-resolution imaging.

The sensitivity of solvatochromic organelle probes towards external stimuli can be finely tuned by developing and testing the probes with different targeting motifs. In principle, it would allow to develop the dyes with accumulation in the same organelle, but with different sensitivity profiles, enabling to design the probes for specific applications. Other opportunities include an application of biological molecules in order to study the cellular compartments, involved in their metabolism, or using genetically introduced self-labeling protein tags, with the fluorophore bound to a corresponding reactive linker.

Grafting photoswitchable solvatochromic fluorophores with organelle-targeted moieties potentially opens a vista towards environment-sensitive organelle probes for super-resolution microscopy.

The organelle-targeted probes can be further improved by designing proper reactive moieties, which will allow to control probe attachment to biomembranes in order to achieve robust and durable organelle staining. This strategy can be of a particular importance for long-term or *in vivo* imaging.

Introduction of reversible bonding strategy would lead to the probes with stimuli-responsive staining properties. In this case, the probe attachment could be controlled by the changes in external pH, oxidative potential or the presence of specific molecules.

Further development of reactive fluorescent probes for plasma membrane lies in the optimization of their molecular design to ensure high accessibility of reactive groups together with high reaction kinetics. The accessibility of reactive groups might be improved by introducing additional linker groups of varied polarity. A possible solution of slow reaction kinetics lies in utilization of click chemistry, *e.g.* strain-promoted azide-alkyne cycloaddition (SPAAC) or tetrazine ligation. We also expect this approach to improve the probe biocompatibility by alleviating the potential reactivity towards the membrane proteins, which might affect their structure and properties.

3. Materials and methods

3.1 General methods

All the reagents were purchased from Sigma-Aldrich or Alfa Aesar or TCI and used as received. MilliQ-water (Millipore) was used in all experiments. NMR spectra were recorded at 20°C (unless stated otherwise) on a BrukerAvance III 400 or BrukerAvance III 500 spectrometer. Mass spectra were obtained using an Agilent Q-TOF 6520 mass spectrometer. Absorption spectra were recorded on an Edinburgh FS5 spectrofluorometer, equipped with a thermostated cell compartment, or Cary 4000-HP spectrophotometer (Varian). Emission spectra were recorded either on an Edinburgh FS5 spectrofluorometer or on Fluoromax 4 spectrofluorometer (Jobin Yvon, Horiba), in both cases equipped with a thermostated cell compartment. Fluorescence quantum yields were measured using Nile Red (NR) in MeOH (λ_{ex}= 520 nm, QY_{ref} = 38%[301] (for all Nile Red probes), Quinine sulphate in 0.5 M sulphuric acid (λ_{ex}= 360 nm, QY_{ref} = 54.6%[302] (for Pro12A and Laurdan), Fluorescein in 0.1 M NaOH (λ_{ex}= 470 nm, QY_{ref} = 0.91)[303] (for Cy2A); Rhodamine 6G in EtOH (λ_{ex}= 510 nm, QY_{ref} = 0.94)[304] (for Cy3A); Cresyl violet in MeOH (λ_{ex}= 546 nm, QY_{ref} = 0.65)[305] (for Cy3.5A); Cresyl violet in EtOH (λ_{ex}= 601 nm, QY_{ref} = 0.67)[305] (for Cy5A); Rhodamine800 in EtOH (λ_{ex}= 623 nm, QY_{ref} = 0.25)[306] (for Cy5.5A); rhodamine B in water (λ_{ex}= 520 nm, QY_{ref} = 31%)[307] (for Cy3az**)** and Dioctadecylcyanine 5 in MeOH (λ_{ex}= 600 nm, QY_{ref} = 33% [308] (for Cy5az**)** as a reference.

Fluorescence quenching experiment (Article 2). Solutions of Laurdan in DOPC LUVs (1 μM of dye for 500 μM total lipid concentration) were made by adding concentrated dye stock solution in DMSO to liposomes, followed by vortexing the mixture and brief heating to 40 °C, followed by another vortexing and slow cooling over 2h to ensure complete binding and disaggregation of Laurdan.

3.2 Chemical synthesis

Fluorescent anionic cyanine plasma membrane probes for live cell and tissue imaging

The synthesis of anionic cyanines was performed starting from either 2-methybenzoxazole or 1,1,2-Trimethyl-1H-benzo[e]indole (Fig. 3.2.1). Compounds **3a**,[309] **3b**[309] and **2d**[310] were synthesized according to the literature procedures.

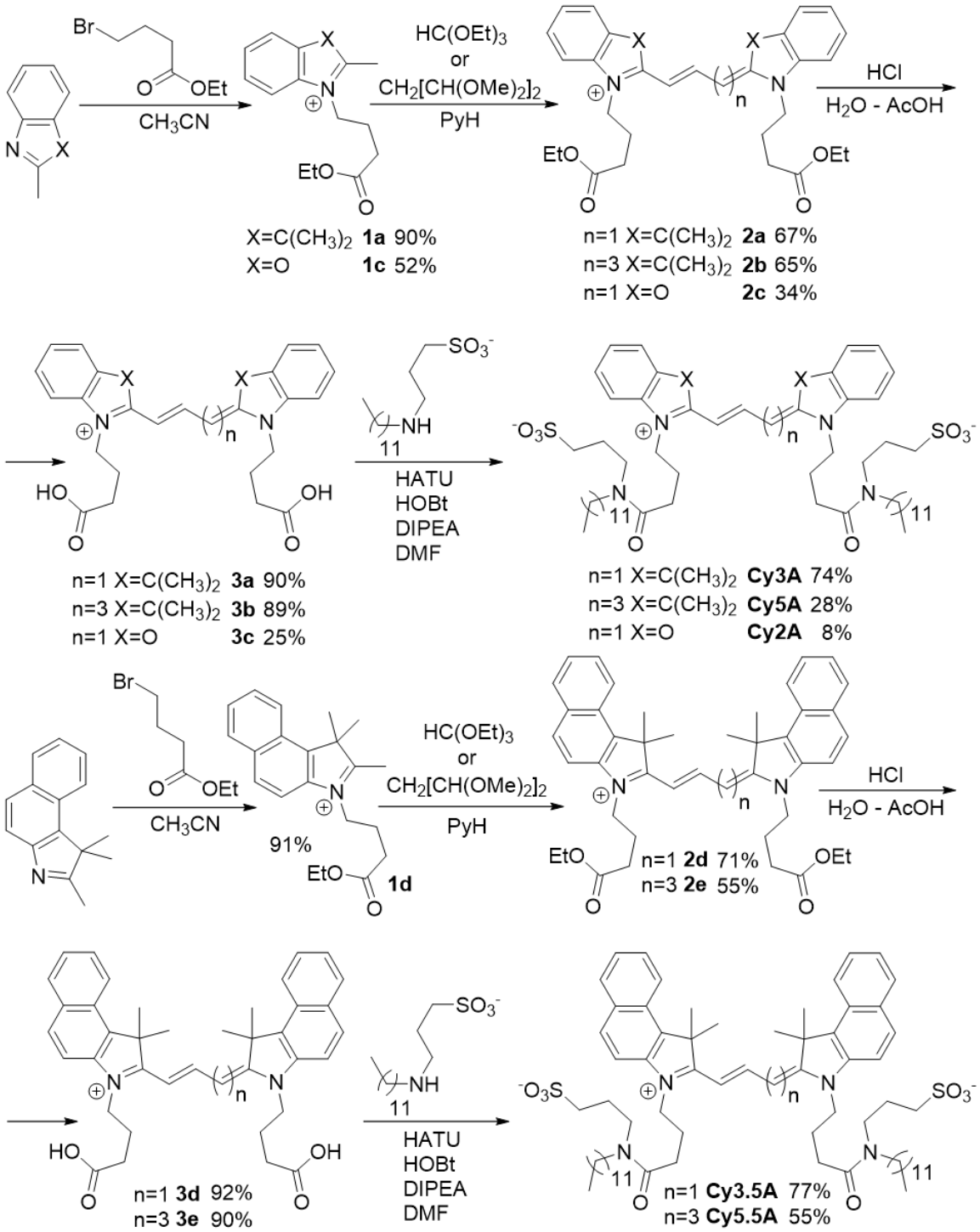

Fig 3.2.1. Synthesis chemes of anionic cyanine probes.

3-(4-ethoxy-4-oxobutyl)-2-methylbenzo[d]oxazol-3-ium (1c)

14.65 g (2.5 eq., 10.74 mL) of ethyl 4-bromobutyrate were added to the saturated solution of KI in 20 mL of dry acetone. The mixture was stirred for 1h, after that the precipitate was filtered off and the solvent was evaporated *in vacuo*.

After this, a solution of 4g (1 eq.) of 2-methylbenzoxazole in 30 mL of dry CH_3CN was added and the resulting mixture was refluxed for 8 days (control by TLC).

After the reaction the inorganic salts were filtered off and the filtrate was diluted with 100 mL of Et_2O. The formed mixture was left at 4 °C for 48h, then the formed crystals were filtered off, washed with *ca.* 5 mL of THF to separate the coloured admixtures and refluxed for 10 minutes in 50 mL of THF. The hot supernatant solution was discarded before cooling and the remaining oil was air-dried.

Compound **1c**: yield 5.66 g (52 %) as yellowish solid. **^{1}H NMR (400 MHz, $CDCl_3$) δ ppm** 8.18 - 8.21 (m, 1 H) 7.76 - 7.83 (m, 1 H) 7.64 - 7.71 (m, 2 H) 4.85 (t, *J*=8.30 Hz, 2 H) 4.00 (q, *J*=7.13 Hz, 2 H) 3.40 (s, 3 H) 2.64 (t, *J*=7.00 Hz, 2 H) 2.26 - 2.35 (m, 2 H) 1.16 (t, *J*=7.13 Hz, 3 H). **^{13}C NMR (101 MHz, Methanol-*d*$_4$) δ ppm** 172.72 ($C_{carboxyl}$) 167.88 (C_{ar}) 147.95 (C_{ar}) 129.81 (C_{ar}) 129.31 (C_{ar}) 128.53 (C_{ar}) 115.09 (C_{ar}) 113.19 (C_{ar}) 60.97 (C_{al}) 47.68 (C_{al}) 30.50 (C_{al}) 23.25 (C_{al}) 16.45 (CH_3) 14.11 (CH_3). **HRMS (ESI), *m/z*:** $[M]^+$ calcd for $C_{14}H_{18}NO_3^+$, 248.1281; found, 248.1282.

Cyanine 3.5 or 5.5 diethyl ester (**2d, 2e**) general procedure

4 g of 3-(4-ethoxy-4-oxobutyl)-1,1,2-trimethyl-1H-benzo[e]indol-3-ium were dissolved in 130 mL of dry pyridine upon heating, then the mixture was heated to 110 °C and 1.5 eq of triethylorthoformate (in case of Cy3.5OEt) or 1.5 eq. of 1,1,3,3-tetramethoxypropane (in case of Cy5.5OEt) were quickly added dropwise to the boiling solution. The mixture was refluxed for 2h (control by TLC).

After the reaction the solvent was evaporated *in vacuo*, then the solid residues were dissolved in DCM and washed with 1M HCl (3 times) and brine (once), dried over Na_2SO_4, then the solvent was evaporated *in vacuo*. The crude product was purified by gradient column chromatography (DCM:MeOH 95:5 to 9:1) (performed 2 times for each compound).

Compound **2d**: yield 2.68 g (71 %) as dark violet solid. **^{1}H NMR (400 MHz, Methanol-*d*$_4$) δ ppm** 8.82 (t, *J*=13.5 Hz, 1 H) 8.32 (d, *J*=7.8 Hz, 2 H) 8.09 (d, *J*=8.8 Hz, 2 H) 8.05 (d, *J*=8.0 Hz, 2 H) 7.66 - 7.80 (m, 4 H) 7.50 - 7.62 (m, 2 H) 6.58 (d, *J*=13.5 Hz, 2 H) 4.36 (t, *J*=7.8 Hz, 4 H) 4.15 (q, *J*=7.2 Hz, 4 H) 2.65 (t, *J*=6.8 Hz, 4 H) 2.17 - 2.26 (m, 4 H) 2.14 (s, 12 H) 1.25 (t, *J*=7.2, 1.00 Hz, 6 H).

Compound **2e**: yield 1.8 g (55 %) as dark blue/green solid. **^{1}H NMR (400 MHz, Methanol-*d*$_4$) δ ppm** 8.43 (t, *J*=13.1 Hz, 2 H) 8.27 (d, *J*=8.5 Hz, 2 H) 8.05 (d, *J*=9.0 Hz, 2 H) 8.02 (d, *J*=8.3 Hz, 2 H) 7.64 - 7.71 (m, 4 H) 7.48 - 7.55 (m, 2 H) 6.69 (t, *J*=12.5 Hz, 1 H) 6.45 (d, *J*=13.8 Hz, 2 H) 4.30 (br t, *J*=7.8 Hz, 4 H) 4.19 (q, *J*=7.0 Hz, 4 H) 2.63 (t, *J*=6.7 Hz, 4 H) 2.11 - 2.24 (m, 4 H) 2.05 (s, 12 H) 1.28 (t, *J*=7.0 Hz, 6 H). **^{13}C NMR (101 MHz, $CDCl_3$) δ ppm** 174.19 ($C_{carboxyl}$) 172.96 (C_{ar}) 153.10 (C_{ar}) 139.45 (C_{ar}) 133.83 (C_{ar}) 131.78 (C_{ar}) 130.61 (C_{ar}) 129.97 (C_{ar}) 128.18 (C_{ar}) 127.66 (C_{ar}) 124.94 (C_{ar}) 122.26 (C_{ar}) 110.67 (C_{ar}) 103.53 (C_{ar}) 60.78 (C_{al}) 51.18 (C_{al}) 43.57 (C_{al}) 30.59 (C_{al}) 27.68 (C_{al}) 22.47 (C_{al}) 14.22 (CH_3). **HRMS (ESI), *m/z*:** $[M]^+$ calcd for $C_{45}H_{51}N_2O_4^+$, 683.3843; found, 683.3850.

Cyanine 2 diethyl ester (**2c**)

5 g of 3-(4-ethoxy-4-oxobutyl)-2-methylbenzo[d]oxazol-3-ium were dissolved in 100 mL of dry pyridine upon heating, then the mixture was heated to 110 °C and 2.50 g (2.81 mL, 1.3 eq.)

of triethylorthoformate were quickly added dropwise to the boiling solution. The mixture was refluxed for 5h (control by TLC).

After the reaction the solvent was evaporated *in vacuo*, then the solid residues were dissolved in DCM and washed with 1M HCl (3 times) and brine (once), dried over Na_2SO_4, then the solvent was evaporated *in vacuo*.

The crude product was purified by gradient column chromatography (DCM:MeOH 95:5 to 85:15) and consecutive second column chromatography (DCM:MeOH 95:5).

Compound **2c**: yield 1.34 g (34 %) as dark red solid. **^{1}H NMR (400 MHz, Methanol-*d*$_4$) δ ppm** 8.44 (t, *J*=13.2 Hz, 1 H) 7.44 - 7.49 (m, 4 H) 7.40 (td, *J*=7.7, 1.0 Hz, 2 H) 7.33 (dq, *J*=7.7, 1.0 Hz, 2 H) 6.48 (t, *J*=13.2 Hz, 2 H) 4.25 (quin, *J*=7.8 Hz, 4 H) 4.14 (q, *J*=7.3 Hz, 4 H) 2.63 (t, *J*=6.4 Hz, 4 H) 2.10 - 2.25 (m, 4 H) 1.27 (t, *J*=7.3 Hz, 6 H). **^{13}C NMR (101 MHz, Methanol-*d*$_4$) δ ppm** 173.15 ($C_{carboxyl}$) 161.92 (C_{ar}) 148.03 (C_{ar}) 146.92 (C_{ar}) 131.30 (C_{ar}) 126.15 (C_{ar}) 125.04 (C_{ar}) 110.68 (C_{ar}) 110.09 ($C_{methylenic}$) 86.85 ($C_{methylenic}$) 60.72 (C_{al}) 43.45 (C_{al}) 30.19 (C_{al}) 22.79 (C_{al}) 14.19 (CH_3). **HRMS (ESI), *m/z*:** $[M]^+$ calcd for $C_{29}H_{33}N_2O_6^+$, 505.2333; found, 505.2348.

Cyanine diacid (**3a-e**) general procedure

900 mg of corresponding cyanine diethyl ester were dissolved in 6 ml of glacial acetic acid, then 4 ml of H_2O and 2 ml of HCl_{conc} were added. The reaction mixture was refluxed for 40 minutes (control by TLC).

After the reaction the solvents were evaporated *in vacuo*, and the solid residue was washed twice with acidified (pH 4) water on filter, then air-dried. In case of compound **3c** an additional purification by gradient column chromatography (DCM:MeOH:HCOOH 98:2:2 to 85:15:3) was needed.

Compound **3a**: yield 739 mg (90 %) as dark red solid. **^{1}H NMR (400 MHz, DMSO-*d*$_6$) δ ppm** 8.36 (t, *J*=13.3 Hz, 1 H) 7.65 (d, *J*=7.3 Hz, 2 H) 7.41 - 7.53 (m, 4 H) 7.30 (t, *J*=7.4 Hz, 2 H) 6.54 (d, *J*=13.3 Hz, 2 H) 4.15 (t, *J*=7.2 Hz, 4 H) 2.43 (t, *J*=7.2 Hz, 4 H) 1.90 - 2.03 (m, 4 H) 1.71 (s, 12 H).

Compound **3b**: yield 734 mg (89 %) as dark blue solid. **^{1}H NMR (400 MHz, Methanol-*d*$_4$) δ ppm** 8.28 (t, *J*=13.2 Hz, 2 H) 7.49 (d, *J*=7.3 Hz, 2 H) 7.33 - 7.45 (m, 4 H) 7.23 - 7.31 (m, 2 H) 6.63 (t, *J*=12.4 Hz, 1 H) 6.37 (d, *J*=13.8 Hz, 2 H) 4.11 - 4.20 (m, 4 H) 2.48 - 2.57 (m, 4 H) 2.00 - 2.11 (m, 4 H) 1.73 (s, 12 H).

Compound **3c**: yield 205 mg (25 %) as dark yellow solid. **^{1}H NMR (400 MHz, DMSO-*d*$_6$) δ ppm** 11.79 (br s, 2 H) 8.16 - 8.37 (m, 1 H) 7.33 - 7.89 (m, 1 H) 6.73 - 7.28 (m, 7 H) 6.30 - 6.73 (m, 2 H) 3.92 - 4.09 (m, 2 H) 3.51 - 3.75 (m, 2 H) 2.11 - 2.36 (m, 4 H) 1.44 - 1.70 (m, 4 H). **^{13}C NMR (101 MHz, Methanol-*d*$_4$) δ ppm** 174.66 (COOH) 173.06 (C_{ar}) 154.11 (C_{ar}) 153.85 (C_{ar}) 130.37 (C_{ar}) 129.58 (C_{ar}) 120.01 (C_{ar}) 117.58 (C_{ar}) 117.10 (C_{ar}) 109.33 (C_{ar}) 60.13 (C_{al}) 31.15 (C_{al}) 23.28 (C_{al}). **HRMS (ESI), *m/z*:** $[M-2H+2Na]^+$ calcd for $C_{25}H_{23}N_2Na_2O_6^+$, 493.1346; found, 493.1366.

Compound **3d**: yield 765 mg (92 %) as dark violet solid. **^{1}H NMR (400 MHz, DMSO-*d*$_6$) δ ppm** 8.56 (t, *J*=13.3 Hz, 1 H) 8.29 (d, *J*=9.5 Hz, 2 H) 8.11 (d, *J*=9.0 Hz, 2 H) 8.08 (d, *J*=8.3 Hz, 2 H) 7.83 (d, *J*=8.8 Hz, 2 H) 7.68 (t, *J*=7.7 Hz, 2 H) 7.53 (t, *J*=7.4 Hz, 2 H) 6.65 (d, *J*=13.3

Hz, 2 H) 4.27 (br t, *J*=6.8 Hz, 4 H) 2.37 (br t, *J*=6.27 Hz, 4 H) 2.05 - 2.10 (m, 2 H) 2.01 (s, 12 H) 1.96 - 1.99 (m, 2 H). **^{13}C NMR (101 MHz, Methanol-*d*$_4$) δ ppm** 175.57 (COOH) 174.74 (C_{ar}) 148.78 (C_{ar}) 140.04 (C_{ar}) 133.57 (C_{ar}) 131.96 (C_{ar}) 130.97 (C_{ar}) 130.43 (C_{ar}) 128.33 (C_{ar}) 127.94 (C_{ar}) 125.46 (C_{ar}) 122.63 (C_{ar}) 112.08 (C_{ar}) 102.98 (C_{ar}) 51.04 (C_{al}) 44.06 (C_{al}) 32.26 (C_{al}) 27.58 (C_{al}) 23.72 (CH_3). **HRMS (ESI), *m/z*:** $[M]^+$ calcd for $C_{39}H_{41}N_2O_4^+$, 601.3061; found, 601.3079.

Compound **3e**: yield 751 mg (90 %) as dark blue/green solid. **^{1}H NMR (400 MHz, DMSO-*d*$_6$) δ ppm** 12.25 (br s, 2 H) 8.50 (t, *J*=13.2 Hz, 2 H) 8.27 (d, *J*=8.5 Hz, 2 H) 8.10 (d, *J*=8.8 Hz, 2 H) 8.07 (d, *J*=8.5 Hz, 2 H) 7.78 (d, *J*=9.0 Hz, 2 H) 7.69 (t, *J*=7.8 Hz, 2 H) 7.53 (t, *J*=7.7 Hz, 2 H) 6.61 (t, *J*=12.5 Hz, 1 H) 6.44 (d, *J*=13.6 Hz, 2 H) 4.25 (br t, *J*=7.2 Hz, 4 H) 2.22 - 2.36 (m, 2 H) 2.03 - 2.16 (m, 4 H) 1.98 (s, 12 H) 1.90 - 1.96 (m, 2 H). **^{13}C NMR (101 MHz, Methanol-*d*$_4$) δ ppm** 174.36 (COOH) 174.29 (C_{ar}) 153.54 (C_{ar}) 140.15 (C_{ar}) 133.64 (C_{ar}) 131.79 (C_{ar}) 130.78 (C_{ar}) 130.40 (C_{ar}) 128.20 (C_{ar}) 128.10 (C_{ar}) 126.11 (C_{ar}) 125.26 (C_{ar}) 122.62 (C_{ar}) 111.93 (C_{ar}) 103.37 (C_{ar}) 51.24 (C_{al}) 43.42 (C_{al}) 30.84 (C_{al}) 27.25 (C_{al}) 22.88 (CH_3). **HRMS (ESI), *m/z*:** $[M]^+$ calcd for $C_{41}H_{43}N_2O_4^+$, 627.3217; found, 627.3235.

3-(dodecylammonio)propane-1-sulfonate, procedure adapted from elsewhere.[311] 4g of dodecylamine were mixed with 1.2 eq. of 1,3-propanesultone in 30 mL of dry acetone. The reaction was refluxed under Ar atmosphere for 24h. After the reaction, the crude product was filtered off, washed 2 times with acetone and recrystallized from ethanol.

Yield 4.58 g (69.2 %) as a white solid. **^{1}H NMR (400 MHz, DMSO-d$_6$ (60 °C)) δ ppm** 0.88 (t, J=6.8 Hz, 3 H) 1.24 - 1.35 (m, 18 H) 1.57 (quin, J=7.6 Hz, 2 H) 1.97 (quin, J=6.4 Hz, 2 H) 2.66 (t, J=6.4 Hz, 2 H) 2.88 (t, J=7.3 Hz, 2 H) 3.06 (t, J=6.4 Hz, 2 H). **MS (ESI), m/z:** $[M]^+$ calcd for $C_{15}H_{32}NO_3S^-$, 306.21; found, 306.21.

Cyanine dialkyl disulfonate (**Cy3A, Cy5A, Cy2A, Cy3.5A, Cy5.5A**) general procedure

2.1 eq. of 3-(dodecylamino)propane-1-sulfonate together with 3 eq. of DIPEA were mixed in 1.5 mL of dry DMF under Ar atmosphere, after this the mixture was stirred for 30 min at 50 °C. In a separate flask, 30 mg of corresponding diacid (100 mg in case of **Cy2A**) were dissolved in 1 mL of dry DMF together with 2.1 eq. of HATU, 1 eq. HOBt and 3 eq. of DIPEA. After 5 minutes, the solution of activated cyanine diacid was transferred to the flask with amine and the final mixture was stirred at 50 °C under Ar atmosphere for 24h (control by TLC).

After the reaction the solvent was evaporated *in vacuo*, and the crude product was purified by exclusive column chromatography (LH 20, DCM:MeOH 1:1 for all compounds) and, consecutively, by preparative TLC (SiO_2, DCM:MeOH 9:1 for **Cy3A**, **Cy5A**, **Cy3.5A**; DCM:MeOH 85:15 for **Cy5.5A**; DCM:MeOH 82:18 for **Cy2A**).

Compound **Cy3A**: yield 41 mg (74 %) as dark red solid. **^{1}H NMR (400 MHz, DMSO-*d*$_6$) δ ppm** 8.37 (t, *J*=13.3 Hz, 1 H) 7.58 - 7.70 (m, 2 H) 7.38 - 7.58 (m, 4 H) 7.23 - 7.34 (m, 2 H) 6.48 - 6.85 (m, 2 H) 4.09 - 4.27 (m, 4 H) 3.08 - 3.29 (m, 8 H) 2.54 - 2.63 (m, 4 H) 2.28 - 2.46 (m, 4 H) 1.88-2.02 (m, 4 H) 1.77 - 1.87 (m, 4 H) 1.70 (br s, 12 H) 1.34-1.46 (m, 4 H) 1.14-1.34 (m, 36 H) 0.80-0.89 (m, 6 H). ^{13}C NMR spectrum could not be obtained due to probe aggregation. **HRMS (ESI), *m/z*:** $[M]^-$ calcd for $C_{61}H_{97}N_4O_8S_2^-$, 1077.6753; found, 1077.6771.

Compound **Cy5A**: yield 15 mg (28 %) as dark blue solid. **^{1}H NMR (400 MHz, DMSO-d_6) δ ppm** 8.34 (t, *J*=13.1 Hz, 2 H) 7.61 (dd, *J*=7.3, 4.0 Hz, 2 H) 7.35 - 7.52 (m, 4 H) 7.19-7.28 (m, 2 H) 6.29 - 6.67 (m, 3 H) 4.07-4.20 (m, 4 H) 3.20 - 3.32 (m, 4 H) 3.17 (d, *J*=5.3 Hz, 4 H) 2.53 - 2.59 (m, 2 H) 2.38 - 2.49 (m, 6 H) 1.85 - 1.99 (m, 4 H) 1.76 - 1.85 (m, 4 H) 1.69 (s, 12 H) 1.35 - 1.47 (m, 4 H) 1.14 - 1.28 (m, 36 H) 0.79 - 0.87 (m, 6 H). ^{13}C NMR spectrum could not be obtained due to probe aggregation. **HRMS (ESI), *m/z*:** $[M]^-$ calcd for $C_{63}H_{99}N_4O_8S_2^-$, 1103.6910; found, 1103.6912.

Compound **Cy2A**: yield 8 mg (8 %) as dark yellow solid. **^{1}H NMR (400 MHz, DMSO-d_6) δ ppm** 8.31 (td, *J*=13.4, 5.3 Hz, 1 H) 7.73 (m, 4 H) 7.36 - 7.54 (m, 4 H) 6.05 - 6.32 (m, 2 H) 4.07 - 4.32 (m, 4 H) 3.11 - 3.28 (m, 8 H) 2.56 - 2.69 (m, 4 H) 2.31 - 2.45 (m, 4 H) 1.94 - 2.07 (m, 4 H) 1.67 - 1.86 (m, 4 H) 1.33 - 1.47 (m, 4 H) 1.10 - 1.32 (m, 36 H) 0.85 (m, 6 H). ^{13}C NMR spectrum could not be obtained due to probe aggregation. **HRMS (ESI), *m/z*:** $[M]^-$ calcd for $C_{55}H_{85}N_4O_{10}S_2^-$, 1025.5713; found, 1025.5754.

Compound **Cy3.5A**: yield 40 mg (77 %) as dark violet solid. **^{1}H NMR (400 MHz, Methanol-d_4) δ ppm** 8.59 (t, *J*=13.5 Hz, 1 H) 8.28 (d, *J*=8.5 Hz, 2 H) 8.12 (t, *J*=9.0 Hz, 2 H) 8.07 (d, *J*=8.3 Hz, 2 H) 7.81 - 7.89 (m, 2 H) 7.67 (t, *J*=7.8 Hz, 2 H) 7.52 (t, *J*=7.5 Hz, 2 H) 6.57 - 6.86 (m, 2 H) 4.23 - 4.39 (m, 4 H) 3.40 - 3.51 (m, 2 H) 3.23 - 3.29 (m, 2 H) 3.10 - 3.23 (m, 4 H) 2.53 - 2.69 (m, 4 H) 2.32 - 2.47 (m, 4 H) 2.02 (s, 12 H) 1.79 - 1.95 (m, 4 H) 1.47 - 1.79 (m, 4 H) 1.30 - 1.40 (m, 4 H) 1.16 - 1.27 (m, 36 H) 0.78 - 0.87 (m, 6 H). ^{13}C NMR spectrum could not be obtained due to probe aggregation. **HRMS (ESI), *m/z*:** $[M]^-$ calcd for $C_{69}H_{101}N_4O_8S_2^-$, 1177.7066; found, 1177.7069.

Compound **Cy5.5A**: yield 28 mg (55 %) as dark blue/green solid. **^{1}H NMR (400 MHz, DMSO-d_6) δ ppm** 8.46 (t, *J*=13.1 Hz, 2 H) 8.25 (d, *J*=8.5 Hz, 2 H) 8.02 - 8.13 (m, 4 H) 7.83 (t, *J*=8.3 Hz, 1 H) 7.77 (t, *J*=9.0 Hz, 1 H) 7.67 (t, *J*=7.0 Hz, 2 H) 7.51 (t, *J*=6.8 Hz, 2 H) 6.60 - 6.75 (m, 1 H) 6.37 - 6.58 (m, 2 H) 4.19 - 4.34 (m, 4 H) 3.40 - 3.55 (m, 2 H) 3.12 - 3.27 (m, 6 H) 2.56 - 2.69 (m, 2 H) 2.31 - 2.48 (m, 6 H) 2.03 - 2.07 (m, 2 H) 1.97 (d, *J*=3.3 Hz, 12 H) 1.64 - 1.90 (m, 6 H) 1.32 - 1.45 (m, 4 H) 1.17 (m, 36 H) 0.74 - 0.89 (m, 6 H). ^{13}C NMR spectrum could not be obtained due to probe aggregation. **HRMS (ESI), *m/z*:** $[M]^-$ calcd for $C_{71}H_{103}N_4O_8S_2^-$, 1203.7223; found, 1203.7243.

Article 1: "Redesigning Solvatochromic Probe Laurdan for Imaging Lipid Order Selectively in Cell Plasma Membranes"

Compound **3b** was synthesized according to known procedures.[311] Synthesis of compounds **1a**-**3a** is based on a synthetic route, similar to one proposed previously for C-Laurdan.[312]

1-(6-bromonaphthalene-2-yl)-propane-1-one (1a). 5 g of 2-bromonaphthalene were dissolved in 25 mL of dry nitrobenzene under Ar atmosphere and the solution was cooled to 0 °C

in an ice bath. After that, 3.56 g (1.1 eq.) of $AlCl_3$ were added portionwise, followed by a dropwise addition of 2.69 g (2.54 mL, 1.2 equiv.) of propionyl chloride, then the reaction mixture was stirred at r.t. for 18 hours.

After the reaction the mixture was quenched with distilled water (50 mL) and extracted three times with EtOAc. The organic phases were combined, washed with brine, dried over Na_2SO_4 and concentrated *in vacuo.* The crude product was purified by recrystallization from ethanol. Yield 3.15 g (50 %) as a colorless solid. **^{1}H NMR (400 MHz, $CDCl_3$)** δ ppm 8.43 (d, *J*=1.0 Hz, 1 H) 8.06 (dd, *J*=8.8, 1.8 Hz, 1 H) 8.04 (d, *J*=1.5 Hz, 1 H) 7.81 (t, *J*=9.2 Hz, 2 H) 7.62 (dd, *J*=8.5, 2.0 Hz, 1 H) 3.12 (q, *J*=7.3 Hz, 2 H) 1.28 (t, *J*=7.2 Hz, 3 H).

Ethyl 2-[(6-propanoylnaphthalene-2-yl)methylamino]acetate (2a). An oven-dried Schlenk flask was evacuated and backfilled with Ar, after that 2 g of compound **1a** were added together with 137 mg (0.08 equiv.) of $Pd(OAc)_2$, 582 mg (0.16 equiv.) of XPhos. 9.95 g (4 equiv.) of Cs_2CO_3 and 2.34 g (2 equiv.) of sarcosine ethyl ester (in form of hydrochloride salt). The Schlenk flask was then capped with rubber septum, evacuated and backfilled with Ar three times. After this, anhydrous dioxane (25 mL) was added and the mixture was stirred for 18h at 100 °C under Ar atmosphere.

After the reaction the mixture was filtered through Celite and concentrated *in vacuo*. The crude product was purified by gradient flash column chromatography (SiO_2, Heptane:EtOAc 9:1 to 2:8). Yield 1.33 g (58 %) as a yellow solid. **^{1}H NMR (400 MHz, $CDCl_3$)** δ ppm 8.33 (d, *J*=1.5 Hz, 1 H) 7.94 (dd, *J*=8.8, 1.8 Hz, 1 H) 7.80 (d, *J*=9.0 Hz, 1 H) 7.65 (d, *J*=8.8 Hz, 1 H) 7.10 (dd, *J*=9.2, 2.6 Hz, 1 H) 6.89 (d, *J*=2.5 Hz, 1 H) 4.17 - 4.23 (m, 4 H) 3.21 (s, 3 H) 3.08 (q, *J*=7.3 Hz, 2 H) 1.27 (t, *J*=7.3 Hz, 3 H) 1.25 (t, *J*=7.2 Hz, 3 H). **^{13}C NMR (101 MHz, $CDCl_3$)** δ ppm 200.47 ($C_{carbonyl}$) 170.50 ($C_{carboxyl}$) 148.75 (C_{ar}) 137.44 (C_{ar}) 130.95 (C_{ar}) 130.88 (C_{ar}) 129.58 (C_{ar}) 126.42 (C_{ar}) 125.67 (C_{ar}) 124.64 (C_{ar}) 115.75 (C_{ar}) 105.96 (C_{ar}) 61.15 (C_{al}) 54.43 (C_{al}) 39.74 (C_{al}) 31.52 (C_{al}) 14.24 (CH_3) 8.64 (CH_3). **HRMS (ESI), *m/z*** $[M+H]^+$ calcd for $C_{18}H_{22}NO_3^+$, 300.1594; found, 300.1611.

N-methyl-N-(6-propionylnaphthalen-2-yl)glycine (3a). 1.2 g of compound **2a** were dissolved in 40 mL of a freshly prepared solution of KOH (0.25 M) in EtOH. The reaction mixture was stirred for 2 days at r. t. (control by TLC). After the reaction the solution was acidified with HCl to pH 2 and the products were extracted with EtOAc three times. The ethyl acetate layers were then combined, dried over Na_2SO_4 and concentrated *in vacuo*. Yield 1,05 g (96 %) as a pale yellow solid. **^{1}H NMR (400 MHz, Methanol-*d*$_4$)** δ ppm 8.41 (d, *J*=1.5 Hz, 1 H) 7.89 (dd, *J*=8.8, 1.8 Hz, 1 H) 7.86 (d, *J*=9.3 Hz, 1 H) 7.67 (d, *J*=8.5 Hz, 1 H) 7.20 (dd, *J*=9.0, 2.5 Hz, 1 H) 6.96 (d, *J*=2.5 Hz, 1 H) 4.29 (s, 2 H) 3.21 (s, 3 H) 3.13 (q, *J*=7.3 Hz, 2 H) 1.24 (t, *J*=7.3 Hz, 3 H). **^{13}C NMR (101 MHz, Methanol-*d*$_4$)** δ ppm 203.18 ($C_{carbonyl}$) 174.45 ($C_{carbonyl}$) 150.92 (C_{ar}) 139.32 (C_{ar}) 132.02 (C_{ar}) 131.75 (C_{ar}) 131.30 (C_{ar}) 127.58 (C_{ar}) 127.01 (C_{ar}) 125.34 (C_{ar}) 117.20 (C_{ar}) 106.70 (C_{ar}) 54.75 (C_{al}) 39.92 (C_{al}) 32.44 (C_{al}) 9.19 (CH_3). **HRMS (ESI), *m/z*** $[M+H]^+$ calcd for $C_{16}H_{18}NO_3^+$, 272.1281; found, 272.1296.

3-(dodecylammonio)propane-1-sulfonate (3b), procedure adapted from elsewhere.[311] 4g of dodecylamine were mixed with 1.2 eq. of 1,3-propanesultone in 30 mL of dry acetone. The reaction was refluxed under Ar atmosphere for 24h. After the reaction, the crude product was filtered off, washed 2 times with acetone and recrystallized from ethanol.

Compound **6a**: yield 4.58 g (69.2 %) as a white solid. **^{1}H NMR (400 MHz, DMSO-d_6 (60 °C)) δ ppm** 0.88 (t, J=6.8 Hz, 3 H) 1.24 - 1.35 (m, 18 H) 1.57 (quin, J=7.6 Hz, 2 H) 1.97 (quin, J=6.4 Hz, 2 H) 2.66 (t, J=6.4 Hz, 2 H) 2.88 (t, J=7.3 Hz, 2 H) 3.06 (t, J=6.4 Hz, 2 H). **MS (ESI), m/z:** $[M]^+$ calcd for $C_{15}H_{32}NO_3S^-$, 306.21; found, 306.21.

3-(N-dodecyl-2-(methyl(6-propionylnaphthalen-2-yl)amino)acetamido)propane-1-sulfonate (Pro12A). 59.5 mg (1.05 equiv.) of 3-(dodecylamino)propane-1-sulfonate (**3b**) and 47.7 mg (65 µL, 2 equiv.) of DIPEA were mixed in 2 mL of dry DMF under Ar atmosphere, after this the mixture was stirred for 30 min at 50 °C. In a separate flask, 50 mg of carboxylic acid **3a** were dissolved in 2 mL of dry DMF together with 73.7 mg (1.05 equiv.) of HATU, 12.5 mg (0.5 equiv.) of HOBt and 95.4 mg (129 µL, 4 equiv.) of DIPEA. After 5 minutes, the solution of activated acid was transferred to the flask with amine and the final mixture was stirred for 24h at 45 °C (control by TLC). After the reaction the solvent was evaporated *in vacuo* and the crude product was purified by preparative TLC (SiO_2; DCM:MeOH 85:15). Compound **Pro12A**: yield 104 mg (82 %) as pale yellow solid (obtained in form of a salt with DIPEA). **^{1}H NMR** (400 MHz, Methanol-d_4) δ ppm 8.37 (s, 1 H) 7.86 (ddd, *J*=8.8, 3.2, 1.7 Hz, 1 H) 7.81 (dd, *J*=9.0, 2.5 Hz, 1 H) 7.63 (dd, *J*=8.8, 5.5 Hz, 1 H) 7.13 (td, *J*=9.4, 2.5 Hz, 1 H) 6.88 (t, *J*=3.0 Hz, 1 H) 4.43 (d, *J*=31.6 Hz, 2 H) 3.54 (dt, *J*=41.9, 8.0 Hz, 2 H) 3.34 - 3.42 (m, 2 H) 3.13 - 3.21 (m, 5 H) 2.79 - 2.96 (m, 2 H) 1.99 - 2.21 (m, 2 H) 1.51 - 1.73 (m, 2 H) 1.18 - 1.31 (m, 21 H) 0.85 - 0.90 (m, 3 H). **^{13}C NMR** (101 MHz, Methanol-d_4) δ ppm 203.00 (d, *J*=5.8 Hz, $C_{carboxyl}$) 171.44 ($C_{carboxyl}$) 151.27 (d, *J*=15.8 Hz, C_{ar}) 139.34 (C_{ar}) 139.30 (C_{ar}) 131.96 (d, *J*=10.2 Hz, C_{ar}) 131.55 (d, *J*=13.3 Hz, C_{ar}) 131.32 (C_{ar}) 127.53 (d, *J*=3.3 Hz, C_{ar}) 126.84 (d, *J*=8.5 Hz, C_{ar}) 125.31 (d, *J*=12.4 Hz, C_{ar}) 117.37 (d, *J*=10.2 Hz, C_{ar}) 106.62 (C_{ar}) 55.96 (C_{al}) 54.97 (d, *J*=12.0 Hz, C_{al}) 47.13 (d, *J*=18.7 Hz, C_{al}) 40.13 (d, *J*=22.6 Hz, C_{al}) 33.20 (C_{al}) 32.41 (C_{al}) 30.82 - 30.96 (m, C_{al}) 30.58 - 30.66 (m, C_{al}) 30.01 (C_{al}) 28.86 (C_{al}) 28.15 (d, *J*=7.9 Hz, C_{al}) 25.68 (C_{al}) 23.86 (C_{al}) 14.58 (C_{al}) 13.28 (CH_3) 9.22 (CH_3). **HRMS (ESI), *m/z*:** $[M+2Na]^+$ calcd for $C_{31}H_{47}N_2O_5SNa_2$, 605.3011; found, 605.3015.

Article 2: "Switchable Solvatochromic Probes for Live-Cell Super-resolution Imaging of Plasma Membrane Organization"

Ethyl 4-((3-methoxyphenyl)amino)butanoate (1a). 5 g of m-anisidine were mixed with 12.34 g (2.2 eq.) of freshly ground K_2CO_3 and 1.35 g (0.2 eq.) of KI in 40 ml of dry DMF, after that 7.93 g of ethyl 4-bromobytanoate was added and the mixture was stirred at 60 °C for 6h (control by TLC) under Ar atmosphere. After the reaction the solvent was evaporated *in vacuo*, the solid residue was dissolved in Et_2O and washed with water and brine. The organic phase was dried over Na_2SO_4 and the solvent was evaporated *in vacuo*. The crude product was purified by column chromatography (SiO_2; Hept:EtOAc 3:1, dry deposit on Celite). The product is to be kept under Ar atmosphere due to oxidation. Compound **1a**: yield 7.69g (79.8 %) as colourless oil. **^{1}H**

NMR (400 MHz, $CDCl_3$) δ ppm 1.23 – 1.30 (td, *J*=7.0, 1.0 Hz, 3 H) 1.95 (quin, *J*=7.0 Hz, 2 H) 2.43 (t, *J*=7.3 Hz, 2 H) 3.17 (t, *J*=7.0 Hz, 2 H) 3.78 (s, 3 H) 4.15 (q, *J*=7.3 Hz, 2 H) 6.17 (t, *J*=2.4 Hz, 1 H) 6.23 (ddd, *J*=8.1, 2.4, 0.8 Hz, 1 H) 6.27 (ddd, *J*=8.1, 2.4, 0.8 Hz, 1 H) 7.08 (t, *J*=8.1 Hz, 1 H). **MS (ESI), *m/z*:** $[M+H]^+$ calcd for $C_{13}H_{20}NO_3^+$, 238.14; found, 238.14.

Ethyl 4-(ethyl(3-methoxyphenyl)amino)butanoate (2a). 7.68 g of compound **1a** were mixed with 15.17 g (7.82 mL, 3 eq.) of ethyl iodide and 11.18 g (3 eq.) of freshly ground K_2CO_3 in 40 mL of dry DMF. The reaction was stirred at 50 °C for 20h (control by TLC) under Ar atmosphere. After the reaction, the solvent was evaporated *in vacuo*, the solid residue was dissolved in DCM and washed with water and brine. The organic phase was dried over Na_2SO_4 and the solvent was evaporated *in vacuo*. The crude product was purified by column chromatography (SiO_2; Hept:EtOAc 4:1, dry deposit on Celite). The product is to be kept under Ar atmosphere due to oxidation. Compound **2a**: yield 6.31g (73.5 %) as colourless oil. **^{1}H NMR (400 MHz, $CDCl_3$) δ ppm** 1.16 (t, *J*=7.0 Hz, 3 H) 1.28 (t, *J*=7.2 Hz, 3 H) 1.93 (quin, *J*=7.3 Hz, 2 H) 2.36 (t, *J*=7.3 Hz, 2 H) 3.28 - 3.33 (m, 2 H) 3.36 (q, *J*=7.0 Hz, 2 H) 3.81 (s, 3 H) 4.16 (q, *J*=7.0 Hz, 2 H) 6.22 - 6.30 (m, 2 H) 6.33 – 6.36 (m, 1 H) 7.13 (t, *J*=8.0 Hz, 1 H). **MS (ESI), *m/z*:** $[M+H]^+$ calcd for $C_{15}H_{24}NO_3^+$, 266.17; found, 266.17.

4-(ethyl(3-hydroxyphenyl)amino)butanoic acid (3a). 5.46 g of compound **2a** were mixed with 40 mL of $HBr_{(conc)}$ and the mixture was refluxed for 8h (control by TLC). After the reaction the solvent was evaporated *in vacuo*, followed by heating to 100 °C under high vacuum for 3h to evaporate the traces of solvent. Compound **3a**: yield 5.60 g (98.0 %) as a colourless solid. **^{1}H NMR (400 MHz, Methanol-d_4) δ ppm** 1.16 (t, *J*=7.3 Hz, 3 H) 1.51 - 1.76 (m, 1 H) 1.76 - 2.03 (m, 1 H) 2.34 - 2.47 (m, 2 H) 3.60 - 3.70 (m, 5 H) 6.99 (dd, *J*=8.0, 2.3 Hz, 1 H) 7.03 (q, *J*=2.3 Hz, 1 H) 7.04 (dt, *J*=4.5, 1.0 Hz, 1 H) 7.06 (dt, *J*=4.5, 1.0 Hz, 1 H) 7.44 (t, *J*=8.0 Hz, 1 H). **MS (ESI), *m/z*:** $[M]^+$ calcd for $C_{12}H_{17}NO_3^+$, 223.12; found, 223.12.

General procedure for 3-(alkylammonio)propane-1-sulfonate (6a and 6b), adapted from elsewhere.[311] 4g of corresponding alkylamine were mixed with 1.2 eq. of 1,3-propanesultone in 30 mL of dry acetone. The reaction was refluxed under Ar atmosphere for 24h. After the reaction, the crude product was filtered off, washed 2 times with acetone and recrystallized from ethanol.

Compound **6a**: yield 4.58 g (69.2 %) as a white solid. **^{1}H NMR (400 MHz, DMSO-d_6 (60 °C)) δ ppm** 0.88 (t, J=6.8 Hz, 3 H) 1.24 - 1.35 (m, 18 H) 1.57 (quin, J=7.6 Hz, 2 H) 1.97 (quin, J=6.4 Hz, 2 H) 2.66 (t, J=6.4 Hz, 2 H) 2.88 (t, J=7.3 Hz, 2 H) 3.06 (t, J=6.4 Hz, 2 H). **MS (ESI), m/z:** $[M]^+$ calcd for $C_{15}H_{32}NO_3S^-$, 306.21; found, 306.21. Compound **6b**: yield 6.56 g (61.4 %) as a white solid. **^{1}H NMR (400 MHz, DMSO-d_6) δ ppm** δ ppm 0.89 (t, J=7.3 Hz, 3 H) 1.33 (sxt, J=7.4 Hz, 2 H) 1.49 - 1.58 (m, 2 H) 1.93 (quin, J=6.8 Hz, 2 H) 2.62 (t, J=6.7 Hz, 2 H) 2.88 (t, J=7.7 Hz, 2 H) 3.04 (t, J=6.8 Hz, 2 H) **MS (ESI), m/z:** $[M]^+$ calcd for $C_{15}H_{32}NO_3S^-$, 194.09; found, 194.08.

4-(ethyl-5-oxo-5*H*-benzo[a]phenoxazin-9-yl)amino)butanoic acid (5a). 2.87 g of 4-(ethyl(3-hydroxyphenyl)amino)butanoic acid (**3a**) were dissolved in 10 mL of water together with 2 mL of $HCl_{(conc)}$ at r.t. After this the mixture was cooled to 0 °C and a solution of 1.33 g (1.1 eq.) of $NaNO_2$ in 10 mL of water was added dropwise at 0 °C. The reaction mixture was stirred for 1.5h at 0 °C, after which the water was removed by lyophilization. The product, 4-(ethyl(3-hydroxy-4-nitrosophenyl)amino)butanoic acid (**4a**), was used for the next step without further purification.

3.24 g of compound **4a** were mixed with 2.78 g (1.5 eq.) of 1-naphthol and 15 ml of dry DMF. The mixture was stirred at 80 °C for 5h. After the reaction the solvent was evaporated *in vacuo*, the solid residue was dissolved in 40 mL of MeOH at 0 °C, followed by a dropwise addition of 1.54 g (0.94 mL) of $SOCl_2$ under dry atmosphere. After 1h of stirring at 0 °C, the mixture was stirred for 20h at r.t., afterwards the solvent was evaporated in vacuo. The methyl ester of **5a** was purified by column chromatography (SiO_2; Hept:EtOAc 1:1, dry deposit on Celite). **^{1}H NMR (400 MHz, $CDCl_3$) δ ppm** 1.26 (t, *J*=7.0 Hz, 3 H) (quin, *J*=7.4 Hz, 2 H) 2.38 - 2.47 (m, 2 H) 3.39 - 3.52 (m, 4 H) 3.73 (s, 3 H) 6.39 (s, 1 H) 6.50 (d, *J*=2.8 Hz, 1 H) 6.69 (dd, *J*=9.0, 2.8 Hz, 1 H) 7.61 (d, *J*=9.0 Hz, 1 H) 7.65 (td, *J*=7.8, 1.4 Hz, 1 H) 7.74 (dt, *J*=7.8, 1.40 Hz, 1 H) 8.30 (dd, *J*=7.8, 1.3 Hz, 1 H) 8.65 (dd, *J*=7.9, 0.9 Hz, 1 H). **^{13}C NMR (101 MHz, $CDCl_3$) δ ppm** 12.38 (CH_2CH_3) 22.54 (C_{al}) 30.90 (C_{al}) 45.59 (C_{al}) 49.85 (C_{al}) 51.81 (C_{OMe}) 96.55 (C_{ar}) 105.74 (C_{ar}) 109.83 (C_{ar}) 123.81 (C_{ar}) 125.05 (C_{ar}) 125.63 (C_{ar}) 129.93 (C_{ar}) 131.09 (C_{ar}) 131.31 (C_{ar}) 131.71 (C_{ar}) 132.01 (C_{ar}) 140.14 (C_{ar}) 146.59 (C_{ar}) 150.80 (C_{ar}) 152.06 (C_{ar}) 173.31 (C_{carbox}) 183.73 (C_{ar}). **HRMS (ESI), m/z:** $[M]^+$ calcd for $C_{23}H_{23}N_2O_4^+$, 390.1580; found, 390.1581.

On the next step, 370 mg of methyl ester of **5a** were dissolved in 15 mL of 20% $HCl_{(aq)}$ and the mixture was stirred for 15h at 90 °C (control by TLC). After the reaction the solvent was removed *in vacuo* and the solid residue was twice washed with water on a filter. Compound **5a**: overall yield 345 mg (7.7 %) as dark red solid. **^{1}H NMR (400 MHz, DMSO-d_6) δ ppm** 1.16 (t, *J*=6.9 Hz, 3 H) 1.81 (quin, *J*=7.5 Hz, 2 H) 2.35 (t, *J*=7.3 Hz, 2 H) 3.44 (quin, *J*=7.5 Hz, 2 H) 3.52 (t, *J*=6.9 Hz, 2 H) 6.32 (s, 1 H) 6.76 (s, 1 H) 6.91 (d, *J*=9.4 Hz, 1 H) 7.63 (d, *J*=8.5 Hz, 1 H) 7.72 (t, *J*=7.5 Hz, 1 H) 7.81 (t, *J*=7.5 Hz, 1 H) 8.13 (d, *J*=7.8 Hz, 1 H) 8.56 (d, *J*=7.8 Hz, 1 H). **^{13}C NMR (101 MHz, DMSO-d_6) δ ppm** 12.73 (CH_3) 22.75 (C_{al}) 31.04 (C_{al}) 41.28 (C_{al}) 45.45 (C_{al}) 49.81 (C_{al}) 78.58 (C_{al}) 96.77 (C_{ar}) 104.87 (C_{ar}) 111.19 (C_{ar}) 123.86 (C_{ar}) 124.23 (C_{ar}) 125.18 (C_{ar}) 125.47 (C_{ar}) 130.44 (C_{ar}) 131.45 (C_{ar}) 132.05 (C_{ar}) 132.08 (C_{ar}) 135.43 (C_{ar}) 146.95 (C_{ar}) 174.66 (C_{ar}) 182.03 (C_{ar}) 192.67 (s, COOH) 217.84 (s, 1 C_{ar}). **HRMS (ESI), m/z:** $[M+Na]^+$ calcd for $C_{22}H_{20}N_2O_4Na^+$, 399.1315; found, 399.1306.

General procedure for 3-(N-alkyl-4(ethyl(5-oxo-5*H*-benzo[a]phenoxazin-9-yl)amino)butanamido)propane-1-sulfonate (NR12A and NR4A). 1.05 eq. of the corresponding 3-(alkylamino)propane-1-sulfonate (6a or 6b) and 20.6 mg (28 µL, 2 eq.) of DIPEA were mixed in 2 mL of dry DMF under Ar atmosphere, after this the mixture was stirred for 30 min at 50 °C. In a separate flask, 30 mg of compound 5a were dissolved in 2 mL of dry DMF together with 32.9 mg (1.05 eq.) of HATU and 20.6 mg (28 µL, 2 eq.) of DIPEA. After 5 minutes, the solution of activated Nile Red acid was transferred to the flask with amine and the final mixture was stirred for 24h at 50 °C (control by TLC). After the reaction the solvent was evaporated *in*

vacuo and the crude product was purified by gradient column chromatography (SiO_2; DCM:MeOH 88:12 to DCM:MeOH 85:15 for **NR12A** and DCM:MeOH 85:15 to DCM:MeOH 82:18 for **NR4A**). Compound **NR12A**: yield 29.9 mg (47.2 %) as dark red solid. **^{1}H NMR (400 MHz, Methanol-*d*$_4$) δ ppm** 0.81 - 0.92 (m, 3 H) 1.11 - 1.33 (m, 19 H) 1.34 - 1.40 (m, 4 H) 1.47 - 1.62 (m, 2 H) 1.91 - 2.00 (m, 2 H) 2.00 - 2.10 (m, 2 H) 2.41 - 2.58 (m, 2 H) 2.78 - 2.89 (m, 2 H) 3.36 - 3.58 (m, 6 H) 6.23 (s, 1 H) 6.55 (dd, *J*=8.8, 2.5 Hz, 1 H) 6.83 (ddd, *J*=12.0, 9.3, 2.5 Hz, 1 H) 7.50 (d, *J*=9.3 Hz, 1 H) 7.57 - 7.66 (m, 1 H) 7.66 - 7.76 (m, 1 H) 8.13 (d, *J*=7.8 Hz, 1 H) 8.53 (d, *J*=7.8 Hz, 1 H). **^{13}C NMR (101 MHz, Methanol-*d*$_4$) δ ppm** 15.29 (CH_3) 15.71 (CH_3) 16.99 (C_{al}) 19.91 (C_{al}) 21.32 (C_{al}) 26.24 (C_{al}) 26.70 (C_{al}) 27.12 (C_{al}) 28.22 (C_{al}) 32.98 (C_{al}) 33.08 (C_{al}) 33.15 (C_{al}) 33.27 (C_{al}) 35.58 (C_{al}) 46.38 (C_{al}) 58.42 (C_{al}) 99.98 (C_{ar}) 108.04 (C_{ar}) 114.78 (C_{ar}) 127.40 (C_{ar}) 128.84 (C_{ar}) 129.18 (C_{ar}) 133.36 (C_{ar}) 135.02 (C_{ar}) 135.21 (C_{ar}) 135.96 (C_{ar}) 141.93 (C_{ar}) 150.61 (C_{ar}) 155.78 (C_{ar}) 156.50 (C_{ar}) 176.93 (C_{ar}) 187.84 (C_{ar}). **HRMS (ESI), m/z:** $[M]^-$ calcd for $C_{37}H_{50}N_3O_6S^-$, 664.3418; found, 664.3422. Compound **NR4A**: yield 32.8 mg (60.5 %) as dark red solid. **^{1}H NMR (400 MHz, Methanol-*d*$_4$) δ ppm** 0.96 (dt, *J*=9.1, 7.4 Hz, 3 H) 1.21 (t, *J*=7.0 Hz, 3 H) 1.30 - 1.41 (m, 4 H) 1.51 - 1.61 (m, 2 H) 1.82 - 1.97 (m, 2 H) 1.97 - 2.12 (m, 2 H) 2.39 - 2.57 (m, 2 H) 2.79 - 2.89 (m, 2 H) 3.34 - 3.57 (m, 6 H) 6.11 (d, *J*=2.0 Hz, 1 H) 6.42 (dd, *J*=9.2, 2.7 Hz, 1 H) 6.72 (td, *J*=8.8, 2.7 Hz, 1 H) 7.37 (dd, *J*=9.2, 3.4 Hz, 1 H) 7.52 - 7.59 (m, 1 H) 7.64 (td, *J*=7.5, 1.3 Hz, 1 H) 8.05 (dd, *J*=7.8, 1.00 Hz, 1 H) 8.38 - 8.44 (m, 1 H) **^{13}C NMR (101 MHz, Methanol-*d*$_4$) δ** 15.39 (CH_3) 15.73 (CH_3) 16.83 (C_{al}) 19.92 (C_{al}) 21.36 (C_{al}) 26.67 (C_{al}) 27.18 (C_{al}) 28.24 (C_{al}) 33.27 (C_{al}) 34.70 (C_{al}) 46.39 (C_{al}) 58.42 (C_{al}) 99.86 (C_{ar}) 107.95 (C_{ar}) 114.70 (C_{ar}) 127.32 (C_{ar}) 128.76 (C_{ar}) 129.08 (C_{ar}) 133.27 (C_{ar}) 134.93 (C_{ar}) 135.14 (C_{ar}) 135.84 (C_{ar}) 141.79 (C_{ar}) 150.44 (C_{ar}) 155.62 (C_{ar}) 156.32 (C_{ar}) 176.84 (C_{ar}) 187.68 (C_{ar}). **HRMS (ESI), m/z**: $[M]^+$ calcd for $C_{29}H_{34}N_3O_6S^-$, 552.2163; found, 552.2168.

Targeted solvatochromic fluorescent probes for imaging lipid order in organelles under oxidative and mechanical stress

Compounds **1** and **NR12A** were synthesized according to the procedures described in the **Article 3.**

(3-(4-(ethyl(5-oxo-5H-benzo[a]phenoxazin-9-yl)amino)butanamido)propyl)triphenylphosphonium(NRMito)

30 mg of compound **1** were dissolved in 1 mL of dry DMF together with 31.9 mg (1.05 eq.) of HATU, 5.4 mg (0.5 eq.) of HOBt and 61.9 mg (6 eq., 84 µL) of DIPEA under Ar atmosphere. After 5 minutes, a solution of 40.3 mg (1.05 eq.) of 3-aminopropyltriphenylphosphonium bromide in 1 mL of dry DMF was added and the mixture was stirred for 24h (control by TLC) under Ar atmosphere. After the reaction the solvent was evaporated *in vacuo* and the product was purified by preparative TLC (SiO_2, DCM:MeOH 92:8). After the TLC the traces of DMF were removed by washing the crystalline product on a filter

twice with diethyl ether and drying. Yield: 26 mg (43.0%) as a dark red solid. **^{1}H NMR (400 MHz, $CDCl_3$) δ ppm** 8.66 (d, *J*=7.5 Hz, 1 H) 8.31 (dd, *J*=7.8, 1.0 Hz, 1 H) 7.58 - 7.82 (m, 18 H) 6.86 (br t, *J*=6.0 Hz, 1 H) 6.76 (dd, *J*=9.2, 2.6 Hz, 1 H) 6.57 (d, *J*=2.5 Hz, 1 H) 6.36 (s, 1 H) 3.37 - 3.54 (m, 6 H) 3.16 - 3.27 (m, 2 H) 2.38 (br t, *J*=7.0 Hz, 2 H) 1.86 - 2.02 (m, 4 H) 1.25 (t, *J*=7.0 Hz, 3 H). **^{13}C NMR (101 MHz, $CDCl_3$) δ ppm** 183.66 (C_{ar}) 173.59 (C_{amide}) 152.16 (C_{ar}) 151.12 (C_{ar}) 146.68 (C_{ar}) 139.53 (C_{ar}) 135.37 (C_{ar}) 133.24 (d, *J*=10.0 Hz, C_{ar}) 132.07 (C_{ar}) 131.65 (C_{ar}) 131.22 (d, *J*=11.4 Hz, C_{ar}) 130.64 (d, *J*=12.65 Hz, C_{ar}) 129.79 (C_{ar}) 125.57 (C_{ar}) 125.01 (C_{ar}) 123.75 (C_{ar}) 118.15 (C_{ar}) 117.29 (C_{ar}) 110.15 (C_{ar}) 105.48 (C_{ar}) 96.42 (C_{ar}) 50.22 (C_{al}) 45.56 (C_{al}) 39.14 (d, *J*=17.8 Hz, C_{al}) 32.82 (C_{al}) 23.25 (C_{al}) 22.49 (d, *J*=3.5 Hz, C_{al}) 20.17 (d, *J*=53.5 Hz, C_{al}) 12.36 (s, C_{al}). **HRMS (ESI), *m/z*:** $[M]^+$ calcd for $C_{43}H_{41}N_3O_3P$, 678.2880; found, 678.2889.

4-(ethyl(5-oxo-5H-benzo[a]phenoxazin-9-yl)amino)-N-(3-morpholinopropyl)butanamide(NRLyso)

30 mg of compound **1** were dissolved in 2 mL of dry DMF together with 31.9 mg (1.05 eq.) of HATU, 5.4 mg (0.5 eq.) of HOBt and 41.2 mg (4 eq., 56 µL) of DIPEA under Ar atmosphere. After 5 minutes, 12.1 mg (1.05 eq, 12.2 µL) of 3-morpholinopropylamine were added and the mixture was stirred for 24h (control by TLC) under Ar atmosphere. After the reaction the solvent was evaporated *in vacuo* and the crude product was purified by preparative TLC (two consecutive purifications, SiO_2; DCM:MeOH 90:10). Yield: 6 mg (15.0%) as a dark red solid. **^{1}H NMR (400 MHz, $CDCl_3$) δ ppm** 8.63 (dd, *J*=8.2, 1.1 Hz, 1 H) 8.29 (dd, *J*=7.8, 1.0 Hz, 1 H) 7.72 (td, *J*=8.0, 1.8 Hz, 1 H) 7.65 (td, *J*=7.8, 1.0 Hz, 1 H) 7.58 (d, *J*=9.3 Hz, 1 H) 7.07 (br t, *J*=4.5 Hz, 1 H) 6.69 (dd, *J*=9.3, 2.8 Hz, 1 H) 6.49 (d, *J*=2.8 Hz, 1 H) 6.36 (s, 1 H) 3.68 (t, *J*=4.6 Hz, 4 H) 3.42 - 3.52 (m, 4 H) 3.39 (q, *J*=6.0 Hz, 2 H) 2.38 - 2.51 (m, 6 H) 2.26 (t, *J*=7.0 Hz, 2 H) 2.00 (quin, *J*=7.3 Hz, 2 H) 1.70 (quin, *J*=6.3 Hz, 2 H) 1.25 (t, *J*=7.2 Hz, 3 H). **^{13}C NMR (101 MHz, DMSO-d_6) δ ppm** 183.76 (C_{ar}) 171.60 (C_{amide}) 152.10 (C_{ar}) 150.97 (C_{ar}) 146.65 (C_{ar}) 140.11 (C_{ar}) 132.04 (C_{ar}) 131.72 (C_{ar}) 131.35 (C_{ar}) 131.12 (C_{ar}) 129.97 (C_{ar}) 125.65 (C_{ar}) 125.03 (C_{ar}) 123.83 (C_{ar}) 109.91 (C_{ar}) 105.72 (C_{ar}) 96.54 (C_{ar}) 67.05 (C_{al}) 57.81 (C_{al}) 53.68 (C_{al}) 49.95 (C_{al}) 45.44 (C_{al}) 39.45 (C_{al}) 33.18 (C_{al}) 24.93 (C_{al}) 23.20 (C_{al}) 12.35 (C_{al}). **HRMS (ESI), *m/z*:** $[M+H]^+$ calcd for $C_{29}H_{35}N_4O_4$, 503.2659; found, 503.2679.

tert-butyl (1-oxo-1-(perfluorophenyl)-5,8,11,14,17,20,23,26,29,32,35-undecaoxa-2-azaheptatriacontan-37-yl)carbamate (2a)

260 mg of BocHN-PEG_{11}-NH_2 were dissolved in 5 mL of dry DCM together with 730 mg (5.5 eq.) of Cs_2CO_3 and the mixture was cooled to 0 °C in an ice bath. Then, 415 mg (4.5 eq., 260 µL) of pentafluorobenzoyl chloride were added and the mixture was stirred for 1h at 0 °C and then for 1h at r.t. under Ar atmosphere. After the reaction the solvent was evaporated *in vacuo*, then 98.7 µL of TFA together with 10 mL of DCM were added to neutralize Cs_2CO_3. After this the solid residue was filtered off, and the solvent was evaporated *in vacuo*. The crude product was purified by column chromatography (SiO_2; DCM:MeOH 95:5, alkaline $KMnO_4$ staining for TLC analysis of the column fractions). Yield: 259 mg (76.6 %) as a colourless oil. **^{1}H NMR (400 MHz, $CDCl_3$) δ ppm** 7.09 (br s, 1 H) 5.04 (br s, 1 H) 3.55 - 3.69 (m, 44 H) 3.53 (br t, *J*=5.1 Hz, 1 H) 3.30 (br q, *J*=5.0 Hz, 2 H) 2.43 (br s, 1 H) 1.43 (s, 9 H). **^{13}C NMR (101 MHz, DMSO-d_6) δ ppm**

157.44 (C_{carbox}) 156.00 (C_{carbox}) 145.29 (C_{ar}) 142.83 (C_{ar}) 138.81 (C_{ar}) 136.27 (C_{ar}) 112.04 (d, *J*=3.7 Hz, C_{ar}) 78.71 - 79.49 (m, C_{al}) 70.48 - 70.62 (m, C_{al}) 70.47 (C_{al}) 70.45 (C_{al}) 70.43 (C_{al}) 70.37 (C_{al}) 70.26 (C_{al}) 70.21 (C_{al}) 69.35 (C_{al}) 40.38 (C_{al}) 40.15 (C_{al}) 28.41 (C_{al}). **HRMS (ESI), *m/z*:** $[M+Na]^+$ calcd for $C_{36}H_{59}F_5N_2O_{14}Na$, 861.3786; found, 861.3807.

N-(35-amino-3,6,9,12,15,18,21,24,27,30,33-undecaoxapentatriacontyl)-2,3,4,5,6-pentafluorobenzamide (**2b**)

240 mg of **1a** were dissolved in 2 mL of dry DCM, after that 2 mL of TFA were added and the mixture was stirred for 2h at r.t. After the reaction the solvent was evaporated *in vacuo*. In order to eliminate traces of TFA, 1 mL of methanol was added, followed by evaporation *in vacuo* (3 times). Yield: 238 mg (97.2%) as a colourless oil. **^{1}H NMR (400 MHz, $CDCl_3$) δ ppm** 7.43 (br s, 1 H) 7.02 (br s, 1 H) 3.78 (t, *J*=5.3 Hz, 2 H) 3.58 - 3.71 (m, 44 H) 3.15 (sxt, *J*=5.4 Hz, 2 H). **^{13}C NMR (101 MHz, DMSO-d_6) δ ppm** 176.96 (C_{amide})159.68 (q, *J*=39.40 Hz, C_{ar}) 158.36 (C_{ar}) 115.33 (q, *J*=287.69 Hz, C_{ar}) 70.26 (C_{al}) 70.23 (C_{al}) 70.15 (C_{al}) 70.12 (C_{al}) 70.09 (C_{al}) 70.04 (C_{al}) 70.01 (C_{al}) 69.89 (C_{al}) 69.84 (C_{al})69.79 (C_{al}) 69.78 (C_{al}) 69.74 (C_{al}) 69.70 (C_{al}) 69.63 (C_{al}) 69.55 (C_{al}) 69.41 (C_{al}) 69.16 (C_{al}) 66.64 (C_{al}) 40.13 (C_{al}) 39.78 (C_{al}) 21.97 (C_{al}). **HRMS (ESI), *m/z*:** $[M+H]^+$ calcd for $C_{31}H_{52}F_5N_2O_{12}$, 739.3441; found, 739.3471.

2,3,4,5,6-pentafluoro-N-(37-oxo-41-(5-oxo-5H-benzo[a]phenoxazin-9-yl)-,6,9,12,15,18,21,24,27,30,33-undecaoxa-36,41-diazatritetracontyl)benzamide($NRER_F$)

30 mg of compound **1** were dissolved in 1 mL of dry DMF together with 31.9 mg (1.05 eq.) of HATU, 5.4 mg (0.5 eq.) of HOBt and 61.9 mg (6 eq., 84 µL) of DIPEA under Ar atmosphere. After 5 minutes, a solution of 71.4 mg (1.05 eq.) of **2b** in 1 mL of dry DMF was added and the mixture was stirred for 24h (control by TLC) under Ar atmosphere. After the reaction the solvent was evaporated *in vacuo*. The crude product was purified by preparative TLC (SiO_2, DCM:MeOH 95:5). Yield: 53 mg (60.6 %) as a dark red oil. **^{1}H NMR (400 MHz, $CDCl_3$) δ ppm** 8.62 (d, *J*=7.5 Hz, 1 H) 8.25 (d, *J*=7.5 Hz, 1 H) 7.70 (td, *J*=7.53, 1.2 Hz, 1 H) 7.62 (td, *J*=7.53, 1.2 Hz, 1 H) 7.57 (d, *J*=9.3 Hz, 1 H) 7.32 - 7.40 (m, 1 H) 6.70 (dd, *J*=9.0, 2.5 Hz, 1 H) 6.56 (br t, *J*=4.5 Hz, 1 H) 6.49 (d, *J*=2.5 Hz, 1 H) 6.35 (s, 1 H) 3.55-3.69 (m, 44 H) 3.39 - 3.50 (m, 8 H) 2.30 (br t, *J*=7.0 Hz, 2 H) 1.98 (quin, *J*=7.3 Hz, 2 H) 1.23 (t, *J*=7.0 Hz, 3 H). **^{13}C NMR (101 MHz, DMSO-d_6) δ ppm** 183.73 (C_{ar}) 172.34 (C_{amide}) 157.63 (C_{amide}) 152.18 (C_{ar}) 151.09 (C_{ar}) 146.68 (C_{ar}) 145.29 (C_{ar}) 142.74 (C_{ar}) 139.71 (C_{ar}) 138.77 (C_{ar}) 136.28 (C_{ar}) 132.05 (C_{ar}) 131.62 (C_{ar}) 131.33 (C_{ar}) 131.17 (C_{ar}) 129.86 (C_{ar}) 125.57 (C_{ar}) 125.09 (C_{ar}) 123.79 (C_{ar}) 112.09 (d, *J*=3.7 Hz, C_{ar}) 110.11 (C_{ar}) 105.52 (C_{ar}) 96.46 (C_{ar}) 70.41 (C_{al}) 70.35 (C_{al}) 70.28 (C_{al}) 70.27 (C_{al}) 70.21 (C_{al}) 70.18 (C_{al}) 70.07 (C_{al}) 69.89 (C_{al}) 69.42 (C_{al}) 50.64 (C_{al}) 50.09 (C_{al}) 45.50 (C_{al}) 40.11 (C_{al}) 39.26 (C_{al}) 32.86 (C_{al}) 23.13 (C_{al}) 12.35 (C_{al}). **HRMS (ESI), *m/z*:** $[M+Na]^+$ calcd for $C_{53}H_{69}F_5N_4O_{15}Na$, 1119.4580; found, 1119.4619.

N-(3-chloropropyl)-4-(ethyl(5-oxo-5H-benzo[a]phenoxazin-9-yl)amino)butanamide($NRER_{Cl}$)

30 mg of compound **1** were dissolved in 1 mL of dry DMF together with 31.9 mg (1.05 eq.) of HATU, 5.4 mg (0.5 eq.) of HOBt and 61.9 mg (6 eq., 84 µL) of DIPEA under Ar

atmosphere. After 5 minutes, a solution of 10.9 mg (1.05 eq.) of 3-chloropropylamine in 1 mL of dry DMF was added and the mixture was stirred for 24h (control by TLC) under Ar atmosphere. After the reaction the solvent was evaporated *in vacuo*, then the solid residue was dissolved in EtOAc and washed with water (x3), dried over Na_2SO_4 and the solvent was evaporated *in vacuo*. The crude product was purified by preparative TLC (SiO_2, DCM:MeOH 98:2). Yield: 14 mg (38.9 %) as a dark red solid. **^{1}H NMR (400 MHz, $CDCl_3$) δ ppm** 8.61 (dd, *J*=8.0, 0.8 Hz, 1 H) 8.22 (dd, *J*=7.9, 0.9 Hz, 1 H) 7.70 (td, *J*=7.6, 1.3 Hz, 1 H) 7.62 (td, *J*=7.6, 1.0 Hz, 1 H) 7.54 (d, *J*=9.0 Hz, 1 H) 6.68 (dd, *J*=9.0, 2.8 Hz, 1 H) 6.48 (d, *J*=2.8 Hz, 1 H) 6.32 (s, 1 H) 6.24 (br t, *J*=5.8 Hz, 1 H) 3.59 (t, *J*=6.4 Hz, 2 H) 3.37 - 3.50 (m, 6 H) 2.31 (t, *J*=7.2 Hz, 2 H) 1.94 - 2.06 (m, 4 H) 1.22 (t, *J*=7.2 Hz, 3 H). **^{13}C NMR (101 MHz, DMSO-*d*$_6$) δ ppm** 183.77 (C_{ar}) 172.50 (C_{amide}) 152.38 (C_{ar}) 151.24 (C_{ar}) 146.71 (C_{ar}) 139.33 (C_{ar}) 132.09 (C_{ar}) 131.51 (C_{ar}) 131.42 (C_{ar}) 131.25 (C_{ar}) 129.83 (C_{ar}) 125.45 (C_{ar}) 125.32 (C_{ar}) 123.89 (C_{ar}) 110.33 (C_{ar}) 105.19 (C_{ar}) 96.45 (C_{ar}) 55.60 (C_{al}) 50.07 (C_{al}) 45.52 (C_{al}) 37.17 (C_{al}) 33.09 (C_{al}) 32.15 (C_{al}) 23.25 (C_{al}) 12.36 (C_{al}). **HRMS (ESI), *m/z*:** $[M-H-Cl+Na]^+$ calcd for $C_{25}H_{25}N_3O_3Na$, 438.1796; found, 438.1802.

tert-butyl (2-dodecanamidoethyl)carbamate (3a)

0.5 g of myristic acid were dissolved in 5 mL of dry DMF together with 874 mg (1.05 eq.) of HATU, 148 mg (0.5 eq.) of HOBt and 850 mg (3 eq., 1.15 mL) of DIPEA under Ar atmosphere. After 5 minutes, a solution of 368 mg (1.05 eq.) of N-Boc-ethylenediamine in 5 mL of dry DMF was added and the mixture was stirred for 24h (control by TLC). After the reaction the solvent was evaporated *in vacuo* and the product was purified by column chromatography (SiO_2, DCM:MeOH 95:5). Yield: 670 mg (80.6 %) as a pale yellowish solid. **^{1}H NMR (400 MHz, $CDCl_3$) δ ppm** 6.10 (br s, 1 H) 4.88 (br s, 1 H) 3.32 - 3.39 (m, 2 H) 3.22 - 3.31 (m, 2 H) 2.16 (t, *J*=8.0 Hz, 2 H) 1.61 (m, 4 H) 1.44 (s, 9 H) 1.20 - 1.34 (m, 18 H) 0.88 (t, *J*=6.8 Hz, 3 H)

N-(2-aminoethyl)dodecanamide (3b)

240 mg of **3a** were dissolved in 2 mL of dry DCM, after that 2 mL of TFA were added and the mixture was stirred for 2h at r.t. After the reaction the solvent was evaporated *in vacuo*. In order to eliminate traces of TFA, 1 mL of methanol was added, followed by evaporation *in vacuo* (3 times). Yield: 241.9 mg (97.0 %) (in a form of TFA salt) as a pale yellowish solid. **^{1}H NMR (400 MHz, $CDCl_3$) δ ppm** 7.37 (br s, 1 H) 3.45 - 3.58 (m, 2 H) 3.05 - 3.21 (m, 2 H) 1.48 - 1.61 (m, 2 H) 1.17 - 1.33 (m, 20 H) 0.87 (t, *J*=7.0 Hz, 3 H)

N-(2-(4-(ethyl(5-oxo-5H-benzo[a]phenoxazin-9-yl)amino)butanamido)ethyl)tetradecanamide(NRGolgi$_E$)

30 mg of compound **1** were dissolved in 1 mL of dry DMF together with 31.9 mg (1.05 eq.) of HATU, 5.4 mg (0.5 eq.) of HOBt and 41.23 mg (4 eq., 55.6 μL) of DIPEA under Ar atmosphere. After 5 minutes, a solution of 22.7 mg (1.05 eq.) of **3b** and 28 μL of DIPEA in 1 mL of dry DCM was added and the mixture was stirred for 24h (control by TLC) under Ar atmosphere. After the reaction the solvent was evaporated *in vacuo* and the crude product was separated by preparative TLC. Yield: 22 mg (43.9 %) as a dark red solid. **^{1}H NMR (400 MHz, $CDCl_3$) δ ppm** 8.63 (d, *J*=7.8 Hz, 1 H) 8.25 (d, *J*=7.8 Hz, 1 H) 7.71 (td, *J*=7.5, 1.0 Hz, 1 H) 7.63 (br td, *J*=7.5,

1.0 Hz, 1 H) 7.56 (d, *J*=9.0 Hz, 1 H) 6.82 (br s, 1 H) 6.69 (dd, *J*=9.0, 2.5 Hz, 1 H) 6.46 - 6.53 (m, 2 H) 6.35 (s, 1 H) 3.35 - 3.52 (m, 8 H) 2.31 (t, *J*=7.3 Hz, 2 H) 2.18 (t, *J*=7.7 Hz, 2 H) 1.93 - 2.03 (m, 2 H) 1.53 - 1.63 (m, 2 H) 1.16 - 1.32 (m, 23 H) 0.87 (t, *J*=6.9 Hz, 3 H). The ^{13}C NMR spectra could not be obtained due to limited solubility of the probe. **HRMS (ESI), *m/z*:** $[M+Na]^+$ calcd for $C_{38}H_{52}N_4O_4Na$, 651.3889; found, 651.3902.

N,N-dicyclohexyl-4-(ethyl(5-oxo-5H-benzo[a]phenoxazin-9-yl)amino)butanamide(NRLD)

30 mg of compound **1** were dissolved in 1 mL of dry DMF together with 31.9 mg (1.05 eq.) of HATU, 5.4 mg (0.5 eq.) of HOBt and 51 mg (5 eq., 70 µL) of DIPEA under Ar atmosphere. After 5 minutes, a solution of 15.2 mg (1.05 eq., 16.7 µL) of dicyclohexylamine in 1 mL of dry DMF was added and the mixture was stirred for 24h (control by TLC) under Ar atmosphere. After the reaction the solvent was evaporated *in vacuo*, the solid residue was dissolved in DCM, washed with water and brine, dried over Na_2SO_4, then the solvent was evaporated *in vacuo*. The crude product was purified by preparative TLC (two consecutive purifications, SiO_2; DCM:MeOH 99:1 and SiO_2; DCM:MeOH 98:2, respectfully). Yield: 30 mg (67.5 %) as a dark red solid. **^{1}H NMR (400 MHz, $CDCl_3$) δ ppm** 8.63 (dd, *J*=8.0, 0.8 Hz, 1 H) 8.29 (dd, *J*=7.8, 1.0 Hz, 1 H) 7.71 (td, *J*=7.5, 1.5 Hz, 1 H) 7.63 (td, *J*=7.5, 1.5 Hz, 1 H) 7.58 (d, *J*=9.0 Hz, 1 H) 6.70 (dd, *J*=9.3, 2.8 Hz, 1 H) 6.50 (d, *J*=2.8 Hz, 1 H) 6.36 (s, 1 H) 3.43 - 3.51 (m, 5 H) 2.40 - 2.60 (m, 2 H) 2.36 (t, *J*=6.5 Hz, 2 H) 1.97 (quin, *J*=7.0 Hz, 2 H) 1.76 - 1.87 (m, 4 H) 1.59 - 1.70 (m, 4 H) 1.46 - 1.57 (m, 4 H) 1.03 - 1.33 (m, 10 H). **^{13}C NMR (101 MHz, DMSO-d_6) δ ppm** 183.72 (C_{ar}) 170.60 (C_{amide}) 152.14 (C_{ar}) 151.17 (C_{ar}) 146.69 (C_{ar}) 139.91 (C_{ar}) 132.07 (C_{ar}) 131.74 (C_{ar}) 131.27 (C_{ar}) 131.08 (C_{ar}) 129.87 (C_{ar}) 125.66 (C_{ar}) 124.99 (C_{ar}) 123.76 (C_{ar}) 109.97 (C_{ar}) 105.67 (C_{ar}) 96.52 (C_{ar}) 50.10 (C_{al}) 45.40 (C_{al}) 30.22 (C_{al}) 26.66 (C_{al}) 26.09 (C_{al}) 25.42 (C_{al}) 25.23 (C_{al}) 22.99 (C_{al}) 12.36 (C_{al}). **HRMS (ESI), *m/z*:** $[M+Na]^+$ calcd for $C_{22}H_{20}N_2O_4Na$, 562.3048; found, 562.3062.

Reactive probes based on bivalent reactive amphiphiles

The following compounds were synthesized according to the literature procedures: 5-(chloromethyl)-2-hydroxy-benzaldehyde (**1b**),[313] 3-(N-dodecylamino)propane-1-sulfonate (**4b**),[314] cyanine diacids (**7a** and **7b**).[309]

N-dodecyl-N-methylpent-4-yn-1-amine (1a)

466 mg (1 equiv.) of N-dodecyl-N-methylamine were mixed with 240 mg (247 µL, 1.2 equiv.) of 5-chloropent-1-yne, 370 mg (500 µL, 1.44 equiv.) of DIPEA and 162 mg (0.5 equiv.) of KI in 5 ml of dry DMF. The mixture was stirred for 72h at 40 °C (control by TLC). After the reaction the solvent was evaporated *in vacuo*, the solid residues were dissolved in Et_2O and washed with 1M aqueous NaOH and brine, dried over Na_2SO_4, after which the solvent was evaporated *in vacuo.* The crude product was purified by exclusive chromatography (SiO_2, DCM:MeOH 92:8). Yield 240 mg (39 %) as a colourless oil. **^{1}H NMR (400 MHz, $CDCl_3$) δ ppm**

3.07 - 3.15 (m, 2 H) 2.93 - 3.01 (m, 2 H) 2.71 (s, 3 H) 2.37 (td, *J*=6.7, 2.5 Hz, 2 H) 2.05 - 2.13 (m, 2 H) 2.04 (t, *J*=2.6 Hz, 1 H) 1.78 - 1.88 (m, 2 H) 1.20 - 1.40 (m, 18 H) 0.88 (t, *J*=6.8 Hz, 3 H).

N,N'-(1,3-phenylenebis(methylene))bis(N-dodecyl-N-methylpent-4-yn-1-aminium) (2a)

110 mg (1 equiv.) of compound **1a** were dissolved in 1 ml of dry CH_3CN, then a solution of 34.6 mg (0.48 equiv.) of 1,3-bis(chloromethyl)benzene in 1 ml of dry CH_3CN was added and the mixture was refluxed for 24h (control by TLC). After the reaction the solvent was evaporated *in vacuo* and the crude product was purified by exclusive column chromatography (LH-20, DCM:MeOH 50:50, two consecutive runs). Yield 80 mg (61 %) as a colourless solid. **^{1}H NMR (400 MHz, Methanol-*d*$_4$) δ ppm** 7.91 (s, 1 H) 7.76 - 7.81 (m, 2 H) 7.70 (dd, *J*=8.5, 7.3 Hz, 1 H) 4.68 (s, 4 H) 3.33 - 3.56 (m, 8 H) 3.06 (s, 6 H) 2.46 (t, *J*=2.8 Hz, 2 H) 2.40 (td, *J*=6.5, 2.4 Hz, 4 H) 2.00 - 2.20 (m, 4 H) 1.79 - 1.97 (m, 4 H) 1.26 - 1.46 (m, 36 H) 0.90 (t, *J*=6.8 Hz, 6 H).

5-(azidomethyl)-2-hydroxy-benzaldehyde (2b)

500 mg (1 equiv.) of compound **1b** were dissolved in 5 mL of dry DMF together with 572 mg (3 equiv.) of NaN_3. He mixture was stirred for 4h at r.t. (control by TLC) under Ar atmosphere. After the reaction the mixture was concentrated *in vacuo* to *ca* 1/3 of initial volume, which was followed by dilution with H_2O and extraction of the product with DCM. The organic phase was then washed with brine, dried over Na_2SO_4 then the solvent was evaporated *in vacuo*. Yield 451 mg (87 %) as a colourless solid. **^{1}H NMR (400 MHz, $CDCl_3$) δ ppm** 11.04 (s, 1 H) 9.91 (d, *J*=0.5 Hz, 1 H) 7.53 (dd, *J*=2.3, 0.5 Hz, 1 H) 7.49 (dd, *J*=8.5, 2.5 Hz, 1 H) 7.02 (d, *J*=8.8 Hz, 1 H) 4.35 (s, 2 H).

N,N'-(1,3-phenylenebis(methylene))bis(N-dodecyl-3-(1-(3-formyl-4-hydroxybenzyl)-1H-1,2,3-triazol-4-yl)-N-methylpropan-1-aminium) (GK12)

40 mg of compound **2a** was dissolved in 2 ml of dry DMF together with 25 mg (2.5 equiv.) of compound **2b**. Separately, 43 mg of $CuSO_4$ (3 equiv.) and 35 mg (4.5 equiv.) of NaAsc were mixed in 200 µL of H_2O. After the formation of heterogeneous yellow slurry the mixture was added to the DMF solution and the resulting reaction mixture was stirred at 50 °C for 20h. After the reaction the solvent was evaporated *in vacuo* and the crude product was purified by exclusive column chromatography (LH-20, DCM:MeOH 50:50). In order to remove the traces of Cu^{2+} the product was dissolved in MeOH and passed through a layer of beads of acidic Amberlite IR-20 ion exchange resin on a glass filter. Yield 27 mg (43 %) as a pale yellowish solid. **^{1}H NMR (400 MHz, DMSO-*d*$_6$) δ ppm** 10.93 (br s, 2 H) 10.27 (s, 2 H) 8.01 (s, 2 H) 7.71 - 7.78 (m, 1 H) 7.64 (br d, *J*=7.5 Hz, 2 H) 7.60 (d, *J*=2.1 Hz, 1 H) 7.53 - 7.59 (m, 1 H) 7.50 (dd, *J*=8.4, 2.1 Hz, 2 H) 7.04 (d, *J*=8.3 Hz, 2 H) 5.51 (s, 4 H) 4.56 (br s, 4 H) 3.21 - 3.38 (m, 8 H) 2.93 (s, 6 H) 2.62 - 2.74 (m, 4 H) 2.01 - 2.23 (m, 4 H) 1.59 - 1.79 (m, 4 H) 1.17 - 1.32 (m, 36 H) 0.85 (t, *J*=6.8 Hz, 6 H). **^{13}C NMR (101 MHz, DMSO-*d*$_6$) δ ppm** 190.97 ($C_{aldehyde}$) 161.20 (C_{ar}) 136.60 (C_{ar}) 129.07 (C_{ar})

128.42 (C_{ar}) 127.55 (C_{ar}) 122.78 (C_{ar}) 118.30 (C_{ar}) 52.42 (C_{al}) 49.06 (C_{al}) 31.75 (C_{al}) 29.48 (C_{al}) 29.42 (C_{al}) 29.32 (C_{al}) 29.17 (C_{al}) 29.05 (C_{al}) 26.36 (C_{al}) 22.55 (C_{al}) 22.29 (C_{al}) 22.04 (C_{al}) 14.41 (CH_3). **HRMS (ESI), *m/z*:** $[M]^{2+}$ calcd for $C_{60}H_{92}N_8O_4^{2+}$, 494.3615; found, 494.3494.

N-Boc-4-aminophenoxyacetone (3a)

5g (1 equiv.) of N-Boc-4-aminophenol were mixed with 3.96 g (1.2 equiv.) of K_2CO_3 and 794 mg (0.2 equiv.) of KI in 20 mL of dry CH_3CN. After this, a solution of 2.20 g (1 equiv., 1.97 mL) of chloroacetone in 20 mL of dry CH_3CN was added dropwise and the resulting mixture was refluxed for 2h (control by TLC) under Ar atmosphere. After the reaction the solid residue was filtered off and solvent was evaporated *in vacuo*. The crude product was purified by column chromatography (SiO_2, DCM:MeOH 95:5). Yield 3.9 g (62 %). **^{1}H NMR (400 MHz, $CDCl_3$) δ ppm** 7.29 (br d, *J*=8.8 Hz, 2 H) 6.80 - 6.85 (m, 2 H) 6.41 (br s, 1 H) 4.50 (s, 2 H) 2.27 (s, 3 H) 1.51 (s, 9 H).

4-aminopnenoxyacetone (4a)

1.2 g (1 equiv.) of compound **3a** were dissolved in 4 mL of CH_2Cl_2, then 4 mL of TFA were added and the mixture was stirred for 2h at r.t. After the reaction the solvents were evaporated *in vacuo*, which was followed by reevaporation with MeOH (3 times). **^{1}H NMR (400 MHz, Methanol-*d4*) δ ppm** 7.30 - 7.35 (m, 2 H) 7.03 - 7.08 (m, 2 H) 4.80 (s, 2 H) 2.23 (s, 3 H). Yield: 1.2 g (95 %) in form of a salt with TFA.

1-(4-(prop-2-yn-1-ylamino)phenoxy)propan-2-one (5a)

1.2 g (1 equiv.) of compound **4a** were mixed with 1.3 g (2.2 equiv.) of K_2CO_3 in 15 mL of dry DMF. After this, a solution of 512 mg (1 equiv., 323 µL) of propargyl bromide in 10 mL of dry DMF was added dropwise and the resulting mixture was stirred for 24h at r.t. (control by TLC) under Ar atmosphere. After the reaction the solvent was evaporated *in vacuo* and the crude product was purified by column chromatography (SiO_2, DCM:MeOH:Et_3N 99:1:1), followed by flash column chromatography (Hept:EtOAc 4:1 to 3:2). Yield 250 mg (29 %) as a colourless solid. **^{1}H NMR (400 MHz, $CDCl_3$) δ ppm** 6.78-6.83 (m, 2 H) 6.65 - 6.69 (m, 2 H) 4.48 (s, 2 H) 3.91 (d, *J*=2.5 Hz, 2 H) 2.28 (s, 3 H) 2.21 - 2.23 (m, 1 H).

N1,N4-bis(4-(2-oxopropoxy)phenyl)-N1,N4-di(prop-2-yn-1-yl)succinamide (6a)

140 mg (2.2 equiv.) of compound **5a** together with 79.9 mg (3.22 equiv., 81.4 µL) of pyridine were dissolved in 0.5 mL of dry DCM. After that, the mixture was cooled to 0°C and a solution of 48.6 mg (1 equiv., 34.5 µL) of succinyl chloride in 1.5 ml of dry DCM was added dropwise. The resulting mixture was stirred for 18h at 0 °C under Ar atmosphere (control by TLC). After the reaction the solvent was evaporated *in vacuo* and the crude product was purified by column chromatography (SiO_2, DCM:MeOH 99:1, then a second gradient column SiO_2, DCM:MeOH 95:5 to 92:8). Yield 127 mg (75 %) as a colourless oil. **^{1}H NMR (400 MHz, $CDCl_3$) δ ppm** 7.23 - 7.29 (m, 4 H) 6.89 - 6.94 (m, 4 H) 4.57 (s, 4 H) 4.41 (d, *J*=2.3 Hz, 4 H) 2.30 (s, 6

H) 2.29 (s, 4 H) 2.17 (t, *J*=2.5 Hz, 2 H). **^{13}C NMR (101 MHz, $CDCl_3$) δ ppm** 204.87 ($C_{carbonyl}$) 171.72 (C_{amide}) 157.57 (C_{ar}) 135.19 (C_{ar}) 129.83 (C_{ar}) 115.53 (C_{ar}) 79.22 (C_{al}) 73.18 (C_{al}) 72.05 (C_{al}) 38.49 (C_{al}) 29.44 (C_{al}) 26.61 (CH_3).

3-(2-chloro-N-dodecylacetamido)propane-1-sulfonate (5b)

500 mg (1 equiv.) of compound **4b** were dissolved in 10 ml of dry CH_3CN together with 631 mg (3 equiv., 851 µL) of DIPEA, the mixture was cooled to 0°C and 920 mg (5 equiv., 648 µL) of chloroacetyl chloride were added dropwise. The mixture was stirred for 2h at 0°C, then for 24h at r.t. under Ar atmosphere. After this, another 631 mg of DIPEA and 920 mg of chloroacetylchloride were added and the mixture was stirred for another 24 h at r.t. After the reaction the solvent was evaporated *in vacuo*. The product was used for the next step without further purification.

3-(2-azido-N-dodecylacetamido)propane-1-sulfonate (6b)

625 mg (1 equiv.) of compound **5b** were dissolved in 7 ml of dry DMF together with 318 mg (3 equiv.) of NaN_3. The mixture was stirred for 4h at r.t. (control by TLC). After the reaction the solvent was evaporated *in vacuo* and the crude product was purified by gradient column chromatography (SiO_2, DCM:MeOH 85:15 to 80:20), followed by recrystallization from CH_3CN with a few drops of 1,4-dioxane. Yield 120 mg (19 %) as a light brownish solid. **^{1}H NMR (400 MHz, Methanol-d_4) δ ppm** 4.11 (d, *J*=18.6 Hz, 2 H) 3.40 - 3.53 (m, 2 H) 3.32 (dt, *J*=39.9, 7.8 Hz, 2 H) 2.82 (t, *J*=7.0 Hz, 2 H) 1.98 - 2.08 (m, 2 H) 1.53 - 1.65 (m, 2 H) 1.25 - 1.38 (m, 18 H) 0.90 (t, *J*=7.0 Hz, 3 H).

3,3'-((2,2'-(((succinylbis((4-(2-oxopropoxy)phenyl)azanediyl))bis(methylene))bis(1H-1,2,3-triazole-4,1-diyl))bis(acetyl))bis(ethylazanediyl))bis(propane-1-sulfonate) (KA12)

40 mg (1 equiv.) of compound **6a** were dissolved in 2 ml of dry DMF together with 84.4 mg (2.5 equiv.) of **6b**. Then, 61.4 mg (3 equiv.) of $CuSO_4$ and 56.5 mg (5 equiv.) of NaAsc were dissolved in 200 µL of H_2O, followed by the formation of homogeneous yellow slurry, which was added to the DMF solution. The final reaction mixture was stirred at 50°C for 20h (control by TLC). After the reaction the solvent was evaporated *in vacuo* and the crude product was purified by exclusive column chromatography (LH-20, DCM:MeOH 50:50). In order to remove the traces of Cu the product was dissolved in MeOH and passed through a layer of beads of acidic Amberlite IR-20 ion exchange resin on a glass filter. Yield 80 mg (77 %) as a pale yellowish solid. **^{1}H NMR (400 MHz, DMSO-d_6) δ ppm** 7.98 - 8.33 (m, 2 H) 6.99 - 7.14 (m, 4 H) 6.84 - 6.99 (m, 4 H) 5.31 - 5.55 (m, 4 H) 4.68 - 5.01 (m, 8 H) 3.13 - 3.54 (m, 10 H) 2.19 - 2.35 (m, 4 H) 2.15 (s, 6 H) 1.73 - 2.01 (m, 4 H) 1.36 - 1.64 (m, 6 H) 1.13 - 1.35 (m, 36 H) 0.84 (br t, *J*=6.0 Hz, 6 H). **^{13}C NMR** could not be recorded due to compound aggregating at high concentration in solution. **HRMS (ESI), *m/z*:** $[M+3H]^+$ calcd for $C_{62}H_{97}N_{10}O_{14}S_2^+$, 1269.6637; found, 1269.6602.

Cyanine bis-(N-Boc-hydrazides) (8a, 8b) general procedure

50 mg (1 equiv.) of cyanine diacid (**7a** or **7b**), 1.05 equiv. of HBTU and 0.5 equiv. of HOBt were dissolved in 1.5 ml of dry DMF, after 5 minutes a solution of 1.05 equiv. of and 1.05 equiv. of DIPEA in 1.5 ml of dry DMF was added and the mixture was stirred for 24h at r.t. After the reaction the solvent was evaporated *in vacuo*, the residue was dissolved in 20 ml of CH_2Cl_2, washed with saturated $NaHCO_3$ aqueous solution (10 ml) and water, dried over $MgSO_4$ and the solvent was evaporated *in vacuo*. The crude product was purified by column chromatography (SiO_2, CH_2Cl_2:MeOH 95:5 for **4a** and SiO_2, CH_2Cl_2:MeOH 9:1 for **4b**). Compound **4a**: yield 43 mg (68 %) as dark red crystals. **^{1}H NMR (400 MHz, Methanol-*d*$_4$) δ** 8.55 (t, J = 13.5 Hz, 1H) 7.53 (d, J = 7.3 Hz, 2H) 7.38-7.49 (m, 4H) 7.26-7.33 (m, 2H) 6.53 (d, J = 13,5 Hz, 2H) 4.21 (br. s, 4H) 2.47 (br. s, 4H) 2.13 (br. s, 4H) 1.76 (s, 12H) 1.38 - 1.56 (m, 18H). **^{13}C NMR (101 MHz, Methanol-*d*$_4$)** □ 208.70 ($C_{carboxyl}$) 174.76 (C_{amide}) 151.04 (C_{ar}) 141.86 (C_{ar}) 140.82 (C_{ar}) 128.64 (C_{ar}) 125.40 (C_{ar}) 122.08 (C_{ar}) 111.26 (C_{ar}) 102.50 (C_{ar}) 49.30 (C_{al}) 43.01 (C_{al}) 37.50 (C_{al}) 29.28 (C_{al}) 27.20 (C_{al}) 26.94 (C_{al}) 22.44 (C_{al}). **MS (ESI), *m/z*:** $[M]^+$ calcd for $C_{41}H_{57}N_6O_6^+$, 729.433; found, 729.386. Compound **4b**: yield 38 mg (61 %) as lustrous dark blue crystals. **^{1}H NMR (400 MHz, Methanol-*d4*) δ** 8.28 (t, J = 12,9 Hz, 2H), 7.22-7.53 (m, 8H), 6.68 (t, J = 12,9 Hz, 1H), 6,33 (d, J = 12.9 Hz, 2H), 4.17 (br. s, 4H), 2,43 (br.s, 4H), 2.11 (br.s, 4H), 1,74 (s, 12H), 1.50 (s, 18H). **^{13}C NMR (101 MHz, Methanol-*d4*) δ ppm** 208.68 ($C_{carboxyl}$) 173.03 (C_{amide}) 156.42 (C_{ar}) 142.11 (C_{ar}) 128.40 (C_{ar}) 124.88 (C_{ar}) 122.00 (C_{ar}) 110.72 (C_{ar}) 49.23 (C_{al}) 48.46 (C_{al}) 42.89 (C_{al}) 35.54 (C_{al}) 29.26 (C_{al}) 27.22 (C_{al}) 26.54 (C_{al}) 22.37 (C_{al}). **MS (ESI), *m/z*:** $[M]^+$ calcd for $C_{43}H_{59}N_6O_6^+$, 755.449; found, 755.438.

Cyanine 3 bishydrazides (Cy3az, Cy5az) general procedure

30 mg of compound **8a** or **8b** were dissolved in 1.5 ml of CH_2Cl_2, afterwards 1.5 ml of TFA was added and the mixture was stirred for 2h. After the reaction solvent was evaporated *in vacuo*, then the residue was dissolved in 2 ml of MeOH, which was afterwards evaporated *in vacuo* (thrice). Compound **Cy3az**: yield 30 mg (96 %) as dark red solid.**^{1}H NMR (400 MHz, Methanol-*d*$_4$) δ** 8.45-8.68 (t, J = 12,1 Hz, 1H), 7.26-7.61 (m, 8H), 6.54 (d, J = 12,1 Hz, 2H), 4.22 (br. s, 4H), 2.81 (s, 1H), 2.56 (br. s, 4H), 2.16 (br. s, 4H), 1.78 (s., 12H). **^{13}C NMR (101 MHz, Methanol-*d*$_4$)** □ 174.82 (C_{amide}) 151.02 (C_{ar}) 141.78 (C_{ar}) 140.83 (C_{ar}) 128.66 (C_{ar}) 125.46 (C_{ar}) 122.17 (C_{ar}) 111.03 (C_{ar}) 102.64 (C_{ar}) 49.30 (C_{al}) 42.96 (C_{al}) 29.32 (C_{al}) 26.97 (C_{al}) 22.03 (C_{al}). **MS (ESI), *m/z*:** $[M^+]$ calcd for $C_{31}H_{41}N_6O_2^+$, 529.328; found, 529.246. Compound **Cy5az**: yield 30 mg (93 %) as dark blue solid. **^{1}H NMR (400 MHz, Methanol-*d*$_4$) δ** 8.28 (t, J = 13,5 Hz, 2H), 7.23-7.54 (m, 8H), 6.66 (t, J = 13,5 Hz, 1H), 6,36 (d, J = 13.5 Hz, 2H), 4.17 (br. s, 4H), 2,52 (br. s, 4H), 2.13 (br. s, 4H), 1,74 (s, 12H). **^{13}C NMR** 173.49 (C_{amide}) 171.69 (C_{ar}) 154.46 (C_{ar}) 142.03 (C_{ar}) 141.23 (C_{ar}) 128.40 (C_{ar}) 124.99 (C_{ar}) 122.09 (C_{ar}) 110.57 (C_{ar}) 103.02 (C_{ar}) 49.24 (C_{al}) 42.70 (C_{al}) 29.13 (C_{al}) 26.55 (C_{al}) 21.86 (C_{al}). **MS (ESI), *m/z*:** $[M^+]$ calcd for $C_{33}H_{43}N_6O_2^+$, 555.344; found, 555.295.

Reactive probes based on functionalized cyanines

The two compounds: 3 dialkyne (**9a**) and 3-((3-azidopropyl)(3-((tert-butoxycarbonyl)amino)propyl)(dodecyl)ammonio)propane-1-sulfonate (**9b**) were kindly provided by Dr. Mayeul Collot. The following compounds were synthesized according to the literature procedures: 3-(N-dodecylamino)propane-1-sulfonate (**12b**),[314] cyanine diacid (**7a**).[309]

Zwitterionic cyanine bis(N-Boc) amine (10a)

58.9 mg (1 equiv.) of cyanine 3 dialkyne (**9a**) in form of perchlorate salt were dissolved in 2.5 ml of dry DMF together with 138 mg (2.4 equiv.) of azido-compound **9b**. Separately, 63 mg (2 equiv.) of $CuSO_4$ and 100 mg (4 equiv.) of NaAsc were dissolved in 250 µL of H_2O, followed by the formation of homogeneous yellow slurry, which was added to the DMF solution. The final reaction mixture was stirred at 60°C overnight (control by TLC). After the reaction the solvent was evaporated *in vacuo* and the crude product was purified by exclusive column chromatography (LH-20, DCM:MeOH 50:50). Yield 130 mg (65 %) as a dark red oil. **^{1}H NMR (400 MHz, Methanol-*d4*) δ ppm** 8.54 (t, *J*=12.5 Hz, 1 H) 7.99 - 8.27 (m, 2 H) 7.55 (d, *J*=7.3 Hz, 2 H) 7.36 - 7.50 (m, 4 H) 7.31 (t, *J*=7.3 Hz, 2 H) 4.46 - 4.62 (m, 4 H) 4.19 - 4.36 (m, 4 H) 3.45 - 3.60 (m, 4 H) 3.05 - 3.17 (m, 4 H) 2.92 - 3.05 (m, 2 H) 2.77 - 2.92 (m, 4 H) 2.35 - 2.49 (m, 4 H) 2.20 - 2.35 (m, 4 H) 1.96 - 2.13 (m, 4 H) 1.80 - 1.90 (m, 4 H) 1.77 (s, 9 H) 1.54 - 1.69 (m, 4 H) 1.41 (s, 18 H) 1.18 - 1.36 (m, 28 H) 0.81 - 0.96 (m, 6 H). **^{13}C NMR** could not be recorded due to aggregation. **MS (ESI), *m/z*:** $[M+H]^{2+}$ calcd for $C_{85}H_{144}N_{12}O_{10}S_2^{2+}$, 778.525; found, 778.559.

Zwitterionic cyanine diamine (11a)

110 mg of compound **10a** were dissolved in 2 mL of CH_2Cl_2, then 2 mL of TFA were added and the mixture was stirred for 2h at r.t. After the reaction the solvents were evaporated *in vacuo*, which was followed by reevaporation with MeOH (3 times). Yield: 108 mg (97 %). **^{1}H NMR (400 MHz, Methanol-*d4*) δ ppm** 8.34 - 8.55 (m, 1 H) 7.91 - 8.31 (m, 2 H) 7.13 - 7.51 (m, 8 H) 6.37 - 6.60 (m, 2 H) 4.37 - 4.60 (m, 4 H) 4.05 - 4.28 (m, 4 H) 3.43 - 3.57 (m, 4 H) 3.26 - 3.41 (m, 4 H) 2.90 - 3.04 (m, 4 H) 2.73 - 2.88 (m, 4 H) 2.28 - 2.45 (m, 4 H) 2.13 - 2.27 (m, 4 H) 1.93 - 2.12 (m, 8 H) 1.67 (s, 12 H) 1.46 - 1.61 (m, 4 H) 1.07 - 1.35 (m, 36 H) 0.73 - 0.86 (m, 6 H). **^{13}C NMR (101 MHz, Methanol-*d4*) δ ppm** 174.68 (C_{ar}) 150.81 (C_{ar}) 141.88 (C_{ar}) 140.82 (C_{ar}) 136.47 (C_{ar}) 128.66 (C_{ar}) 126.11 (C_{ar}) 125.44 (C_{ar}) 122.16 (C_{ar}) 111.07 (C_{ar}) 102.91 (C_{ar}) 58.95 (C_{al}) 57.25 (C_{al}) 55.75 (C_{al}) 55.35 (C_{al}) 49.23 (C_{al}) 36.27 (C_{al}) 31.63 (C_{al}) 29.32 (C_{al}) 29.22 (C_{al}) 29.03 (C_{al}) 28.86 (C_{al}) 26.98 (C_{al}) 25.98 (C_{al}) 22.30 (C_{al}) 21.39 (C_{al}) 19.99 (C_{al}) 17.77 (C_{al}) 17.64 (C_{al}) 13.02 (CH_3). **MS (ESI), *m/z*:** $[M+H]^{2+}$ calcd for $C_{75}H_{128}N_{12}O_6S_2^{2+}$, 678.471; found, 678.453.

Reactive zwitterionic cyanine Cy3ZCl

25 mg (1 equiv.) of compound **11a** were dissolved in 2 ml of dry CH_2Cl_2 together with 8.1 mg (4.2 equiv., 10.9 µL) of DIPEA, then the solution was cooled to 0 °C. After that, a solution of 4.0 mg (2.9 µL, 2.2. equiv.) of chloroacetyl chloride in 1 mL of dry CH_2Cl_2 was added and the resulting mixture was stirred for 20 min at 0 °C followed by 16h at r.t. under Ar atmosphere. After the reaction the solvent was evaporated *in vacuo* and the crude product was purified by exclusive column chromatography (LH-20, DCM:MeOH 50:50). Yield 8 mg (34 %). **^{1}H and ^{13}C NMR**

could not be recorded due to strong aggregation. **MS (ESI), *m/z*:** $[M+H]^+$ calcd for $C_{79}H_{130}Cl_2N_{12}O_8S_2^+$, 1508.89; found, 1508.87.

Reactive zwitterionic cyanine Cy3ZM

5.6 mg (2.4 equiv.) of 2,5-Dihydro-2,5-dioxo-1*H*-pyrrole-1-acetic acid were dissolved in 2 ml of dry DMF together with 13.4 mg (2.4 equiv.) of HATU and 36 mg (25.2 equiv.) of DIPEA. After 5 minutes a solution of 25 mg (1 equiv.) of compound **11a** in 2 ml of dry DMF was added and the mixture was stirred for 24h at r.t. under Ar atmosphere. After 24h, additional 1 mL of dry DMF, containing 5.3 mg of 2,5-Dihydro-2,5-dioxo-1*H*-pyrrole-1-acetic acid and 13.4 mg of HATU was added, and the reaction mixture was stirred for 4h (control by TLC). After the reaction the solvent was evaporated *in vacuo*, and the crude product was extracted with DCM (x2) from a concentrated aqueous $NaClO_4$ solution. The combined organic phases were dried over Na_2SO_4 and the solvent was evaporated *in vacuo*. The crude product was purified by exclusive column chromatography (LH-20, DCM:MeOH 50:50). Yield: 9 mg (35 %). **^{1}H and ^{13}C NMR** could not be recorded due to strong aggregation. **MS (ESI), *m/z*:** $[M+H]^{2+}$ calcd for $C_{87}H_{134}N_{14}O_{12}S_2^{2+}$, 815.484; found, 815.460.

N'-propargyl-N-Boc-ethylenediamine (12a)

1.5 g of propargyl bromide (1 equiv., 1.81 mL of 80% solution in toluene) was mixed with 5.83 g (3 equiv.) of N-Boc-ethylenediamine and 5.22 g (3 equiv.) of K_2CO_3 in 15 mL of dry DMF. The mixture was stirred for 24h at r.t. under Ar atmosphere (control by TLC). After the reaction the solvent was evaporated *in vacuo* and the crude product was purified by gradient column chromatography (DCM:MeOH 98:2 to 96:4). Yield: 1.25 g (52 %) **^{1}H NMR (400 MHz, $CDCl_3$) δ ppm** 3.41 (d, *J*=2.5 Hz, 2 H) 3.22 (br q, *J*=5.6 Hz, 2 H) 2.80 (t, *J*=5.9 Hz, 2 H) 2.21 (t, *J*=2.4 Hz, 1 H) 1.42 (s, 9 H).

Cyanine dialkyne bis(N-Boc)amine (13a)

170.0 mg (1 equiv.) of cyanine diacid **7a** was mixed with 233.6 mg (2.1 equiv.) of HATU and 227 mg (306 µL, 6 equiv.) of DIPEA in 5 mL of dry DMF. After 5 min a solution of 121.7 mg of compound **12a** (2.1 equiv.) in 3 mL of dry DMF was added and the reaction mixture was stirred for 24h at r.t. under Ar atmosphere (control by TLC). After the reaction, the solvent was evaporated *in vacuo*. The solid residue was dissolved in DCM and washed with water, dried over Na_2SO_4 and the solvent was evaporated *in vacuo*. The crude product was purified by column chromatography (DCM:MeOH 9:1). Yield: 171 mg (68 %). **^{1}H NMR (400 MHz, Methanol-d4) δ ppm** 8.57 (t, *J*=13.6 Hz, 1 H) 7.55 (d, *J*=7.3 Hz, 2 H) 7.41 - 7.50 (m, 4 H) 7.28 - 7.35 (m, 2 H) 6.51 - 6.60 (m, 2 H) 4.16 - 4.25 (m, 4 H) 3.50 - 3.61 (m, 4 H) 3.22 - 3.30 (m, 4 H) 2.81 (s, 4 H) 2.66 - 2.79 (m, 6 H) 2.09 - 2.19 (m, 4 H) 1.78 (s, 12 H) 1.40 (s, 18 H). **^{13}C NMR (101 MHz, Methanol-d4) δ ppm** 140.84 (C_{ar}) 128.66 (C_{ar}) 125.40 (C_{ar}) 122.14 (C_{ar}) 72.09 (s, 1 C) 49.30 (s, 1 C) 43.28 (s, 1 C) 37.94 (s, 1 C) 37.49 (s, 1 C) 35.56 (C_{al}) 30.26 (C_{al}) 27.38 (C_{al}) 26.95 (C_{al}) 22.09 (C_{al}).

3-(5-azido-N-dodecylpentanamido)propane-1-sulfonate (13b)

311 mg (1 equiv.) of 5-azidopentanoic acid were dissolved in 10 mL of dry DMF together with 867 mg (1.05 eq.) of HATU and 702 mg (2.5 eq., 945 µL) of DIPEA under Ar atmosphere. After 5 minutes, a solution of 700 mg (1.05 eq.) of compound **12b** and 561 mg (2 eq., 757 µL) of DIPEA in 10 mL of dry DMF was added and the mixture was stirred for 24h (control by TLC) under Ar atmosphere. After the reaction the solvent was evaporated *in vacuo* and the product was purified gradient column chromatography (SiO_2, DCM:MeOH 85:15 to 80:20). Yield: 1.02 g (77 %) (in form of a salt with DIPEA) as a pale yellowish oil. **^{1}H NMR (400 MHz, Methanol-*d*$_4$) δ ppm** 3.44 - 3.54 (m, 2 H) 3.32 - 3.36 (m, 4 H) 2.76 - 2.85 (m, 2 H) 2.39 - 2.48 (m, 2 H) 1.97 - 2.08 (m, 2 H) 1.50 - 1.73 (m, 6 H) 1.22 - 1.35 (m, 18 H) 0.90 (t, *J*=7.0 Hz, 3 H).

Cyanine disulphonate bis(N-Boc)amine (14a)

150 mg (1 equiv.) of compound **13a** were dissolved in 5 ml of dry DMF together with 165 mg (2.4 equiv.) of compound **13b**. Then, 87.6 mg (2.2 equiv.) of $CuSO_4$ and 126 mg (4 equiv.) of NaAsc were dissolved in 500 µL of H_2O, followed by the formation of homogeneous yellow slurry, which was added to the DMF solution. The final reaction mixture was stirred at 60°C overnight (control by TLC). After the reaction the solvent was evaporated *in vacuo* and the crude product was purified by exclusive column chromatography (LH-20, DCM:MeOH 50:50). Yield 218 mg (73 %) as a dark red solid. **^{1}H NMR (400 MHz, Methanol-*d*$_4$) δ ppm** 8.43 - 8.61 (m, 1 H) 7.99 - 8.42 (m, 1 H) 7.50 (d, *J*=6.5 Hz, 2 H) 7.33 - 7.48 (m, 4 H) 7.27 (d, *J*=6.8 Hz, 2 H) 6.38 - 6.74 (m, 2 H) 4.00 - 4.58 (m, 8 H) 3.34 - 3.74 (m, 8 H) 3.12 - 3.29 (m, 10 H) 2.48 - 2.91 (m, 8 H) 2.24 - 2.46 (m, 4 H) 1.83 - 2.24 (m, 12 H) 1.74 (s, 12 H) 1.40 - 1.58 (m, 8 H) 1.34 (s, 18 H) 1.10 - 1.29 (m, 36 H) 0.85 (t, *J*=6.70 Hz, 6 H). **^{13}C NMR** was not recorded due to aggregation. **HRMS (ESI), *m/z*:** $[M]^-$ calcd for $C_{91}H_{147}N_{14}O_{14}S_2^-$ 1724.0668; found, 1724.0663

Reactive anionic cyanine diamine (Cy3NHA)

165 mg of compound **14a** were dissolved in 2 mL of CH_2Cl_2, then 2 mL of TFA were added and the mixture was stirred for 2h at r.t. After the reaction the solvents were evaporated *in vacuo*, which was followed by reevaporation with MeOH (3 times). Yield: 161 mg (96 %). **^{1}H NMR (400 MHz, Methanol-*d*$_4$) δ ppm** 8.46 - 8.59 (m, 1 H) 7.51 (br d, *J*=7.0 Hz, 2 H) 7.34 - 7.49 (m, 4 H) 7.28 (br t, *J*=6.9 Hz, 2 H) 6.46 - 6.65 (m, 2 H) 4.34 - 4.53 (m, 4 H) 4.12 - 4.28 (m, 4 H) 3.64 - 3.85 (m, 4 H) 3.36 - 3.53 (m, 6 H) 3.08 - 3.30 (m, 8 H) 2.68 - 2.99 (m, 8 H) 2.32 - 2.45 (m, 4 H) 2.05 - 2.17 (m, 4 H) 1.86 - 2.04 (m, 8 H) 1.74 (s, 12 H) 1.40 - 1.58 (m, 8 H) 1.32 - 1.38 (m, 4 H) 1.13 - 1.31 (m, 36 H) 0.85 (br t, *J*=6.5 Hz, 6 H). **^{13}C NMR** could not be recorded due to compound aggregating at high concentration in solution. **HRMS (ESI), *m/z*:** $[M+3Na]^{2+}$ calcd for $C_{81}H_{131}N_{14}O_{10}S_2Na_3^{2+}$ 796.4660; found, 796.4666.

Reactive anionic cyanine bis(chloroacetamide) Cy3ClA

25 mg (1 equiv.) of compound **Cy3NHA** were dissolved in 2 ml of dry CH_2Cl_2 together with 104 mg (17 equiv.) of Cs_2CO_3. Then, the mixture was cooled to 0°C and a solution of 21.4 µL (17 equiv.) of chloroacetyl chloride in 1 mL of dry CH_2Cl_2 was added dropwise. After this, the reaction mixture was stirred for 20 min at 0°C and then for 16h at r.t. under Ar atmosphere. After the reaction the solvent was evaporated *in vacuo* and the crude product was purified by

exclusive column chromatography (LH-20, DCM:MeOH 50:50). Yield 21 mg (76 %) as a dark red solid. **^{1}H NMR (400 MHz, Methanol-*d*$_4$) δ ppm** 8.48 - 8.60 (m, 1 H) 7.92 - 8.15 (m, 2 H) 7.54 (d, *J*=7.3 Hz, 2 H) 7.46 - 7.51 (m, 1 H) 7.39 - 7.46 (m, 3 H) 7.30 (t, *J*=7.0 Hz, 2 H) 6.52 - 6.67 (m, 2 H) 4.65 - 4.76 (m, 4 H) 4.36 - 4.47 (m, 4 H) 4.16 - 4.27 (m, 4 H) 4.05 (d, *J*=14.0 Hz, 4 H) 3.69 - 3.79 (m, 1 H) 3.37 - 3.62 (m, 10 H) 3.20 - 3.30 (m, 4 H) 3.09 - 3.19 (m, 1 H) 2.66 - 2.90 (m, 8 H) 2.34 - 2.48 (m, 4 H) 2.07 - 2.20 (m, 4 H) 1.88 - 2.06 (m, 10 H) 1.77 (s, 12 H) 1.45 - 1.63 (m, 8 H) 1.35 - 1.39 (m, 2 H) 1.21 - 1.34 (m, 34 H) 0.89 (t, *J*=6.8 Hz, 6 H). **^{13}C NMR** could not be recorded due to compound aggregating at high concentration in solution. **HRMS (ESI), *m/z*:** $[M]^-$ calcd for $C_{85}H_{133}Cl_2N_{14}O_{12}S_2^-$ 1675.9051; found, 1675.9018

Reactive anionic cyanine bis(4-(bromomethyl)benzamide) Cy3BrA

4-(bromomethyl)benzoyl chloride was prepared according to the procedure: 1.0 g (1 equiv.) of 4-(bromomethyl)benzoic acid was mixed with 1.10 g (0.67 mL, 2 equiv.) of $SOCl_2$ in 10 mL of dry CH_3CN. The mixture was refluxed for 2h, followed by solvent evaporation *in vacuo*. The obtained acyl chloride was stored and handled under Ar atmosphere and used without further purification.

31.4 mg (1 equiv.) of compound **Cy3NHA** were dissolved in 2 ml of dry CH_2Cl_2 together with 62.3 mg (10 equiv.) of Cs_2CO_3. Then, the mixture was cooled to 0°C and a solution of 37.7 mg (10 equiv.) of 4-(bromonethyl)benzoyl chloride in 1 mL of dry CH_2Cl_2 was added dropwise. After this, the reaction mixture was stirred for 1h at 0°C and then for 1h at r.t. under Ar atmosphere. After the reaction the solvent was evaporated *in vacuo* and the crude product was purified by exclusive column chromatography (LH-20, DCM:MeOH 50:50). Yield 18 mg (57 %) as a dark red oil. **^{1}H NMR (400 MHz, Methanol-*d*$_4$) δ ppm** 8.63 - 9.11 (m, 1 H) 8.29 - 8.63 (m, 2 H) 7.05 - 8.23 (m, 17 H) 6.32 - 6.69 (m, 2 H) 5.86 - 6.11 (m, 1 H) 5.32 - 5.45 (m, 10 H) 4.51 - 4.66 (m, 4 H) 4.30 - 4.50 (m, 4 H) 4.00 - 4.23 (m, 4 H) 3.54 - 3.77 (m, 4 H) 3.37 - 3.54 (m, 4 H) 3.12 - 3.28 (m, 4 H) 2.69 - 2.92 (m, 4 H) 2.26 - 2.49 (m, 4 H) 1.85 - 2.22 (m, 18 H) 1.74 (s, 12 H) 1.33 - 1.62 (m, 8 H) 1.09 - 1.34 (m, 32 H) 0.80 - 0.89 (m, 6 H). **^{13}C NMR** could not be recorded due to compound aggregating at high concentration in solution. **HRMS (ESI), *m/z*:** $[M-2Br+2OH]^-$ calcd for $C_{97}H_{143}N_{14}O_{14}S_2^-$ 1792.0355; found, 1792.0303.

In order to confirm the structure and reactivity of the compound, an adduct with dimethylamine was synthesized by mixing an analytical sample of **Cy3BrA** with an excess of NMe_2 in THF. After 1h of stirring at r.t. the solvent was evaporated *in vacuo* and the solid residue was analyzed by mass-spectrometry. **HRMS (ESI), *m/z*:** $[M+NH_4+Na+H]^{2+}$ calcd for $C_{97}H_{146}N_{15}O_{12}S_2Na^{2+}$ 944.569; found, 944.5318.

3.3 Preparation of model lipid membranes

Preparation of large unilamellar vesicles (LUVs). All types of LUVs were prepared by the following procedure. A stock solution of corresponding lipid(s) in chloroform was placed into a round-neck flask, after which the solvent was evaporated *in vacuo* and phosphate buffer (20 mM, pH 7.4) was added. After all the solid was dissolved a suspension of multilamellar vesicles was extruded by using a Lipex Biomembranes extruder (Vancouver, Canada). The size of the filters was first 0.2 μm (7 passages) and thereafter 0.1 μm (10 passages). This generates monodisperse LUVs with a mean diameter of 0.12 μm as measured with a Malvern Zetamaster 300 (Malvern, U.K.). Phospholipid:Cholesterol molar ratio in case of DOPC/Chol and Sphing/Chol was 1:0.9.

Preparation of giant unilamellar vesicles (GUVs) (Article 2). GUVs were prepared by electroformation. Lipid stock (DOPC:SM:Chol 2:2:1) was spread onto two parallel platinum wires attached to a custom-built Teflon-coated chamber and left briefly to evaporate the solvent. Wires were passed under nitrogen gas before submersion in 300 mM sucrose. 10 Hz AC current was applied for 1 hour to trigger vesicles swelling at 70 °C, followed by 2 Hz for 30 minutes with slow cooling.

Preparation of giant unilamellar vesicles (GUVs) (Article 3). All types of GUVs used were prepared by the following procedure. A stock solution of corresponding lipid(s) in chloroform was 30 min. were generated by electroformation in a home-built liquid cell (University of Odense, Denmark), using previously described procedures.[15] A 0.1 mM solution of lipids in chloroform was deposited on the platinum wires of the chamber, and the solvent was evaporated under vacuum for 30 min. The chamber, thermostated at 55 °C, was filled with a 300 mM sucrose solution, and a 2-V, 10-Hz alternating electric current was applied to this capacitor-like configuration for ca. 2 h. Then, a 50 μL aliquot of the obtained stock solution of GUVs in sucrose (cooled down to room temperature) was added to 200 μL of 300 mM glucose solution containing 200 nM of the probe (obtained by adding corresponding dye stock solution in DMSO to glucose solution, final DMSO volume <0.32%) to give the final suspension of stained GUVs used in microscopy experiments.

Preparation of giant plasma membrane vesicles (GPMVs). GPMVs were prepared as previously described. [315] Briefly, cells seeded out on a 60 mm petri dish (≈70 % confluent) were washed with GPMV buffer (150 mM NaCl, 10 mM Hepes, 2 mM CaCl2, pH 7.4) twice. 2 mL of GPMV buffer was added to the cells. 25 mM PFA and 20 mM DTT (final concentrations) were added in the GPMV buffer. The cells were incubated for 2 h at 37 °C. Then, GPMVs were collected by pipetting out the supernatant. GPMVs were labelled by adding Pro12A (or Laurdan and C-Laurdan) with a final concentration of 50 nM.

Preparation of supported lipid bilayers. Supported lipid bilayers were prepared by vesicle fusion of small unilamellar vesicles (SUVs) as previously described[316]. Briefly, 1,2-dioleoyl-sn-glycero-3-phosphocholine (DOPC) and sphingomyelin were purchased from Avanti Polar Lipids (850375C, 860062C). Cholesterol was purchased from Sigma (C8667). Each lipid was separately dissolved in chloroform. To prepare SUVs, lipid solutions were mixed in a pre-

cleaned round-bottom flask at the designated ratios and chloroform was evaporated under nitrogen flow. The lipid cake was rehydrated with ~60 ºC Milli-Q water to the concentration of ~2 mg/mL, then sonicated at ~60 ºC for ~40 min until clear SUV suspension was formed. To form a supported lipid bilayer, the SUV suspension and buffer solution (150 mM NaCl, 10 mM HEPES, 3 mM $CaCl_2$) were gently added to a pre-cleaned, hydrophilic coverslip at 1:4 ratio. The coverslip was incubated at ~60 ºC for ~15 min, and then was thoroughly rinsed with Dulbecco's Phosphate Buffered Saline (DPBS). The lipid bilayer was imaged with 10 nM NR12A, NR4A, NR12S, and Nile Red in DPBS.

3.4 Cell Lines, Culture Conditions, and Treatment

Cell Lines, Culture Conditions, and Treatment (Article 1). KB ATCC CCL-17) cells were grown in Dulbecco`s Modified Eagle Medium (DMEM, Gibco Invitrogen), supplemented with 10% fetal bovine serum (FBS, Lonza), 1% l-Glutamine (Sigma Aldrich) and 1% antibiotic solution (penicillin-streptomycin, Gibco-Invitrogen) at 37 °C in a humidified 5% CO_2 atmosphere. Cells were seeded onto a chambered coverglass (Ibidi) at a density of 7×10^4 cells/well 24 h before the microscopy measurement. For cellular microscopy experiments, the attached KB cells in Ibidi dishes were washed twice with warm Hank`s balanced salt solution (HBSS, Gibco Invitrogen), after that 1 mL of dye solution in HBSS was added and the cells were incubated for 10 min. at r.t.

Cell Lines, Culture Conditions, and Treatment (**Article 2**). CHO cells were maintained in DMEM-F12 medium supplemented with 10% FBS medium and 1% L-glutamine. Cells were transfected with the plasmids using Lipofectamine 3000 as described in manufacturer's protocol.

Cell Lines, Culture Conditions, and Treatment (Article 3). HeLa cells (ATCC CCL-2) and KB ATCC CCL-17) cells were grown in Dulbecco`s Modified Eagle Medium (DMEM, Gibco Invitrogen), supplemented with 10% fetal bovine serum (FBS, Lonza), 1% l-Glutamine (Sigma Aldrich) and 1% antibiotic solution (penicillin-streptomycin, Gibco-Invitrogen) at 37 °C in a humidified 5% CO_2 atmosphere. Cells were seeded onto a chambered coverglass (Ibidi) at a density of 5×10^4 cells/well 24 h before the microscopy measurement. For conventional microscopy experiments, the attached HeLa cells in Ibidi dishes were washed twice with warm Dulbecco`s Phosphate buffered saline (DPBS, Dominique Dutscher), after that 1 mL of 20 nM dye solution in DPBS was added and the cells were incubated for 10 min. at r.t. Concentrations used for photobleaching experiments were 20 nM for NR4A, NR12S, and NR; 7 nM for NR12A. For super-resolution measurements, COS-7 (ATCC CRL-1651) and HeLa (ATCC CCL-2) cells

were maintained in DMEM supplemented with 10% FBS in 5% CO_2 at 37C. For imaging, cells were plated on 18-mm #1.5 glass coverslips. When cells reached ~50% confluency after 24~48 hr, the coverslip was mounted on a metal holder (CSC-18; Bioscience Tools) in the imaging media (L15 with 20 mM HEPES). Cells were imaged with 10 nM NR4A or Nile Red, or 20 nM NR12S in the imaging media at room temperature. For fixed cell experiments, cells were fixed in 3% paraformaldehyde + 0.1% glutaraldehyde in DPBS for 20 min at room temperature. After fixation, the sample was treated with freshly prepared 0.1% $NaBH_4$ in DPBS for 5 min, and thoroughly washed with DPBS three times.

Cell Lines, Culture Conditions, and Treatment (Article 4). HeLa cells (ATCC CCL-2) cells were grown in Dulbecco`s Modified Eagle Medium (DMEM, Gibco Invitrogen), supplemented with 10% fetal bovine serum (FBS, Lonza), 1% l-Glutamine (Sigma Aldrich) and 1% antibiotic solution (penicillin-streptomycin, Gibco-Invitrogen) at 37 °C in a humidified 5% $CO_2$ atmosphere. KB (ATCC CCL-17) cells were grown in Dulbecco`s Modified Eagle Medium (DMEM, Gibco Invitrogen), supplemented with 10% fetal bovine serum (FBS, Lonza), 1% l-Glutamine (Sigma Aldrich), 1% non-essential amino acid solution (Gibco-Invitrogen) and 1% MEM vitamin solution (Gibco-Invitrogen).at 37 °C in a humidified 5% CO_2 atmosphere. Cells were seeded onto a chambered coverglass (Ibidi) at a density of 5×10^4 cells/well 24 h before the microscopy measurement. For microscopy imaging, the attached cells in Ibidi dishes were washed once with warm Hanks` balanced salt solution (HBSS, Gibco-Invitrogen), after that 1 mL of corresponding dye solution in warm HBSS was added and the cells were incubated for: 10 min. at r.t. for NR12A, NRLD or Nile Red; 20 min at 37 °C for $NRER_F$ and $NRER_{Cl}$; 45 min at 37 °C for NRLyso and NRMito. For $NRGolgi_E$ probe the attached cells in Ibidi dishes were washed twice with cold Hanks` balanced salt solution (HBSS, Gibco-Invitrogen), after that 1 mL of cold solution of dye conjugate with BSA (1:1 molar ratio) or with β-cyclodextrine (1:6 molar ratio) was added and the cells were incubated for 30 min at 4 °C followed by washing with warm HBSS and further incubation for 30 min at 37 °C.

For colocalization experiments, commercial organelle-targeting probes were added together with solvatochromic probes in the following concentrations: 50 nM of WGA Alexa 488 conjugate (Invitrogen) for NR12A; 50 nM of MitoTracker Green FM (Invitrogen) for NRMito; 50 nM of LysoTracker Green DND-26 (Invitrogen) for NRLyso; 200 nM (for $NRER_F$) or 500 nM (for $NRER_{Cl}$) of ERTracker Green (Invitrogen); 500 nM of BODIPY 493/503 (Invitrogen) for NRLD); 2.5 μM (in form of 1:1 molar ratio conjugate with BSA) or 150 nM (in 1 mM solution of β-cyclodextrine) of BODIPY FL C_5-Ceramide (Invitrogen) for $NRGolgi_E$.

Cell Lines, Culture Conditions, and Treatment (Reactive probes based on bivalent reactive amphiphiles; Reactive probes based on functionalized cyanines).

HeLa cells (ATCC CCL-2) and KB ATCC CCL-17) cells were grown in Dulbecco`s Modified Eagle Medium (DMEM, Gibco Invitrogen), supplemented with 10% fetal bovine serum (FBS, Lonza), 1% l-Glutamine (Sigma Aldrich) and 1% antibiotic solution (penicillin-streptomycin, Gibco-Invitrogen) at 37 °C in a humidified 5% CO_2 atmosphere. Cells were seeded onto a chambered coverglass (Ibidi) at a density of 5×10^4 cells/well 24 h before the microscopy

measurement. For conventional microscopy experiments, the attached HeLa cells in Ibidi dishes were washed twice with warm Hank`s balanced salt solution (HBSS, Gibco Invitrogen), incubated with 50 nM of probes in HBSS for 10 minutes and imaged without a washing step.

For reactive anionic cyanine probes, the cells were incubated for 10 minutes at r.t. with a 50 nM solution of a corresponding probe in HBSS (pH 7.4) or HEPES-HBSS (pH 8.4) and imaged without a washing step. In case of using TCEP, the cells were pre-treated with 100 μM solution of TCEP in HBSS for 15 minutes at r.t. prior to staining. After the imaging, the HBSS was changed with a complete growth medium and the cells were incubated for 30 minutes at r.t., followed by a second microscopy imaging in an Opti-MEM reduced serum medium.

3.5 Intracranial dye injection and cranial window implantation

All animal experiments were conducted in accordance with institutional guidelines and approved by the Government of Upper Bavaria. 8-week old C56/Bl6N mice were obtained from Charles River Laboratories (Kisslegg, Germany). Cranial window implantation was performed as described in [317]. Before use, surgical tools were sterilized in a glass-bead sterilizer (FST). Mice were anesthetized by an intra-peritoneal injection of MMF (medetomidine (0.5 mg/kg), fentanyl (0.05 mg/kg), and midazolam (5mg/kg)). Subsequently, mice were placed onto a heating blanket (37 °C) and the head was fixed in a stereotactic frame. Eyes were protected from drying by applying eye ointment (Bepanthen, Bayer). The scalp was washed with swabs soaked with 70 % ethanol. A flap of skin covering the cranium was excised using small scissors. The periosteum was scraped away with a scalpel. The prospective craniotomy location (1.5-2.5 mm AP and 0-4 mm ML relative to bregma) was marked with a biopsy punch (diameter 4 mm, Integra LifeSciences). The exposed skull around the area of interest was covered with a thin layer of dental acrylic (iBond Self Etch, Hereaus Kulzer) and hardened with a LED polymerization lamp (Demi Plus, Kerr). A dental drill (Schick Technikmaster C1, Pluradent) was used to thin the skull around the marked area. After applying a drop of sterile phosphate buffered saline (DPBS, Gibco, Life Technologies) on the craniotomy the detached circular bone flap was removed with forceps. For the *in vivo* imaging, a concentrated stock solution of Cy3.5A in DMSO was added to the 1 mM solution of Me-β-Cyclodextrin in PBS to create a 20 μM solution of Cy3.5A, immediately used for imaging. 300 nl of probe solution were injected at 200 μm depth from the brain surface via a Nanoliter 2000 Injector (World Precision Instruments) at a speed of 30 nl/min. A circular coverslip (4 mm diameter, VWR International) was placed onto the craniotomy and glued to the skull with histoacryl adhesive (Aesculap). The exposed skull was covered with dental acrylic (Tetric Evoflow A1 Fill, Ivoclar Vivadent) and a head-post was attached parallel to the window

for head-fixing mice subsequently under the 2-photon laser scanning microscope (LSM 7 MP, Carl Zeiss Ltd.).

3.6 Fluorescence microscopy

Fluorescence microscopy (Article 1). Cellular imaging was performed using Nikon Ti-E inverted microscope, equipped with CFI Plan Apo ×60 oil (NA = 1.4) objective, X-Light spinning disk module (CREST Optics) and a Hamamatsu Orca Flash 4 sCMOS camera with a bandpass filter 531 ± 40 nm (Semrock) or 593 ± 40 nm (Semrock) or a longpass filter >647 nm (Semrock). The excitation in confocal mode was provided by a 488 nm or 532 nm or 638 nm diode laser (OXXIUS). The exposure time in confocal mode was set to 500 ms per image frame. All the images were recorded using NIS Elements and then processed using Fiji software.

***In vivo* 2-photon microscopy.** *In vivo* 2-photon imaging was performed using a multiphoton LSM 7 MP microscope (Zeiss) equipped with a Ti:Sa laser (Chameleon Vision II from Coherent, Glasgow, Scotland), a 20x water immersion objective (W Plan-Apochromat 20x/1.0 NA, Zeiss) and a motorized stage as described in [318]. The membrane probe was excited at 830 nm. The emission was collected after a LP>570 nm filter by a non-descanned detector (photomultiplier tube GaAsP, Zeiss). Throughout the imaging session mice were kept on a heating pad to keep body temperature at 37 °C (Fine Science Tools GmbH). For overview images, 3D stacks of 100 µm depth with 3 µm axial resolution and 1024×1024 pixels per image frame (0.4 µm/pixel) were acquired in multiphoton mode of the microscope. To resolve dendritic spines and axonal boutons, high-resolution images from single neurites were taken with 0.7 µm axial resolution and 512 × 256 pixels per image frame (0.1 µm per pixel) with the laser power kept below 50 mW to avoid phototoxicity.

Confocal fluorescence microscopy. (**Article 2**) All imaging was done at room temperature (21-23 °C). Samples were imaged with a Zeiss LSM 780 confocal microscope. Spectral imaging was done as described before.[319] Cells were incubated with Pro12A (or Laurdan and C-Laurdan) with a final concentration of 0.8 µM in PBS for 5 minutes. After the labelling, the cells were washed once and the imaging was performed in L15 medium. Pro12A, Laurdan and C-Laurdan were excited with 405 nm and emission collected between 410-600 nm.

Fluorescence microscopy (Article 3). Cellular imaging was performed using Nikon Ti-E inverted microscope, equipped with CFI Plan Apo ×60 oil (NA = 1.4) objective, X-Light spinning disk module (CREST Optics) (in case of confocal imaging) and a Hamamatsu Orca Flash 4 sCMOS camera with a bandpass filter 593 ± 20 nm (Semrock FF01-593/40-25). The excitation in confocal mode was provided by a 532 nm diode laser (OXXIUS). The exposure time in confocal mode was set to 500 ms per image frame. For photobleaching experiments and widefield

imaging, the excitation was provided by light emitting diode (SpectraX) at 550 nm. The 550-nm light power was set to 4.33 mW at the sample level. The diameter of the wide-field illumination spot was 420 μm, according to a photobleaching test, so that the power density used at 550 nm was 3.14 $W \cdot cm^{-2}$. The exposure time in widefield mode was set to 500 ms per image frame. Photobleaching tests were performed by illuminating the samples continuously over 60 seconds in widefield mode, followed by imaging immediately after the illumination and after incubation for 10 min at r.t. All the images were recorded using NIS Elements and then processed using Fiji software.

Confocal imaging of GUVs was performed on a Leica TSC SPE confocal microscope with HXC PL APO 63x/1.40 OIL CS objective. The excitation light was provided by a 488 nm laser while the fluorescence was detected at two spectral ranges: 550–600 ($I_{550-600}$) and 600–650 ($I_{600-650}$) in sequential mode by rapid switching to minimize drift, a sum of 4 or 5 images is shown. All the parameters at each channel were left constant, illumination power was adjusted to achieve good signal for each probe. The laser power settings were: 30% of max. intensity for DOPC GUVs for all probes, 10% of max. intensity for Sph/Chol or DOPC/Sph/Chol GUVs for NR12A, NR12S and Nile Red and 100% of intensity for Sph/Chol or DOPC/Sph/Chol GUVs for NR4A. The ratiometric images were generated by using special macros under ImageJ that divides the image of the $I_{550-600}$ channel by that of the $I_{600-650}$ channel. For each pixel, a pseudo-color scale is used for coding the ratio, while the intensity is defined by the integral intensity recorded for both channels at the corresponding pixel.

3D-PAINT and SR-PAINT super-resolution microscopy. 3D-PAINT and SR-PAINT imaging were performed with a home-built setup based on a Nikon Ti-E inverted fluorescence microscope, as previously described.[276] Briefly, a 561-nm laser (Coherent) was coupled to the back focal plane of an oil-immersion objective lens (Nikon CFI Plan Apochromat lambda 100x, NA1.45). A translational stage shifted the laser to the edge of the objective, thus illuminating ~1 μm into the sample at a typical power density of ~2 kW/cm^2. For 3D-PAINT, emission was filtered by a bandpass filter (ET605/70m, Chroma), and passed through a cylindrical lens (f = 1000 mm) to achieve astigmatism for axial localization.[320] Final image was projected onto an EM-CCD camera (iXon Ultra 897, Andor), which operated at 110 frames per second for 256x256 pixels for ~50,000 frames, or 200 frames per second for 256x128 pixels for ~100,000 frames. For SR-PAINT, emission was filtered with a long-pass filter (ET575lp, Chroma) and a short-pass filter (FF01-758/SP, Semrock), and cropped at the image plane of the microscope camera port to a width of ~4 mm. The cropped intermediate image was collimated by an achromatic lens (f = 80 mm), and was split into two paths at a 50:50 beam splitter (BSW10, Thorlabs). In Path 1, emission was focused by an achromatic lens (f = 75 mm) onto one-half of an EM-CCD camera. In Path 2, emission was dispersed by an equilateral calcium fluoride prism (PS863, Thorlabs) before being focused by an achromatic lens (f = 60 mm) onto the other half of the same camera. Wavelength calibration was performed using fluorescent beads and narrow bandpass filters, as previously described.[321]

Fluorescence microscopy (Article 4). Cellular imaging was performed using Nikon Ti-E inverted microscope, equipped with CFI Plan Apo ×60 oil (NA = 1.4) objective, X-Light spinning disk module (CREST Optics) and a Hamamatsu Orca Flash 4 sCMOS camera with a

bandpass filter 531/40 nm (Semrock) or 600/50 nm (Semrock). The excitation in confocal mode was provided by 488 nm or 532 nm diode laser (OXXIUS).The exposure time in confocal mode was set to 500 ms per image frame. All the images were recorded using NIS Elements and then processed using Fiji software. Pearson`s correlation coefficients for colocalization were calculated using Coloc2 Fiji plugin.

Ratiometric confocal imaging of KB cells was performed on a Leica TSC SPE confocal microscope with HXC PL APO 63x/1.40 OIL CS objective. The excitation light was provided by a 488 nm laser while the fluorescence was detected at two spectral ranges: 550–600 nm ($I_{550-600}$) and 600–650 nm ($I_{600-650}$) in sequential mode by rapid switching to minimize drift, a sum of 5 images is shown (20 images in case of hyperosmotic stress experiments with NR12A). All the parameters at each channel were left constant, illumination power was adjusted to achieve good signal for each probe. The laser power settings were: 8% of max. intensity for NRLD; 9% of max. intensity for NRLyso; 12% of max. intensity for $NRER_{Cl}$ and NRMito; 30% of max. intensity for NR12A for oxidative stress experiments and 60% for hyperosmotic stress experiments; 45% of max. intensity for $NRER_F$; 70% of max. intensity for $NRGolgi_E$. The ratiometric images were generated by using special macros under ImageJ that divides the image of the $I_{550-600}$ channel by that of the $I_{600-650}$ channel. For each pixel, a pseudo-color scale is used for coding the ratio, while the intensity is defined by the integral intensity recorded for both channels at the corresponding pixel. Oxidative stress was induced by incubating cells with 2 mM solution of H_2O_2 in HBSS for 1h at 37°C with consecutive washing with fresh HBSS.[322] In all cases microscopy imaging was started 70 minutes after the end of incubation with H_2O_2. Hyperosmotic stress was induced by replacing half of the cell medium with 1M sucrose solution immediately followed by imaging.[46]

Fluorescence microscopy (Reactive probes based on bivalent reactive amphiphiles; Reactive probes based on functionalized cyanines). Cellular imaging was performed using Nikon Ti-E inverted microscope, equipped with CFI Plan Apo ×60 oil (NA = 1.4) objective, X-Light spinning disk module (CREST Optics) and a Hamamatsu Orca Flash 4 sCMOS camera with a bandpass filter 531/40 nm (Semrock) or 600/50 nm (Semrock). The excitation in confocal mode was provided by 532 nm diode laser (OXXIUS). The exposure time in confocal mode was set to 500 ms per image frame. All the images were recorded using NIS Elements and then processed using Fiji software.

References

1. Lakowicz, J.R., *Principles of Fluorescence Spectroscopy, 3rd ed.* 2006: Springer, Boston, MA.
2. Demchenko, A.P., *Introduction to Fluorescence Sensing*. 2009: Springer, Dordrecht.
3. Keereweer, S., et al., *Optical image-guided surgery--where do we stand?* Mol Imaging Biol, 2011. **13**(2): p. 199-207.
4. Luo, S., et al., *A review of NIR dyes in cancer targeting and imaging.* Biomaterials, 2011. **32**(29): p. 7127-38.
5. Fu, Y. and N.S. Finney, *Small-molecule fluorescent probes and their design.* RSC Advances, 2018. **8**(51): p. 29051-29061.
6. Zhang, X., et al., *Near-infrared molecular probes for in vivo imaging.* Curr Protoc Cytom, 2012. **Chapter 12**: p. Unit12 27.
7. Johnson, I., *Fluorescent probes for living cells.* Histochem J, 1998. **30**(3): p. 123-40.
8. Klymchenko, A.S., *Solvatochromic and Fluorogenic Dyes as Environment-Sensitive Probes: Design and Biological Applications.* Acc Chem Res, 2017. **50**(2): p. 366-375.
9. Kucherak, O.A., et al., *Fluorene Analogues of Prodan with Superior Fluorescence Brightness and Solvatochromism.* The Journal of Physical Chemistry Letters, 2010. **1**(3): p. 616-620.
10. Ma, Y., et al., *Time-Resolved Laurdan Fluorescence Reveals Insights into Membrane Viscosity and Hydration Levels.* Biophys J, 2018. **115**(8): p. 1498-1508.
11. Montana, V., D.L. Farkas, and L.M. Loew, *Dual-wavelength ratiometric fluorescence measurements of membrane potential.* Biochemistry, 1989. **28**(11): p. 4536-9.
12. Klymchenko, A.S. and R. Kreder, *Fluorescent Probes for Lipid Rafts: From Model Membranes to Living Cells.* Chem. Biol., 2014. **21**(1): p. 97-113.
13. Lingwood, D. and K. Simons, *Lipid rafts as a membrane-organizing principle.* Science, 2010. **327**(5961): p. 46-50.
14. Bagatolli, L.A., *To see or not to see: Lateral organization of biological membranes and fluorescence microscopy.* Biochimica Et Biophysica Acta-Biomembranes, 2006. **1758**(10): p. 1541-1556.
15. Kucherak, O.A., et al., *Switchable Nile Red-Based Probe for Cholesterol and Lipid Order at the Outer Leaflet of Biomembranes.* J. Am. Chem. Soc., 2010. **132**(13): p. 4907-4916.
16. Niko, Y., et al., *Bright and photostable push-pull pyrene dye visualizes lipid order variation between plasma and intracellular membranes.* Sci Rep, 2016. **6**: p. 18870.
17. Klymchenko, A.S. and Y. Mely, *Fluorescent environment-sensitive dyes as reporters of biomolecular interactions.* Prog Mol Biol Transl Sci, 2013. **113**: p. 35-58.
18. Cohen, B.E., et al., *Probing protein electrostatics with a synthetic fluorescent amino acid.* Science, 2002. **296**(5573): p. 1700-3.
19. Venkatraman, P., et al., *Fluorogenic probes for monitoring peptide binding to class II MHC proteins in living cells.* Nat Chem Biol, 2007. **3**(4): p. 222-8.
20. Karpenko, I.A., et al., *Red fluorescent turn-on ligands for imaging and quantifying G protein-coupled receptors in living cells.* Chembiochem, 2014. **15**(3): p. 359-63.
21. Grabowski, Z.R., K. Rotkiewicz, and W. Rettig, *Structural changes accompanying intramolecular electron transfer: focus on twisted intramolecular charge-transfer states and structures.* Chem Rev, 2003. **103**(10): p. 3899-4032.
22. Demchenko, A.P., K.C. Tang, and P.T. Chou, *Excited-state proton coupled charge transfer modulated by molecular structure and media polarization.* Chem Soc Rev, 2013. **42**(3): p. 1379-408.

23. Klymchenko, A.S., et al., *Modulation of the solvent-dependent dual emission in 3-hydroxychromones by substituents.* New Journal of Chemistry, 2003. **27**(9).
24. Klymchenko, A.S. and A.P. Demchenko, *Multiparametric probing of intermolecular interactions with fluorescent dye exhibiting excited state intramolecular proton transfer.* Physical Chemistry Chemical Physics, 2003. **5**(3): p. 461-468.
25. Demchenko, A.P., et al., *Monitoring Biophysical Properties of Lipid Membranes by Environment-Sensitive Fluorescent Probes.* Biophysical Journal, 2009. **96**(9): p. 3461-3470.
26. Shynkar, V.V., et al., *Two-color fluorescent probes for imaging the dipole potential of cell plasma membranes.* Biochim Biophys Acta, 2005. **1712**(2): p. 128-36.
27. Klymchenko, A.S., et al., *Fluorescent probe based on intramolecular proton transfer for fast ratiometric measurement of cellular transmembrane potential.* J Phys Chem B, 2006. **110**(27): p. 13624-32.
28. Klymchenko, A.S., et al., *Visualization of lipid domains in giant unilamellar vesicles using an environment-sensitive membrane probe based on 3-hydroxyflavone.* Biochim Biophys Acta, 2009. **1788**(2): p. 495-9.
29. Demchenko, A.P., et al., *Monitoring biophysical properties of lipid membranes by environment-sensitive fluorescent probes.* Biophys J, 2009. **96**(9): p. 3461-70.
30. Shynkar, V.V., et al., *Fluorescent biomembrane probe for ratiometric detection of apoptosis.* Journal of the American Chemical Society, 2007. **129**(7): p. 2187-2193.
31. Sedgwick, A.C., et al., *Excited-state intramolecular proton-transfer (ESIPT) based fluorescence sensors and imaging agents.* Chem Soc Rev, 2018. **47**(23): p. 8842-8880.
32. Yan, F., et al., *Fluorescein applications as fluorescent probes for the detection of analytes.* TrAC Trends in Analytical Chemistry, 2017. **97**: p. 15-35.
33. Ramette, R.W. and E.B. Sandell, *Rhodamine B Equilibria.* Journal of the American Chemical Society, 1956. **78**(19): p. 4872-4878.
34. Lukinavicius, G., et al., *A near-infrared fluorophore for live-cell super-resolution microscopy of cellular proteins.* Nat Chem, 2013. **5**(2): p. 132-9.
35. Lukinavicius, G., et al., *Fluorogenic Probes for Multicolor Imaging in Living Cells.* J Am Chem Soc, 2016. **138**(30): p. 9365-8.
36. Grimm, J.B., et al., *A general method to improve fluorophores for live-cell and single-molecule microscopy.* Nat Methods, 2015. **12**(3): p. 244-50, 3 p following 250.
37. Fin, A., et al., *Oligothiophene amphiphiles as planarizable and polarizable fluorescent membrane probes.* Angew Chem Int Ed Engl, 2012. **51**(51): p. 12736-9.
38. Colom, A., et al., *A fluorescent membrane tension probe.* Nat. Chem., 2018. **10**(11): p. 1118-1125.
39. Lieber, A.D., et al., *Front-to-rear membrane tension gradient in rapidly moving cells.* Biophys J, 2015. **108**(7): p. 1599-1603.
40. Lieber, A.D., et al., *Membrane tension in rapidly moving cells is determined by cytoskeletal forces.* Curr Biol, 2013. **23**(15): p. 1409-17.
41. Pontes, B., et al., *Membrane tension controls adhesion positioning at the leading edge of cells.* J Cell Biol, 2017. **216**(9): p. 2959-2977.
42. Gauthier, N.C., T.A. Masters, and M.P. Sheetz, *Mechanical feedback between membrane tension and dynamics.* Trends Cell Biol, 2012. **22**(10): p. 527-35.
43. Gauthier, N.C., et al., *Temporary increase in plasma membrane tension coordinates the activation of exocytosis and contraction during cell spreading.* Proc Natl Acad Sci U S A, 2011. **108**(35): p. 14467-72.
44. Masters, T.A., et al., *Plasma membrane tension orchestrates membrane trafficking, cytoskeletal remodeling, and biochemical signaling during phagocytosis.* Proc Natl Acad Sci U S A, 2013. **110**(29): p. 11875-80.

45. Dal Molin, M., et al., *Fluorescent Flippers for Mechanosensitive Membrane Probes.* Journal of the American Chemical Society, 2015. **137**(2): p. 568-571.
46. Goujon, A., et al., *Mechanosensitive Fluorescent Probes to Image Membrane Tension in Mitochondria, Endoplasmic Reticulum, and Lysosomes.* J Am Chem Soc, 2019. **141**(8): p. 3380-3384.
47. Haidekker, M.A. and E.A. Theodorakis, *Ratiometric mechanosensitive fluorescent dyes: Design and applications.* J Mater Chem C Mater, 2016. **4**(14): p. 2707-2718.
48. Kuimova, M.K., et al., *Molecular rotor measures viscosity of live cells via fluorescence lifetime imaging.* J Am Chem Soc, 2008. **130**(21): p. 6672-3.
49. Wu, Y.L., et al., *Molecular rheometry: direct determination of viscosity in L-o and L-d lipid phases via fluorescence lifetime imaging.* Physical Chemistry Chemical Physics, 2013. **15**(36): p. 14986-14993.
50. Kim, H.M., et al., *Two-photon fluorescent turn-on probe for lipid rafts in live cell and tissue.* J Am Chem Soc, 2008. **130**(13): p. 4246-7.
51. Chambers, J.E., et al., *An Optical Technique for Mapping Microviscosity Dynamics in Cellular Organelles.* ACS Nano, 2018. **12**(5): p. 4398-4407.
52. Li, L.L., et al., *BODIPY-Based Two-Photon Fluorescent Probe for Real-Time Monitoring of Lysosomal Viscosity with Fluorescence Lifetime Imaging Microscopy.* Anal Chem, 2018. **90**(9): p. 5873-5878.
53. Nipper, M.E., et al., *Detection of liposome membrane viscosity perturbations with ratiometric molecular rotors.* Biochimie, 2011. **93**(6): p. 988-94.
54. Zhu, D., et al., *Application of Molecular Rotors to the Determination of the Molecular Weight Dependence of Viscosity in Polymer Melts.* Macromolecules, 2007. **40**(21): p. 7730-7732.
55. Loutfy, R.O. and D.M. Teegarden, *Effect of polymer chain tacticity on the fluorescence of molecular rotors.* Macromolecules, 1983. **16**(3): p. 452-456.
56. Hawe, A., V. Filipe, and W. Jiskoot, *Fluorescent molecular rotors as dyes to characterize polysorbate-containing IgG formulations.* Pharm Res, 2010. **27**(2): p. 314-26.
57. Kung, C.E. and J.K. Reed, *Fluorescent molecular rotors: a new class of probes for tubulin structure and assembly.* Biochemistry, 1989. **28**(16): p. 6678-86.
58. Kubankova, M., et al., *Molecular rotors report on changes in live cell plasma membrane microviscosity upon interaction with beta-amyloid aggregates.* Soft Matter, 2018. **14**(46): p. 9466-9474.
59. Su, D., et al., *Motion-induced change in emission (MICE) for developing fluorescent probes.* Chem Soc Rev, 2017. **46**(16): p. 4833-4844.
60. Haidekker, M.A., et al., *A ratiometric fluorescent viscosity sensor.* J Am Chem Soc, 2006. **128**(2): p. 398-9.
61. Yang, Z., et al., *A self-calibrating bipartite viscosity sensor for mitochondria.* J Am Chem Soc, 2013. **135**(24): p. 9181-5.
62. Vyšniauskas, A. and M.K. Kuimova, *A twisted tale: measuring viscosity and temperature of microenvironments using molecular rotors.* International Reviews in Physical Chemistry, 2018. **37**(2): p. 259-285.
63. Howell, S., et al., *Intrinsic and extrinsic temperature-dependency of viscosity-sensitive fluorescent molecular rotors.* J Fluoresc, 2012. **22**(1): p. 457-65.
64. Vysniauskas, A., et al., *Unravelling the effect of temperature on viscosity-sensitive fluorescent molecular rotors.* Chem Sci, 2015. **6**(10): p. 5773-5778.
65. Arai, S., et al., *A molecular fluorescent probe for targeted visualization of temperature at the endoplasmic reticulum.* Sci Rep, 2014. **4**: p. 6701.
66. Arai, S., et al., *Mitochondria-targeted fluorescent thermometer monitors intracellular temperature gradient.* Chem Commun (Camb), 2015. **51**(38): p. 8044-7.

67. Humeniuk, H.V., et al., *White-Fluorescent Dual-Emission Mechanosensitive Membrane Probes that Function by Bending Rather than Twisting.* Angew Chem Int Ed Engl, 2018. **57**(33): p. 10559-10563.
68. Zhang, Z., et al., *Excited-State Conformational/Electronic Responses of Saddle-Shaped N,N'-Disubstituted-Dihydrodibenzo[a,c]phenazines: Wide-Tuning Emission from Red to Deep Blue and White Light Combination.* J Am Chem Soc, 2015. **137**(26): p. 8509-20.
69. Wurthner, F., T.E. Kaiser, and C.R. Saha-Moller, *J-aggregates: from serendipitous discovery to supramolecular engineering of functional dye materials.* Angew Chem Int Ed Engl, 2011. **50**(15): p. 3376-410.
70. Okamoto, A., *ECHO probes: a concept of fluorescence control for practical nucleic acid sensing.* Chem Soc Rev, 2011. **40**(12): p. 5815-28.
71. Bouhedda, F., et al., *A dimerization-based fluorogenic dye-aptamer module for RNA imaging in live cells.* Nat Chem Biol, 2020. **16**(1): p. 69-76.
72. Karpenko, I.A., et al., *Fluorogenic squaraine dimers with polarity-sensitive folding as bright far-red probes for background-free bioimaging.* J Am Chem Soc, 2015. **137**(1): p. 405-12.
73. Mizusawa, K., Y. Takaoka, and I. Hamachi, *Specific cell surface protein imaging by extended self-assembling fluorescent turn-on nanoprobes.* J Am Chem Soc, 2012. **134**(32): p. 13386-95.
74. Collot, M., et al., *Bright fluorogenic squaraines with tuned cell entry for selective imaging of plasma membrane vs. endoplasmic reticulum.* Chem Commun (Camb), 2015. **51**(96): p. 17136-9.
75. Hong, Y., J.W. Lam, and B.Z. Tang, *Aggregation-induced emission: phenomenon, mechanism and applications.* Chem Commun (Camb), 2009(29): p. 4332-53.
76. Mei, J., et al., *Aggregation-Induced Emission: Together We Shine, United We Soar!* Chem Rev, 2015. **115**(21): p. 11718-940.
77. Leung, N.L., et al., *Restriction of intramolecular motions: the general mechanism behind aggregation-induced emission.* Chemistry, 2014. **20**(47): p. 15349-53.
78. Wang, E., et al., *A highly selective AIE fluorogen for lipid droplet imaging in live cells and green algae.* J Mater Chem B, 2014. **2**(14): p. 2013-2019.
79. Leung, C.W., et al., *A photostable AIE luminogen for specific mitochondrial imaging and tracking.* J Am Chem Soc, 2013. **135**(1): p. 62-5.
80. Yu, Y., et al., *Cytophilic fluorescent bioprobes for long-term cell tracking.* Adv Mater, 2011. **23**(29): p. 3298-302.
81. Liu, H., et al., *A facile, sensitive and selective fluorescent probe for heparin based on aggregation-induced emission.* Talanta, 2014. **118**: p. 348-52.
82. Sanji, T., et al., *Fluorescence "turn-on" detection of melamine with aggregation-induced-emission-active tetraphenylethene.* Chemistry, 2012. **18**(48): p. 15254-7.
83. Hong, Y., et al., *Quantitation, visualization, and monitoring of conformational transitions of human serum albumin by a tetraphenylethene derivative with aggregation-induced emission characteristics.* Anal Chem, 2010. **82**(16): p. 7035-43.
84. Wang, F., et al., *A highly sensitive "switch-on" fluorescent probe for protein quantification and visualization based on aggregation-induced emission.* Chem Commun (Camb), 2012. **48**(59): p. 7395-7.
85. Liu, Y., et al., *Simple biosensor with high selectivity and sensitivity: thiol-specific biomolecular probing and intracellular imaging by AIE fluorogen on a TLC plate through a thiol-ene click mechanism.* Chemistry, 2010. **16**(28): p. 8433-8.
86. Kwok, R.T., et al., *Biosensing by luminogens with aggregation-induced emission characteristics.* Chem Soc Rev, 2015. **44**(13): p. 4228-38.

87. Yu, C.Y.Y., et al., *A photostable AIEgen for nucleolus and mitochondria imaging with organelle-specific emission.* J Mater Chem B, 2016. **4**(15): p. 2614-2619.
88. Wang, Z., et al., *Specific Fluorescence Probes for Lipid Droplets Based on Simple AIEgens.* ACS Appl Mater Interfaces, 2016. **8**(16): p. 10193-200.
89. Ashoka, A.H., et al., *Solvatochromic Near-Infrared Probe for Polarity Mapping of Biomembranes and Lipid Droplets in Cells under Stress.* J Phys Chem Lett, 2019. **10**(10): p. 2414-2421.
90. Valanciunaite, J., et al., *Polarity Mapping of Cells and Embryos by Improved Fluorescent Solvatochromic Pyrene Probe.* Analytical Chemistry, 2020. **92**(9): p. 6512-6520.
91. Owen, D.M., et al., *Quantitative imaging of membrane lipid order in cells and organisms.* Nat Protoc, 2011. **7**(1): p. 24-35.
92. Liu, T., et al., *Quantitatively mapping cellular viscosity with detailed organelle information via a designed PET fluorescent probe.* Sci Rep, 2014. **4**: p. 5418.
93. Jimenez-Sanchez, A., E.K. Lei, and S.O. Kelley, *A Multifunctional Chemical Probe for the Measurement of Local Micropolarity and Microviscosity in Mitochondria.* Angew Chem Int Ed Engl, 2018. **57**(29): p. 8891-8895.
94. Ghosh, S., et al., *Fluorescence Dynamics in the Endoplasmic Reticulum of a Live Cell: Time-Resolved Confocal Microscopy.* Chemphyschem, 2016. **17**(18): p. 2818-23.
95. Iaea, D.B. and F.R. Maxfield, *Membrane order in the plasma membrane and endocytic recycling compartment.* PLoS One, 2017. **12**(11): p. e0188041.
96. Jiang, N., et al., *Ratiometric fluorescence imaging of cellular polarity: decrease in mitochondrial polarity in cancer cells.* Angew Chem Int Ed Engl, 2015. **54**(8): p. 2510-4.
97. Guo, R., et al., *A novel mitochondria-targeted rhodamine analogue for the detection of viscosity changes in living cells, zebra fish and living mice.* J Mater Chem B, 2018. **6**(18): p. 2894-2900.
98. Dunn, K.W., M.M. Kamocka, and J.H. McDonald, *A practical guide to evaluating colocalization in biological microscopy.* Am J Physiol Cell Physiol, 2011. **300**(4): p. C723-42.
99. Lombard, J., *Once upon a time the cell membranes: 175 years of cell boundary research.* Biol Direct, 2014. **9**: p. 32.
100. Parton, R.G. and K. Simons, *The multiple faces of caveolae.* Nat Rev Mol Cell Biol, 2007. **8**(3): p. 185-94.
101. Rello, S., et al., *Morphological criteria to distinguish cell death induced by apoptotic and necrotic treatments.* Apoptosis, 2005. **10**(1): p. 201-8.
102. Jia, H.R., et al., *Efficient cell surface labelling of live zebrafish embryos: wash-free fluorescence imaging for cellular dynamics tracking and nanotoxicity evaluation.* Chem Sci, 2019. **10**(14): p. 4062-4068.
103. Weissleder, R. and M.J. Pittet, *Imaging in the era of molecular oncology.* Nature, 2008. **452**(7187): p. 580-9.
104. Scott, B.L., et al., *Membrane bending occurs at all stages of clathrin-coat assembly and defines endocytic dynamics.* Nat Commun, 2018. **9**(1): p. 419.
105. Zhou, J., et al., *Fluorescent Diagnostic Probes in Neurodegenerative Diseases.* Adv Mater, 2020: p. e2001945.
106. Sezgin, E., et al., *The mystery of membrane organization: composition, regulation and roles of lipid rafts.* Nat. Rev. Mol. Cell Biol., 2017. **18**(6): p. 361-374.
107. Kinoshita, M., et al., *Raft-based sphingomyelin interactions revealed by new fluorescent sphingomyelin analogs.* J Cell Biol, 2017. **216**(4): p. 1183-1204.
108. Baumgart, T., S.T. Hess, and W.W. Webb, *Imaging coexisting fluid domains in biomembrane models coupling curvature and line tension.* Nature, 2003. **425**(6960): p. 821-4.

109. Dietrich, C., et al., *Lipid rafts reconstituted in model membranes.* Biophysical Journal, 2001. **80**(3): p. 1417-1428.
110. Amaro, M., et al., *Laurdan and Di-4-ANEPPDHQ probe different properties of the membrane.* J Phys D Appl Phys, 2017. **50**(13): p. 134004.
111. Zhang, Y.L., J.A. Frangos, and M. Chachisvilis, *Laurdan fluorescence senses mechanical strain in the lipid bilayer membrane.* Biochem Biophys Res Commun, 2006. **347**(3): p. 838-41.
112. Zwaal, R.F.A. and A.J. Schroit, *Pathophysiologic implications of membrane phospholipid asymmetry in blood cells.* Blood, 1997. **89**(4): p. 1121-1132.
113. Murate, M., et al., *Transbilayer distribution of lipids at nano scale.* Journal of Cell Science, 2015. **128**(8): p. 1627-1638.
114. Lorent, J.H., et al., *Plasma membranes are asymmetric in lipid unsaturation, packing and protein shape.* Nat Chem Biol, 2020. **16**(6): p. 644-652.
115. Su, D.D., et al., *Motion-induced change in emission (MICE) for developing fluorescent probes.* Chemical Society Reviews, 2017. **46**(16): p. 4833-4844.
116. Sherin, P.S., et al., *Visualising the membrane viscosity of porcine eye lens cells using molecular rotors.* Chemical Science, 2017. **8**(5): p. 3523-3528.
117. Klymchenko, A.S., *Solvatochromic and Fluorogenic Dyes as Environment-Sensitive Probes: Design and Biological Applications.* Acc. Chem. Res., 2017. **50**(2): p. 366-375.
118. Ashoka, A.H., et al., *Solvatochromic Near-Infrared Probe for Polarity Mapping of Biomembranes and Lipid Droplets in Cells under Stress.* Journal of Physical Chemistry Letters, 2019. **10**(10): p. 2414-2421.
119. Han, X.Y., et al., *A mitochondrial-targeting near-infrared fluorescent probe for bioimaging and evaluating endogenous superoxide anion changes during ischemia/reperfusion injury.* Biomaterials, 2018. **156**: p. 134-146.
120. de la Haba, C., et al., *Effect of oxidative stress on plasma membrane fluidity of THP-1 induced macrophages.* Biochimica Et Biophysica Acta-Biomembranes, 2013. **1828**(2): p. 357-364.
121. Kreder, R., et al., *Solvatochromic Nile Red probes with FRET quencher reveal lipid order heterogeneity in living and apoptotic cells.* ACS Chem Biol, 2015. **10**(6): p. 1435-42.
122. Liu, C., M.G. Tian, and W.Y. Lin, *A unique polarity-sensitive photothermal sensitizer revealing down-regulated mitochondrial polarity during photo-induced cell death.* Journal of Materials Chemistry B, 2020. **8**(4): p. 752-757.
123. Jiang, N., et al., *Ratiometric Fluorescence Imaging of Cellular Polarity: Decrease in Mitochondrial Polarity in Cancer Cells.* Angewandte Chemie-International Edition, 2015. **54**(8): p. 2510-2514.
124. Monsigny, M., et al., *Sugar-lectin interactions: how does wheat-germ agglutinin bind sialoglycoconjugates?* Eur J Biochem, 1980. **104**(1): p. 147-53.
125. Owen, D.M., et al., *Sub-resolution lipid domains exist in the plasma membrane and regulate protein diffusion and distribution.* Nat Commun, 2012. **3**: p. 1256.
126. Collot, M., et al., *MemBright: A Family of Fluorescent Membrane Probes for Advanced Cellular Imaging and Neuroscience.* Cell Chemical Biology, 2019. **DOI: 10.1016/j.chembiol.2019.01.009**.
127. Kilin, V., et al., *Fluorescence lifetime imaging of membrane lipid order with a ratiometric fluorescent probe.* Biophys J, 2015. **108**(10): p. 2521-2531.
128. Collot, M., et al., *BODIPY with Tuned Amphiphilicity as a Fluorogenic Plasma Membrane Probe.* Bioconjug Chem, 2019. **30**(1): p. 192-199.
129. Darwich, Z., et al., *Detection of apoptosis through the lipid order of the outer plasma membrane leaflet.* Biochim Biophys Acta, 2012. **1818**(12): p. 3048-54.

130. Ziomkiewicz, I., et al., *Dynamic conformational transitions of the EGF receptor in living mammalian cells determined by FRET and fluorescence lifetime imaging microscopy.* Cytometry A, 2013. **83**(9): p. 794-805.
131. Darwich, Z., et al., *Imaging lipid order changes in endosome membranes of live cells by using a Nile Red-based membrane probe.* RSC Adv., 2014. **4**(17): p. 8481-8488.
132. Neuberg, P., et al., *Photopolymerized micelles of diacetylene amphiphile: physical characterization and cell delivery properties.* Chem Commun (Camb), 2015. **51**(58): p. 11595-8.
133. Zhang, X., et al., *Photostable bipolar fluorescent probe for video tracking plasma membranes related cellular processes.* ACS Appl Mater Interfaces, 2014. **6**(15): p. 12372-9.
134. Lopez-Duarte, I., et al., *A molecular rotor for measuring viscosity in plasma membranes of live cells.* Chem Commun (Camb), 2014. **50**(40): p. 5282-4.
135. Wu, D., et al., *A DIE responsive NIR-fluorescent cell membrane probe.* Biochim Biophys Acta Biomembr, 2018. **1860**(11): p. 2272-2280.
136. Mukherjee, T., et al., *Imaging mitochondria and plasma membrane in live cells using solvatochromic styrylpyridines.* J Photochem Photobiol B, 2020. **203**: p. 111732.
137. Kwiatek, J.M., et al., *Characterization of a new series of fluorescent probes for imaging membrane order.* PLoS One, 2013. **8**(2): p. e52960.
138. Tian, M., et al., *A single fluorescent probe enables clearly discriminating and simultaneously imaging liquid-ordered and liquid-disordered microdomains in plasma membrane of living cells.* Biomaterials, 2017. **120**: p. 46-56.
139. Dahal, D., et al., *An NIR-emitting ESIPT dye with large stokes shift for plasma membrane of prokaryotic (E. coli) cells.* Sensors and Actuators B: Chemical, 2018. **259**: p. 44-49.
140. Jiang, Y.W., et al., *In Situ Visualization of Lipid Raft Domains by Fluorescent Glycol Chitosan Derivatives.* Langmuir, 2016. **32**(26): p. 6739-45.
141. Wang, H.Y., et al., *Imaging plasma membranes without cellular internalization: multisite membrane anchoring reagents based on glycol chitosan derivatives.* J Mater Chem B, 2015. **3**(30): p. 6165-6173.
142. Kreder, R., et al., *Blue fluorogenic probes for cell plasma membranes fill the gap in multicolour imaging.* RSC Advances, 2015. **5**(29): p. 22899-22905.
143. Heek, T., et al., *An amphiphilic perylene imido diester for selective cellular imaging.* Bioconjug Chem, 2013. **24**(2): p. 153-8.
144. Vakuliuk, O., et al., *Modified Isoindolediones as Bright Fluorescent Probes for Cell and Tissue Imaging.* Chemistry, 2019. **25**(58): p. 13354-13362.
145. Shi, L., et al., *An AIE-Based Probe for Rapid and Ultrasensitive Imaging of Plasma Membranes in Biosystems.* Angew Chem Int Ed Engl, 2020. **59**(25): p. 9962-9966.
146. Cui, Q., et al., *Binding-Directed Energy Transfer of Conjugated Polymer Materials for Dual-Color Imaging of Cell Membrane.* Chemistry of Materials, 2016. **28**(13): p. 4661-4669.
147. Smith, R.A., et al., *Mitochondrial pharmacology.* Trends Pharmacol Sci, 2012. **33**(6): p. 341-52.
148. Bodin, P. and G. Burnstock, *Purinergic signalling: ATP release.* Neurochem Res, 2001. **26**(8-9): p. 959-69.
149. Zorova, L.D., et al., *Mitochondrial membrane potential.* Anal Biochem, 2018. **552**: p. 50-59.
150. Gao, P., et al., *Fluorescent probes for organelle-targeted bioactive species imaging.* Chem Sci, 2019. **10**(24): p. 6035-6071.
151. Xu, W., et al., *Discerning the Chemistry in Individual Organelles with Small-Molecule Fluorescent Probes.* Angew Chem Int Ed Engl, 2016. **55**(44): p. 13658-13699.

152. Wen, Y., F. Huo, and C. Yin, *Organelle targetable fluorescent probes for hydrogen peroxide.* Chinese Chemical Letters, 2019. **30**(10): p. 1834-1842.
153. Okamoto, K., Perlman, P. S., Butow, R. A. , *Targeting of green fluorescent protein to mitochondria.* Methods Cell Biol., 2001. **65**: p. 277-283.
154. Liang, Q., et al., *Reduction of mutant huntingtin accumulation and toxicity by lysosomal cathepsins D and B in neurons.* Mol Neurodegener, 2011. **6**: p. 37.
155. Schneider, L. and J. Zhang, *Lysosomal function in macromolecular homeostasis and bioenergetics in Parkinson's disease.* Mol Neurodegener, 2010. **5**: p. 14.
156. Holtzman, E., *Lysosomes*. 1989.
157. Terman, A., et al., *Lysosomal labilization.* IUBMB Life, 2006. **58**(9): p. 531-9.
158. Zhu, H., et al., *Fluorescent Probes for Sensing and Imaging within Specific Cellular Organelles.* Acc Chem Res, 2016. **49**(10): p. 2115-2126.
159. Ren, M., et al., *Mitochondria and lysosome-targetable fluorescent probes for HOCl: recent advances and perspectives.* J Mater Chem B, 2018. **6**(12): p. 1716-1733.
160. Lodish, H.F., A. Berk, C. Kaiser, M. Krieger, M. Scott, A. Bretscher, H. Ploegh, and P. Matsudaira., *Molecular cell biology 6th ed.* 2008: W. H. Freeman and Co., New York.
161. Wagner, N., et al., *A Click Cage: Organelle-Specific Uncaging of Lipid Messengers.* Angew Chem Int Ed Engl, 2018. **57**(40): p. 13339-13343.
162. Zhang, H., et al., *Fluorene-derived two-photon fluorescent probes for specific and simultaneous bioimaging of endoplasmic reticulum and lysosomes: group-effect and localization.* J Mater Chem B, 2013. **1**(40): p. 5450-5455.
163. Hirschberg, C.B., P.W. Robbins, and C. Abeijon, *Transporters of nucleotide sugars, ATP, and nucleotide sulfate in the endoplasmic reticulum and Golgi apparatus.* Annu Rev Biochem, 1998. **67**: p. 49-69.
164. Hirayama, T., et al., *A Golgi-targeting fluorescent probe for labile Fe(ii) to reveal an abnormal cellular iron distribution induced by dysfunction of VPS35.* Chem Sci, 2019. **10**(5): p. 1514-1521.
165. Ishida, M., et al., *Synthetic self-localizing ligands that control the spatial location of proteins in living cells.* J Am Chem Soc, 2013. **135**(34): p. 12684-9.
166. Erdmann, R.S., et al., *Super-resolution imaging of the Golgi in live cells with a bioorthogonal ceramide probe.* Angew Chem Int Ed Engl, 2014. **53**(38): p. 10242-6.
167. Fan, L., et al., *A Golgi-targeted off-on fluorescent probe for real-time monitoring of pH changes in vivo.* Chem Commun (Camb), 2019. **55**(47): p. 6685-6688.
168. Marks, D.L., R. Bittman, and R.E. Pagano, *Use of Bodipy-labeled sphingolipid and cholesterol analogs to examine membrane microdomains in cells.* Histochem Cell Biol, 2008. **130**(5): p. 819-32.
169. Zhang, W., et al., *Two-photon fluorescence imaging reveals a Golgi apparatus superoxide anion-mediated hepatic ischaemia-reperfusion signalling pathway.* Chem Sci, 2019. **10**(3): p. 879-883.
170. Li, R.S., et al., *Chiral nanoprobes for targeting and long-term imaging of the Golgi apparatus.* Chem Sci, 2017. **8**(10): p. 6829-6835.
171. Li, P., et al., *Golgi Apparatus Polarity Indicates Depression-Like Behaviors of Mice Using in Vivo Fluorescence Imaging.* Anal Chem, 2019. **91**(5): p. 3382-3388.
172. Martin, S. and R.G. Parton, *Lipid droplets: a unified view of a dynamic organelle.* Nat Rev Mol Cell Biol, 2006. **7**(5): p. 373-8.
173. Farese, R.V., Jr. and T.C. Walther, *Lipid droplets finally get a little R-E-S-P-E-C-T.* Cell, 2009. **139**(5): p. 855-60.
174. Olzmann, J.A., C.M. Richter, and R.R. Kopito, *Spatial regulation of UBXD8 and p97/VCP controls ATGL-mediated lipid droplet turnover.* Proc Natl Acad Sci U S A, 2013. **110**(4): p. 1345-50.

175. Fam, T.K., A.S. Klymchenko, and M. Collot, *Recent Advances in Fluorescent Probes for Lipid Droplets.* Materials (Basel), 2018. **11**(9).
176. Collot, M., et al., *Ultrabright and Fluorogenic Probes for Multicolor Imaging and Tracking of Lipid Droplets in Cells and Tissues.* J Am Chem Soc, 2018. **140**(16): p. 5401-5411.
177. Kang, M., et al., *A near-infrared AIEgen for specific imaging of lipid droplets.* Chem Commun (Camb), 2016. **52**(35): p. 5957-60.
178. Geoffrey M. Cooper, R.E.H., *The Cell: A Molecular Approach. 6th ed.* 2014: Sinauer Associates, Inc., Sunderland, MA.
179. Horobin, R.W., J.C. Stockert, and F. Rashid-Doubell, *Fluorescent cationic probes for nuclei of living cells: why are they selective? A quantitative structure-activity relations analysis.* Histochem Cell Biol, 2006. **126**(2): p. 165-75.
180. Zheng, M.L., et al., *Comparison of staining selectivity for subcellular structures by carbazole-based cyanine probes in nonlinear optical microscopy.* Chembiochem, 2011. **12**(1): p. 52-5.
181. Abbe, E., *Beiträge zur Theorie des Mikroskops und der mikroskopischen Wahrnehmung.* Archiv für Mikroskopische Anatomie, 1873. **9**(1): p. 413-468.
182. Hell, S.W. and J. Wichmann, *Breaking the diffraction resolution limit by stimulated emission: stimulated-emission-depletion fluorescence microscopy.* Opt Lett, 1994. **19**(11): p. 780-2.
183. Klar, T.A. and S.W. Hell, *Subdiffraction resolution in far-field fluorescence microscopy.* Opt Lett, 1999. **24**(14): p. 954-6.
184. Hofmann, M., et al., *Breaking the diffraction barrier in fluorescence microscopy at low light intensities by using reversibly photoswitchable proteins.* Proc Natl Acad Sci U S A, 2005. **102**(49): p. 17565-9.
185. Eggeling, C., et al., *Lens-based fluorescence nanoscopy.* Q Rev Biophys, 2015. **48**(2): p. 178-243.
186. Heintzmann, R. and M.G.L. Gustafsson, *Subdiffraction resolution in continuous samples.* Nature Photonics, 2009. **3**(7): p. 362-364.
187. Li, H. and J.C. Vaughan, *Switchable Fluorophores for Single-Molecule Localization Microscopy.* Chem Rev, 2018. **118**(18): p. 9412-9454.
188. Moerner, W.E. and M. Orrit, *Illuminating single molecules in condensed matter.* Science, 1999. **283**(5408): p. 1670-6.
189. Yildiz, A., et al., *Myosin V walks hand-over-hand: single fluorophore imaging with 1.5-nm localization.* Science, 2003. **300**(5628): p. 2061-5.
190. Pertsinidis, A., Y. Zhang, and S. Chu, *Subnanometre single-molecule localization, registration and distance measurements.* Nature, 2010. **466**(7306): p. 647-51.
191. Rust, M.J., M. Bates, and X. Zhuang, *Sub-diffraction-limit imaging by stochastic optical reconstruction microscopy (STORM).* Nat Methods, 2006. **3**(10): p. 793-5.
192. Betzig, E., et al., *Imaging intracellular fluorescent proteins at nanometer resolution.* Science, 2006. **313**(5793): p. 1642-5.
193. Hess, S.T., T.P. Girirajan, and M.D. Mason, *Ultra-high resolution imaging by fluorescence photoactivation localization microscopy.* Biophys J, 2006. **91**(11): p. 4258-72.
194. Huang, B., H. Babcock, and X. Zhuang, *Breaking the diffraction barrier: super-resolution imaging of cells.* Cell, 2010. **143**(7): p. 1047-58.
195. Sahl, S.J., S.W. Hell, and S. Jakobs, *Fluorescence nanoscopy in cell biology.* Nat Rev Mol Cell Biol, 2017. **18**(11): p. 685-701.
196. Sharonov, A. and R.M. Hochstrasser, *Wide-field subdiffraction imaging by accumulated binding of diffusing probes.* Proc Natl Acad Sci U S A, 2006. **103**(50): p. 18911-6.

197. Balzarotti, F., et al., *Nanometer resolution imaging and tracking of fluorescent molecules with minimal photon fluxes.* Science, 2017. **355**(6325): p. 606-612.
198. Thompson, R.E., D.R. Larson, and W.W. Webb, *Precise Nanometer Localization Analysis for Individual Fluorescent Probes.* Biophysical Journal, 2002. **82**(5): p. 2775-2783.
199. Mortensen, K.I., et al., *Optimized localization analysis for single-molecule tracking and super-resolution microscopy.* Nat Methods, 2010. **7**(5): p. 377-81.
200. Heilemann, M., et al., *Carbocyanine dyes as efficient reversible single-molecule optical switch.* J Am Chem Soc, 2005. **127**(11): p. 3801-6.
201. Bates, M., T.R. Blosser, and X. Zhuang, *Short-range spectroscopic ruler based on a single-molecule optical switch.* Phys Rev Lett, 2005. **94**(10): p. 108101.
202. Bates, M., et al., *Multicolor super-resolution imaging with photo-switchable fluorescent probes.* Science, 2007. **317**(5845): p. 1749-53.
203. Bates, M., et al., *Multicolor super-resolution fluorescence imaging via multi-parameter fluorophore detection.* Chemphyschem, 2012. **13**(1): p. 99-107.
204. Bock, H., et al., *Two-color far-field fluorescence nanoscopy based on photoswitchable emitters.* Applied Physics B, 2007. **88**(2): p. 161-165.
205. Folling, J., et al., *Fluorescence nanoscopy by ground-state depletion and single-molecule return.* Nat Methods, 2008. **5**(11): p. 943-5.
206. Heilemann, M., et al., *Subdiffraction-resolution fluorescence imaging with conventional fluorescent probes.* Angew Chem Int Ed Engl, 2008. **47**(33): p. 6172-6.
207. Heilemann, M., et al., *Super-resolution imaging with small organic fluorophores.* Angew Chem Int Ed Engl, 2009. **48**(37): p. 6903-8.
208. Dempsey, G.T., et al., *Photoswitching mechanism of cyanine dyes.* J Am Chem Soc, 2009. **131**(51): p. 18192-3.
209. Gidi, Y., et al., *Unifying Mechanism for Thiol-Induced Photoswitching and Photostability of Cyanine Dyes.* J Am Chem Soc, 2020. **142**(29): p. 12681-12689.
210. Vaughan, J.C., et al., *Phosphine quenching of cyanine dyes as a versatile tool for fluorescence microscopy.* J Am Chem Soc, 2013. **135**(4): p. 1197-200.
211. Dempsey, G.T., et al., *Evaluation of fluorophores for optimal performance in localization-based super-resolution imaging.* Nat Methods, 2011. **8**(12): p. 1027-36.
212. van de Linde, S., et al., *Photoinduced formation of reversible dye radicals and their impact on super-resolution imaging.* Photochem Photobiol Sci, 2011. **10**(4): p. 499-506.
213. Vaughan, J.C., S. Jia, and X. Zhuang, *Ultrabright photoactivatable fluorophores created by reductive caging.* Nature Methods, 2012. **9**(12): p. 1181-1184.
214. Kuhn, R. and A. Winterstein, *Reduktionen mit Zinkstaub in Pyridin, I. Mitteil.: Umkehrbare Hydrierung und Dehydrierung bei Cyanin-Farbstoffen.* Berichte der deutschen chemischen Gesellschaft (A and B Series), 1932. **65**(10): p. 1737-1742.
215. Kundu, K., et al., *Hydrocyanines: a class of fluorescent sensors that can image reactive oxygen species in cell culture, tissue, and in vivo.* Angew Chem Int Ed Engl, 2009. **48**(2): p. 299-303.
216. Lehmann, M., et al., *Multicolor Caged dSTORM Resolves the Ultrastructure of Synaptic Vesicles in the Brain.* Angew Chem Int Ed Engl, 2015. **54**(45): p. 13230-5.
217. Michie, M.S., et al., *Cyanine Conformational Restraint in the Far-Red Range.* J Am Chem Soc, 2017. **139**(36): p. 12406-12409.
218. Belov, V.N., et al., *Rhodamines NN: a novel class of caged fluorescent dyes.* Angew Chem Int Ed Engl, 2010. **49**(20): p. 3520-3.
219. Kolmakov, K., et al., *Masked red-emitting carbopyronine dyes with photosensitive 2-diazo-1-indanone caging group.* Photochem Photobiol Sci, 2012. **11**(3): p. 522-32.

220. Belov, V.N., et al., *Masked rhodamine dyes of five principal colors revealed by photolysis of a 2-diazo-1-indanone caging group: synthesis, photophysics, and light microscopy applications.* Chemistry, 2014. **20**(41): p. 13162-73.
221. Mitchison, T.J., *Polewards microtubule flux in the mitotic spindle: evidence from photoactivation of fluorescence.* J Cell Biol, 1989. **109**(2): p. 637-52.
222. Gee, K.R., E.S. Weinberg, and D.J. Kozlowski, *Caged Q-rhodamine dextran: a new photoactivated fluorescent tracer.* Bioorganic & Medicinal Chemistry Letters, 2001. **11**(16): p. 2181-2183.
223. Kobayashi, T., et al., *Highly activatable and rapidly releasable caged fluorescein derivatives.* J Am Chem Soc, 2007. **129**(21): p. 6696-7.
224. Bley, F., K. Schaper, and H. Gorner, *Photoprocesses of molecules with 2-nitrobenzyl protecting groups and caged organic acids.* Photochem Photobiol, 2008. **84**(1): p. 162-71.
225. Kobayashi, T., et al., *Highly activatable and environment-insensitive optical highlighters for selective spatiotemporal imaging of target proteins.* J Am Chem Soc, 2012. **134**(27): p. 11153-60.
226. Wysocki, L.M., et al., *Facile and general synthesis of photoactivatable xanthene dyes.* Angew Chem Int Ed Engl, 2011. **50**(47): p. 11206-9.
227. Grimm, J.B., et al., *Synthesis of a Far-Red Photoactivatable Silicon-Containing Rhodamine for Super-Resolution Microscopy.* Angew Chem Int Ed Engl, 2016. **55**(5): p. 1723-7.
228. Grimm, J.B., et al., *Carbofluoresceins and carborhodamines as scaffolds for high-contrast fluorogenic probes.* ACS Chem Biol, 2013. **8**(6): p. 1303-10.
229. Lavis, L.D., T.Y. Chao, and R.T. Raines, *Fluorogenic label for biomolecular imaging.* ACS Chem Biol, 2006. **1**(4): p. 252-60.
230. Tian, Z. and A.D. Li, *Photoswitching-enabled novel optical imaging: innovative solutions for real-world challenges in fluorescence detections.* Acc Chem Res, 2013. **46**(2): p. 269-79.
231. Seefeldt, B., et al., *Spiropyrans as molecular optical switches.* Photochem Photobiol Sci, 2010. **9**(2): p. 213-20.
232. Zhu, M.Q., et al., *Spiropyran-based photochromic polymer nanoparticles with optically switchable luminescence.* J Am Chem Soc, 2006. **128**(13): p. 4303-9.
233. Tian, Z., et al., *Single-chromophore-based photoswitchable nanoparticles enable dual-alternating-color fluorescence for unambiguous live cell imaging.* J Am Chem Soc, 2009. **131**(12): p. 4245-52.
234. Wan, W., et al., *Antiphase dual-color correlation in a reactant-product pair imparts ultrasensitivity in reaction-linked double-photoswitching fluorescence imaging.* J Am Chem Soc, 2015. **137**(13): p. 4312-5.
235. Hu, D., et al., *Photoswitchable nanoparticles enable high-resolution cell imaging: PULSAR microscopy.* J Am Chem Soc, 2008. **130**(46): p. 15279-81.
236. Deniz, E., et al., *Photoactivatable Fluorophores for Super-Resolution Imaging Based on Oxazine Auxochromes.* The Journal of Physical Chemistry C, 2012. **116**(10): p. 6058-6068.
237. Petriella, M., et al., *Superresolution imaging with switchable fluorophores based on oxazine auxochromes.* Photochem Photobiol, 2013. **89**(6): p. 1391-8.
238. Cusido, J., et al., *A Photochromic Bioconjugate with Photoactivatable Fluorescence for Superresolution Imaging.* The Journal of Physical Chemistry C, 2016. **120**(23): p. 12860-12870.
239. Zhang, Y., et al., *Photoactivatable BODIPYs designed to monitor the dynamics of supramolecular nanocarriers.* J Am Chem Soc, 2015. **137**(14): p. 4709-19.

240. Tomasulo, M., S. Sortino, and F.M. Raymo, *A new family of photochromic compounds based on the photoinduced opening and thermal closing of [1,3]oxazine rings.* Journal of Photochemistry and Photobiology A: Chemistry, 2008. **200**(1): p. 44-49.
241. Zou, Y., et al., *Amphiphilic diarylethene as a photoswitchable probe for imaging living cells.* J Am Chem Soc, 2008. **130**(47): p. 15750-1.
242. Uno, K., et al., *In situ preparation of highly fluorescent dyes upon photoirradiation.* J Am Chem Soc, 2011. **133**(34): p. 13558-64.
243. Roubinet, B., et al., *Fluorescent Photoswitchable Diarylethenes for Biolabeling and Single-Molecule Localization Microscopies with Optical Superresolution.* J Am Chem Soc, 2017. **139**(19): p. 6611-6620.
244. Irie, M., *Diarylethenes for Memories and Switches.* Chem Rev, 2000. **100**(5): p. 1685-1716.
245. Tian, H. and S. Yang, *Recent progresses on diarylethene based photochromic switches.* Chem Soc Rev, 2004. **33**(2): p. 85-97.
246. Irie, M., et al., *Photochromism of diarylethene molecules and crystals: memories, switches, and actuators.* Chem Rev, 2014. **114**(24): p. 12174-277.
247. Li, C., et al., *A trident dithienylethene-perylenemonoimide dyad with super fluorescence switching speed and ratio.* Nat Commun, 2014. **5**: p. 5709.
248. Fukaminato, T., et al., *Single-molecule fluorescence photoswitching of a diarylethene-perylenebisimide dyad: non-destructive fluorescence readout.* J Am Chem Soc, 2011. **133**(13): p. 4984-90.
249. Li, C., et al., *Water-Soluble Polymeric Photoswitching Dyads Impart Super-Resolution Lysosome Highlighters.* Macromolecules, 2014. **47**(24): p. 8594-8601.
250. Li, C., et al., *Photoswitchable aggregation-induced emission of a dithienylethene–tetraphenylethene conjugate for optical memory and super-resolution imaging.* RSC Advances, 2013. **3**(23).
251. Gu, X., et al., *A Mitochondrion-Specific Photoactivatable Fluorescence Turn-On AIE-Based Bioprobe for Localization Super-Resolution Microscope.* Adv Mater, 2016. **28**(25): p. 5064-71.
252. Willets, K.A., et al., *Novel fluorophores for single-molecule imaging.* J Am Chem Soc, 2003. **125**(5): p. 1174-5.
253. Willets, K.A., et al., *Nonlinear optical chromophores as nanoscale emitters for single-molecule spectroscopy.* Acc Chem Res, 2005. **38**(7): p. 549-56.
254. Lord, S.J., et al., *DCDHF fluorophores for single-molecule imaging in cells.* Chemphyschem, 2009. **10**(1): p. 55-65.
255. Lord, S.J., et al., *Azido push-pull fluorogens photoactivate to produce bright fluorescent labels.* J Phys Chem B, 2010. **114**(45): p. 14157-67.
256. Lord, S.J., et al., *A photoactivatable push-pull fluorophore for single-molecule imaging in live cells.* J Am Chem Soc, 2008. **130**(29): p. 9204-5.
257. Lee, H.L., et al., *Superresolution imaging of targeted proteins in fixed and living cells using photoactivatable organic fluorophores.* J Am Chem Soc, 2010. **132**(43): p. 15099-101.
258. Sigal, Y.M., R. Zhou, and X. Zhuang, *Visualizing and discovering cellular structures with super-resolution microscopy.* Science, 2018. **361**(6405): p. 880-887.
259. Schermelleh, L., R. Heintzmann, and H. Leonhardt, *A guide to super-resolution fluorescence microscopy.* J Cell Biol, 2010. **190**(2): p. 165-75.
260. Folling, J., et al., *Photochromic rhodamines provide nanoscopy with optical sectioning.* Angew Chem Int Ed Engl, 2007. **46**(33): p. 6266-70.
261. Belov, V.N., et al., *Rhodamine spiroamides for multicolor single-molecule switching fluorescent nanoscopy.* Chemistry, 2009. **15**(41): p. 10762-76.

262. Folling, J., et al., *Fluorescence nanoscopy with optical sectioning by two-photon induced molecular switching using continuous-wave lasers.* Chemphyschem, 2008. **9**(2): p. 321-6.
263. Chen, X., et al., *Fluorescent chemosensors based on spiroring-opening of xanthenes and related derivatives.* Chem Rev, 2012. **112**(3): p. 1910-56.
264. Kim, H.N., et al., *A new trend in rhodamine-based chemosensors: application of spirolactam ring-opening to sensing ions.* Chem Soc Rev, 2008. **37**(8): p. 1465-72.
265. Grimm, J.B., et al., *A general method to fine-tune fluorophores for live-cell and in vivo imaging.* Nat Methods, 2017. **14**(10): p. 987-994.
266. Belov, V.N. and M.L. Bossi, *Photoswitching Emission with Rhodamine Spiroamides for Super-resolution Fluorescence nanoscopies.* Israel Journal of Chemistry, 2013. **53**(5): p. 267-279.
267. Lee, M.K., et al., *Enzymatic activation of nitro-aryl fluorogens in live bacterial cells for enzymatic turnover-activated localization microscopydagger.* Chem Sci, 2013. **42**: p. 220-225.
268. Roldan, M.D., et al., *Reduction of polynitroaromatic compounds: the bacterial nitroreductases.* FEMS Microbiol Rev, 2008. **32**(3): p. 474-500.
269. Kuo, C. and R.M. Hochstrasser, *Super-resolution microscopy of lipid bilayer phases.* J Am Chem Soc, 2011. **133**(13): p. 4664-7.
270. Lew, M.D., et al., *Three-dimensional superresolution colocalization of intracellular protein superstructures and the cell surface in live Caulobacter crescentus.* Proc Natl Acad Sci U S A, 2011. **108**(46): p. E1102-10.
271. Sezgin, E., et al., *Polarity-Sensitive Probes for Superresolution Stimulated Emission Depletion Microscopy.* Biophys J, 2017. **113**(6): p. 1321-1330.
272. Zhang, Z., et al., *Ultrahigh-throughput single-molecule spectroscopy and spectrally resolved super-resolution microscopy.* Nat Methods, 2015. **12**(10): p. 935-8.
273. Dong, B., et al., *Super-resolution spectroscopic microscopy via photon localization.* Nat Commun, 2016. **7**: p. 12290.
274. Mlodzianoski, M.J., et al., *Super-Resolution Imaging of Molecular Emission Spectra and Single Molecule Spectral Fluctuations.* PLoS One, 2016. **11**(3): p. e0147506.
275. Bongiovanni, M.N., et al., *Multi-dimensional super-resolution imaging enables surface hydrophobicity mapping.* Nature Communications, 2016. **7**: p. 9.
276. Moon, S., et al., *Spectrally Resolved, Functional Super-Resolution Microscopy Reveals Nanoscale Compositional Heterogeneity in Live-Cell Membranes.* J Am Chem Soc, 2017. **139**(32): p. 10944-10947.
277. Yan, R., et al., *Spectrally Resolved and Functional Super-resolution Microscopy via Ultrahigh-Throughput Single-Molecule Spectroscopy.* Acc Chem Res, 2018. **51**(3): p. 697-705.
278. Daly, B., J. Ling, and A.P. de Silva, *Current developments in fluorescent PET (photoinduced electron transfer) sensors and switches.* Chem Soc Rev, 2015. **44**(13): p. 4203-11.
279. Zidovetzki, R. and I. Levitan, *Use of cyclodextrins to manipulate plasma membrane cholesterol content: Evidence, misconceptions and control strategies.* Biochimica Et Biophysica Acta-Biomembranes, 2007. **1768**(6): p. 1311-1324.
280. Owen, D.M., et al., *Quantitative imaging of membrane lipid order in cells and organisms.* Nature Protocols, 2012. **7**(1): p. 24-35.
281. Liu, S.-L., et al., *Orthogonal lipid sensors identify transbilayer asymmetry of plasma membrane cholesterol.* Nature Chemical Biology, 2017. **13**(3): p. 268-274.
282. Vanni, S., et al., *A sub-nanometre view of how membrane curvature and composition modulate lipid packing and protein recruitment.* Nat Commun, 2014. **5**: p. 4916.

283. Pinot, M., et al., *Lipid cell biology. Polyunsaturated phospholipids facilitate membrane deformation and fission by endocytic proteins.* Science, 2014. **345**(6197): p. 693-7.
284. Yin, H., L. Xu, and N.A. Porter, *Free radical lipid peroxidation: mechanisms and analysis.* Chem Rev, 2011. **111**(10): p. 5944-72.
285. Steinkuhler, J., et al., *Mechanical properties of plasma membrane vesicles correlate with lipid order, viscosity and cell density.* Commun Biol, 2019. **2**: p. 337.
286. Oncul, S., et al., *Liquid ordered phase in cell membranes evidenced by a hydration-sensitive probe: effects of cholesterol depletion and apoptosis.* Biochim Biophys Acta, 2010. **1798**(7): p. 1436-43.
287. Yin, H., L. Xu, and N.A. Porter, *Free radical lipid peroxidation: mechanisms and analysis.* Chem. Rev., 2011. **111**(10): p. 5944-72.
288. Ashoka, A.H., et al., *Solvatochromic Near-Infrared Probe for Polarity Mapping of Biomembranes and Lipid Droplets in Cells under Stress.* J. Phys. Chem. Lett., 2019. **10**(10): p. 2414-2421.
289. Nilsson, E., R. Ghassemifar, and U.T. Brunk, *Lysosomal heterogeneity between and within cells with respect to resistance against oxidative stress.* Histochem. J., 1997. **29**(11-12): p. 857-65.
290. Lenaz, G., *Role of mitochondria in oxidative stress and ageing.* Biochim. Biophys. Acta Bioenerg., 1998. **1366**(1-2): p. 53-67.
291. Ott, M., et al., *Mitochondria, oxidative stress and cell death.* Apoptosis, 2007. **12**(5): p. 913-922.
292. Chaudhuri, P.K., B.C. Low, and C.T. Lim, *Mechanobiology of Tumor Growth.* Chem. Rev., 2018. **118**(14): p. 6499-6515.
293. Mammoto, T., A. Mammoto, and D.E. Ingber, *Mechanobiology and Developmental Control*, in *Annu. Rev. Cell Dev. Biol.*, R. Schekman, Editor. 2013, Annual Reviews: Palo Alto. p. 27-61.
294. Ladoux, B. and R.M. Mege, *Mechanobiology of collective cell behaviours.* Nat. Rev. Mol. Cell Biol., 2017. **18**(12): p. 743-757.
295. Palacios-Serrato, E., D. Araiza-Olivera, and A. Jiménez-Sánchez, *Fluorescent Probe for Transmembrane Dynamics during Osmotic Effects.* Anal. Chem., 2020. **92**(5): p. 3888-3895.
296. Lim, R.K. and Q. Lin, *Bioorthogonal chemistry: recent progress and future directions.* Chem Commun (Camb), 2010. **46**(10): p. 1589-600.
297. Madl, C.M. and S.C. Heilshorn, *Bioorthogonal Strategies for Engineering Extracellular Matrices.* Adv Funct Mater, 2018. **28**(11).
298. Lang, K. and J.W. Chin, *Bioorthogonal reactions for labeling proteins.* ACS Chem Biol, 2014. **9**(1): p. 16-20.
299. Kool, E.T., D.H. Park, and P. Crisalli, *Fast hydrazone reactants: electronic and acid/base effects strongly influence rate at biological pH.* J Am Chem Soc, 2013. **135**(47): p. 17663-6.
300. Boutureira, O. and G.J. Bernardes, *Advances in chemical protein modification.* Chem Rev, 2015. **115**(5): p. 2174-95.
301. Deda, M.L., et al., *Organometallic emitting dyes: Palladium(II) nile red complexes.* Journal of Organometallic Chemistry, 2005. **690**(4): p. 857-861.
302. Brouwer, A.M., *Standards for photoluminescence quantum yield measurements in solution (IUPAC Technical Report).* Pure and Applied Chemistry, 2011. **83**(12): p. 2213-2228.
303. Porres, L., et al., *Absolute measurements of photoluminescence quantum yields of solutions using an integrating sphere.* J Fluoresc, 2006. **16**(2): p. 267-72.

304. Fischer, M. and J. Georges, *Fluorescence quantum yield of rhodamine 6G in ethanol as a function of concentration using thermal lens spectrometry.* Chemical Physics Letters, 1996. **260**(1-2): p. 115-118.
305. Isak, S.J. and E.M. Eyring, *Fluorescence quantum yield of cresyl violet in methanol and water as a function of concentration.* The Journal of Physical Chemistry, 1992. **96**(4): p. 1738-1742.
306. Alessi, A., M. Salvalaggio, and G. Ruzzon, *Rhodamine 800 as reference substance for fluorescence quantum yield measurements in deep red emission range.* Journal of Luminescence, 2013. **134**: p. 385-389.
307. Chen, H., et al., *Synthesis, structural characterization, and thermoresponsivity of hybrid supramolecular dendrimers bearing a polyoxometalate core.* Chemistry, 2013. **19**(33): p. 11051-61.
308. Magde, D., G.E. Rojas, and P.G. Seybold, *Solvent Dependence of the Fluorescence Lifetimes of Xanthene Dyes.* Photochemistry and Photobiology, 1999. **70**(5): p. 737-744.
309. Shulov, I., et al., *Protein-Sized Bright Fluorogenic Nanoparticles Based on Cross-Linked Calixarene Micelles with Cyanine Corona.* Angew Chem Int Ed Engl, 2016. **55**(51): p. 15884-15888.
310. Langhals, H., et al., *Cyanine dyes as optical contrast agents for ophthalmological surgery.* J Med Chem, 2011. **54**(11): p. 3903-25.
311. Sakai, K., et al., *Fluorocarbon-hydrocarbon gemini surfactant mixtures in aqueous solution.* Colloids and Surfaces a-Physicochemical and Engineering Aspects, 2009. **333**(1-3): p. 26-31.
312. Mazeres, S., et al., *Characterization of M-laurdan, a versatile probe to explore order in lipid membranes.* F1000Res, 2014. **3**: p. 172.
313. Cort, A.D., et al., *A novel ditopic zinc-salophen macrocycle: a potential two-stationed wheel for [2]-pseudorotaxanes.* Org Biomol Chem, 2006. **4**(24): p. 4543-6.
314. Sakai, K., et al., *Fluorocarbon–hydrocarbon gemini surfactant mixtures in aqueous solution.* Colloids and Surfaces A: Physicochemical and Engineering Aspects, 2009. **333**(1-3): p. 26-31.
315. Sezgin, E., et al., *Elucidating membrane structure and protein behavior using giant plasma membrane vesicles.* Nat Protoc, 2012. **7**(6): p. 1042-51.
316. Moon, S., et al., *Spectrally Resolved, Functional Super-Resolution Microscopy Reveals Nanoscale Compositional Heterogeneity in Live-Cell Membranes.* J. Am. Chem. Soc., 2017. **139**(32): p. 10944-10947.
317. Luckner, M., et al., *Label-free 3D-CLEM Using Endogenous Tissue Landmarks.* iScience, 2018. **6**: p. 92-101.
318. Khalin, I., et al., *Ultrabright Fluorescent Polymeric Nanoparticles with a Stealth Pluronic Shell for Live Tracking in the Mouse Brain.* ACS Nano, 2020. **14**(8): p. 9755-9770.
319. Sezgin, E., et al., *Spectral imaging to measure heterogeneity in membrane lipid packing.* Chemphyschem, 2015. **16**(7): p. 1387-94.
320. Huang, B., et al., *Three-dimensional super-resolution imaging by stochastic optical reconstruction microscopy.* Science, 2008. **319**(5864): p. 810-3.
321. Zhang, Z., et al., *Ultrahigh-throughput single-molecule spectroscopy and spectrally resolved super-resolution microscopy.* Nature Methods, 2015. **12**(10): p. 935-938.
322. de la Haba, C., et al., *Effect of oxidative stress on plasma membrane fluidity of THP-1 induced macrophages.* Biochim Biophys Acta, 2013. **1828**(2): p. 357-64.

4. Resume of thesis in English

Introduction

Fluorescence microscopy is a powerful technique for non-invasive study of live cells.[1] However, this technique relies on the performance of fluorescent probes used in the experiments. The major characteristics of a fluorescent probe include brightness, photostability, absorption and emission maxima of fluorophore,[2] as well as probe selectivity towards the target. We were particularly interested in probes for biological membranes, which are present both at cell surface (plasma membranes) and in the intracellular compartments of organelles. Efficient biomembrane probes should combine multiple functions, such as specific targeting of a given biomembrane, sensitivity to its local properties and compatibility with advanced microscopy techniques (in particular super-resolution microscopy). Specific targeting of organelle membranes in live cells generally exploits either chemical targeting groups[3-5] or an introduction of a biological molecule, utilizing cell machinery to accumulate the probe in target organelle.[6, 7] Sensitivity to the local properties of biomembranes, including polarity, viscosity and lipid order, can be achieved using environment-sensitive probes, capable of altering their fluorescence emission in response to changes in the parameters of microenvironment.[8] Finally, compatibility of the probe with super-resolution microscopy allows to image the biological membranes beyond the resolution limited by the light diffraction. Single molecule localization microscopy requires the probe to undergo fluorescence ON/OFF switching, which can be achieved by reversible photoreactions, photoactivation or reversible probe binding.

My PhD project has the following aim:

To design multifunctional fluorescent probes that: (i) target specific membrane compartments of cells (e.g. plasma membranes and organelles); (ii) respond to the local properties of their environment (such as polarity and lipid order); (iii) provide ON/OFF switching required for super-resolution microscopy; (iv) optionally exhibit chemical reactivity towards biomolecules or other agents.

Results and discussion

Membrane probes based on cyanines. The first part of the project was dedicated to the development of plasma membrane (PM) probes with reactable moieties, which would allow to control probe attachment to biomembranes by reacting with biomolecules or introduced agents, resulting in robust and durable staining. A number of cyanine-based probes with zwitterionic PM targeting motifs was developed (Fig. 1), however the probes showed significant staining of glass or plastic surface of imaging plates and rapid internalization in live cells, supposedly due to overall positive charge of the probes.

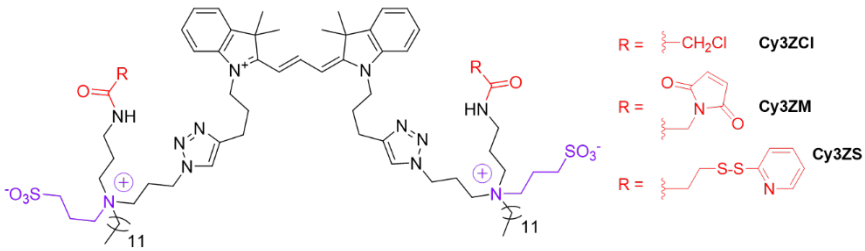

Fig. 1. Structures of reactable cyanine PM probes with zwitterionic targeting motifs

As a possible solution, we developed a new anionic PM-targeting moiety based on 3-(alkylammonio)propane-1-sulfonates due to their facile synthesis and functionalization. Its performance was then tested by synthesizing a palette of five cyanine dyes with different spectral properties, each bearing two membrane-targeting moieties (Fig. 2, A).

In spectroscopy experiments with large unilamellar vesicles (LUVs) anionic cyanine probes exhibit relatively high quantum yields, being 39-192-fold higher compared to the corresponding values in phosphate buffer, thus providing a fluorogenic response towards the presence of model membranes. Microscopy experiments in live KB cells show, that in comparison to its analogue with zwitterionic targeting motifs our anionic probe Cy5A shows significantly less nonspecific surface staining (Fig. 2, B) together with higher brightness and significantly decreased probe internalization (Fig. 2, C-D). Additionally, colocalization experiments with WGA Alexa-488 conjugate reveal high PM selectivity of anionic cyanine probes together with slow internalization. Currently, the probes are in course of testing for live brain tissue imaging.

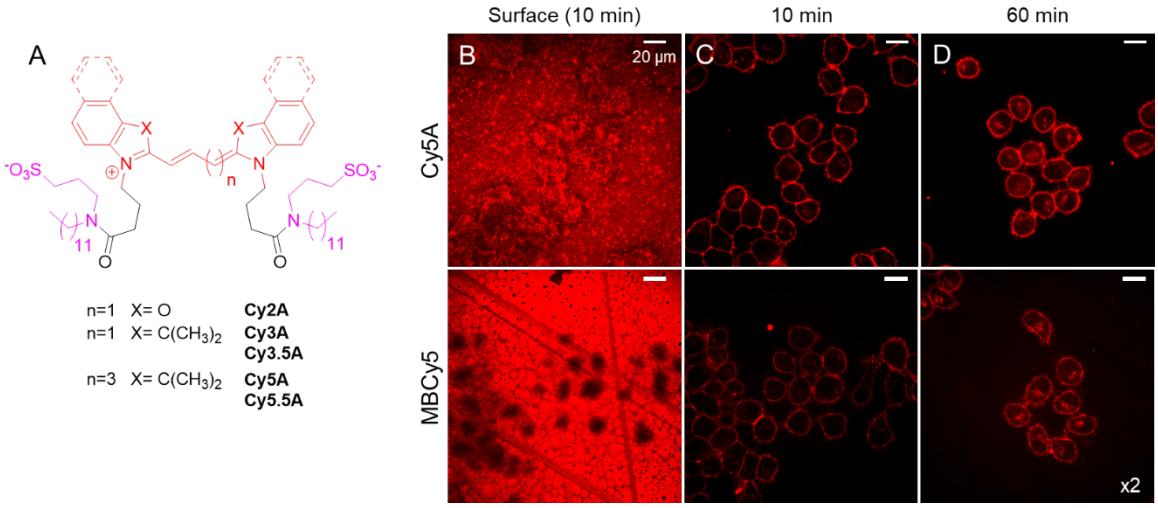

Fig. 2. Structures of anionic cyanine PM probes (A) and their performance in live cells (B-D) vs zwitterionic counterparts

Having obtained more effective plasma membrane targeting group, we synthesized anionic cyanine PM probes, bearing different reactable groups (Fig. 3). Cellular microscopy experiments showed high PM selectivity, however, the experiments on chemical reactivity were not conclusive and required additional study.

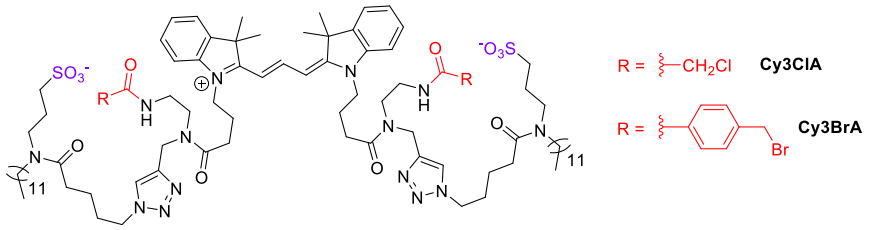

Fig. 3. Structures of anionic cyanine PM probes with reactable groups

Membrane probes based on solvatochromic dyes. On the other hand, based on the successful results obtained for cyanine-based PM probes, next we aimed to graft our membrane-targeting anionic anchor group to environment-sensitive (solvatochromic) dyes. These dyes are particularly interesting for lipid membrane research because they can detect changes in the lipid order by change in their emission colour.[9] For this purpose, we selected two fluorophores – Laurdan and Nile Red. Widely used Laurdan probe was totally redesigned using anionic targeting moiety to yield a new probe Pro12A (Fig. 4).

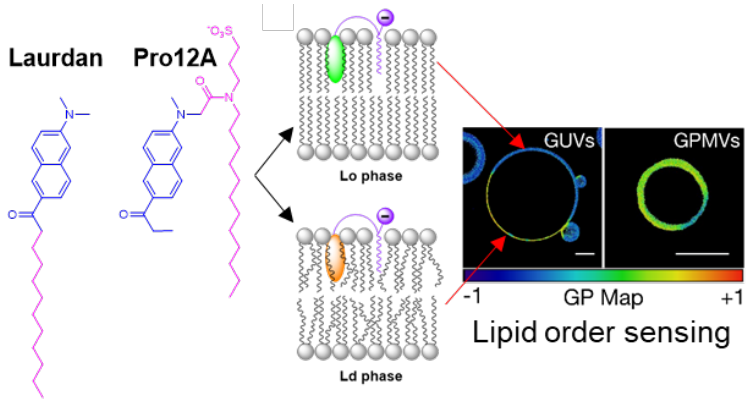

Fig. 4. Structure and mechanism of sensing of Pro12A probe.

In spectroscopy experiments with LUVs Pro12A showed 2-3 fold higher fluorescence quantum yield together with higher sensitivity to lipid order compared to parent Laurdan probe. Moreover, our probe stained exclusively the outer leaflet of biomembranes, showing much faster binding kinetics due to an improved solubility in aqueous medium. In live cell microscopy experiments, Pro12A showed much lower internalization compared to Laurdan and C-laurdan probes (Fig. 5, A-D). Additionally, Pro12A exhibited high sensitivity to cholesterol extraction (Fig. 5, E) and an absence of cross-talk with a number of orange/red proteins and dyes, enabling accurate multicolour cell imaging. We expect that the new probe will replace the commonly used Laurdan in all applications at the cell membrane level. The results were submitted for publication.

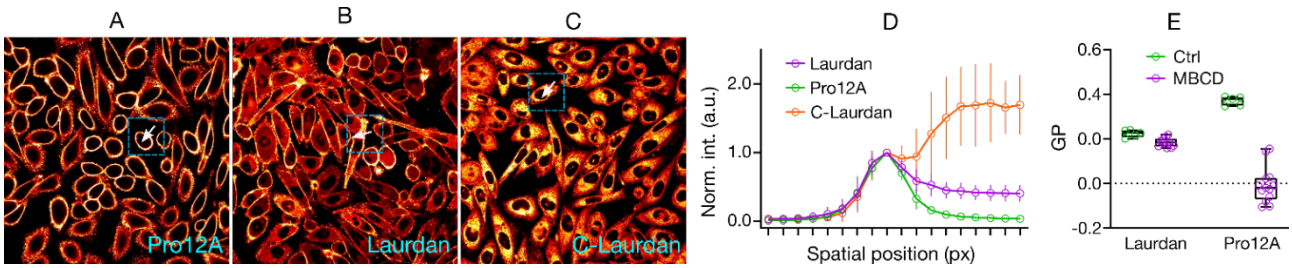

Fig. 5. Confocal microscopy of Pro12A (A) vs Laurdan (B) and C-Laurdan (C) in live CHO cells. Intensity profiles (D) across cell plasma membranes in the highlighted regions in A-C. Response of Pro12A and Laurdan to methyl-β-cyclodextrin treatment (E).

Next, we aimed at creating a plasma membrane-targeted solvatochromic Nile Red probe for super-resolution microscopy. In order to increase the photostability of the probes, we developed a functionalization strategy using the N-alkyl chain of Nile Red (Fig. 6, A). By varying the length of alkyl chain of our membrane anchor group (Fig 6, A), we synthesized a probe NR12A with quasi-irreversible membrane binding, suitable for conventional microscopy, and a reversibly binding probe NR4A, with an expected ON/OFF behavior, necessary for the super-resolution microscopy (Fig. 6, B).

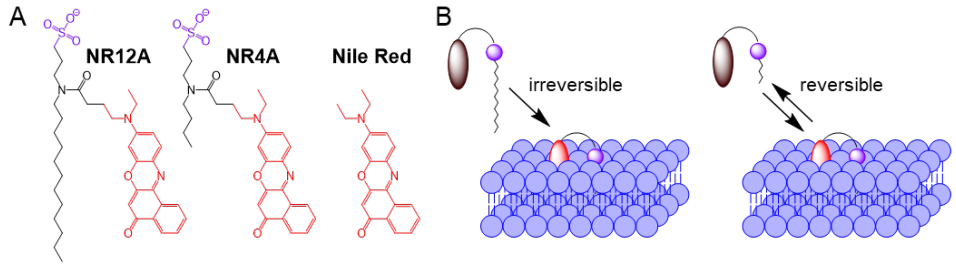

Fig. 6. Structure (A) and mechanism of binding (B) of NR12A and NR4A

Spectroscopy experiments with LUVs revealed that our new probes retain sensitivity towards lipid order and possess high quantum yields in liposomes together with improved photostability. Moreover, the results confirmed the much higher membrane affinity of NR12A vs NR4A. In cellular experiments, conventional probe NR12A showed high brightness and photostability together with specific staining of plasma membranes, which allowed, for instance,

to obtain 3D-images of plasma membranes of live KB cells (Fig 7, A). Probe NR4A exhibited high performance in super-resolution (PAINT) microscopy (Fig 7, B). Moreover, this probe allowed visualization of nanoscopic protrusions and invaginations (Fig. 7, C-D) on live cell plasma membrane.

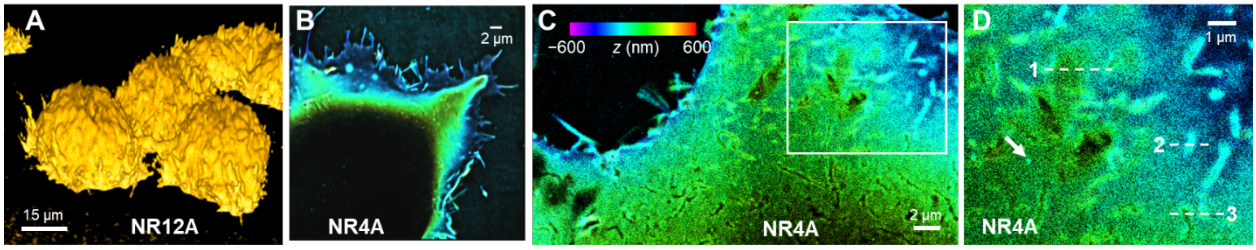

Fig. 7. (A) 3D confocal images of live KB cells stained with NR12A. (B) Zoom-out view of 3D PAINT image of live COS-7 cell with NR4A. (C) 3D PAINT image of the top plasma membrane of a HeLa cell with NR4A. (D) Zoom-in of the white box in (C).

Spectrally-resolved PAINT (SR-PAINT) imaging revealed that protrusions and invaginations have lower lipid order compared to the flat membrane regions (Fig. 8, A-B), suggesting a subtle connection between membrane morphology and lipid organization. In fixed cells, NR4A is able to penetrate plasma membrane, which results in intracellular membrane staining (Fig. 8, C). Thus, we developed powerful tools that combine specific targeting, sensing and ON/OFF switching capabilities for biomembrane research. These results were published.

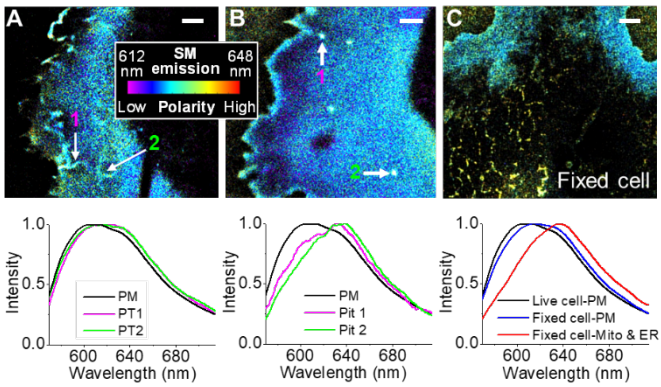

Fig. 8. SR-PAINT with NR4A for the plasma membrane of live COS-7 cells with tube-like protrusions (A) and cluster structures (B). NR4A SR-PAINT of a fixed COS-7 cell (C), showing staining for both the plasma membrane and internal membranes. Averaged single-molecule spectra at different parts of the pictures are represented below each corresponding image.

Organelle-targeted solvatochromic probes. Finally, in order to study intracellular membrane structures, we synthesized an array of organelle-targeted solvatochromic probes, basing on Nile Red fluorophore with chemical targeting moieties for endoplasmic reticulum (ER), mitochondria, lysosomes, Golgi apparatus and lipid droplets (Fig. 9, A). These probes were expected to change their emission colour depending on the local polarity and lipid order and detect changes in the organelles under the external stimuli, such as oxidative stress or hyperosmotic shock (Fig. 9, B).

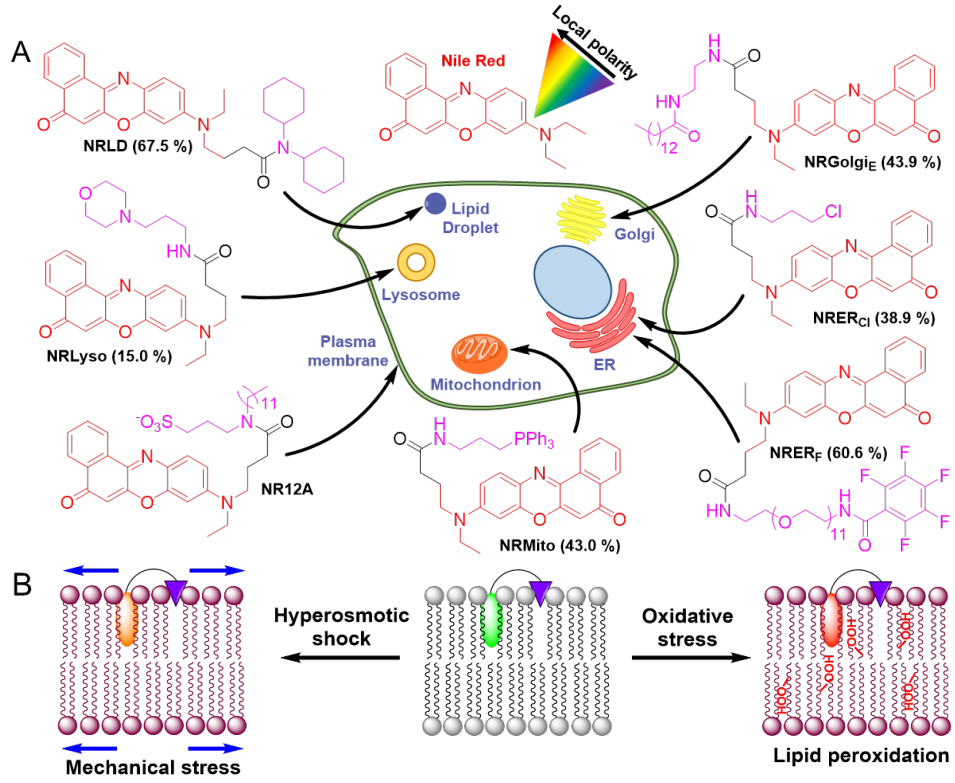

Fig. 9. Structures, localization (A) and sensing mechanism (B) of Nile Red organelle probes.

Microscopy results in live KB cells showed that our organelle-targeting probes colocalize well with corresponding organelle-specific commercial markers, indicating good organelle selectivity. Moreover, Nile Red probes showed differences in polarity within the organelles in live KB cells as well as different level of response towards the oxidative stress (Fig. 10).

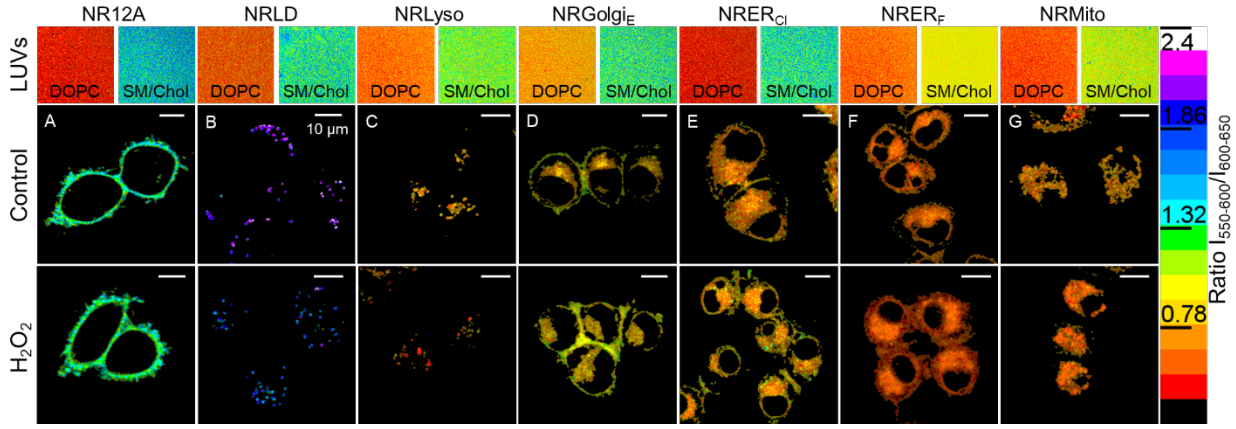

Fig. 10. Ratiometric microscopy imaging of the response to oxidative stress of live KB cells stained by solvatochromic organelle probes.

The organelle-specific probes were also able to sense hyperosmotic shock in live cells, with a varied level of response from different organelles. This work provided an evidence that each organelle membrane shows its unique polarity profile and characteristic response to the external stress. Based on these results, a manuscript for publication has been prepared.

Conclusions

In the search for new multifunctional fluorescent probes for biomembrane research, several key steps were accomplished.

During the first part of the project we have created a plasma membrane-targeting anchor group, based on anionic amphiphilic 3-(dodecylamino)propane-1-sulfonate moiety and validated its efficiency with a number of cyanine fluorophores. Live-cell microscopy showed that the new targeting group allowed to diminish probe internalization and non-specific binding to the surface of support. Additionally, we obtained cyanine-based membrane-targeting probes bearing reactive groups, which can potentially graft covalently with membrane proteins.

Next, we applied the new anchor group to polarity-sensitive probes based on Laurdan and Nile Red. The new probe based on Laurdan features superior fluorescence quantum yields and sensitivity towards lipid order, and it stains exclusively the outer membrane leaflet, while also showing slow internalization and compatibility with a number of orange/red proteins and dyes for live cell imaging. Then, using Nile Red dye and membrane-targeting moieties with varied alkyl chain length, we obtained two plasma membrane probes with varied affinity to biomembranes: high-affinity probe, suitable for conventional microscopy, and low affinity probe, undergoing reversible binding-controlled ON/OFF switching, suitable for super-resolution microscopy. The latter probe allowed to visualize nanoscale protrusions and invaginations of plasma membrane in live cells, revealing their lower lipid order.

Finally, we created an array of environment-sensitive solvatochromic Nile Red-based probes with organelle-targeted groups for ER, mitochondria, Golgi, lipid droplets and lysosomes. The probes were able to sense differences in polarity and lipid order within different organelles, as well as an organelle-specific response towards external stimuli, such as oxidative stress and hyperosmotic shock, as revealed by ratiometric microscopy experiments in live cells.

Overall, we developed new design strategies for organelle-specific biomembrane probes, based on conventional and environment-sensitive fluorescent probes. The obtained probes are expected to find direct applications for biological research, especially for advanced fluorescence microscopy.

These probes can be further improved by introducing proper reactable moieties, which will allow to control the probe attachment to the target. Introduction of reversible bonding strategy opens a possibility to create the probes with stimuli-responsive staining.

References

1. Demchenko, A.P., *Introduction to Fluorescence Sensing*. 2009: Springer, Dordrecht.
2. Fu, Y. and N.S. Finney, *Small-molecule fluorescent probes and their design.* RSC Advances, 2018. **8**(51): p. 29051-29061.
3. Gao, P., W. Pan, N. Li, and B. Tang, *Fluorescent probes for organelle-targeted bioactive species imaging.* Chem Sci, 2019. **10**(24): p. 6035-6071.
4. Xu, W., Z. Zeng, J.H. Jiang, Y.T. Chang, and L. Yuan, *Discerning the Chemistry in Individual Organelles with Small-Molecule Fluorescent Probes.* Angew Chem Int Ed Engl, 2016. **55**(44): p. 13658-13699.
5. Zhu, H., J. Fan, J. Du, and X. Peng, *Fluorescent Probes for Sensing and Imaging within Specific Cellular Organelles.* Acc Chem Res, 2016. **49**(10): p. 2115-2126.
6. Okamoto, K., Perlman, P. S., Butow, R. A. , *Targeting of green fluorescent protein to mitochondria.* Methods Cell Biol., 2001. **65**: p. 277-283.
7. Li, R.S., P.F. Gao, H.Z. Zhang, L.L. Zheng, C.M. Li, J. Wang, Y.F. Li, F. Liu, N. Li, and C.Z. Huang, *Chiral nanoprobes for targeting and long-term imaging of the Golgi apparatus.* Chem Sci, 2017. **8**(10): p. 6829-6835.
8. Klymchenko, A.S., *Solvatochromic and Fluorogenic Dyes as Environment-Sensitive Probes: Design and Biological Applications.* Acc Chem Res, 2017. **50**(2): p. 366-375.
9. Klymchenko, A.S. and R. Kreder, *Fluorescent Probes for Lipid Rafts: From Model Membranes to Living Cells.* Chem. Biol., 2014. **21**(1): p. 97-113.

5. Résumé de thèse en Français

Introduction

La microscopie fluorescente est une technique puissante pour une étude non-invasive des cellules vivantes.[1] Cependant, cette technique est basée sur la performance des sondes fluorescentes utilisées dans les expériences. Les principales caractéristiques d'une sonde fluorescente sont la brillance, la photostabilité, les maxima d'absorption et d'émission du fluorophore,[2] mais aussi la sélectivité de la sonde vers la cible. Nous nous sommes particulièrement intéressés aux sondes sur des membranes biologiques, qui sont présentes à la fois à la surface des cellules (membranes plasmiques) et dans les compartiments intracellulaires des organites. Les sondes efficaces sur les biomembranes doivent combiner de multiples fonctions comme le ciblage spécifique d'une membrane donnée, la sensibilité à l'environnement et la comptabilité avec les techniques microscopiques avancées (comme la microscopie à super-résolution). Le ciblage spécifique des organites dans les cellules vivantes exploite généralement soit des groupements chimiques ciblés,[3-5] soit l'introduction d'une molécule biologique qui utilise la machinerie cellulaire pour accumuler la sonde dans l'organite cible.[6, 7] La sensibilité à les propriétés locales des biomembranes incluant la polarité, la viscosité et l'ordre des lipides peut être réalisée en utilisant des sondes sensibles à l'environnement, capables de modifier leur émission de fluorescence en réponse à des changements de paramètres du microenvironnement.[8] En conclusion, la compatibilité d'une sonde avec la microscopie à super-résolution permet d'imager les membranes biologiques au-delà de la limite de résolution de la diffraction de la lumière. La localisation de molécules uniques par microscopie exige que la sonde subisse la commutation « ON/OFF » qui peut être réalisé par des photoréactions réversibles, par photoactivation ou par fixation réversible avec la cible.

Mon projet de thèse a pour objectif de :

Concevoir des sondes fluorescentes multifonctionnelles qui : (i) ciblent des compartiments de cellules spécifiques (par exemple membranes plasmiques et organites) ; (ii) réagissent aux propriétés locales de leur environnement (comme la polarité et l'ordre des lipides) ; (iii) fournissent une commutation « ON/OFF » nécessaire pour la microscopie à super-résolution ; (iv) montrent éventuellement une réactivité envers les biomolécules et autres agents.

Résultats et discussions

Sondes membranaires basée sur des cyanines. La première partie du projet est consacrée au développement de sondes à membrane plasmique (PM) avec des groupements fonctionnels potentiellement réactifs, qui permettraient de contrôler la fixation des sondes sur les biomembranes par la réaction avec des biomolécules ou des agents introduits, donnant lieu à un marquage robuste et durable. Une série de sondes basée sur des cyanines a été développée avec des motifs zwitterioniques ciblant la PM (Fig. 1), cependant les sondes marquaient significativement la surface en verre ou en plastique des plaques d'imagerie et montaient une rapide internalisation dans les cellules vivantes, probablement dû à la charge positive globale des sondes.

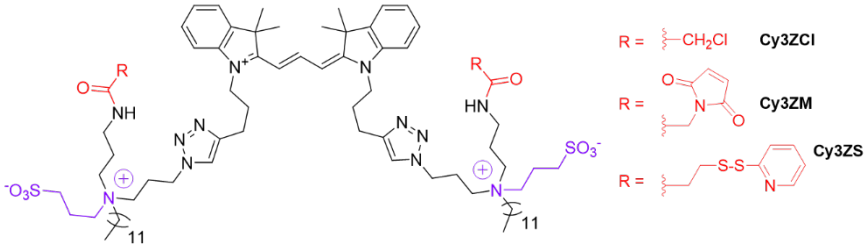

Fig. 1. Structures des sondes PM cyanines réactifs avec des motifs zwitterioniques cibles.

Comme une solution possible, nous avons développé un nouveau fragment anionique ciblant le PM, basé sur des 1-sulfonates de 3-(alkylammonium)propane à cause de leur synthèse et fonctionnalisation faciles. Sa performance a été ensuite testée en synthétisant une série de cinq colorants cyanines avec des propriétés spectrales différentes, chacun montrant deux groupements fonctionnels ciblant les membranes (Fig. 2, A).

Dans les expériences spectroscopiques avec les liposomes unilamellaires de grande taille (LUVs), les sondes cyanines anioniques montaient des rendements quantiques relativement élevés, 39-192 fois plus élevés que les valeurs obtenues dans un tampon phosphate, fournissant ainsi une réponse fluorogénique sur la présence de membranes modèles. Les expériences microscopiques dans les cellules KB vivantes montaient que par comparaison avec son analogue avec des motifs zwitterioniques ciblant, notre sonde anionique Cy5A montre beaucoup moins de marquage de surface non spécifique (Fig. 2, B) ainsi qu'une brillance plus élevée et une diminution significative de l'internalisation de la sonde (Fig. 2, C-D). De plus, des expériences de colocalisation avec le conjugué WGA Alexa-488 révélaient une sélectivité élevée des sondes cyanines anioniques envers la membrane plasmique avec une internalisation plus lente. Actuellement, ces sondes sont en cours de tests pour pour l'imagerie des tissus cérébraux vivants.

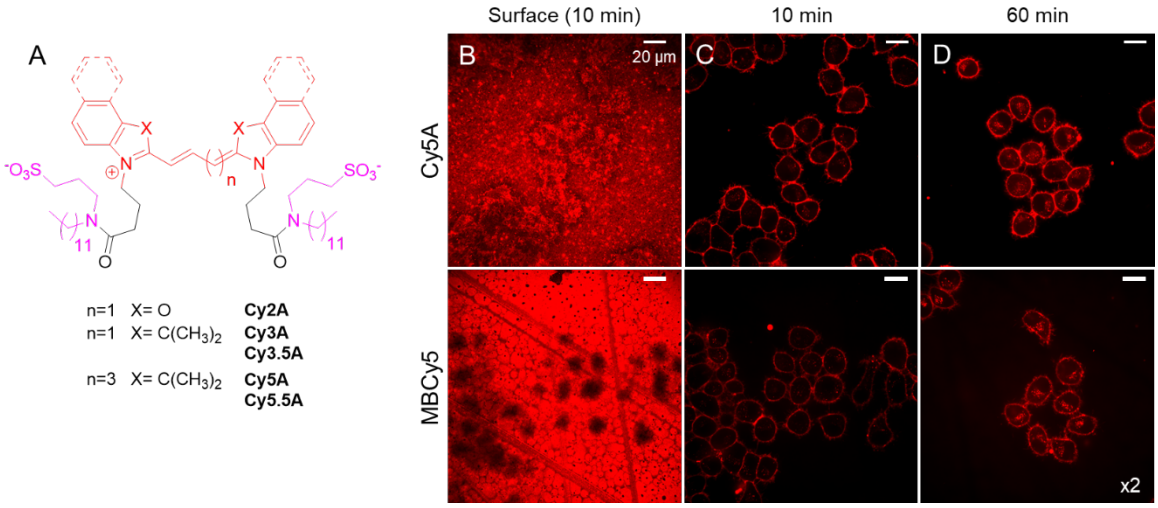

Fig. 2. Structures des sondes PM cyanines anioniques (A) et leurs performances dans les cellules vivantes (B-D) vs analogues zwitterioniques.

Après avoir obtenu le groupement ciblant la PM plus efficace, nous avons synthétisé des sondes cyanines anioniques ciblant les membranes plasmiques et portant différents groupements potentiellement réactifs (Fig. 3). Les expériences de microscopie cellulaire montraient une sélectivité élevée envers la membrane plasmique, cependant les expériences sur la réactivité chimique étaient non concluantes et demandent une étude supplémentaire.

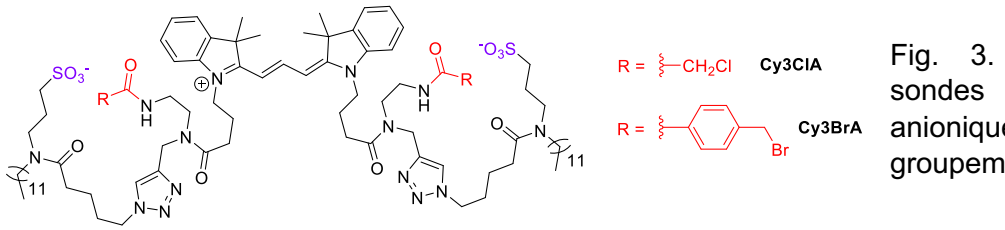

Fig. 3. Structures des sondes PM cyanines anioniques avec des groupements réactifs.

Sondes membranaires basées sur des colorants solvatochromiques. D'autre part, sur la base des résultats obtenus pour les sondes PM cyanines, nous avons cherché par la suite à greffer des colorants solvatochromiques, sensible à son environnement, avec un groupement d'ancrage anionique ciblant la membrane. Ces colorants sont particulièrement intéressants dans

la recherche sur les membranes lipidiques, parce qu'ils peuvent détecter des changements de l'ordre des lipides par modification de leur couleur d'émission.[9] Dans ce but, nous avons sélectionné deux fluorophores – Laurdan et Rouge de Nil. La sonde Laurdan largement utilisée a été totalement repensée en utilisant le fragment anionique ciblé pour obtenir la nouvelle sonde Pro12A (Fig. 4).

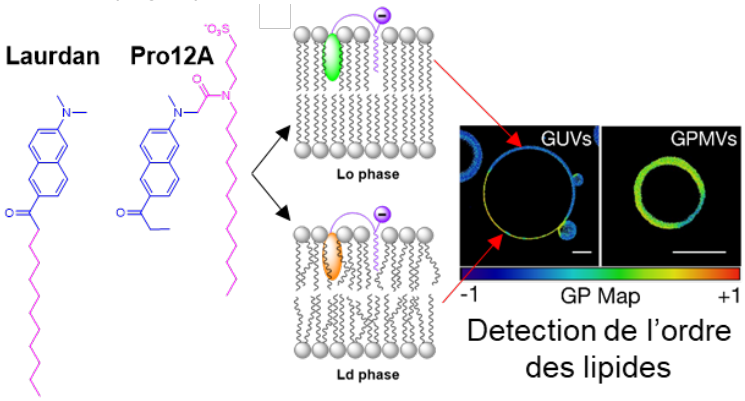

Fig. 4. Structure et mécanisme de détection de la sonde Pro12A.

Dans les expériences spectroscopiques avec les liposomes unilamellaires de grande taille (LUVs), Pro12A montait un rendement quantique de fluorescence 2-3 fois plus élevé avec une meilleure sensibilité dans l'ordre des lipides en comparaison à la sonde d'origine Laurdan.

De plus, notre sonde ne marquait que le feuillet externe des biomembranes, montrant une cinétique de liaison plus rapide grâce à une meilleure solubilité en milieu aqueux. Dans les expériences de microscopie sur les cellules vivantes, Pro12A montrait une internalisation beaucoup plus lente par comparaison aux sondes Laurdan et C-Laurdan (Fig. 5, A-D). En outre, Pro12A affichait une plus forte sensibilité à l'extraction du cholestérol (Fig. 5, E) et une absence de diaphonie avec un nombre de protéines et colorants oranges/rouges, permettant une imagerie cellulaire précise et multicolore. Nous nous attendons à ce que cette nouvelle sonde replace la Laurdan, largement utilisée, dans toutes les applications au niveau des membranes cellulaires. Les résultats sont soumis à publication.

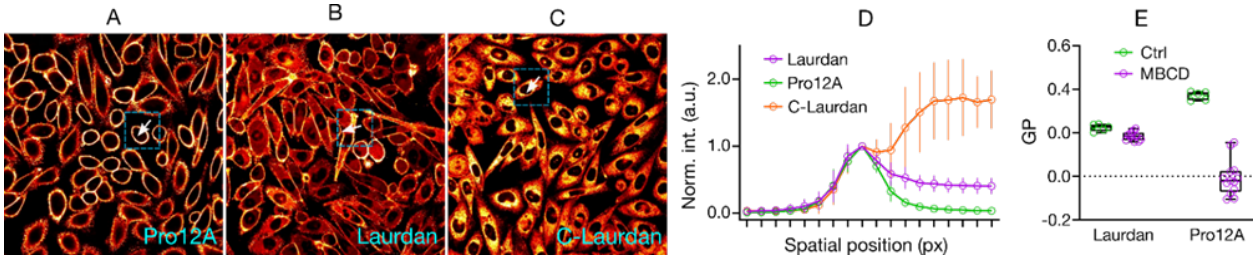

Fig. 5. Microscopie confocale de Pro12A (A) comparé à Laurdan (B) and C-Laurdan (C) dans les cellules vivantes CHO. Profils d'intensité (D) à travers les membranes plasmatiques dans les régions mises à l'évidence en A-C. Réponse de Pro12A et Laurdan après traitement au méthyl-β-cyclodextrine (E).

Par la suite, nous avons visé à créer des sondes solvatochromiques à base de Rouge de Nil, ciblant des membranes plasmiques pour la microscopie à super-résolution. Dans le but d'augmenter la photostabilité de nos sondes, nous avons développé une stratégie de fonctionnalisation en utilisant les chaines N-alkyles du Rouge de Nil (Fig. 6, A). En variant la longueur de la chaine alkyle de notre groupe d'ancrage membranaire (Fig. 6, A), nous avons synthétisé une sonde NR12A avec une fixation membranaire quasi-irréversible, valable pour la microscopie conventionnelle et une sonde NR4A avec une fixation membranaire réversible avec la commutation « ON/OFF » attendue, nécessaire pour la microscopie à super-résolution (Fig. 6, B).

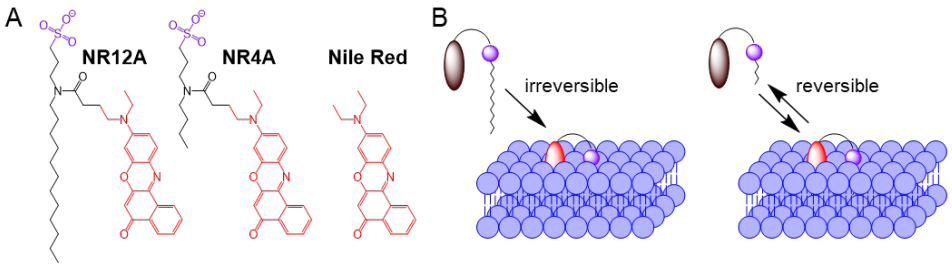

Fig. 6. Structure (A) et mécanisme de fixation (B) de NR12A et NR4A.

Les expériences spectroscopiques avec les LUVs révélaient que nos nouvelles sondes conservaient une sensibilité envers l'ordre des lipides et possédaient des rendements quantiques élevés dans les liposomes parallèlement à une photostabilité accrue. De plus, les résultats confirmaient une plus grande affinité membranaire de NR12A par rapport à NR4A. Dans les expériences sur les cellules, la sonde conventionnelle NR12A a montré une brillance et une photostabilité élevées avec un marquage spécifique des membranes plasmiques, permettant, par exemple, d'obtenir des images en 3D de membranes plasmiques sur des cellules vivantes de KB (Fig. 7, A). La sonde NR4A montait un excellent résultat en microscopie à super-résolution (PAINT) (Fig. 7, B). En outre, cette sonde a permis la visualisation de protrusions et d'invaginations nanoscopiques (Fig. 7, C-D) sur des membranes plasmiques de cellules vivantes.

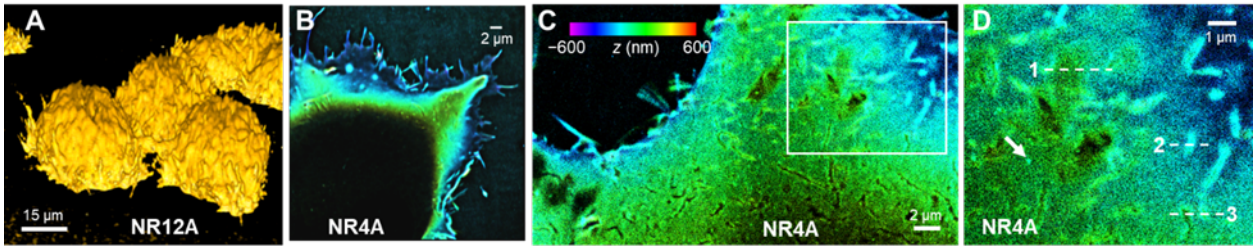

Fig. 7. (A) Images confocales 3D des cellules vivantes KB marquées avec NR12A. (B) Zoom arrière d'une image 3D PAINT de cellules vivantes COS-7 avec NR4A. (C) Image 3D PAINT de membrane plasmique supérieure d'une cellule HeLa avec NR4A. (D) Zoom avant du rectangle blanc vu dans (C).

L'imagerie PAINT résolue spectralement (SR-PAINT) a révélé que les protrusions et les invaginations ont un ordre des lipides diminué en comparaison aux régions membranaires plates (Fig. 8, A-B), suggérant une subtile connexion entre la morphologie membranaire et l'organisation des lipides. Dans les cellules fixées, NR4A est capable de pénétrer la membrane plasmique, entrainant le marquage des membranes intracellulaires (Fig. 8, C). Ainsi, nous avons développé des outils puissants qui combinent le marquage spécifique, la sensibilité et la capacité de la commutation « ON/OFF » pour la recherche sur les biomembranes. Les résultats sont publiés.

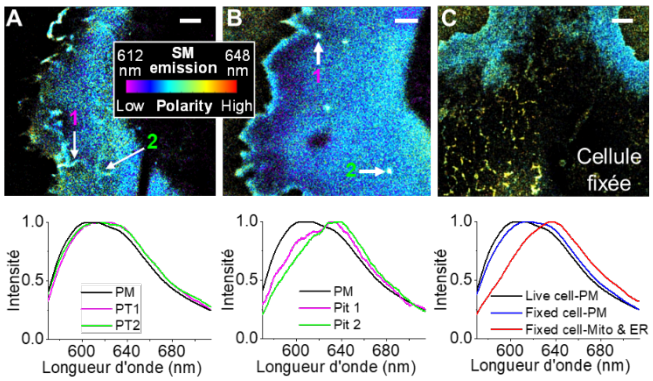

Fig. 8. SR-PAINT avec NR4A pour les membranes plasmiques de cellules vivantes COS-7 avec des protubérances tubulaires (A) et structures en amas (B). SR-PAINT avec NR4A d'une cellule fixée COS-7 (C), montrant un marquage à la fois de la membrane plasmique et des membranes internes. Spectres moyennés des molécules uniques dans les parties différentes de l'image sont représentés

en-dessous de chaque image correspondante.

Sondes solvatochromiques ciblant les organites. Finalement, afin d'étudier les structures membranaires intracellulaires, nous avons synthétisé une série de sondes solvatochromiques ciblant les organites, basées sur le fluorophore Rouge de Nil avec des groupements chimiques ciblés sur le réticulum endoplasmique (ER), la mitochondrie, les liposomes, l'appareil de Golgi et les gouttelettes lipidiques (Fig. 9, A). Ces sondes devraient modifier leur couleur d'émission en fonction de la polarité de l'environnement et de l'ordre des lipides et détecter des changements dans les organites sous des stimuli externes, comme le stress oxydatif ou le choc hyperosmotique (Fig. 9, B).

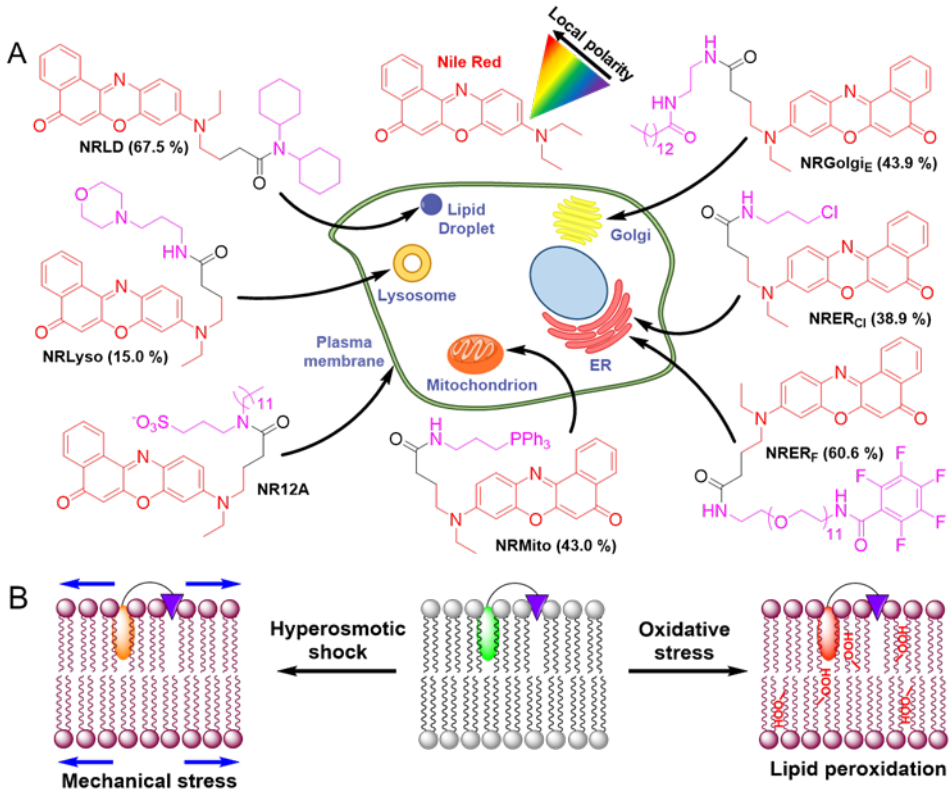

Fig. 9. Structures, localisation (A) et mécanisme de détection (B) de sondes organites de Rouge de Nil.

Les résultats de microscopie sur les cellules vivantes KB montaient que les sondes ciblant les organites se colocalisent bien avec les marqueurs commerciaux spécifiques aux organites correspondants, indiquant une bonne sélectivité envers les organites. De plus, les sondes Rouge de Nil révélaient des différences en polarité dans les organites des cellules vivantes KB aussi bien qu'un niveau de réponse différent au stress oxydatif (Fig. 10).

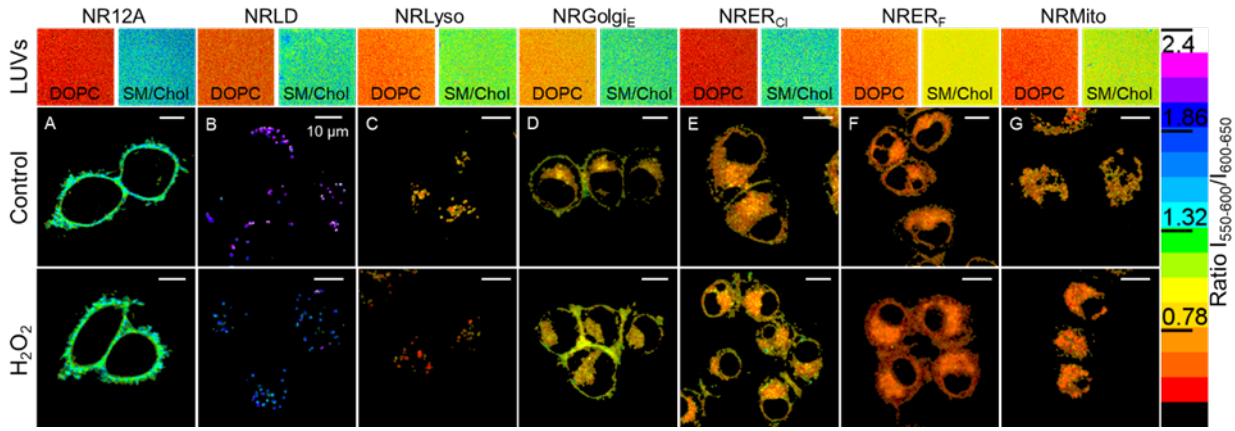

Fig. 10. Imagerie par microscopie ratiométrique de la réponse au stress oxydatif de cellules KB vivantes marquées par des sondes organites solvatochromiques.

Les sondes spécifiques des organites étaient aussi capables de détecter un choc hyperosmotique dans les cellules vivantes, avec un niveau de réponse varié pour les organites différents. Ce travail a fourni une preuve que chaque organite membranaire montre un profil de polarité unique et une réponse caractéristique au stress externe. Sur la base de ces résultats, la rédaction d'une publication à été préparé.

Conclusions

Plusieurs étapes clés ont été accomplies dans la recherche de nouvelles sondes fluorescentes multifonctionnelles dans le domaine des biomembranes.

Durant la première partie du projet, nous avons créé un fragment d'ancrage ciblant la membrane plasmique basé sur un fragment anionique amphiphile, le 1-sulfonate de 3-(alkylammonium)propane et validé son efficacité sur un nombre de fluorophores cyanines. La microscopie en fluorescence de cellules vivantes a montré que le nouveau fragment ciblé permet de diminuer l'internalisation de la sonde et la fixation non spécifique à la surface du support. De plus, nous avons obtenu des sondes ciblant des membranes basées sur des cyanines et portant des groupements réactifs qui peuvent potentiellement se greffer de façon covalente sur les protéines de membranes.

Par la suite, nous avons utilisé un nouveau fragment d'ancrage avec des sondes sensibles à la polarité comme le Laurdan et le Rouge de Nil. La nouvelle sonde basée sur le Laurdan est caractérisée par des rendements quantiques de fluorescence supérieurs et une meilleure sensibilité envers l'ordre des lipides; elle marque exclusivement le feuillet externe de la membrane, montrant une faible internalisation et une compatibilité avec un nombre de protéines et des colorants oranges/rouges pour l'imagerie des cellules vivantes. Puis, en utilisant le Rouge de Nil et des fragments ciblant des membranes avec différentes longueurs de chaines alkyles, nous avons obtenu deux sondes à membranes plasmiques avec une affinité variée sur les biomembranes : sonde avec une forte affinité, valable pour la microscopie conventionnelle et sonde avec une affinité faible, développant une commutation « ON/OFF » contrôlé par la fixation réversible, adaptée à la microscopie à super-résolution. Cette dernière sonde nous a permis de visualiser des protrusions et des invaginations à l'échelle nanométrique de membranes plasmiques dans les cellules vivantes, révélant un ordre des lipides diminué.

Finalement, nous avons créé une série de sondes solvatochromiques sensibles à l'environnement, basées sur le Rouge de Nil, avec des groupements ciblant les organites comme le réticulum endoplasmique, la mitochondrie, l'appareil de Golgi, les gouttelettes lipidiques et les liposomes. Ces sondes sont capables de percevoir les différences de polarité et l'ordre des lipides entre les différents organites, aussi bien qu'une réponse spécifique envers des stimuli externes comme le stress oxydatif et le choc hyperosmotique, comme le montraient les expériences de microscopie ratiométrique dans les cellules vivantes.

En général, nous avons élaboré des nouvelles stratégies pour des sondes biomembranaires spécifiques d'organites basées sur des sondes fluorescentes conventionnelles et sensibles à l'environnement. Nous attendons que les sondes obtenues trouvent des applications directes dans la recherche biologique et surtout dans les techniques avancées de microscopie fluorescente.

Ces sondes peuvent être améliorées par la suite, en introduisant des groupements réactifs appropriés qui permettront de contrôler la fixation de la sonde sur la cible. L'introduction d'une stratégie de liaison réversible ouvre la possibilité de créer des sondes avec un marquage sensible aux stimuli.

Références bibliographiques

1. Demchenko, A.P., *Introduction to Fluorescence Sensing*. 2009: Springer, Dordrecht.
2. Fu, Y. and N.S. Finney, *Small-molecule fluorescent probes and their design.* RSC Advances, 2018. **8**(51): p. 29051-29061.
3. Gao, P., W. Pan, N. Li, and B. Tang, *Fluorescent probes for organelle-targeted bioactive species imaging.* Chem Sci, 2019. **10**(24): p. 6035-6071.
4. Xu, W., Z. Zeng, J.H. Jiang, Y.T. Chang, and L. Yuan, *Discerning the Chemistry in Individual Organelles with Small-Molecule Fluorescent Probes.* Angew Chem Int Ed Engl, 2016. **55**(44): p. 13658-13699.
5. Zhu, H., J. Fan, J. Du, and X. Peng, *Fluorescent Probes for Sensing and Imaging within Specific Cellular Organelles.* Acc Chem Res, 2016. **49**(10): p. 2115-2126.
6. Okamoto, K., Perlman, P. S., Butow, R. A. , *Targeting of green fluorescent protein to mitochondria.* Methods Cell Biol., 2001. **65**: p. 277-283.
7. Li, R.S., P.F. Gao, H.Z. Zhang, L.L. Zheng, C.M. Li, J. Wang, Y.F. Li, F. Liu, N. Li, and C.Z. Huang, *Chiral nanoprobes for targeting and long-term imaging of the Golgi apparatus.* Chem Sci, 2017. **8**(10): p. 6829-6835.
8. Klymchenko, A.S., *Solvatochromic and Fluorogenic Dyes as Environment-Sensitive Probes: Design and Biological Applications.* Acc Chem Res, 2017. **50**(2): p. 366-375.
9. Klymchenko, A.S. and R. Kreder, *Fluorescent Probes for Lipid Rafts: From Model Membranes to Living Cells.* Chem. Biol., 2014. **21**(1): p. 97-113.

List of publications

1. Danylchuk D.I., Moon S., Xu K. and Klymchenko A.S. // *Switchable Solvatochromic Probes for Live-Cell Super-resolution Imaging of Plasma Membrane Organization* // Angew Chem Int Ed Engl. 2019 Oct 14;58(42):14920-14924. *doi: 10.1002/anie.201907690*

2. Valanciunaite J., Kempf E., Seki H., Danylchuk D.I, Peyriéras N., Niko Y. and Klymchenko A.S. // *Polarity Mapping of Cells and Embryos by Improved Fluorescent Solvatochromic Pyrene Probe* // Anal. Chem. 2020, 92, 9, 6512–6520. *doi: 10.1021/acs.analchem.0c00023*

3. Danylchuk D.I., Sezgin E., Chabert P. and Klymchenko A.S. // *Redesigning Solvatochromic Probe Laurdan for Imaging Lipid Order Selectively in Cell Plasma Membranes* // Anal. Chem. 2020, 2020, 92, 21, 14798–14805. *doi:* 10.1021/acs.analchem.0c03559

4. Danylchuk D.I., Jouard P. and Klymchenko A.S. // *Targeted solvatochromic fluorescent probes for imaging lipid order in organelles under oxidative and mechanical stress //* Manuscript in revision.

5. Danylchuk D.I., Khalin I., Chabert P., Filser S., Plesnila N. and Klymchenko A.S. // *Fluorescent anionic cyanine plasma membrane probes for live cell and in vivo imaging* // Manuscript in preparation.

List of presentations

1. Danylchuk D.I., Moon S., Xu K. and Klymchenko A.S. /*Solvatochromic membrane probes for super-resolution imaging of lipid order* // 2019 ESB- IUPB World Congress, 25th – 30th August, 2019, Barcelona, Spain. (poster presentation)

2. Danylchuk D.I., Moon S., Xu K. and Klymchenko A.S. /*Biomembrane probs for super-resolution imaging of lipid order in live cells* // Les Journées du Campus Illkirch, 1st – 2nd April, 2019, IGBMC, Illkirch, France. (oral talk)

3. Rodik R. V., Danylchuk D. I., Kalchenko V. I and Klymchenko A. S. / *Design of Protein-sized bright fluorogenic nanoparticles via reversible click-reaction of cationic imidazolium calixarenes* // 8th International Conference "Chemistry of nitrogen containing heterocycles" in memoriam of Prof. Valeriy Orlov, 12th – 16th November, 2018, Kharkiv, Ukraine (poster presentation).

UNIVERSITÉ DE STRASBOURG

Dmytro DANYLCHUK
Environment-sensitive targeted fluorescent probes for live-cell imaging

EDSC
École Doctorale des Sciences Chimiques

Résumé

Le ciblage, l'imagerie et le sondage spécifiques des membranes plasmiques et des organites intracellulaires peuvent être faits par des sondes fluorescentes à façon sensibles à la polarité. Ici, un nouveau fragment ciblant la membrane plasmique à été développé et testé dans cinq colorants cyanines, montrant d'excellentes performances en microscopie cellulaire et *in vivo*. Le fragment à été greffé à un fluorophore solvatochrome Prodan, donnant une sonde de membrane plasmique avec une sensibilité élevée à l'ordre lipidique. Le rouge de Nil, greffé aux fragments avec les chaînes alkyles C12 et C4, à donné deux sondes solvatochromes à membrane plasmique : NR12A pour la microscopie conventionnelle, et NR4A pour la microscopie à super-résolution PAINT. Le rouge de Nil avec des groupes ciblant les organites à donné un éventail de sondes sensibles à la polarité et à l'ordre lipidique dans les membranes des organites. Les sondes synthétisées trouveront des applications en bioimagerie, biologie cellulaire, biophysique ou mécanobiologie.

Mots clefs : sondes fluorescentes, membrane plasmique, ciblage des organites, ordre lipidique, microscopie à super-résolution.

Résumé en anglais

Specific targeting, imaging and probing of cell plasma membranes and intracellular organelles can be addressed by rationally designed polarity-sensitive fluorescent probes. Here, a new efficient plasma membrane-targeting moiety was developed and tested in five cyanine dyes, showing excellent performance in cellular and *in vivo* microscopy. Next, the targeting moiety was grafted to a solvatochromic dye Prodan, yielding a plasma membrane probe with high lipid order sensitivity. Modifying a Nile Red using the moieties with varied alkyl chain lengths resulted in two solvatochromic plasma membrane probes: NR12A with high affinity to membranes for conventional microscopy, and NR4A, a low-affinity probe for PAINT super-resolution microscopy. Tethering Nile Red with organelle-targeted groups yielded an array of probes, able to sense polarity and lipid order in organelle membranes. The synthesized probes will find applications in bioimaging, cell biology, biophysics or mechanobiology.

Keywords: fluorescent probes, plasma membrane, organelle-targeting, lipid order, super-resolution microscopy.